A NOVEL FLUORESCENCE BASED METHOD OF ASSESSING SUBSURFACE DAMAGE IN OPTICAL MATERIALS

by

Wesley Bryant Williams

A dissertation submitted to the faculty of
The University of North Carolina at Charlotte
in partial fulfillment of the requirements
for the degree of Doctor of Philosophy
in Mechanical Engineering

Charlotte

2009

Approved by:

____

Dr. Brigid A. Mullany

____

Dr. Kent Curran

____

Dr. Angela D. Davies

____

Dr. Scott Smith

____

Dr. Stuart Smith

© 2009
Wesley Bryant Williams
ALL RIGHTS RESERVED

ABSTRACT

WESLEY BRYANT WILLIAMS. A novel fluorescence based method of assessing subsurface damage in optical materials. (Under the direction of DR. BRIGID A. MULLANY)

Lapping and polishing are loose abrasive finishing processes that have been used to achieve critical surface parameters in optical materials for centuries. These processes remove material from the surface through a variety of mechanical and chemical interactions. These interactions influence not only the surface of the finished material, but also the subsurface, the region immediately beneath the surface. These processes may induce a damaged layer of cracks, voids and stressed material below the surface. This subsurface damage (SSD) can create optical aberrations due to diffraction, propagate to the surface, and reduce the laser induced damage threshold of the material.

It is difficult to detect SSD, as these defects lie beneath the surface. Methods have been developed to detect SSD, but they can have notable limitations regarding sample size and material, preparation time, or they can be destructive in nature. The author tested a non-destructive method for assessing SSD that consisted of tagging the abrasive slurries used in loose abrasive finishing with quantum dots (nano-sized fluorescent particles). Subsequent detection of fluorescence on the processed surface is hypothesized to indicate SSD.

Quantum dots present during the lapping process were retained in the glass sample through subsequent polishing and cleaning processes. The quantum dots were

successfully imaged by both wide field and confocal fluorescence microscopy techniques. The detected fluorescence highlighted defects that were not observable with optical or interferometric microscopy. Analysis indicates that most dots are firmly embedded in the surface, however examination of confocal fluorescence scans beneath the surface did show incidences of quantum dots at depths up to 10 µm beneath the surface. The incidence of these deep features was less than 20% of the sites examined. Etching of the samples exhibiting fluorescence confirmed the presence of SSD and provided a conservative SSD depth estimate of 10 µm. These etching results confirm the hypothesis that quantum dots can tag SSD. Further testing demonstrated that for quantum dots to be embedded in the surface they must experience the dynamics of the lapping process, and that quantum dots can only tag brittle fracture sites.

Quantum dots that were introduced to YAG samples during loose abrasive finishing were only retained on the surface and at levels consistent with simple exposure to quantum dots prior to cleaning, possibly highlighting surface defects that were not apparent with conventional microscopy. Subsequent etching of the YAG samples showed low levels of fracture in the subsurface region, indicating few suitable defects to house the quantum dots.

In addition to the research above, an instrument was design and built to measure the axial and torque loads during loose abrasive finishing. Experiments with this measurement head showed expected increases in material removal rate and surface roughness with increased axial load. Results from these tests were also used to

corroborate SSD depth estimates from glass samples finished with quantum dot laden slurries.

ACKNOWLEDGMENTS

Nothing that I have accomplished to this point would have been plausible without the continued assistance of countless people. In my doctoral research, Dr. Brid Mullany has provided the firm foundation to transform me from being a designer into a researcher. She has pushed to me seek a greater understanding of the literature, expect more from my experiments, and most importantly expect more from my writing. These high expectations have been balanced with understanding when I have been pulled in numerous directions by obligations both voluntary and unavoidable. I have also benefitted from Dr. Mullany's success in grant writing, as this work was financially supported by the National Science Foundation (Grant #0620783).

I am also fortunate to have enjoyed interactions with my committee members in other capacities at the university. Dr. Kent Curran was always a sound voice on the Graduate Council whose thorough preparation allowed him to see both the crux of the issues before the council as well as the potential unintended consequences of well-intentioned proposals. In addition to her technical prowess, Dr. Angela Davies provided a much-needed example of a highly involved researcher who managed to balance those demands with being a parent for small children and a spouse to a partner in an equally demanding profession. Being in Dr. Scott Smith's classes set the bar for how I would like to be as an instructor. Beyond a rigorous understanding of the material, he understood the students and how to structure the class and the assignments to make the material stick. Finally, for every time I tried ease up on myself and say 'There is no way that one person could be expected to know all this.' my interactions with Dr. Stuart Smith

dispelled me of this notion. His ability to recall and apply information across a wide range of disciplines remains an ideal to which I aspire.

In addition to my committee, countless people at UNC Charlotte have made the experience memorable. John Brien, Roland Hege and Jimmie Miller were all excellent sources of technical advice and social distraction. Tracey Beauregard has been a guardian angel guiding me through the sometimes Byzantine bureaucracy of forms and policies for graduate students. Alan, Beth, Pam, Rahul and Shane all made working in lab more festive with their company. Dr. Gloria Elliott and Dr. Terry Xu were a tremendous help providing access to equipment, expertise, and students whenever I requested it. Dr. Pat Moyer in the Department of Physics and Optical Science was very tolerant of my constant requests for access to the microscope and Wes Parker. Not enough can be said of the work that Wes Parker did in supporting me through this work. Through countless hours in a dark lab looking at samples and troubleshooting equipment, he rarely complained. He served as a sounding board on a wide range of topics and could be credited with me retaining my perspective through it all.

Outside the academic world, I have excellent support within industry. My colleagues from my time at GlaxoSmithKline were excellent sources of information for a freshly minted engineer. In various ways, Adrian, Charlie, David showed me what it meant to be an engineer while Frank, John, and Keith showed me how to not run afoul of machinists, while still being an engineer. Those relationship were mirrored in my time at Northrop Grumman Synoptics, where Jerry, Mark, and Bryan provided great

examples of engineering while Mario, Brian and Tom took the time necessary to show an intern how things worked in production.

Beyond my academic and industrial experience, there have been relationships that have stood out in hindsight as being instrumental in where I have ended up. My time at the North Carolina School of Science and Math both as a student and as a mentor has provided a foundation for learning and friendships that I lean on time and again. Following my undergraduate studies, I had the good fortune to work with Jimmie Johnson, a machinist at Durham Technical Community College. His patience and good natured ribbing transformed me from a 'book engineer' into someone who could actually design and build something. In my studies at Georgia Tech, Dr. Farrokh Mistree was a standout, challenging many of my assumptions about engineering, learning, and myself in general. Most recently, Nobuyuki Zettsu and Osaka University invigorated my research with their hospitality at their symposium on Atomically Controlled Fabrication. Their interest in my research gave me a much needed new perspective that helped to push the experiments forward.

Finally, I must thank my family for their endless support in my ventures. I have experienced enough to know that a supportive family is not to be taken for granted, and mine have been outstanding. From my grandparents who instilled a value for learning and education at an early age to my sister whose overachievement took the pressure of her older brother to be 'the good kid'. Mom and Dad were great during those critical years, calling me out for mediocre performances (even when mediocre performance were sufficient) yet being supportive and understanding of me at times when I struggled

to understand myself. I was fortunate in marriage that I added a father-in-law and mother-in-law that have supported and appreciated my work, with Kathy in particular unleashing her inner scientist with her queries of my research and lists of recommended reading.

Finally, my wife Suzanne has been exceedingly patient through my research. At countless law firm socials she has stoically answered “He is a student” when asked “What does your husband do?” She has not complained (excessively) about my meager financial contribution to the family and has stepped up with Herculean endurance to carry my share of the parenting responsibilities as countless deadlines have come up in my research. She has tolerated rants when equipment was not available and prodded me to get things done when it was available. I could not have done it without her.

TABLE OF CONTENTS

LIST OF ABBREVIATIONS xvi

LIST OF SYMBOLS xviii

DISCLAIMER xxi

CHAPTER 1. INTRODUCTION 1

1.1 Applications of the Research 2

1.2 Structure of the Dissertation 3

CHAPTER 2. LITERATURE REVIEW 6

2.1 Lapping and Polishing: History, Applications, and Understanding 6

2.1.1 Polishing History and Applications 7

2.1.2 Lapping and Polishing Metrics 10

2.1.3 Lapping and Polishing Setups 14

2.1.4 Lapping and Polishing Material Removal Mechanisms 17

2.2 Polishing Processing Monitoring 25

2.2.1 Slurry Monitoring 26

2.2.2 Polishing Dynamics Monitoring 26

2.2.3 Thermal Measurements 29

2.3 Subsurface Damage 30

2.3.1 Mechanisms that Generate Subsurface Damage 31

2.3.2 Some Indentation Experiments related to SSD 38

2.3.3 Traditional Methods of Assessing Subsurface Damage 39

2.3.4 Recent Methods for Assessing Subsurface Damage 46

2.4 Instrumentation 51

2.4.1 Optical Microscopy 51

2.4.2 White Light Interferometer 54

2.4.3 Atomic Force Microscope 55

2.4.4 Wide Field Fluorescence Microscope 57

2.4.5 Confocal Scanning Laser Microscopy 58

2.5 Fluorescence and Quantum Dots 62

2.5.1 Quantum Dots 64

CHAPTER 3. EXPERIMENTAL PROCEDURES 67

3.1 Loose Abrasive Finishing 67

3.1.1 Equipment 68

3.1.2 Consumables 69

3.1.3 Finishing Processes 73

3.1.4 Analytic Processes 75

3.2 Sample Measurements 76

3.2.1 Material Removal Rate 77

3.2.2 Optical Microscope 78

3.2.3 Wide Field Fluorescence Microscope 79

3.2.4 White Light Interferometer 79

3.2.5 Profilometer 80

3.2.6 Atomic Force Microscope 80

3.2.7 Confocal Microscope 81

3.2.8 Confocal Fluorescence Control Samples 95

3.2.9 A Note about the Sequence of Measurements 101

3.3 Etching 102

3.3.1 Etching Equipment 103

3.3.2 Glass Etching 104

3.3.3 YAG Etching 105

3.4 Initial Loose Abrasive Processing Results 108

3.4.1 Glass Process 109

3.4.2 YAG Process 110

CHAPTER 4. MODEL OF QUANTUM DOT AND SURFACE INTERACTIONS 113

4.1 Model 113

4.1.1 Hypothesized Interactions of Quantum Dots with the Lapped and Polished Surface 114

4.1.2 Model for Quantum Dot Interaction with the Glass Surface 114

4.1.3 Assumptions of the current presented model 119

4.2 Cleaning Tests 122

4.2.1 Cleaning Test Procedure (Wide Field Fluorescence) 123

4.2.2 Wide Field Test Results 123

4.2.3 Cleaning Test Procedure (Confocal Fluorescence) 124

4.2.4 Cleaning Test Results (Confocal Fluorescence) 124

4.3 Micro Indentation Tests 125

4.3.1 Equipment 125

4.3.2 Micro Indentation Process 125

4.3.3 Fluorescence Results 127

4.4 Discussion 129

CHAPTER 5. QUANTUM DOTS IN LOOSE ABRASIVE SLURRIES WITH GLASS 131

5.1 Procedures 131

5.1.1 Lapped and Polished with no Quantum Dots 131

5.1.2 Immersion 110 132

5.1.3 Lapped and Polished with Quantum Dots (LPQ) 132

5.1.4 Lapped and Polished with Quantum Dots then Etched (LPQ-E) 132

5.1.5 Lapped and Polished with Quantum Dots the Pitch Polished (LPQ-P) 133

5.1.6 Pad Polished with Quantum Dots PQ30 133

5.1.7 Lapped, Immersed in Quantum Dots, Pad Polished without Quantum Dots (LIQP) 134

5.1.8 A note about sample storage 134

5.2 Results 135

5.2.1 Lapped and Polished (without Quantum Dots) LP 135

5.2.2 Immersion 110 135

5.2.3 Lapped and Polished with Quantum Dots (LPQ) 137

5.2.4 Lapped and Polished with Quantum Dots then Etched (LPQ-E) 145

5.2.5 Lapped and Polished with Quantum Dots the Pitch Polished (LPQ-P) 146

5.2.6 Pad Polished with Quantum Dots PQ30 156

5.2.7 Lapped, Immersed in Quantum Dots, Pad Polished without Quantum Dots (LIQP) 159

5.3 Discussion 160

5.3.1 Retention of Quantum Dots based on Sample Processing 161

5.3.2 Comparison of Defect Depths 165

5.3.3 Summary of Findings 169

CHAPTER 6. QUANTUM DOTS IN LOOSE ABRASIVE SLURRIES WITH YAG 171

6.1 Procedures 171

6.1.1 YAG Control 171

6.1.2 YAG Immersion 450 172

6.1.3 YAG Lapped and Polished in the presence of Quantum Dots (YLPQ) 172

6.2 Results 172

6.2.1 YAG Control 173

6.2.2 YAG Immersion 450 173

6.2.3 YLPQ 174

6.3 Discussion 179

CHAPTER 7. DESIGN AND APPLICATION OF A LOOSE ABRASIVE PROCESS (LAP) MEASUREMENT HEAD AND PRELIMINARY RESULTS 182

7.1 Design of the Loose Abrasive Process Measurement Head 182

7.1.1 Design Requirements and Proposed Solution 182

7.1.2 Mechanical Design of the LAP Measurement Head 185

7.1.3 Electrical Design of the LAP Measurement Head 189

7.1.4 Labview Interface for the LAP Measurement Head 191

7.2 Variable Load Lapping with the LAP Measurement Head 192

7.2.1 Equipment 192

7.2.2 Procedures 193

7.2.3 Material Removal Rate Results 194

7.2.4 Fractured Sample Results 196

7.2.5 Discussion 199

CHAPTER 8. CONCLUSIONS AND FUTURE WORK 206

8.1 Conclusions 206

8.2 Future Work 212

8.2.1 Recommended Experiments 212

8.2.2 Recommended Larger Projects 217

REFERENCES 221

APPENDIX A: MATLAB CODE FIAT.M 231

APPENDIX B: MATLAB CODE HOTSPOT.M 237

APPENDIX C: MATLAB CODE FIAT.M 238

APPENDIX D: ADDITIONAL CONFOCLAL FLUORESCENCE IMAGES AND FEATURE PROFILES 239

APPENDIX E: PUBLICATIONS AND PRESENTATIONS OF THIS RESEARCH 243

LIST OF ABBREVIATIONS

AFM	Atomic Force Microscope
CMP	Chemical Mechanical Planarization
CSLM	Confocal Scanning Laser Microscope
DIC	Differential Interference Contrast
FWHP	Full Width Half Power
HF	Hydrofluoric Acid
I110	Glass samples that were immersed in quantum dots for 110 minutes before being cleaned
LIDT	Laser Induced Damage Threshold
LIQP	Lapped Glass Samples Immersed in Quantum Dots then Pad Polished
LMS	Laser Modulated Scattering
LPQ	Glass samples lapped with a quantum dot tagged slurry, immersed in quantum dots then pad polished with a quantum dot tagged slurry
LPQ-E	LPQ samples that have undergone a quick etching process
LPQ-P	LPQ samples that have undergone an additional pitch polishing process
MRF	Magneto Rheological Finishing
MRR	Material Removal Rate
NA	Numerical Aperture
Nd:YAG	Neodymium Doped Yttrium Aluminum Garnet

PQ30	Glass samples which were not polished, but were pad polished with quantum dot tagged slurries
PTM	Photothermal Microscopy
SPCM	Single Photon Counting Module
SSD	Subsurface Damage
TIRM	Total Internal Reflection Microscopy
WLI	White Light Interferometer
XRD	X-Ray Diffraction
YAG	Yttrium Aluminum Garnet
YLPQ	YAG samples lapped with a quantum dot tagged slurry, immersed in quantum dots then pad polished with a quantum dot tagged slurry

LIST OF SYMBOLS

A	Hamaker Constant
A_C	Contact Area
A_P	Cross Sectional Area of the Particle
a	Contact radius
a_0	Contact radius (no load)
C	Chemical Phenomenon Driving Material Removal
C_D	Coefficient of Drag
D	Diameter of the Quantum Dot
$D_{abrasive}$	Diameter of the Abrasive
D_S	Sample diameter
E	Modulus of Elasticity
E_K	Composite Modulus
F_D	Force of Drag
F_{VDW}	van der Waals Force
h	Sample Height
I	Fluorescence Intensity
I_0	Maximum Fluorescence Intensity
K	Axial Scaling Factor
K_P	Preston Coefficient
L	Axial Load
M	Mechanical Phenomenon Driving Material Removal

M_{HYDRO}	Moment Applied by Hydrodynamic Forces
M_{VDW}	Moment Applied by Adhesion Forces
MRR	Material Removal Rate
NA	Numerical aperture
n	Index of Refraction
P	Contact Load
p_0	Characteristic Stress
R	Radius of the Platen
R_a	Average Surface Roughness
R_C	Rate Factor for Absorption
R_q	Root Mean Squared Surface Roughness
R_0	Base Rate of Material Removal
r	Separation distance
r_{DIFF}	Resolution
Re	Reynolds Number
U	Total System Energy
U_E	Elastic Strain Energy
U_S	Fracture Surface Energy
v	Velocity of the Fluid
v_{max}	Maximum Velocity of the Tool Relative to the Workpiece
W_L	External Load Work
w	Laser Beam Width

x	Displacement along the x-axis
y	Displacement along the y-axis
y_i	Measured Deviation from the Mean Line
z	Displacement along the z-axis
α	Indenter Geometry Parameter
Δd	Depth of Material Removed
ΔH	Change in Height
Δm	Mass Removed
Δt	Change in Time
Δs	Distance Traveled
$\Delta \gamma$	Work of Adhesion
ε	Equilibrium Spacing
θ	Angle of Incidence
λ	Wavelength
μ	Viscosity
ν	Poisson ratio
ρ	Slurry Density
ρ_W	Sample Density
σ_{11}	Principle Stress
σ_{22}	Principle Stress
σ_{33}	Principle Stress
ω	Rotational Speed of the Platen

DISCLAIMER

This material is based upon the work supported by the Nation Science Foundation under Grant No. 0620783. Any opinions, findings, and conclusions or recommendations expressed in this material are those of the authors and do not necessarily reflect the views of the National Science Foundation.

CHAPTER 1. INTRODUCTION

This work uses fluorescent quantum dots (nanoscale semiconductor crystals) added to abrasive slurries as a means to detect subsurface damage that is created as a result of the loose abrasive finishing of optical materials. The overall goal of this research is to provide a workshop level assessment of damage that lies beneath a smooth polished surface that is undetectable by conventional microscopy or interferometry. Additional academic insights into the mechanisms of defect generation in particular and material removal are also obtained.

The addition of quantum dots to the loose abrasive slurries offers the possibility of highlighting SSD defects because a) the quantum dots are present while the dynamics that generate the defects take place, b) the dots are sufficiently small (approximately 7.8 nm in diameter) to be able to travel into the defects, and c) the dots exhibit high levels of fluorescence that will be easily detected. The fluorescence from the quantum dots is detected with a custom confocal microscope that can image fluorescence both on and beneath the surface. The ability of the confocal setup to exclude out of focus fluorescence enables determining the depth of the quantum dot (and damage) in the sample.

Samples of glass and YAG (yttrium aluminum garnet) were finished with quantum dot tagged abrasive slurries. Confocal fluorescence microscopy detected

subsurface damage (tagged by fluorescing quantum dots) in glass samples that was undetectable with conventional microscopy, white light interferometry, and atomic force microscopy. Confocal fluorescence microscopy was also found to highlight surface features that were otherwise only detected with atomic force microscopy.

The presence of the subsurface defects was confirmed by etching procedures that were developed for both the glass and YAG specimens. Examination of the etched surfaces confirmed the presence of subsurface damage in all samples with significant fluorescence, and provided conservative SSD depth estimates of 10 μm and 3 μm for glass and YAG respectively. Some types of subsurface defects were not detected with the quantum dots, such as SSD due to scratches (plastic deformation) and chatter marks (dynamic stress fields).

1.1 Applications of the Research

Subsurface damage (SSD) is a key concern for high energy optics as it can serve as an initiation site for further defects development. These defects can lead to internal reflections or absorption that can lead to thermal gradients and catastrophic failure of the components. Components that have been processed to remove SSD have higher laser induced damage thresholds (LIDT), meaning that they handle higher levels of energy without risking the aforementioned failures. Components that undergo a final coating operation are also subject to SSD concerns as the heat and pressure of the coating operations can cause defects in the subsurface to propagate to the surface, degrading its quality. The optics in these cases range in cost from hundreds of dollars (for a YAG laser rod) to millions of dollars (for the coated optics for a lithography

system). The appearance of SSD in these applications can lead to costly rework to remove the damage in the component, replacement of the component if the damage cannot be removed, or possible damage to adjacent components in the event of a failure.

Given the detrimental effects of SSD on their final products, industries involved in producing high quality optical components could make use of the techniques described in this research. The addition of quantum dots to the slurries used in process validation or troubleshooting batches would provide valuable quick insights into whether or not SSD in the form of brittle fractures is still present in the workpiece. This method offers significant advantages over existing SSD detection techniques in that it is quicker due to less sample preparation and has lower associated capital costs.

1.2 Structure of the Dissertation

The dissertation starts with a review of the history, applications, and importance of polishing optical components. The key parameters for characterizing polished components are identified and explained, particularly focusing in on subsurface damage, the polishing parameter of most interest in this work. The section then finishes with an overview of the instrumentation and techniques used to assess polished surfaces as well as background on fluorescence and quantum dots, which play a key role in the novel means proposed for assessing subsurface damage.

Chapter 3 covers the measurement equipment and procedures as well as other equipment and procedures utilized in this research. This is followed by details of the lapping and polishing procedures which were developed to produce high quality

surfaces on glass and YAG samples, while reliably inducing a layer of subsurface. The etching procedures used to assess the presence of subsurface damage in both the glass and YAG samples as well as the process validation results are presented.

Chapter 4 presents a model for quantum dot interactions with a glass surface, identifying the relevant forces that would lead toward adhesion or removal of the particles during polishing. The modeling is then verified with experimental results confirming that diffusion of quantum dots is not a concern. The chapter finishes with procedures and results for two preliminary experiments. The first being a test of the effectiveness of cleaning procedures and the second whether quantum dots are retained in micro indentation defects created in their presence.

Chapters 5 and 6 cover how the lapping and polishing procedures established in Chapter 3 were modified to introduce quantum dots into the process. The fluorescence results for various sample treatments are reported and compared to conventional measures and some initial conclusions are drawn.

Chapter 7 shifts focus to the polishing measurement head, with the first portion focusing on the design requirements and design process that resulted in the current embodiment. The second portion details how the measurement head was used to perform variable load lapping of glass samples and reports on how those variations in sample loading influenced the depth of fractures that extended from the lapped surface into the bulk of the material.

A final chapter summarizes the finding of the previous chapters, offering analysis and conclusions. The natural avenues for future work are identified and multiple appendices provide additional supporting information.

CHAPTER 2. LITERATURE REVIEW

As ancient methods of processing material, lapping and polishing have a long history. This chapter covers some of that history, looking at the applications that have required loose abrasive finishing and driven the need for greater understanding of the process. This is followed by an introduction to the important metrics for lapped and polished parts and an overview of typical loose abrasive finishing setups. Subsurface damage, the main topic of this dissertation, is outlined in Chapter 2.3 with attention to both the theory for its generation as well as existing methods for detecting subsurface damage. A chapter on instrumentation covers basic theory and operation of the numerous instruments used in this research. The literature review concludes with a primer on fluorescence and quantum dots which play a key role in the novel means of investigating subsurface damage described in Chapters 5 and 6.

2.1 Lapping and Polishing: History, Applications, and Understanding

Lapping and polishing are manufacturing processes where loose abrasives travel across a workpiece, removing material to meet critical dimensions, smooth the surface and remove tool marks and damage from previous processing[1] [2]. The processes are characterized by low material removal rates compared to other manufacturing processes (turning and milling) but smoother surface finishes [3]. Lapping and polishing are most akin to grinding (another multipoint cutting operation), but differ from

grinding in that the abrasives are not rigidly fixed to the tool and the loading is much lower. The mobility of the abrasive particles and the lower loads results in a smoother surface with lapping polishing, but comes at the expense of a much lower material removal rate compared to grinding [4]. These low material removal rates makes polishing components a costly proposition in terms of time and money, but it remains one of the few manufacturing processes able to achieve sub nanometer roughness[1, 3].

The distinction between lapping and polishing is not clear, but there are some general guidelines. Lapping processes involve slurry of larger abrasive particles, a hard pad or platen, and often result in a non-specular (matte) finish. Polishing processes utilize slurries with smaller abrasive particles (submicron), pitch tools or pads that offer some compliance, and most importantly produce a mirror like finish. The material removal mechanisms between lapping and polishing are thought to be quite different as well, with lapping being dominated by brittle fracture as a result of loading on the abrasives while the material removal mechanisms in polishing are more complex, including both the physical loading as well as the chemistry of the system.

2.1.1 Polishing History and Applications

Parts are lapped and polished for reasons of both function and aesthetics. A polished part which reflects light and images is often perceived as being more attractive, more valuable and more refined. This made polishing a key process historically for jewelers as polished metals and gemstones could command higher prices. There are artifacts from the Bronze Minoans and Neolithic Chinese that show evidence of polishing with corundum circa 1500 BC and 3500 BC respectively [5]. Evidence of

diamond polishing has been dated back to nearly 500BC in India and 2500 BC in China [5].

Some evidence in Egyptian archaeology indicate that lenses have been polished as far back as 2600 BC [6], either by hand or simple lathes, to create lifelike eyes for statues. According to Woods, lenses get their first clear reference in literature in Aristophanes Greek satire, *The Clouds*, from 424 BC[6]. By 1299, lenses were more commonly seen as eyeglasses became more prevalent. Quality varied greatly though as lens production was still based on handcrafting [6].

The scientific approach to lens crafting began with da Vinci who designed a machine that would simultaneously grind several lenses at once. While there is no evidence that the device was built, it did shown a key insight in that the lenses were made of spherical regions[6]. With Galileo's use of a telescope in astronomy, the scientific community's interest in lenses and lens crafting increased dramatically. To produce repeatable optics, the glass workpiece was mounted in a lathe that was then hand cranked as a tool tip ground the rough contour. The contour was matched against a metal gage, which was crafted to match a compass drawn arc [6]. Even with these simple lathes, innovations were common to improve performance, such as flywheels to smooth out the variations of hand cranked power and a pivoting boring bar that enabled accurate hemispherical cuts [6]. This direct lathe grinding of lens gave way to the lathe turning of the tools instead. Metal laps were cut to the negative of the desired contour (convex for concave) then used with a series of finer abrasives to grind the optic[6]. Given the competitive nature of science, it was essential to have the best

optics available lest a rival have a leg up in research. This meant that notable figures in the fields of astronomy, physics and optics like Galileo, Kepler, Sir Isaac Newton and Lord Rayleigh were compelled to develop a better understanding of polishing as it related to the quality of their optical components [6-9]. This desire for improved optics for astronomy still drives innovation in grinding and polishing optics both for massive telescope projects and the thousands of amateur astronomers who take pride in grinding and polishing their own mirrors.

With the advent of lasers in the 1960s, polishing processes were extended to new optical materials in the form of laser crystals such as rare earth doped yttrium aluminum garnet (YAG). As with the historical opticians, current researchers look to polishing to provide better finishes on laser crystals and the associated optics. Optics with fewer defects introduce fewer aberrations into measurements and have a higher laser induced damage threshold, both of which enable more cutting edge research and applications.

The most recent drivers for advancing polishing have come from the semiconductor industry, where chemical-mechanical polishing and planarization are used to produce flat surfaces for the addition of subsequent layers in the manufacture of multiple layer interconnects for computer chips. Lithographers have also pushed the envelope for optics as they seek ever finer line dimensions to increase the component density on integrated circuits.

Polishing research has gone through brief periods which have focused on the fundamentals of the polishing process, but as an enabling technology, most of the

research has been application driven. As it currently stands much of the accumulated knowledge about polishing is material and process dependent with few unifying fundamentals that can be applied to new processes and materials. If polishing is to move more fully from an art into a science, the goal for polishing research should be a state where the underlying fundamentals of material removal are sufficiently understood that product outcomes can be reasonably predicted given process parameters.

2.1.2 Lapping and Polishing Metrics

In applications beyond polishing for cosmetic or aesthetic reasons, components and processes are judged based on a variety of metrics. Polishing as means to meet functional requirements grew alongside the field of optics. Lenses and mirrors both require the low surface roughness that can be achieved through polishing. This is driven by the relationship that a specular (mirror like) reflection off a surface requires a surface roughness (R_a) less than 1/8th of the wavelength of the incident light, based on the Rayleigh criterion as shown in Equation 2-1 below, where θ is the angle of incidence and λ is the wavelength of the light.

$$R_a < \frac{\lambda}{8\cos\theta} \text{ taking } \theta=0, \; R_a < \frac{\lambda}{8}$$ Equation 2-1

For light in the visible spectrum, this means wavelengths ranging from 400 nm to 700 nm, the roughness has to be less than 50 nm. Extensions of the Rayleigh criterion put the threshold for a smooth surface at R_a values < λ/25 [10], which gives values in the range of 16 nm. Of the traditional manufacturing processes, only polishing is able to

meet these finish requirements under typical operating conditions as reflected in Figure 2-1 below.

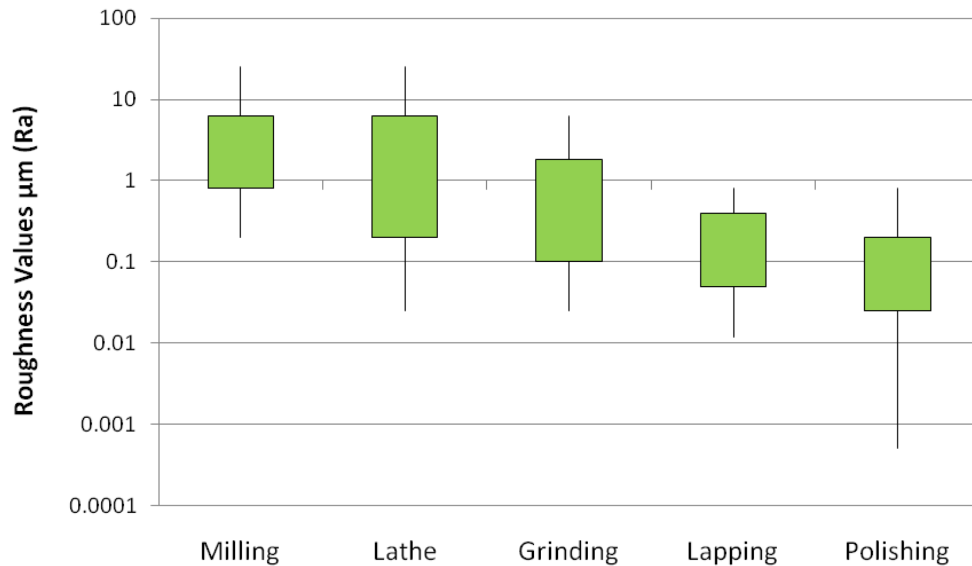

Figure 2-1. Typical Roughness Values for Various Manufacturing Processes [3]. The typical ranges of values are noted with the green rectangles, while the extreme cases for each process are noted with the lines.

Process that have been recently developed such as diamond turning, microgrinding, and ion milling are also now able to produce surfaces of similar roughness. These processes however introduce their own limitations and requirements regarding sample material, sample size, capital investment, and environmental control.

Material Removal Rate

Material removal rate (MRR) is a metric that is used to characterize the polishing process, not the part being polished. Chiefly an economic concern, material removal rate determines the throughput of a polishing process. Typically reported in depth per unit time (µm / hour), it is an equivalent measure to material removal rates for

traditional manufacturing processes (such a lathe and mill operations) and can be used in a similar fashion for engineering economics and production analysis [11].

Form

Form describes the geometric specifications for a part. Components are typically ground to near final shape, the lapped and polished to improve the surface finish and remove the subsurface damage from previous steps.

Surface Roughness

Surface roughness is a measure of the profile variation from the mean value. It is frequently reported as a R_a value or a R_q value, which correspond to average of the absolute deviations or the root mean squared of the deviations.

$$R_a = \frac{1}{n}\sum_{i=1}^{n}|y_i|$$

$$R_q = \sqrt{\frac{1}{n}\sum_{i=1}^{n}y_i^2}$$ Equations 2-2 and 2-3

Where y_i is the deviation at sample i (where i goes from 1 to n) from the mean line for all sample points and n is the total number of points sampled as shown in Figure 2-2.

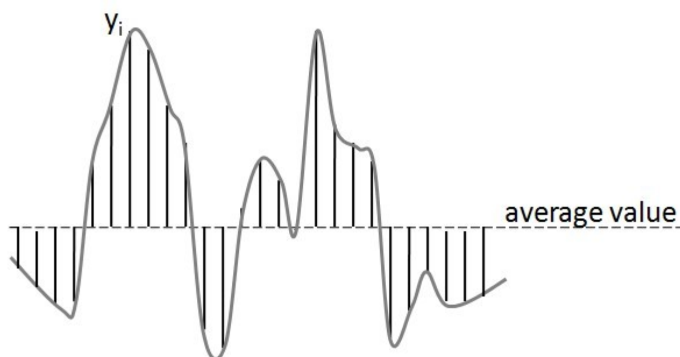

Figure 2-2. Illustration of Ra and Rq calculations.

As noted before in equation 2-1, surface roughness is important as it determines whether or not a surface will be specular for a given wavelength and angle of incidence. Recent demands for shorter wavelength optics for lithography systems, which allow for the resolution of smaller features and denser packing of components on semiconductor chips, have pushed the need for ever smoother surfaces.

Surface Quality

In addition to surface roughness requirements, many optical components are specified to meet surface quality requirements. US Military Specification for the Inspection of Optical Components, MIL-O-13830A, is a commonly used example in the United States. The surface requirements in this standard are listed as scratch and dig numbers, where lower numbers denote a lower number of acceptable defects and thus a higher quality optic. The first number in these designations refers to the maximum width (in µm) of any scratch, while the second number refers to the maximum diameter of any dig (in µm) that is acceptable for that grade of optic [12]. It is important to note that the numbers cited in these specifications do not correspond to the actual size or prevalence of defects, rather they classify the grade of the optic. As an example common research optics would be specified a 60-40 surface quality while an optic for a demanding laser application would be specified as a 10-5.

Subsurface Damage

Subsurface damage (SSD) is a layer of defects and stressed material that exists beneath an apparently good ground or polished surface without indications of the damage being apparent at the surface. These defects can negatively impact the

performance of optical components by introducing optical aberrations, if aggravated they can propagate to the surface [13] or by reducing the laser induced damage threshold (LIDT)—the measure of how much energy can be passed through an optical component without risking catastrophic failure [14]. Without apparent indications of the damage at surface, SSD is difficult to detect. Traditionally it has been assessed by etching to remove the topmost layer of the surface—exposing the defects that lie beneath [15] as well as a related technique of dimpling [13] and taper polishing. More recent methods include ion channeling, photothermal microscopy and X-ray diffraction. A more thorough treatment of subsurface damage and its detection is found in Chapter 2.3 below.

2.1.3 Lapping and Polishing Setups

Full Aperture Lapping and Polishing Setup

Full aperture polishing is characterized by a tool that is larger than the workpiece, such that the entire surface of the workpiece is in contact with the tool, which is rotating. The tool is a platen which is coated with either a layer of pitch or a pad made of a compliant material (felt, polyurethane, etc.) [16]. The surface of the tool is then flooded with an abrasive slurry to distribute the particles across the surface. Given the compliance of either pitch or the pad, abrasive particles can become embedded in the surface of the tool and be transported across the surface of the workpiece. A contact load between the workpiece and the tool is provided either by a dead weight or pressure from an overarm on the workpiece. In either case the workpiece is free to rotate about its axis, but it is controlled in translation by either a

quill connecting the overarm to the workpiece carrier or a carrier ring if a dead weight is used to provide the load. The quill and overarm arrangement provides translation by sweeping the workpiece across the rotating tool. The carrier ring varies the position of the workpiece with respect to the tool by a rotation similar to that of a planetary gear. These motions help to insure that no one area of the workpiece is polished by the same region of the tool throughout the process. It also works to maintain the form of platen which would rapidly be worn out of specification if the workpiece were left in one area.

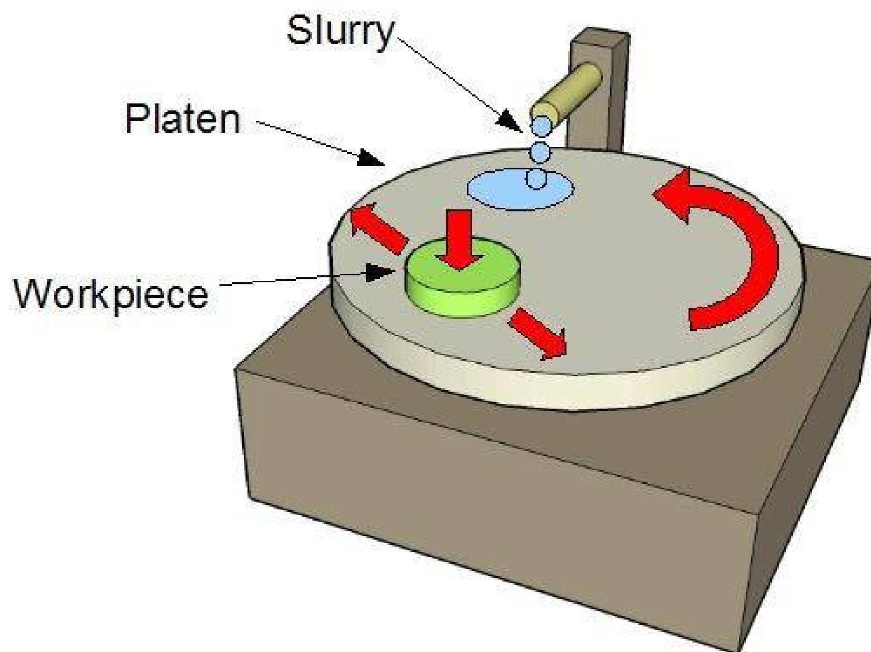

Figure 2-3: Schematic of a Full Aperture Polishing Setup

Full aperture polishing is used to produce surfaces with a constant radius, either spherical geometries or flat surfaces (which have an infinite radius).

Sub-Aperture Polishing Setup

In sub-aperture polishing, the tool is smaller than the workpiece is moved to various locations on the workpiece to remove material. The surface of the workpiece is flooded with abrasive slurry. As in full aperture polishing, the tool surface is a layer of pitch or a flexible pad that is rotated and brought into contact with the workpiece. In this case the tool is moved by an articulated arm, with the dwell time at each location on the part set to remove the appropriate amount of material.

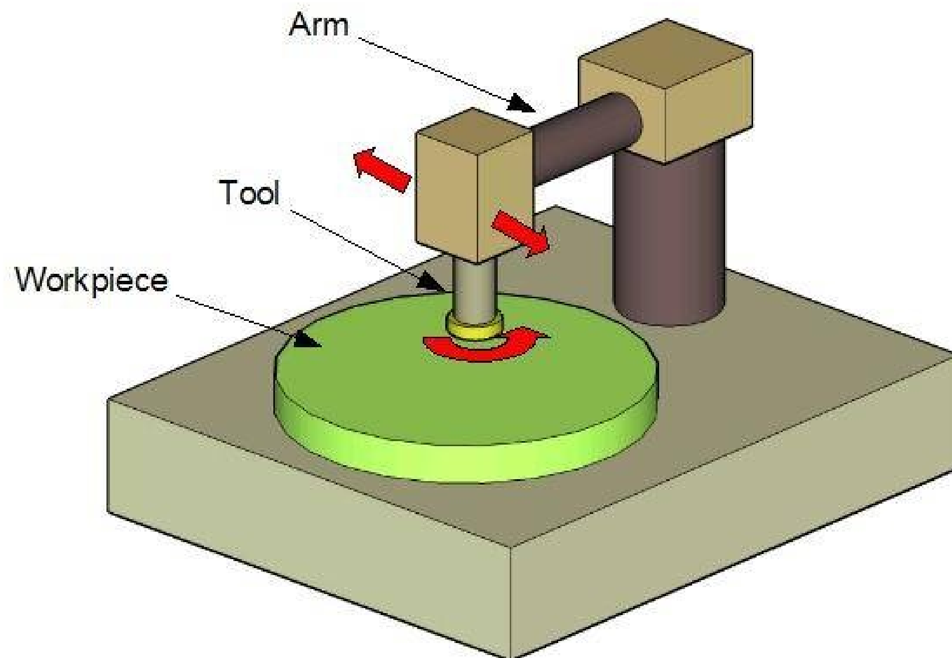

Figure 2-4: Schematic of a Sub-Aperture Polishing Setup

Sub-aperture polishing is often utilized for workpieces that are not flat or spherical. These complex geometries like aspheres or free-form optics require multiple iterations of measuring and polishing. Each cycle of polishing then measuring the

component is used to calculate the material removal that was performed and the material removal that is required in the next step. This iterative process of removing material, then measuring the workpiece, and calculating polishing dwell times for further form correct requires a high level of computer support and integration.

Typical loads for both full aperture and sub-aperture polishing are in the range of kiloPascals. Relative speeds between the workpiece and the tool are in the range of tens of cm/s.

2.1.4 Lapping and Polishing Material Removal Mechanisms

Despite the critical role that polished components play in many applications there is a lack of knowledge about the fundamentals that influence the removal of material from the workpiece and the resulting surface [16]. Material removal is generally thought to be a combination of brittle fracture, plastic flow or chemical effects. Early models were developed that were purely mechanical models, but over time thermal and chemical aspects have been included as their importance has been realized.

Mechanical Models

Newton, as an early optician, viewed polishing as a purely mechanical process where abrasive particles removed material producing scratches in the surface [7]. Abrasives were viewed as a multitude of particles that were indented into the workpiece and ploughed material out of the workpiece as they were dragged along by the tool. As such, the smaller abrasive particles produced smaller scratches and a better surface finish. This understanding has led to the common workplace practice of using a

succession of finer abrasives to polish a part. Larger abrasive particles are initially selected to quickly remove material and achieve the form requirements, while smaller abrasives are used in the end to achieve better surface finishes [2].

Variations to this mechanical view started to emerge in the 20th century with researchers such as Beilby and French proposing that material at the surface of the polished glass flowed into the scratches, smoothing the surface [15, 17-19]. This phenomenon was seen with smaller abrasives, leading Beilby to believe that it was based on a different mechanism than material removal with larger abrasives. This flow was thought to be facilitated by softening of the glass due to a rise in temperature due to friction between the tool and workpiece[8]. While experiments with a thermometer embedded in a polisher detected a negligible rise in temperature [19] further calculations assuming point contacts between the tool and workpiece showed the feasibility of sufficient localized heating to enable softening [20]. Experiments conducted into the 1950s lent support to the notion of material flow [21-23]. In particular the Rawston experiments and the Levengood and Fowler experiments showed conditions under which scratches (Rawston) or fractures (Levengood and Fowler) could be polished over and filled, confirming the presence of the Beilby layer.

Concurrent to the heated discussion in the 1920s over material flow and thermal softening, material redeposition was being discussed as a means to explain the amorphous layer at the surface [24]. N. K. Adam suggested that some of the molecules abraded away by the polishing process were deposited randomly as they were carried away from their initial location. Such a random distribution would give rise an

amorphous layer like the one Beilby and French believed to be a result of material flow and surface fusion.

While joining other researchers at the time looking at the general theory of polishing, F.W. Preston also developed an empirical model for polishing that stated the rate of material removal was proportional to the pressure and the relative speed between the tool and workpiece [25] as shown in Equation 2-4.

$$\frac{\Delta H}{\Delta t} = K_p \times \left(\frac{L}{A_C}\right) \times \left(\frac{\Delta s}{\Delta t}\right)$$ Equation 2-4

Where ΔH is the change in height, Δt is the change in time, L is the applied load, A_C is the contact area, Δs is the distance traveled and K_p is a proportionality constant that encompasses all other variables such as chemistry for a particular setup. Preston's equation is representative of focus on empirical models over general theory that dominated polishing research during the 60s and 70s. Much of the research during this period was application specific and focused on maximizing material removal rates while maintaining acceptable surface finishes.

Chemical Mechanical Models

While mechanical models provide relatively simple description of interactions during polishing, studies that varied slurry chemistry within mechanically consistent setups and produced dramatically different material removal rates and surface finishes showed that solely mechanical models are insufficient for describing finishing processes. The limitations of the mechanical models become more significant as the abrasive

particle size decreased, with predicted material removal rates and final surface roughness being off by orders of magnitude [26].

These discrepancies lead to a renewed interest in the chemical mechanisms for material removal as a possible explanation. Norman Brown in his research at Lawrence Livermore speculated on chemical actions whereby the water in the slurry chemically attacked the material in the region stressed by the travel of the abrasive particle across the surface [27]. Lee Cook expanded on this concept of "chemical tooth" to develop a model where diffusion of water into the glass surface caused dissolution under load. Molecules from this dissolved layer are then adsorbed on to the surface of the abrasive particles as they travel past, a portion of which are redeposited onto the surface [26]. The chemical and mechanical phenomenon reinforce one another, with the mechanical stresses induced by the travelling abrasives facilitating the diffusion of water and the dissolution of the surface layer making it easier for removal by the abrasive particles. In Cook's model [26], the maximum rate for this adsorption occurs when the pH of the slurry coincides with the isoelectric point (IEP) of the abrasive as shown in Equation 2-5, where R_c is the rate factor, (R-O) is the single oxygen bond strength of the abrasive, pH is the pH of the slurry, and IEP is the isoelectric point of the abrasive.

$$R_c = \frac{1}{\log_{10}\left[(R-O)\times\left|pH-IEP\right|\right]}$$ Equation 2-5

Representative work from the Laboratory for Laser Energetics in Rochester [28] compared the material removal rates and surface finishes for three types of glass with three different abrasive slurries at three different pH values, for a total of twenty-seven

different combinations. Within some abrasive-workpiece pairing, slurry pH was found to change the material removal rates and surface finishes by an order of magnitude [28] and provided partial agreement with the Cook model, except in cases where the slurry was corrosive to the workpiece tested. Research by Tesar, Fuchs, and Hed at Lawrence Livermore[29, 30] produced results that deviated sharply from the predictions of the Cook model, with the maximum material removal rates and best surface finishes occurring at a pH of 4 well away from the pH 7 IEP of the ceria abrasive being used. Explanations for these deviations focus on the differences in experimental setups (low slurry flow rate and no recirculation in Tesar's experiments) and challenges in obtaining reliable zeta potential measurements.

Ed Paul used the approach of a model linking the chemical modification of the surface and mechanical removal and redeposition of this modified material in his work developing a model describing chemical mechanical polishing [31-34]. While much of the work is intended for copper and tungsten wafers, the concepts of chemically active sites, mass transport and governing equations are suitably general to be useful in polishing glass as well. In particular, Paul simplifies his equation to the following form [32].

$$MRR = R_0 + \frac{C \times M}{C + M}$$

Equation 2-6

Where MRR is the material removal rate, C is the chemical phenomenon driving material removal and M are the mechanical phenomenon driving material removal. Looking at Equation 4, if either the chemical (C) or mechanical (M) contributions are

small the rate of material removal will be proportional to that smaller factor [32]. It is easy to see how changes in chemistry or mechanics of a polishing process could dramatically affect the polish regime and the associated dominant factors.

A related approach in modeling chemical mechanical polishing is advanced by Luo and Dornfeld [35-37] who start with a model based on Preston's equation for material removal, then modify it to account for chemical effects on the surface hardness as well as the number of particles involved in polishing.

Four Component Model of Lapping and Polishing Material Removal

In an effort to structure the investigations of what remains unknown about polishing processes, Evans et al [16] proposed in a recent CIRP paper that the interaction between four components would govern material removal. These components are the workpiece, the fluid, the granules, and the lap, each of which have chemical and mechanical properties that can influence material removal. The key parameters of interest for the four components are listed below, but the reader is strongly encouraged to reference the source material by Evans et al [16] for a thorough treatment of the subject matter.

Workpiece

The workpiece obviously is the material that is intended to be modified by the process. The chemical composition of the workpiece is critical as it will affect the chemical interactions that take place with both the fluid and the granules. The bulk mechanical properties of hardness and elastic modulus are critical for describing the interactions between the granules and the workpiece surface, whether it is calculation

of indentation into the workpiece or the contact area between the workpiece and granule. In some instances the crystallographic orientation of the workpiece is also critical as it determines the effective material properties.

Fluid

The fluid is the liquid carrier that transports the granules. The chemical properties are critical as that will determine the behavior with respect to the workpiece (diffusing into the surface or even slightly etching the surface) and the granule (favoring agglomeration or disintegration). From a mechanical standpoint, the viscosity of the fluid (along with the pressure and relative velocity) can play a significant role in determining the contact regime between the workpiece and lap.

Granules

It would be easy to use abrasives in place of granules, but the authors intentionally avoided this terminology as it implies a means of material removal (abrasion) instead of describing the component for what it is which may remove material by a means entirely different than abrasion (adsorption/chemical tooth for example). The mechanical properties of hardness and shape as well as the chemical composition are key in determining the types of interactions.

Lap

The final component in this quartet is the lap, which is defined broadly enough to include the stiff plates used in lapping as well as platens topped with a layer of pitch, cloth or foam pads. In either embodiment, the lap is responsible for the relative motion

between the workpiece, fluid and abrasives. Defining parameters for the lap are the surface topography, wear rates and bulk modulus.

Pairwise Interactions

Evans et al [16] first consider interactions between any two of these fours components to determine what governs the relative importance in material removal. An example of this pairwise interaction would be between the workpiece and fluid components of the model. Dissolution, etching and passivation are presented as mechanisms for material removal that are only dependent upon the fluid and the workpiece [16]. In this example, the mechanisms are driven by the chemistry of the fluid-workpiece interface which determines whether the workpiece dissolves in the fluid, is etched by the fluid or forms a surface layer that is distinct from the bulk, but mechanical properties such as the fluid flow could play a role in determining the availability of the chemical components.

Triplet Interactions

After summarizing the relationships of pairwise interaction Evans et al [16] extended the method to triplets, or the interaction of three components. As an example, by considering the granules as well as the fluid-workpiece pair mentioned previously, you have a workpiece-fluid-granule triplet. If the fluid is dissolving or etching the workpiece surface, that can assist with mechanical removal of workpiece material by the abrasive, by weakening the bonds holding surface molecules[16]. In the event that the fluid is chemically inert with respect to the workpiece, it can still influence the

granules ability to remove material by transporting away polished material to reveal new sites for activity[16].

Application of the Four Component Model

With all the possible combinations of pairwise and triplet interactions considered, Evan et al [16] apply this model to existing processes such as diamond lapping, magneto rheological finishing, tungsten chemical-mechanical planarization, and mechanical-chemical glass polishing. In the case of diamond lapping, a mechanical model of the workpiece-lap-granule triplet is found to be sufficient to describe the process. In the case of tungsten CMP and glass polishing however, it is clear that a more complex models are required that include both the chemical and mechanical aspects of several pairwise and triplet interactions. As only a single example of pairwise and triplet interactions are given, the reader is encouraged to visit the Evans paper for a thorough treatment of these interactions and their applicability to existing finishing processes.

2.2 Polishing Processing Monitoring

Increasingly stringent technical requirements (form, finish, etc.) as well as business requirements (production rate & cost) have driven the need for a greater understanding and control of the polishing process. Attributes of the slurry and general dynamics associated with the tool and workpiece can all contribute to the final condition of the workpiece.

2.2.1 Slurry Monitoring

A common slurry parameter that is monitored is slurry pH. Slurry pH is a critical parameter as it can drastically affect the material removal rate (MRR) as was found by Tesar, Fuchs and Hed [30] at Lawrence Livermore in the polishing of fused silica with cerium oxide slurries, where material removal rates and surface finished improved dramatically when the slurry pH was lowered to 4 from the normal 6-8 range. At UNC Charlotte, Alan Landis found slurry pH dramatically affected MRR, but in his research polishing silica with cerium-oxide abrasives [38] that superior material removal occurred at pH 7.

Slurry density can also be monitored to ensure an equivalent availability of abrasives in the slurry. Particle size characteristics can also be monitored, often through centrifugal sedimentation [30], which can provide insights into the behavior of the abrasive particles (are they breaking down or agglomerating for example). Monitoring the dimensions of particles in the slurry is also important to identifying rogue particles such as workpiece materials, agglomerated abrasives, other contaminants from the environment and insuring that they are not reintroduced to the polishing process as such rogue particles can degrade the surface and subsurface integrity of the workpiece [39].

2.2.2 Polishing Dynamics Monitoring

Loading

Going back to the famous Preston equation, MRR is proportional to both the pressure and the relative velocity of the workpiece. As would be expected, both

quantities are of interest to those optimizing polishing processes. The relative velocities are calculated from the spindle speeds, tool radius, eccentric speeds and the eccentric sweep. In the case of full aperture polishing, loading is controlled through either a dead weight or active application of force. In the dead weight configuration, the quill does not bottom out in the receiver allowing it to translate the workpiece through the eccentric motion without providing a significant effect on the loading. Actively applied loads in full aperture polishing are transmitted through an overarm, which can be driven by an air cylinder. The applied load in this case is calculated based on the reading from pressure gage and the dimensions of the air cylinder. This requires the quill to be bottomed out in the receiver, but the spherical end of the quill in the receiver acts as a gimbal which permits some rotation of the workpiece to match the tool. In Landis' experiments, a load cell was also embedded in the receiver that mates with the quill [38]. Measuring the load at this location was seen to better reflect the loads that were actually applied to the workpiece. This setup showed cyclical load variations of ±20 N around a nominal value of 27 N (for cylinder pressure of 69 kPa) [38].

Friction

The force of friction between the workpiece and the tool has also been the subject of much interest as polishers have long noted different resistances to a workpiece traveling across a tool during polishing [29]. Changes in the frictional force between the tool and workpiece have been studied as a means to assess the contact regime, degradation in the tool or a change in the structure of the workpiece. Using a tool dynamometer, Kim et al noted in their experiments [40] that the coefficient of

friction between the tool and workpiece drops dramatically at the start of a CMP process, before reaching a steady state after roughly 10 minutes.

In her CMP research, Mullany [41]used a load cell in contact with the platen spindle to measure the frictional force of between the tool and workpiece. Changes in these frictional forces are a result of changing the hydrodynamics, correlated with a shift from the elastic contact regime through the combined contact regime toward the purely hydrodynamic regime [41]. These changes are illustrated with a Stribeck curve (derived for the bearing industry) which plots the coefficient of friction against the Hersey number (the product of the viscosity and velocity divided by the applied pressure) (Figure 2-5). Low values for the Hersey number reflect a low relative velocity, low fluid viscosity, high pressure, or a combination of the three. These parameters insure that this region is characterized by a regime of mixed contact where both the fluid and the elastic material beneath are carrying some of the load. As the Hersey number increases due to a more viscous fluid, a higher velocity or a reduction in pressure the fluid takes a greater portion of the loading and there is less contact with the underlying elastic material. This transition from support mainly through elastic contact to increasing hydrodynamic support is accompanied by a reduction in the coefficient of friction as the workpiece increasingly glides across the tool, supported by the fluid. Once the Hersey number increases to the point that there is no contact between the tool and workpiece, the system has entered a purely hydrodynamic regime, where further increases in the speed will cause the friction to increase due to higher hydrodynamic drag.

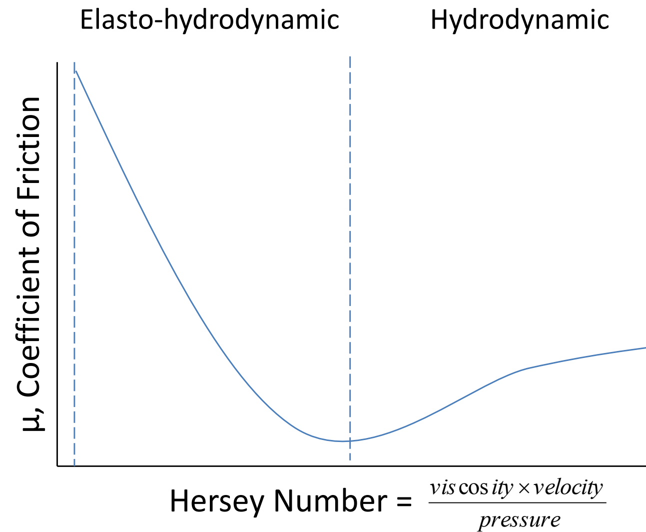

Figure 2-5. A representative Stribeck curve shows how plotting changes in the coefficent of friction against the Hersey number can indicate changes in the contact regime.[41]

Stein and Hetherington [42] attempted to use carrier motor current as an indirect measure of friction between the tool and workpiece as a predictor for pad failure in the CMP of a tungsten wafer. While the same measurement technique had been used successfully to determine when metal layers had been polished through on ILDs, carrier motor current was too inconsistent to serve as a reliable predictor of pad failure [42]. Frictional forces in polishing have also been investigated with respect to crystal orientation when polishing diamond by Gillo et all [43]. By attaching strain gages to the support arm holding the diamond against the rotating tool, wear rates were found to be highly anisotropic with correlations between the wear rates and the coefficient of friction.

2.2.3 Thermal Measurements

The research by Kim et all [40] and Mullany [41] also involved temperature measurements. Initially, these measurements were seen as important due to the effect

that large temperature changes can have on the hardness of the workpiece (and the real contact area as a result) and the rate of chemical reactions between the slurry and the workpiece. In practice however, the temperature increases observed were not large enough to appreciably affect the hardness of the materials. As the heat generated is a result of the friction between the tool and workpiece, the temperature rise was seen to vary linearly with the product of the pressure and velocity in Kim's research [40], as measured with an IR camera. Mullany's research also used a thermal imaging system that was sensitive to radiation in the IR spectrum, and found friction alone could not account for the temperature rise in the polishing system, with the difference being attributed to exothermic reactions between slurry constituents and the workpiece [41].

2.3 Subsurface Damage

Subsurface damage is a layer of cracks, pits and voids that exist below an apparently smooth polished surface. These defects can cause aberrations in optical components and reduce the laser induced damage threshold (LIDT), a measure of how much energy can be passed through an optic without risking catastrophic failure, in high energy laser optics [14]. Subsurface damage is also a concern for its reduction of the mechanical strength of polished surface where it can reduce the impact strength of glass windows [44] or in quartz oscillators where the cyclical loading can cause cracks to propagate.

Depending on the fabrication process for the component, SSD may be obscured by a polished layer up to 1 μm thick. The layer of defects may extend up to 100 μm

beneath the surface, with another 100 μm of stressed and deformed material beneath as shown in the conceptual illustration of SSD formulated by Hed et al [45] (Figure 2-6).

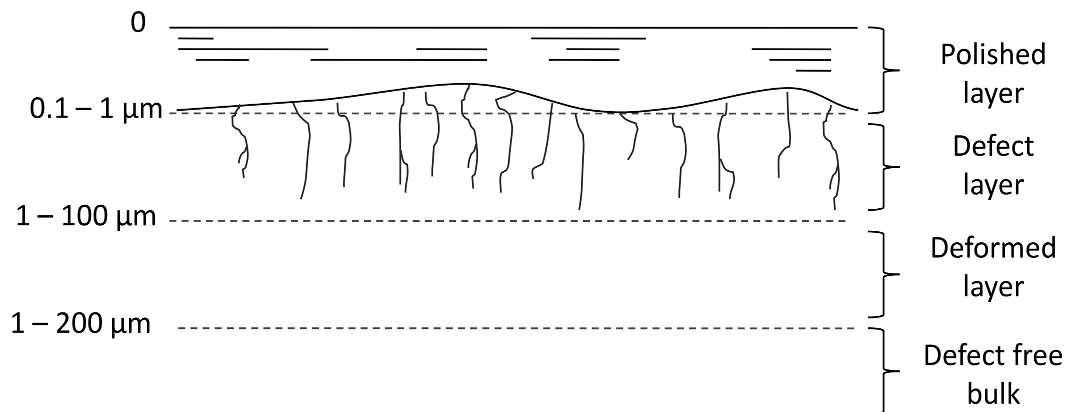

Figure 2-6. Conceptual illustration of subsurface damage [45, 46].

2.3.1 Mechanisms that Generate Subsurface Damage

Subsurface damage is generally accepted to be a result of brittle fracture that occurs during the grinding and lapping of materials. These brittle fractures result either from a simple brittle fracture where a highly load particle induces a stress field beneath it that interacts with dominant defect in the workpiece or when the dynamic stress fields of a travelling abrasive interact with these dominant flaws in the material and leave it in a highly an unstable state that is prone to fracture.

Simple Brittle Fracture

The first mechanism considered is simple brittle fracture of the material due to the applied load carried by the abrasive particles. Much of what is accepted about the SSD generated as a result of brittle fracture comes from the field of fracture mechanics and the related indentation studies. Fracture mechanisms as a result of indentation have been studied extensively for a wide range of materials and applications [47] and

abrasive particle is taken as the analog for the indenter. The fracture process is divided into two stages: initiation and propagation [47]. Initiation is governed by the existence of previous flaws in the material, a result of either prior manufacturing steps in the material's history or a defect induced by indentation [47]. Whether or not these precursor defects become full fledged fractures depends on their size, location within the stress field and the proximity and prevalence of other precursor defect sites [47].

As one of the key factors in determining which precursor defects develop into cracks, the stress fields produced by different loading geometries are of interest. Four types of loading are considered in the literature; point loading, spherical indenter, blunt indenter loading, and sharp indenter loading. These geometries are shown below where 'P' is the applied load and 'a' is the contact radius, which denotes the area of contact between the indenter and surface[47] (Figure 2-7).

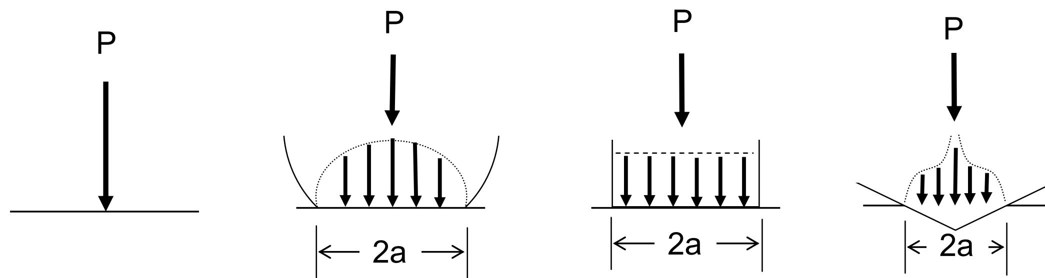

Figure 2-7. Different Indenter Geometries. (left to right). Point load, spherical indenter, blunt indenter and sharp indenter, where 'a' denotes the contact radius.

Each of these geometries produces different contours for principle stresses in the material during indentation which are plotted to show areas of high stress and transition for the respective geometries. The coordinate system for these principle stresses is shown below in Figure 2-8, where P is the applied load which acts along the z-

axis. The stressed element is located at a radius of R from the point of loading. The first principle stress acts along a line that is perpendicular to the z-axis and intersects both the z-axis and stress element. The second principle stress is a hoop stress that is perpendicular to both z-axis and the first principle stress. The third principle stress acts parallel to the z-axis [47]. The orientation of these principle stresses is shown in Figure 2-8 below.

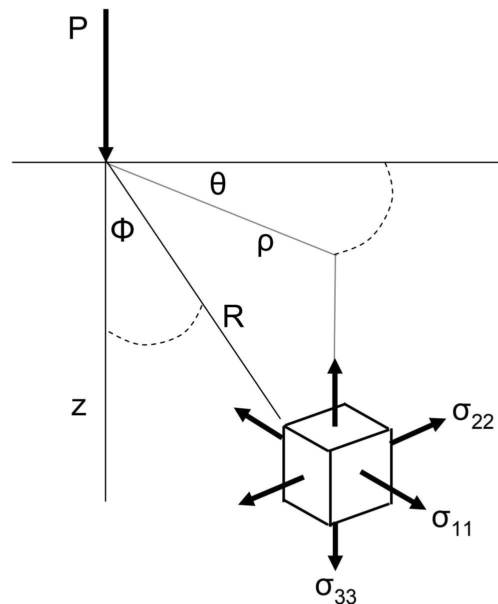

Figure 2-8. Principle Stresses During Indentation from [47]

The stress contours are then plotted out to predict what types of fractures might occur in the specimen as a result of indentation. The contours are labeled in terms of the characteristic stress of the indenter which is defined by the following equation.

$$p_0 = \frac{L}{\alpha \pi a^2} \quad \text{Equation 2-7}$$

Where L is the applied load, α is a dimensionless parameter based on the geometry of the indenter (α =1 for axially symmetric geometries) and 'a' is the contact radius. In the case of a spherical indenter the principle stress fields have been well studied by researchers and representative plots are shown below in Figure 2-9.

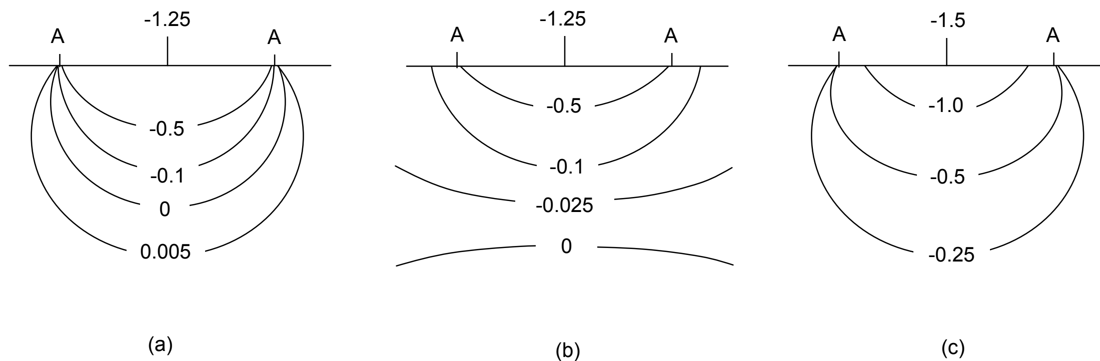

Figure 2-9. Representative Principle Stress Fields from a Spherical Indenter, where A is the contact radius. (a) σ_{11}, (b) σ_{22} and (c) σ_{33} from [47].

In the context of loose abrasive finishing, higher loads generate greater stresses in the workpiece, leading to a greater prevalence of fractures and greater depths at which sufficient stresses will occur to initiate fractures from existing defects in the material. In grinding a lapping, the primary mechanism of material removal is the intersection of brittle fractures. Higher loads increase the rate of material removal as well as the depth and prevalence of subsurface damage [48], supporting the relationship between the degree of brittle fracture and the degree of subsurface damage. This type of subsurface damage appears as scattered (sometimes intersecting) fissures on the sample surface after it has been etched to remove the smooth plastically deformed topmost layer (Figure 2-10).

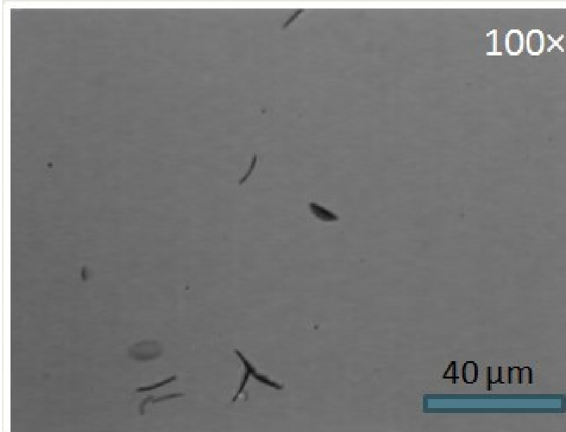

2-10. Examples of brittle fractures in a glass sample that was lapped, polished, then etched.

Dynamic Stresses in Proximity to a Traveling Abrasive Particle

The loading during indentation is not a static process and the dynamics of the loading can play a role in determine the type and extent of fracture. These dynamic loads can occur as a result of the loading and unloading or as a result of the indenter being translated across the surface. Dynamic indenter loading is of the most interest in lapping and polishing research as it most closely approximates the action of the abrasives as they travel across the surface. As Goodman and Hamilton calculated [49], localized compressive stress fields in the region of a traveling spherical indenter deviate dramatically from the stresses due to static indentation. The leading edge of the indenter experiences increased compressive loads while the trailing edge experiences tensile stresses (Figure 2-11).

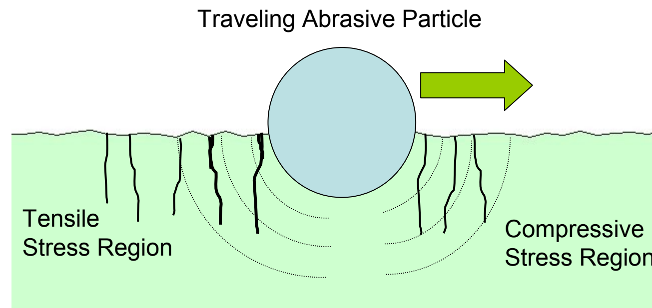

Figure 2-11. Compressive and Tensile Stress Regions Around a Traveling Abrasive Particle.

The magnitudes of these stresses are based on the normal loading as well as the coefficient of friction between the indenter and workpiece. The compressive stresses can cause brittle fractures which are further aggravated by the tensile stress fields that trail the abrasive particle [26]. These fractures may be covered up by flow of surface material or they may simply not be open to the surface in the absence of localized stresses, but they can be easily detected with etching which reveals a series of collinear crescent chatter marks (Figure 2-12).

2-12. Glass sample etched to reveal SSD 'chatter marks' characteristic of dynamic stresses around a traveling abrasive.

This theory is supported by the fact that at high loads and larger abrasive diameters, material removal in glasses in primarily through brittle fracture during lapping [50]. At low loads and smaller diameters, material removal primarily occurs through scratching and plastic flow in a ductile regime for the material [50]. The brittle fractures leave behind radial or median cracks that may become SSD, while the plastic deformation of lower loading lapping leaves behind a highly stressed material in a thin layer at the surface that may have undergone plastic flow.

Once a fracture has been initiated, it will propagate based on the external loading such an energy balance is maintained.

$$U = (-W_L + U_E) + U_S \qquad \text{Equation 2-8}$$

Where U is the total energy of the system, W_L is the work of the external load, U_E is the elastic strain energy in the sample and U_S is the surface energy of the fracture faces [47]. As the work W_L increases the fracture length increases (which increases the surface area of the fracture faces and the associated surface energy), maintaining energy balance in the system. In the case of the traveling indenter, the tensile stress fields provide the external loading that further exacerbates the defects that have been created.

Given that brittle fracture is the accepted means of generating SSD, it comes as little surprise that researchers at the Laboratory for Laser Energetics at the University of Rochester found a correlation between the depth of SSD in a glass sample and the hardness and fracture toughness of the specimen [51]. Increased Knoop hardness was

seen to limit the depth of subsurface, while increased fracture toughness was seen to enable subsurface defects to extend farther into the bulk of the specimen.

2.3.2 Some Indentation Experiments related to SSD

Static indents can be represented with analytic equations where the critical load to initiate fracture can be found based on the indenter geometry and the material properties [39]. For example, Lawn found with static loading of fused silica with a sharp indenter, the critical load was 0.02 N [52]. For sliding indenters (which most closely approximate travelling abrasives), the applied load as well as geometry of local contact between the indenter and surface govern the types of features that are created in the surface with low loads only inducing plastic scratches in the surface, while higher loads lead to easily recognizable radial fractures and lateral cracks [39]. Loads that are higher still result in the plastically deformed track degenerating into a 'rubble-like appearance' [39] which obscures evidence of the radial and lateral cracks.

These critical loads play a key role in the transition from grinding and lapping operations to polishing operations. During grinding and lapping, larger diameter abrasives are used, which leads to fewer points of contact on the workpiece and higher loads per point. Suratwala estimated that with a 0.5 μm ceria abrasive particle, a fill factor of 0.3, and the assumption that all particles were load bearing that the load per particle would be in the range of 10^{-9}-10^{-6} N, orders of magnitude lower than what is required to produce fractures in fused silica [39]. Calculations like these support the notion that SSD is generated not during polishing operations, but rather during the brittle fracture of grinding and lapping.

More recently Suratwala and other researchers at Lawrence Livermore National Laboratories [39] examined the effect of rogue particles on the subsurface damage generated by loose abrasive finishing. In their experiments, a rogue particle was a significantly larger size than the abrasive particles being used and represented either a contaminant or an agglomeration of abrasive particles. The introduction of even small amounts of these rogue particles were seen to increase the prevalence of SSD as the researchers hypothesize that these anomalous particles carry a disproportionately high load which leads to greater brittle fracture.

2.3.3 Traditional Methods of Assessing Subsurface Damage

Given the importance of removing SSD from components, numerous methods have been employed over the years to explicitly detect SSD or relatively assess SSD in optical components. Brinksmeier [53], Lucca [54] and Shen [55] have all published excellent reviews of the various means of assessing SSD. Key methods are summarized below, but the reader is encouraged to view these sources for a more thorough treatment of the techniques.

As it cannot be detect by contact methods or interferometry, it has traditionally been assessed through destructive tests such as etching, taper polishing and dimpling. These traditional methods share several common traits in that they involved an etching process, are destructive to the sample and are limited by the resolution of the optical microscope used for observations.

Etching

Etching has been used since Beilby [15]to reveal structure beneath the surface. Proponents of the surface flow theory held that this was due to the etchant preferentially attacking the amorphous layer which had flown into surface scratches. Samples are etched then be examined under a microscope to observe any visible defects. Samples are etched successively until there are no visible defects, indicating that the SSD layer has been etched through revealing the undamaged bulk. An example of glass etched with dilute hydrofluoric acid to reveal SSD (Figure 2-13).

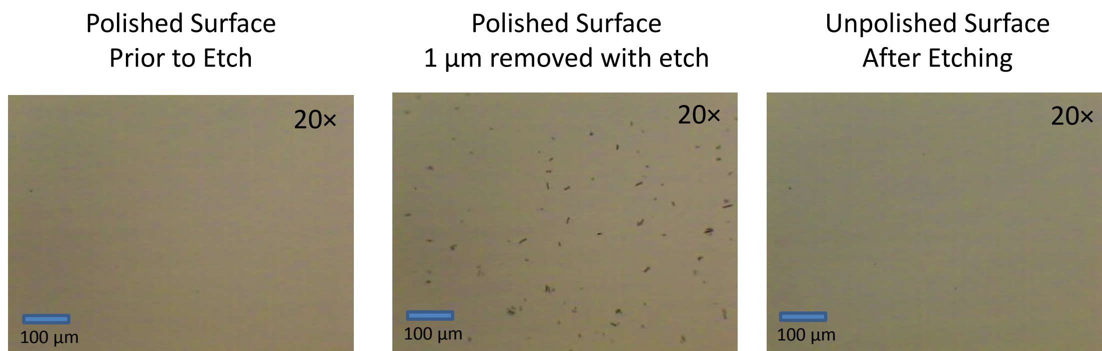

Figure 2-13. Glass surface etched in hydrofluoric acid to reveal the subsurface damage that lies beneath. The left image is of the polished sample surface prior to etching. The middle image shows the surface after 1 μm has been removed by etching. The right image shows the surface which was not polished, but has had 1 μm removed by etching as a comparison.

Etching can also be used assess the depth of SSD by looking at variations in the etch rate [56]. Preston looked at the mass loss of 'greyed' (matte) and polished glass discs subject to a dilute hydrofluoric acid etch. The 'greyed' sample lost mass rapidly early in the etching procedure as the rough surface provided a large surface area to be attacked by the acid (Figure 2-14). Within 3 minutes the etch rate had dropped to a 25%

of the initial value as the etching process normalized the surface, diminishing the greater asperities. After further etching, the etch rate stabilized at roughly 10% of the initial value.

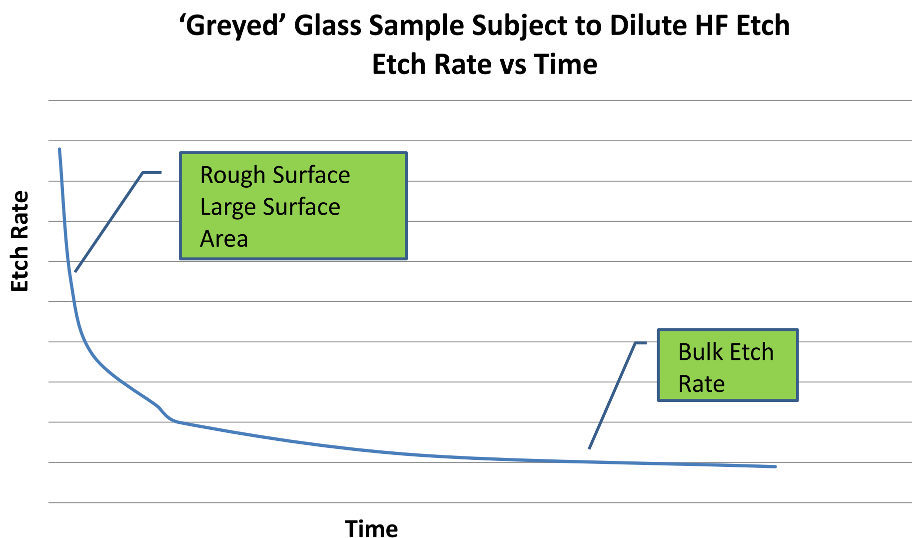

Figure 2-14. Conceptual graph showing changes in the etch rate for a 'greyed' (lapped) surface. The etch rate drops considerably from the peak initial value when the etchant is attacking the damage, highly stressed surface.

The polished sample displayed a similar, albeit less dramatic trend (Figure 2-15). The long term etch rates were equivalent to those measured for the 'greyed' samples, but the initial etch rates were only 37% higher. This is expected given that the smoother surface provides less available surface area than the matte surface. The question then becomes why is there a difference at all between the polished surface and the undisturbed bulk. Preston postulated that this initial difference was due to the initial etching being of a different phase [56] that due to defects and strain present in the phase was preferentially attacked by the etchant.

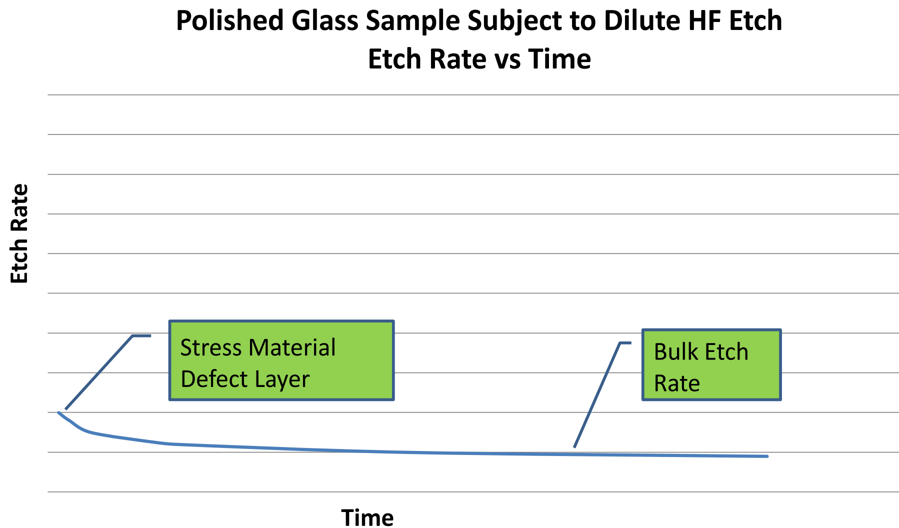

Figure 2-15. Conceptual graph showing the changes in etch rate for a polished surface. The change in the etch rate is much less dramatic than the change seen in the lapped sample as the polishing produces less damage and stress than lapping, leaving the polished surface more akin to the bulk in terms of resistance to etching.

Taper Polishing

Taper polishing enhances the etching process by providing a measure of the depth of damage. A sample with SSD is mounted at an angle for a final polishing stage. This polishing at an angle produces a taper on the sample. This taper is then exposed to a dilute etch to highlight the fractures in the SSD layer. By using the geometry of the setup, and measurements from optical microscopy of where the SSD layer begins and ends, the depth of SSD can be calculated. This method is limited in that it is destructive to the sample and limited by optical resolution in the size of defects that can be detected. Polishing to reveal SSD also raises the question of what level of SSD is being induced by the polishing process. The assumption is that with low loads and small abrasive, this polishing step will be a minor contribution to the overall depth of SSD.

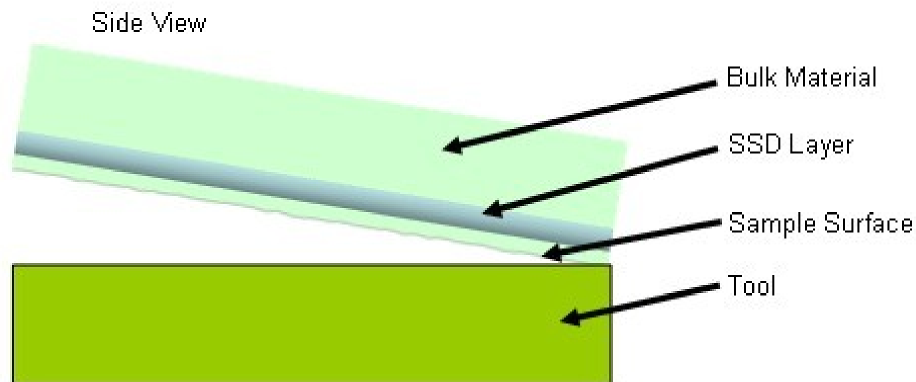

Figure 2-16. Taper Polishing Sample Orientation

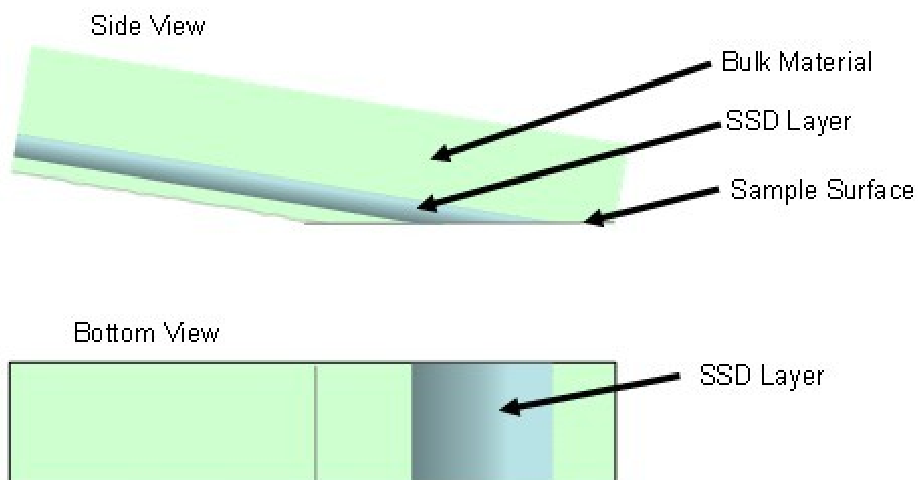

Figure 2-17. Taper Polishing Side and Top View showing geometrical relationship between the damaged region and the depth of SSD.

Dimpling

Dimpling is related to taper polishing in that it polishes a known geometry into the surface, which is then lightly etched to emphasize the defects in the subsurface damage layer [13]. In dimpling, a metal sphere is used with a fine abrasive to polish a divot of a known radius into the surface. As with taper polishing, dimpling has the disadvantage of possibly inducing subsurface damage during the polishing, but like taper

polishing this damage is assumed to be negligible compared to the SSD from previous steps. Care must also be taken in selecting an appropriate material for the dimpling tool. A ball that is of insufficient hardness will be polished and lose shape before polishing the correct geometry into the workpiece being examined. Similarly, a ball that reacts chemically with the slurry could scratch or contaminate the surface with the products of the reaction. Dimpling is best suited for finely ground and lapped surfaces where the degree of damage is much greater than what may be induced by the dimpling itself.

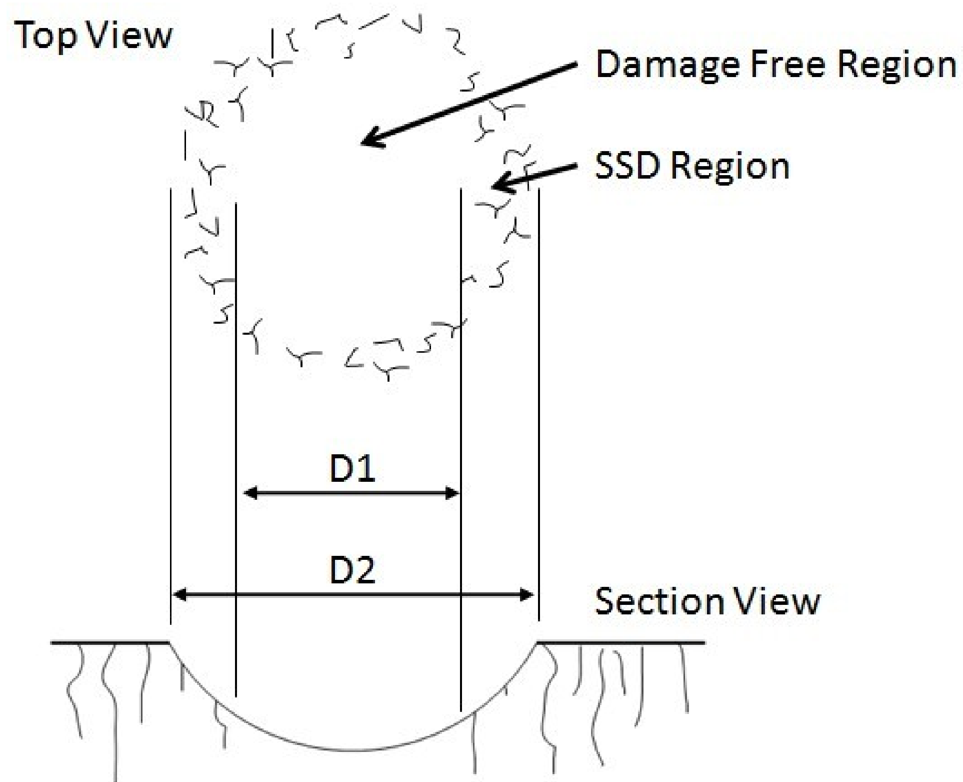

Figure 2-18. Conceptual illustration of a dimple test.

Estimating SSD from Surface Roughness

As subsurface damage cannot be detected by surface measurements, there has been significant interest in finding correlations between measurable surface properties and the degree of subsurface damage that lies beneath. The earliest work on these correlations come from Preston who through optical microscopy found SSD to extend to a depth equal to roughly three times the peak to valley surface roughness of a ground surface[56]. Further work was done by Aleinkov [57] who examined a range of glass lapped with SiC abrasives and found SSD depth to extend to roughly four times the peak to valley roughness. Edwards and Hed at LLNL [58]found the SSD to extend up to 6.3 times the peak to valley roughness. Edwards values are much larger than those recently observed by Lambropoulos who found SSD depths were consistently less than twice the peak to valley roughness. Some of the differences in the coefficients can be attributed to the different instruments used to measure the peak to valley roughness, with Hed using a stylus profilometer and Lambropoulos utilizing a white light interferometer [59].

Estimating SSD from Abrasive Dimensions

In a similar vein to the previous chapter, there has been interest in determining correlations between the size of abrasive particles used and the depth of subsurface damage generated. As abrasive particle sizes are readily available, such correlations would provide easy estimates of subsurface damage depths induced by a finishing process. By examining a range of abrasives and glasses, Lambropoulos developed the following equation to bound the depth of SSD [60].

$$0.3D_{abrasive}^{0.68} \leq SSD(\mu m) \leq 2D_{abrasive}^{0.85} \quad \text{Equation 2-9}$$

Where d is the diameter of the abrasive particle used during the grinding of the sample.

Miller and colleagues at Lawrence Livermore National Laboratories examined fused silica samples subject to a variety of fixed and loose abrasive processes [59] for signs of SSD using a magnetorheological finishing technique. There findings are consistent with Lambropoulos in that larger abrasive particles induced deeper subsurface damage and fixed abrasives generally produced deeper fractures than loose abrasives.

2.3.4 Recent Methods for Assessing Subsurface Damage

Confocal Scanning Laser Microscopy

A confocal scanning laser microscope was used to detect subsurface damage by shifting the focal plane from the surface to the interior of the optic. As the sample is scanned, the point by point intensity of reflected light is recorded. The increases in reflected light are attributed to scatter or reflections due to damage or defects located in the subsurface [61]. In the system used, the ability of the confocal microscope to reject light from outside the focal plane resulted in a vertical resolution of roughly 150 nm [61].

In 2009, Neuport et al reported on using confocal fluorescence microscopy to image the subsurface damage in ground fused silica [62]. The ground surfaces were dimpled with a magneto rheological finishing (MRF) machine and the dimple area was examined with both optical microscopy and fluorescence microscopy. They found that the fluorescence microscopy revealed subsurface damage features that were not

detected in the reflected light mode. Spectral analysis of the emitted fluorescence also showed that the emissions were consistent with the emission spectra of the oil based lubricant used during the grinding.

Total Internal Reflection Microscopy

Total internal reflection microscopy (TIRM) directs a polarized bean of light at a transparent sample at an angle greater than the critical angle needed for total reflection. In a perfect sample, this would reflect all of the light back out (none would be transmitted through the sample). The inclusions in the sample however cause a portion of the light to be scattered and it is this scattering which is detected with a brightfield microscope or Nomarski microscope[63, 64]. TIRM is capable of resolving defects less than 1 μm in width and 100 nm in depth over a field of view 1 mm^2 [65]. By adding a half wave plate and a polarizing cube, Kranenberg et al were able to determine the depth of a defect beneath a polished fused silica flat [66]. An extension of TIRM measures the intensity of the scattered light and correlates changes in intensity of the laser beam to changes in the structure of the surface and subsurface [67].

Photothermal Microscopy

Damage sites in the subsurface can possess different optical or thermal properties than the surrounding material, whether from a fracture, contamination or inhomogeneous region [68]. These differences are utilized in photothermal microscopy (PTM) where energy from a pulsed laser is absorbed by the defect site. That absorbed energy is converted to heat which raises the temperature around the defect. The rise in temperature changes the index of refraction which deflects probe beam which is

coincident with pulsed beam. Sample regions without defects do not have absorption gradients and thus would not see the diffraction inducing thermal gradients. The technique is able to resolve contamination defects as small as 100 nm [69]but is sensitive to the absorption characteristics of the defect which vary based on the material and pulsed laser wavelength .

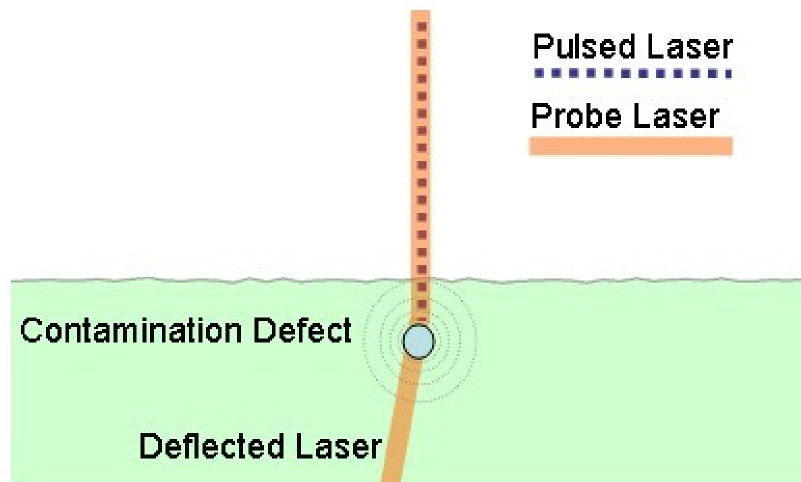

Figure 2-19. Photothermal Microscopy Schematic

Laser Modulated Scattering

Laser modulated scattering utilizes the same principle of photothermal microscopy, that defects or contaminants in the subsurface of a material will exhibit a different energy absorption than the bulk material. This differential absorption will lead to stresses and distortions within the material, but unlike PTM which measures the deviations in a probe beam caused by these defect regions, LMS measures how those distortions affect the scatter of light from the probe beam [70].

Raman Spectroscopy

Raman spectroscopy, or inelastic light scattering, measures the frequency shift of monochromatic light that is incident on a sample [54]. Analysis of these frequency shifts can provide insights into the stresses in crystalline and amorphous materials. Stressed materials exhibit a split of the frequency of light detected compared to a single frequency peak for unstressed material [53]. This splitting of the peak is due to the stresses causing changes in the lattice spacing within the material, with compressed bonds leading to lower frequencies and stretched bonds leading to higher frequencies [53]. While non-destructive, Raman spectroscopy is limited in the depths it can measure by the absorption of the material (on the order of 1 μm for a 514 nm wavelength light source) and can achieve spatial resolutions on the order of the wavelength of light utilized [53].

Ion Channeling

Ion channeling uses the interaction of particles having MeV energies with the atoms comprising lattice near the surface of a sample (< 1 μm) [71]. In case of a perfect lattice, most of these particles are funneled through the spaces between the atoms when the ion source is aligned with the crystallographic axis. Imperfections in the lattice however cause a large portion of those ions to be reflected or scattered back from the surface. This results in a taller and broader peak of backscatter yield than would be expected in a perfect sample. Work has been done looking at single crystals on CdS [71] as well as ZnO and ZnSe [72] that has been subject to both diamond turning and polishing.

X-ray Diffraction

X-ray diffraction much like Raman spectroscopy measures the change in scatter due to lattice strain and defects in the crystal lattice [54]. X-ray diffraction has the advantage of being able to work in opaque materials, but like Raman it is limited by the depth of penetration of the beam (roughly 2 μm) to the near surface region. A variation called grazing X-ray diffraction operates below the critical angle for reflection and examines the resulting scatter. Higher energy X-rays (8 keV range) were found to be highly effected by SSD at depths up to 2 μm in samples of Zerodur, fused-silica and BK-7 glass [73].

Magneto rheological Finishing

Magneto rheological finishing (MRF) is an extension of the dimpling polishing in that it polishes a known geometry into a sample surface being examined for subsurface damage [74]. The unique nature of the MRF process however allows it to perform this polishing without inducing significant SSD itself. MRF accomplishes this by being a non-load bearing process, where the surface is polished with a magnetic slurry [74, 75]. A magnetic field is used to stiffen a region within the slurry which is moved by the rotating head relative to the surface. As contact takes place through this stiffened region of the slurry, there is less transmission of load and vibrations from the system that could induce SSD during the material removal which would be indistinguishable from the prior SSD. MRF also offers an advantage over dimpling in that tool wear and contamination are less of concern. The magnetic field that makes the ribbon rigid prevents relative motion of the abrasive against the tool which would otherwise cause some level of

abrasion. MRF has been used to assess the SSD in varied materials including fused silica [59] as well as hard ceramics [76]. As with taper polishing and dimpling, the damage is observed with optical instruments.

2.4 Instrumentation

Assessing polishing metrics and SSD can require a significant selection of instruments. Each instrument brings a set of capabilities that justify its use. The capabilities and theories of operation are covered briefly for several key instruments below.

Table 1. Comparison of Various Instruments Used in this Research

Instrument	*Advantages*	*Disadvantages*	*Field of View*	*Resolution (Limits)*
Optical Microscope	*Quick, non-contact*		*130 µm × 180 µm At 100×*	*Diffraction limited camera resolution (~250 nm)*
White Light Interferometer	*Quick, non-contact*	*Only a surface measurement*	*80 µm × 110 µm At 65×*	*Diffraction limited camera resolution (~250 nm)*
Atomic Force Microscope	*Resolution of features below the diffraction limit*	*Slow, contact method, tip wear*	*80 µm × 80 µm (maximum)*	*Limited by the probe tip radius*
Wide Field Fluorescence Microscope	*Quick, non-contact*	*Out of focus fluorescence*		*Diffraction limited and by the camera resolution*
Confocal Fluorescence Microscope	*Sharp images, rejects out of focus fluorescence*	*Slow*	*40 µm × 40 µm (maximum)*	*Diffraction limited can detect features below the diffraction limit*

2.4.1 Optical Microscopy

An optical microscope is used to magnify an image so that details and features which cannot be resolved with the naked eye are made visible for observation by the human eye or other imaging device. In the earliest and most simple configuration a single convex lens was placed between the object and the eye. This lens, along with the eye's cornea, spread out the rays of light coming from the sample to cover a larger

portion of the retina. This increased coverage of the retina enabled discrimination of detail that could not be discerned unaided [77].

Refinement of this simple design brought about the compound microscope where an image is magnified first by an objective lens and then by a lens in the eyepiece such that a 2× objective and 10× eyepiece result in a total of 20× magnification of the image. Compound microscopes can also incorporate a number of other improvements to reduce chromatic aberrations (different wavelengths of light being focused to different focal points) and spherical aberrations (the projection of a flat focal plane onto a spherical image surface) [77].

Powerful magnification is an asset in a microscope setup, but the resolution of the image is limited by factors outside the overall magnification. Points in sample appear as discs in the image as observed by researchers such as Abbe, Airy and Rayleigh. The ability of a microscope to resolve minute features in close proximity (separated by a distance r_{DIFF}) is limited by the numerical aperture (N.A.) and the wavelength of light (λ) being used as shown in equation 2-10.

$$r_{DIFF} = \frac{\lambda}{2N.A.} \qquad \text{Equation 2-10}$$

where $N.A. = n\sin(u)$

Where n is the refractive index of the medium and u is half the angle formed by the light entering the optic. As such, numerical aperture is a measure of the breadth of the cone of light being focused by the optic. A higher numerical aperture allows resolution of smaller features in an objective. The tradeoff with higher numerical apertures is that it reduces the depth of focus.

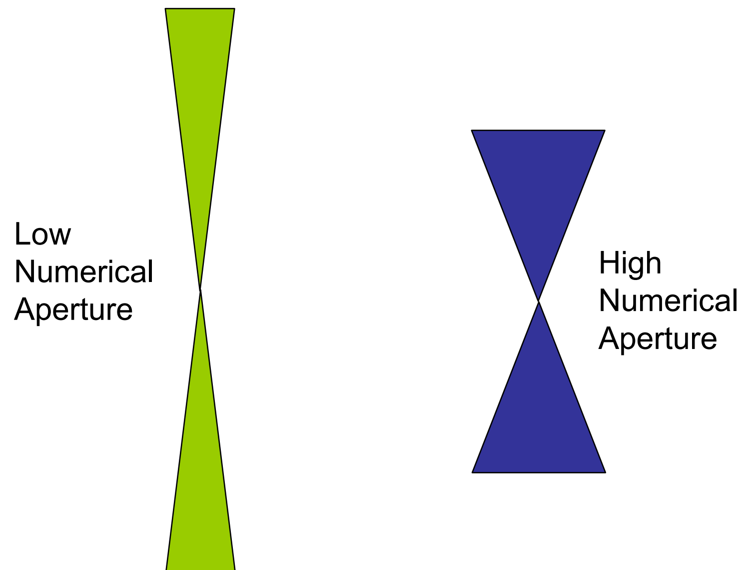

Figure 2-20. Illustration of the differences in high and low numerical aperture.

Operation

The specimen to be examined is placed on the sample stage and illuminated with condensed light either from above (for opaque samples) or below (for transparent samples). A low power objective is used initially and the sample stage is translated up and down to bring features on the sample (such as edges or defects) into focus. Assuming the other objectives in the turret are parafocal, progressively higher objectives are rotated into use and the focus is finely adjusted until sufficient magnification is achieved.

Advantages and Characteristics

Optical microscopy is a well established field where a surface can quickly be examined for features unseen by the naked eye. They are used extensively for qualitative assessments of optical components based on standards that look for “scratch” and “dig” defects on the surface. The prevalence and lateral size of these

defects are then used to categorize the quality of the optic based on standardized criteria. These simple observations can be augmented by a variety of different techniques including Differential Interference Contrast. Differential Interference Contrast (DIC) produces contours of black and white on a grey background. These contours map to slight differences in the optical path length traveled by adjacent polarized beams. Given that the geometric distances traveled are equivalent, these changes in optical path length are a result of changes in the index of refraction. Highlighting these areas of varied refractive index makes locating defects easier as it emphasizes the stressed material nearby.

Disadvantages

Finding focus on a high quality transparent surface is difficult with an optical microscope as the surface by its nature should be free of features that can be crisply resolved. Traditional microscopes are unable to resolve the submicron sized defects that are the precursors to LID sites [69] due to the diffraction limit of the lateral resolution [78]. In addition, optical microscopes do not provide information about the vertical dimension of features. The exceptions to this limitation are in taper polishing and dimpling, which as mentioned before allow for depth calculations based on known geometry. Vertical dimensions can also be acquired by sectioning and rotating the sample to examine the surface from the side.

2.4.2 White Light Interferometer

Operation

Optical interferometry is based on the wave properties of light, specifically the constructive and destructive interference of wavefronts [79]. This interference is created by the different optical path lengths traveled by a divided wavefront where the optical path length is the product of the geometric distance and the refractive index [79]. In white light interferometry, the primary fringe is taken as the zero value, then either the sample or reference surface is moved causing those wavefronts to shift. The offsets that produce maximal contrast at a given location then correspond to the height of that position relative to the zero fringe [78].

Advantages and Characteristics

White light interferometers allow for a quick measurement of a surface topography with nanometer resolution without contacting the surface that is being measured.

Disadvantages

The WLI is subject to the same lateral resolution limits based on diffraction as optical microscopy. Furthermore, it requires light to be reflected back to build a surface profile. This necessitates the surface being reflective and limits the data that can be acquired from steep slopes (which do not reflect light back to the instrument).

2.4.3 Atomic Force Microscope

Operation

Atomic force microscopy is a form of scanning probe microscopy where a special microfabricated tip on a small cantilever contacts a surface to measure the topography [80]. The tip or sample then moves in a raster pattern over the sample area to acquire

data throughout the scan area during which time the probe tip maintains contact with the surface [80]. The height measurements are obtained through deflections in the cantilever which are measured by movements of laser beam reflected off the cantilever onto a photodiode detector. An actuator moves the entire cantilever assembly up or down to maintain the reflected laser spot in the center of the photodiode detector[80]. This movement is controlled through integral and proportional feedback loop the gains of which are set in the software.

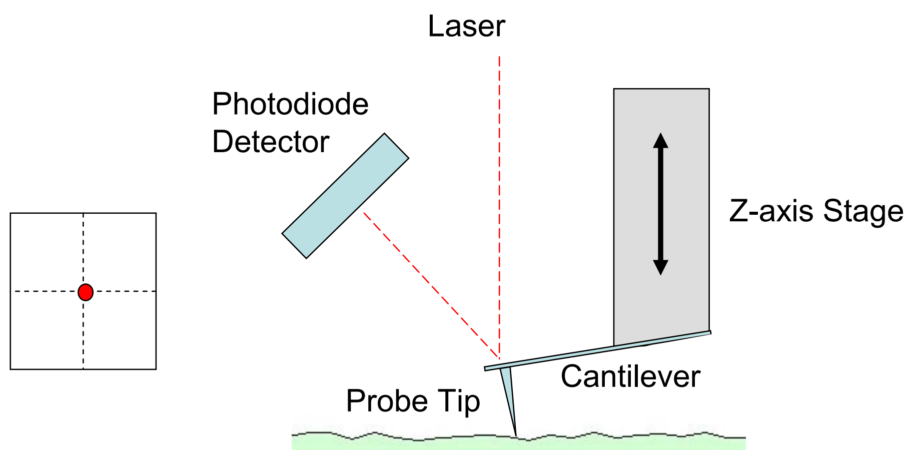

Figure 2-21. Basic Operation of an Atomic Force Microscope

<u>Advantages and Characteristics</u>

The tip and cantilever assembly is very sensitive to changes in the topography, easily deflecting to trace the surface during the scan. These deflections are further magnified by the laser bouncing off the back of the cantilever to the photodiode detector some distance away, acting as an optical lever.

The scan length is easily adjusted allowing for a wide variety of sample areas. The number of samples per line can also be adjusted depending on the need for speedy measurements (fewer points per line) or greater resolution (more points per line).

Disadvantages

While the vertical resolution of an AFM is very sensitive, the lateral resolution is limited by the probe tip radius. Probes with a large tip radius will encounter surface asperities sooner in their transit across the surface and begin to deflect earlier than smaller tip radius probes. Similarly, large tip radius probes will not be able to fully travel into cracks or pits with a width less than the tip diameter. The influence of the tip radius on measurements also means that tip wear will affect measurements. Highly reflective surfaces can also pose a problem if the laser light incident on the surface interferes with light reflected from the surface. This however can be addressed by ensuring that the laser is centered on the cantilever and using cantilevers with reflective coatings on the back to increase the signal to the photodiode detector[80].

As a point by point contact measurement, scan speed is limited since traveling at high speeds can cause the tip to skip across the surface, missing key features, and/or damage the tip. At higher resolutions, scans can easily take over half an hour to complete and create data files of significant size.

2.4.4 Wide Field Fluorescence Microscope

Operation

A wide field fluorescence microscope operates in much the same was a traditional optical microscope. The key differences come in the illumination source and the filters on the resulting fluorescence. Unlike a conventional microscope the illumination provided by the light source is not intended to illuminate features on the sample, but rather to excite fluorescent material in the sample to fluoresce. The filters

that are used on the observed fluorescence attenuate fluorescence outside the spectra range anticipated for the probe in use, enhancing the observed contrast by eliminating stray sources of light.

Advantages and Characteristics

Wide field fluorescence images are obtained relatively quickly as the entire region is illuminated and imaged at once. Appropriate filtering of the resulting fluorescence emphasizes the fluorescent features by attenuating unwanted wavelengths of light. Initially considered an impediment by researchers in ultraviolet microscopy, fluorescence microscopy enabled numerous advances in cellular biology during the 20th century [81].

Disadvantages

Bulk materials that autofluoresce at the wavelength of excitation add noise to the signal, particularly if the autofluorescence spectra overlaps with that of the fluorescent probe and filter used. Features highlighted by fluorescence may appear larger due to 'flare' of the fluorescence detected by the microscope. Finally, images from the widefield fluorescence microscope can include significant fluorescence from sources outside the focal plane.

2.4.5 Confocal Scanning Laser Microscopy

Operation

While being comprised of similar components, confocal scanning laser microscopy is quite different from conventional microscopy in that the sample is illuminated point by point instead of being fully illuminated and imaged at once. The

image from the surface is refined further by going through a pinhole which prevents light from adjacent sources (both lateral and outside the focal plane) from reaching the detector [78].

Confocal microscopy was pioneered by Minsky, who devised a setup where light from outside the focal plane is largely prevented from reaching the light detector [82]. By scanning and assembling an array of these points, a 2-D image can be formed and a series of these 2-D images (or optical slices) can be stacked to form a 3-D representation of the subject. Confocal microscopy is utilized for its ability to image planes beneath the surface of a sample [78] which lends it to biological imaging applications where it is used to acquire optical sections of living specimens which have been treated with fluorescent dyes.

The CSLM excites and images a small, but finite volume in the sample. Ideally, the volume is rotationally symmetric about the Z axis (perpendicular to the sample surface), but stretch along the Z axis compared to the X and Y axis by a factor K. The radius in the X-Y plane is set by the wavelength of the light, index of refraction and the numerical aperture of the optics, ideally approaching the diffraction limit[83]. In a perfect system, the scaling factor K is based solely on the numerical aperture and the index of refraction of the sample, with a minimum value of roughly 2. In practice, K increases when focal setup changes, either through thicker cover glass, mismatched indexes of refraction, optical aberrations, or a laser beam that is not fully expanded on the back of the objective [83].

The intensity of fluorescence in the volume of the sample that is excited laser and efficiently detected is described by Equation 2-11 [83].

$$I = I_0 e^{-2(x^2+y^2+\frac{z^2}{K^2})/w^2}$$

Equation 2-11

Where I_0 is the peak intensity, x, y, and z are the distances from the center of focus, w is the beam width at $1/e^2$ of the peak intensity, and K is the scaling factor mentioned previously. As a result, the intensity of fluorescence drops of quickly with lateral displacement, but more slowly with axial displacement as shown in Figures 2-22 and 2-23. The scaling factor K can be viewed as the axial sensitivity of ability to reject out of focus fluorescence as compared to the lateral performance.

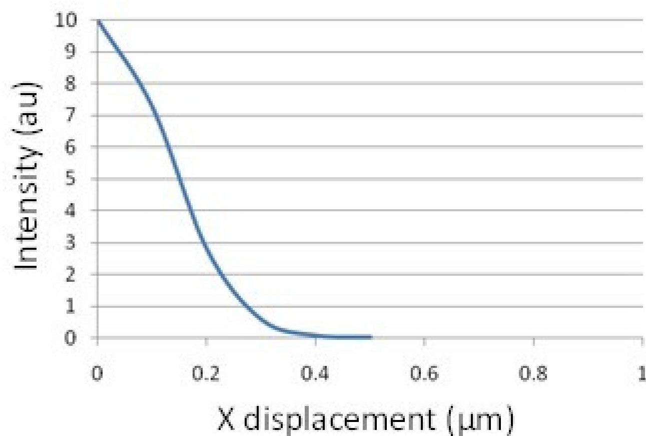

Figure 2-22. Intensity falloff with lateral displacement from the center of the beam, based on Equation 2-9 with w=0.25 µm and K=4.

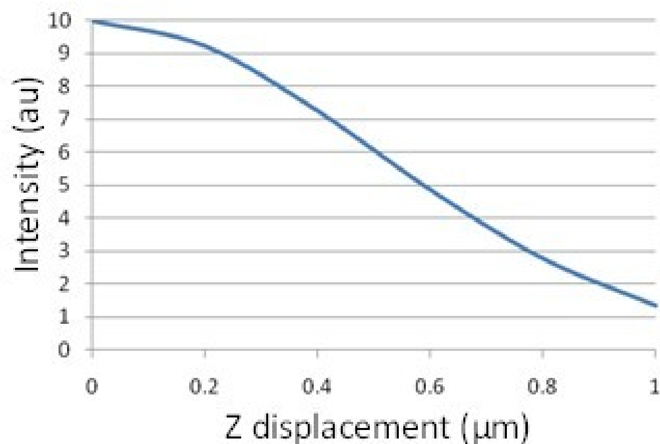

Figure 2-23. Intensity falloff with axial displacement from the center of the beam, based on Equation 2-9 with w=0.25 µm and K=4.

These models for confocal volume have been validated by imaging fluorescent beads (100 nm diameter) dried on a glass slide that was then indexed through multiple focal planes (in 100 nm steps) [84].

Advantages and Characteristics

The rejection of light outside the focal plane, coupled with exclusion of light from points adjacent to the focus point reduces haze and increases the sharpness of the image [85]. The lateral resolution improvements over conventional microscopes as well as the ability to focus beneath a sample surface lead to its use in the inspection of surface topographies for semiconductors and subsurface integrity of transparent material [86] [61]. Finally, the confocal fluorescence microscope can excite and detect fluorescent probes much smaller than the diffraction limited spot size. In the resulting image, the probes appear as diffraction limited dots which are much larger than the actual probe (~ 0.25 µm for a 10 nm quantum dot for example), but are detected nonetheless.

Disadvantages

Measurements with the confocal microscope are much slower than a conventional microscope due to the point by point illumination of the sample. Scan rates are limited by the stability of the stage as well as the required resolution of the measured intensity values (higher scan rates result in lower resolution photon counts).

2.5 Fluorescence and Quantum Dots

Fluorescence is a luminescence phenomenon by which an atom absorbs a high energy photon (short wavelength) and emits a lower energy photon (longer wavelength) [81]. The fluorescence takes place in three main stages: excitation, relaxation and fluorescence [81]. Excitation, also known as absorption, takes the energy from the high energy photon and moves an electron from its ground state into an excited energy state. During relaxation, the electron falls to the lowest level of that excited energy state. Finally, during fluorescence, the electron falls back to its original ground state [81]. It is during this fall back to the ground state that a photon, at a lower energy than the incoming photon, is released, emitting a longer wavelength of light [81].

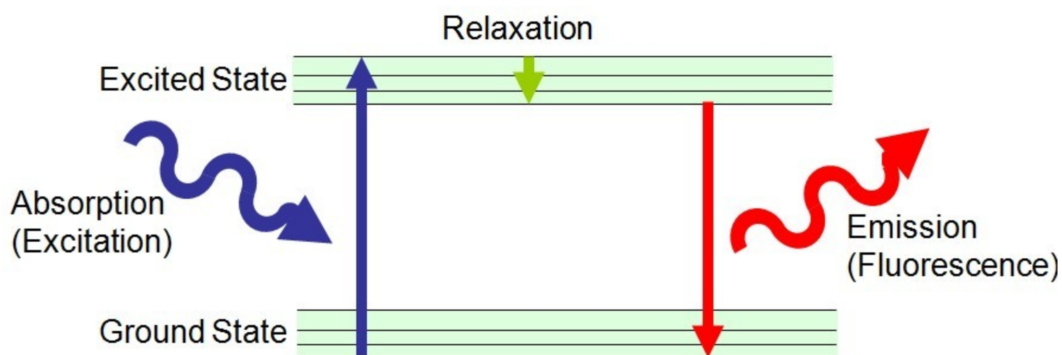

Figure 2-24. Energy States during Fluorescence

A fluorescent material can go through this process many times (hundreds to tens of thousands of cycles depending on the material) before it is photobleached and loses the ability to fluoresce [81]. This loss occurs because of a breakdown of the fluorescent molecule or that the molecule's electrons end up in a stable state that cannot be excited by incoming photons.

Fluorescent materials are so named for the description of the phenomenon in the fluorspar by the British scientists Sir George Stokes [81]. Fluorescent molecules are commonly referred to as fluorochromes or probes. Once they are combined with a larger molecule through adsorption or covalent bonding, they are called fluorophores, which can be divided into two categories; intrinsic, which occur naturally, and extrinsic, which are synthesized or biologically modified.

Fluorescent materials are characterized by their absorption and emission spectra. Examples of two common fluorescent probes are shown below in Figures 2-25 and 2-26. A common characteristic of both spectra is the relative breadth of the absorption and emission spectra and the amount of overlap of the spectra. Broad absorption spectra are desirable, in that they allow for the use of numerous excitation sources. The amount of overlap between the absorption and emission spectra is problematic however as it makes it difficult to separate emitted fluorescence from light that may be reflected from the excitation source.

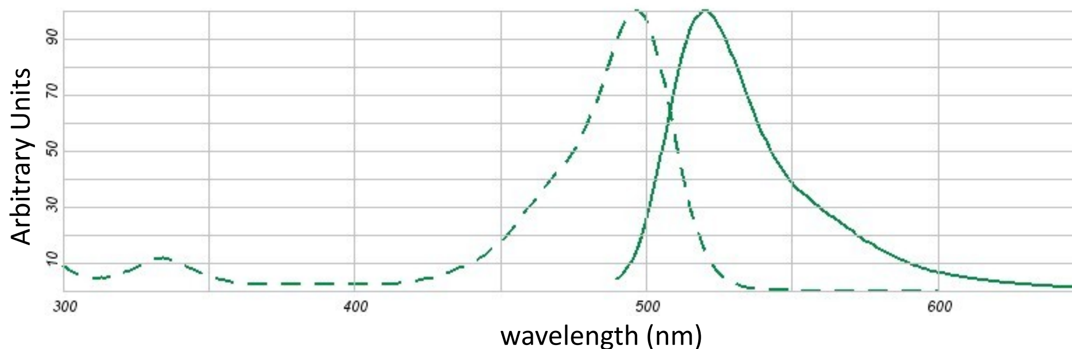

Figure 2-25. The absorption (dotted line) and emission (solid line) spectra for Rhodamine [87].

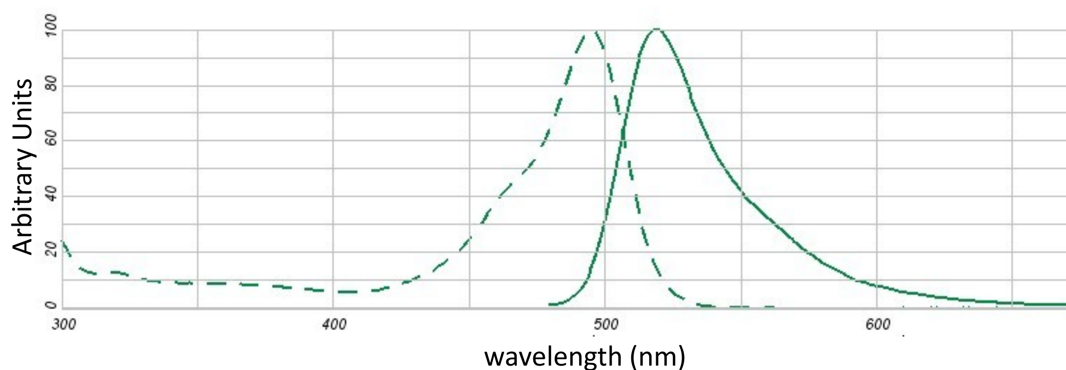

Figure 2-26. The absorption (dotted line) and emission (solid line) spectra for FITC (fluorescein) [87].

2.5.1 Quantum Dots

Quantum dots are nanometer scale semiconductor crystals such as cadmium-selenide (CdSe) and lead sulfide (PbS) that fluoresce when subject to excitation. Discovered by Louis Brus at Bell Labs in 1983 [88], these nanocrystals exhibit three dimensions of quantum confinement. They exhibit a number of characteristics that make them more desirable than organic fluorescent dyes including a broad absorption spectra, narrow tunable emission spectra, higher quantum yields, and resistance to photobleaching [89, 90]. The broad absorption spectra allow for the quantum dots to be excited by a variety of sources while the narrow emission spectra allow for precise

filtering to eliminate other sources of fluorescence. Their emission peaks are typically 30 nm full width half power (FWHP) [89] and are tunable by careful control of the crystal diameter (Figure 2-27).

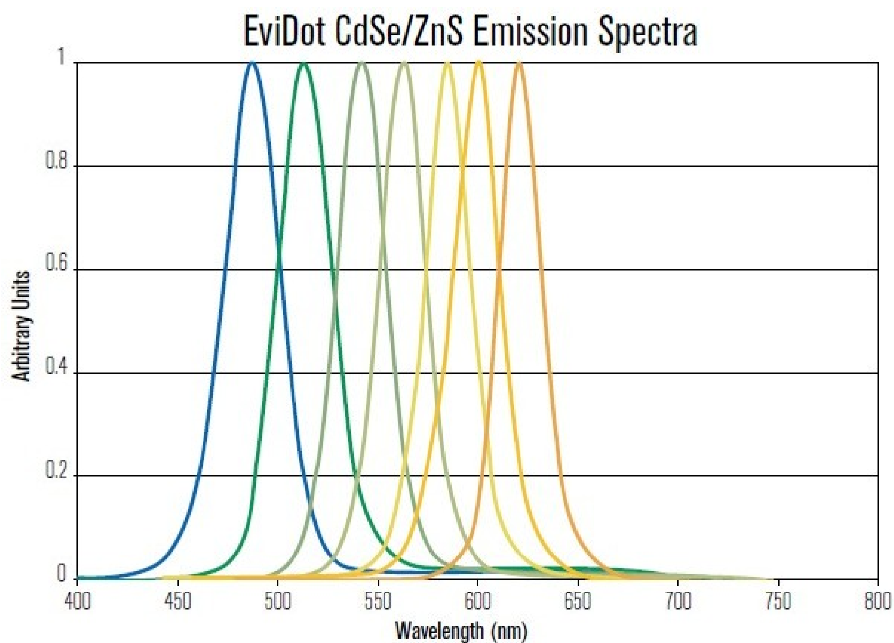

2-27. Quantum dot emission spectra [89].

These core semiconductor crystals can be coated with a shell that improves their performance by reducing surface defects that can reduce the quantum yield [91]. This is the formulation used with Evident Technologies EviDots which are comprised of a CdSe core surrounded by zinc-sulfide (ZnS) shell. This outer shell is coated with a ligand layer roughly 2 nm thick that increases the solubility in the desired solvent (Figure 2-28).

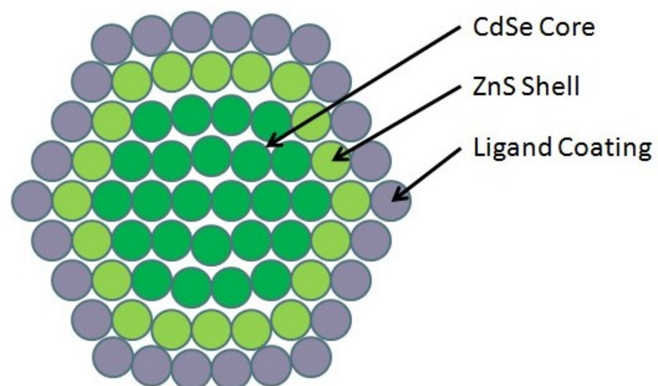

Figure 2-28. Structure of a Core-Shell Quantum Dot

CHAPTER 3. EXPERIMENTAL PROCEDURES

The glass and YAG samples investigated in the course of this research were subject to a variety of processes to a) modify the surface and then b) measure and quantify the surface. The first section covers the equipment, consumables and procedures used for lapping and polishing the glass samples. The second section explains the various instruments used to measure the samples and goes into detail on the techniques used for analyzing the confocal fluorescence microscope images. The third subsection details the etching procedures used to reveal subsurface damage in polished glass and YAG. Finally, the last section provides some initial results showing that the described procedures do in fact produce high quality surfaces on glass and YAG samples that have subsurface damage beneath.

3.1 Loose Abrasive Finishing

The loose abrasive finishing of the glass and YAG samples consisted of two steps unless otherwise noted. The first step involved lapping the samples by hand on a rotating iron platen. In the second step, the samples were pad polished on a Strasbaugh overarm polisher.

3.1.1 Equipment

Strasbaugh Lapping Station

Lapping was performed on a Strasbaugh model 6UR1 with an iron platen which provides spindle rotation.

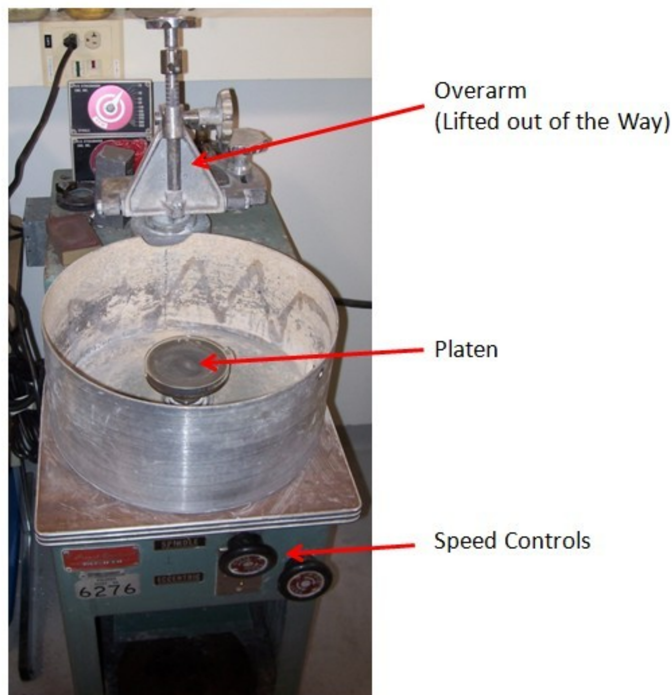

Figure 3-1. Strasbaug Lapping Station (front view).

Strasbaugh Overarm Polisher

A Strasbaugh nFocus Overarm Polisher, model 66DF was used for the pad and pitch polishing processes. It features variable speed drives and digital readouts for both the spindle rotation and eccentric sweep. Polishing pressure can be adjusted with the system pneumatics and the system has been plumbed for slurry recirculation.

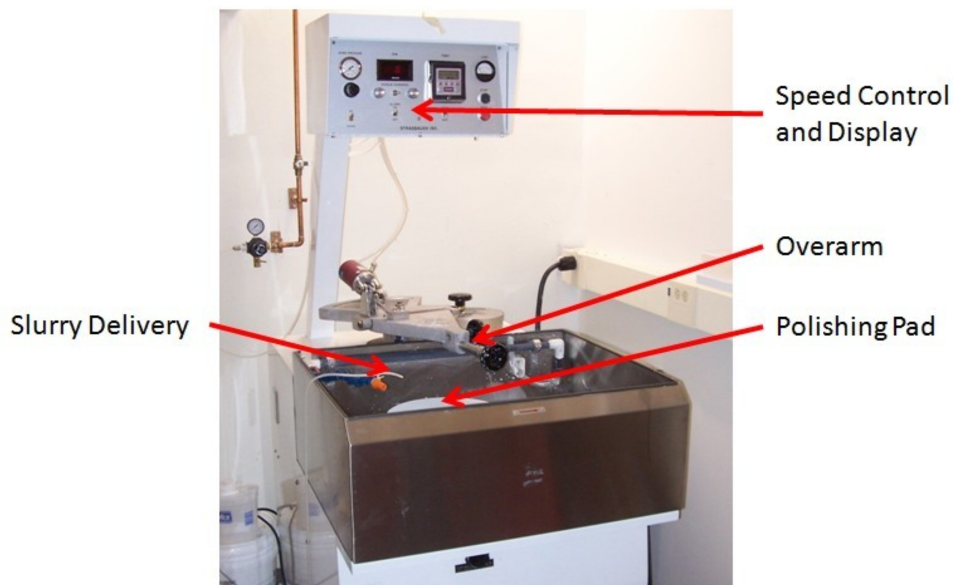

Figure 3-2. Strasbaugh nFocus OverArm Polisher.

Peristaltic Pump

A Simon variable speed peristaltic pump was used to provide slurry recirculation in the pad and pitch polishing processes described later in this chapter. Silicone tubing was routed through the pump to connect the slurry reservoir to the slurry delivery point above the polishing pad.

3.1.2 Consumables

The consumables used define the key process parameters of workpiece (sample), tool (pad, platen, or pitch) as well as the fluid and abrasives (slurry).

Glass Workpieces

Corning 0215 glass microscope slides were used as samples in the lapping and polishing tests. The primary constituents of soda lime glass are SiO_2 (73%), Na_2O (14%), CaO (7%), MgO (4%), and Al_2O_3 (2%) and it has a density of 2.40 g/cc [92]. The samples

are economical and easy to work with, but the multiple constituents in the glass make for more complex chemical interactions than a material like fused silica[29]. The slides were found to have a relatively undamaged subsurface layer (based on etching and microscope examination) which meant that SSD found after processing could be attributed to the lapping and polishing procedures used in the experiment, not a preexisting condition. The samples came in the form of microscope slides which were nominally 25 mm × 75 mm × 1 mm. These samples were fractured into samples that were nominally 25 mm × 25 mm × 1mm in order to fit in the sample stage on the confocal microscope.

YAG Workpieces

YAG (Yttrium Aluminum Garnet) is a synthetic crystal used as a laser medium in solid state lasers. It is doped with other materials such as neodymium, erbium, chromium and cerium. Undoped YAG has a chemical formula $Y_3Al_5O_{12}$, a density of 4.55 g/cc, and a melting point of 1950°C[93]. It is valued for being a high gain medium with high efficiency as well as being mechanically strong. It is fabricated using the Czochralski technique, where high purity constituents are melted in a crucible and a seed crystal is introduced to the melt, then slowly extracted to produce a boule of material.

The YAG samples used in these experiments were undoped YAG cylinders provided by Northrop Grumman Synoptics. The cylinders had a diameter of 10.25 mm and a height of 6.67 mm (as measured with a Mitutoyo micrometer). As received, they had an 'inspection polish' but had not been processed to remove SSD.

Polishing Pads

Dacron Polishing Cloth pads from Pace Technologies were used to polish the glass samples. The woven pads have a low nap and are commonly used as intermediate polishing pads [94]. A grooved polyurethane pad was used to polish the YAG samples. In both cases the adhesive backing of the pads was used to attach the pads to the Stasbaugh polisher's aluminum platen.

Workpiece Holders

During the pad polishing process, the samples were then mounted with adhesive tape to an aluminum disc with a receiver for the overarm quill on the Strasbaugh polisher, Figure 3-3.

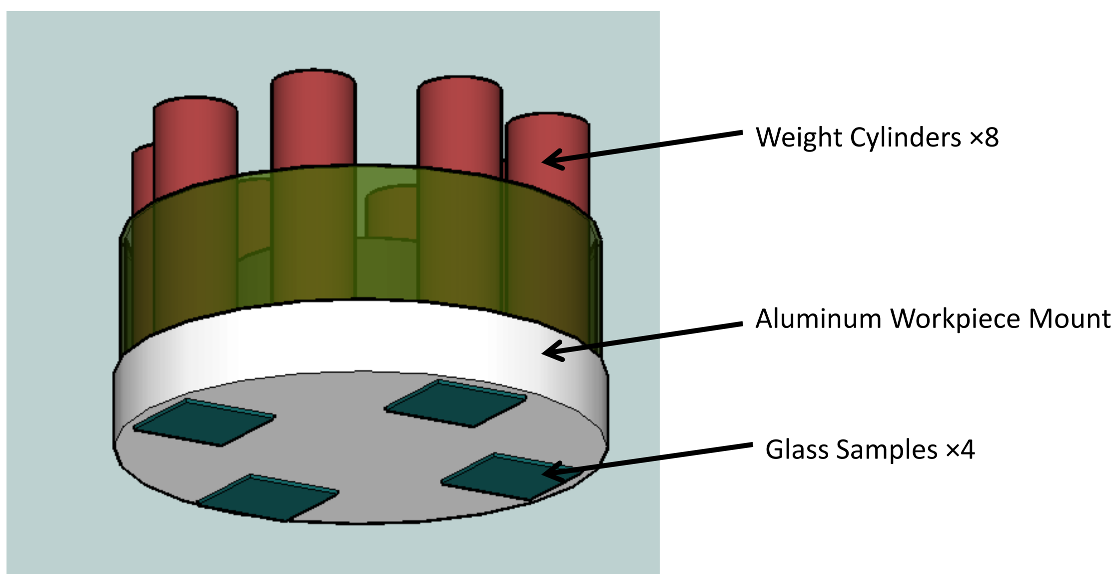

Figure 3-3. Polishing workpiece holder, viewed from below

The weight cylinders were used to provide consistent polishing loads after it was observed in Alan Landis' research that the pneumatic system for the Strasbaugh nFocus

overarm polisher induced significant load variations during the sweep of the workpiece across the polishing pad.

Lapping Slurry

The lapping slurry consisted of a mixture of 20 μm aluminum oxide abrasive particles (UNALUM 600) mixed with distilled water.

Polishing Slurries

The glass samples were polished with a ceria slurry (Hastillite PO) with a mean particle size of 0.45 μm that was diluted 1:8 with distilled water. The slurry was allowed to flow and fully cover the tool (pad or pitch tool) prior to the start of polishing. The slurry was recirculated with a variable speed peristaltic pump and stirred with a magnetic stirrer to prevent separation and settling of the components.

The YAG samples were polished with a submicron aluminum oxide slurry provided by Northrop Grumman Synoptics. This slurry was chosen to maximize the usefulness of the eventual results for our industrial partner, Northrop Grumman Synoptics. As a proprietary slurry, the exact composition was undisclosed. As with the ceria slurry, the aluminum oxide slurry was recirculated with the variable speed peristaltic pump and stirred with the magnetic stirrer.

Slurry Monitoring

Slurry composition was controlled by careful measurement of the constituents utilizing both the available glassware and the Ohaus Adventurer Pro balance (described below). Where it was required, slurry pH was monitored with litmus paper with seven color points over a pH range of 3.0 to 9.0.

3.1.3 Finishing Processes

Glass

Glass samples were taped to a mounting block and lapped by hand (estimated 17 kPa pressure) for 20 minutes on an iron platen rotating at 20 RPM using the lapping slurry described previously. The slurry was not recirculated, but was added to the platen periodically throughout the lapping process to keep the platen covered. Distilled water was also added dropwise to the platen if the slurry appeared to be drying out or agglomerating. The samples were removed from the mounting block and cleaned with IPA soaked tissues to prevent transfer of the 20 μm abrasives into the subsequent polishing process.

These samples were then polished on a Dacron pad rotating at 15 RPM for 30 minutes with the eccentric sweeping at 6 RPM over 180 mm. The ceria slurry was re-circulated at 120 mL / minute with the peristaltic pump. The samples were removed from the workpiece holder and cleaned with IPA soaked tissues prior to measurement.

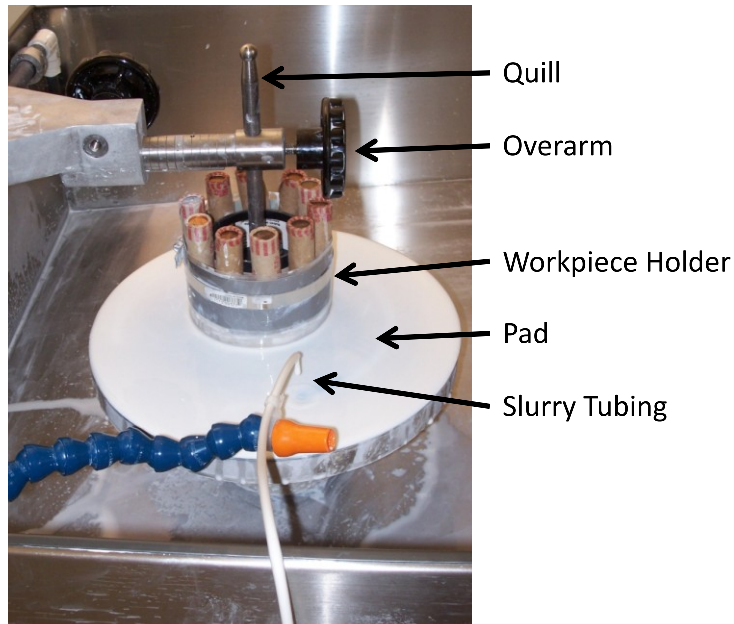

Figure 3-4. Photograph of the pad polishing with a Dacron Pad and Hastilite PO slurry.

YAG

The basic steps were the same, consisting of a lapping stage and a polishing stage. The increased hardness of YAG, and consequently the much lower material removal rates, necessitated a much longer process.

The YAG samples were lapped by hand (estimated 25 kPa pressure) for 30 minutes on an iron platen rotating at 20 RPM using a lapping slurry previously described. The YAG samples were then polished for six hours on the grooved polyurethane pad at a pressure of 85.5 kPa with the spindle rotating at 20 RPM and the eccentric sweeping over 180 mm at 6 RPM.

3.1.4 Analytic Processes

In addition to the finishing processes described above, two additional analytical processes were performed on selected glass samples. The need for these additional processes is described in Chapter 5.

Pitch Polishing

Select glass samples were subject to a pitch polishing step. A 300 mm diameter pitch tool was made of Acculap Standard (synthetic pitch, equivalent to Gugolz 64) which was poured onto an aluminum platen. X-Y grooves with approximately 10 mm spacing were scored onto the surface (Figure 3-5).

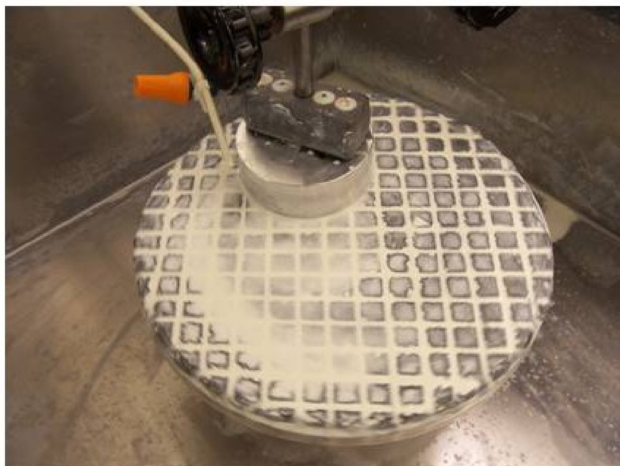

Figure 3-5. A photograph of the groove Acculap synthetic pitch tool performing a final polish on glass samples lapped and pad polished.

The tool was broken in and charged with the same Hastilite PO slurry used for pad polishing, which was recirculated at 60 mL/min. The samples were polished under a load of 7.5 kPa, with a platen speed and arm sweep of 15 and 3.5 rpm respectively. The goal for this finishing step was not to improve the surface, but to simply remove any

surface debris. Following the pitch polishing, the samples were cleaned with IPA soaked tissues before they were measured.

Short Duration Surface Etch

A short duration etch was also used to clean select glass samples after they had been lapped and pad polished. This step consisted of immersing the glass sample for 10 seconds in a 2% solution of hydrofluoric acid. The samples were rinsed in a beaker of distilled water before being dried and cleaned with IPA soaked tissues.

3.2 Sample Measurements

As was noted in the literature review, numerous instruments are used to assess the quality and characteristics of a lapped or polished surface. This chapter details the particular equipment and settings used to characterize the samples in future chapters. The magnifications, field of view, and resolutions of the equipment are summarized in Table 2.

Table 2. Instrument Magnifications, Field of View and Resolution.

Instrument	*Magnification*	*Field of View*	*Resolution*
Mitutoyo Finescope	*50×*	*340 µm × 255 µm*	*530 nm/pixel*
	100×	*170 µm × 255 µm*	*265 nm/pixel*
Olympus Biosystems Wide Field Fluorescence Microscope	*40×*	*370 µm × 280 µm*	*550 nm/pixel*
Zygo White Light Interferometer	*65×*	*110 µm × 80 µm*	
Mitutoyo SJ-400		*Five 0.8 mm line traces*	
Dimension 3110 Atomic Force Microscope		*40 µm × 40 µm*	*156 nm/pixel*[1]
Confocal Fluorescence Microscope		*40 µm × 40 µm*	*156 nm/pixel*[2]

The resolution of the system is dependent on the probe tip radius in use.
The apparent size of fluorescent features is diffraction limited to no smaller than 250 nm.

3.2.1 Material Removal Rate

The material removal rate of the various lapping and polishing processes was calculated by measuring the physical dimensions of the specimens as well as the mass. These measurements were used in turn to calculate the mass loss, the volume lost (based on the density), and the depth of material removed when the lost volume was removed from the affected face.

Dimensional Measurements

The dimensions of length, width, and thickness (or diameter and height for YAG samples) were made with a Mitutoyo micrometer. Prior to each use, the micrometer was checked to ensure that it was appropriately zeroed. The micrometer has a resolution of 0.0001” with a vernier scale and multiple measurements were taken to ensure accurate reading of the vernier scale.

Mass Measurements

Material removal rate calculations were based on the mass loss of the samples. Samples were measured before being processed and after processing on the Ohaus Adventurer Pro balance. The balance has a resolution of 0.1 mg and was zeroed before each use.

3.2.2 Optical Microscope

Optical microscopes provide a quick way to observe a polished surface at a higher magnification and identify features that would escape detection with the unaided eye. In the case of a well polished, defect free surface, it can be difficult to establish focus on the surface with certainty. In the absence of surface defects, focus was established at the edge of the sample and slowly adjusted as the field of view was moved to the center of the sample.

The Mitutoyo Finescope located in the metrology lab in the Duke Centennial Building was the primary microscope used in these experiments. Images were typically taken at magnifications of 20×, 50× and 100×. In the case of varied magnifications at the same sample location, slight stage adjustments were made to keep relevant features in the field of view. Images were captured with a camera controlled by Motic image capture software, typically at resolutions of 640×480 pixels. Occasionally images were taken with the Olympus BX51 microscope (coupled with a ColorView IIIu camera and DE Details software) located on the 2nd floor microscope lab of the Duke building. The Olympus has magnifications and software similar to the Finescope as well as the capability of using differential interference contrast to highlight surface defects.

3.2.3 Wide Field Fluorescence Microscope

The widefield fluorescence microscope was used to provide a quick measurement of the presence or absence of gross fluorescence on a sample. Dr. Elliott's Olympus BioSystem model 1X81, located on the 4th floor of the Woodward building was used. Images were taken utilizing the 'Lucifer Yellow' filter on the resulting fluorescence. Scan data such as the exposure time and magnification are saved along with a 16-bit TIFF data file. All images presented in this dissertation are 8-bit TIFF files exported from the raw 16-bit TIFF data.

3.2.4 White Light Interferometer

White Light Interferometry provides a quick, non-contact measurement of the surface roughness of smooth, specular samples. The Zygo Newview Scanning White Light Interferometer located in the metrology lab in the Duke Centennial Building was used as the white light interferometer in all of these experiments. The instrument is controlled with MetroPro software from the Zygo corporation which also reports the parameters of interest from the scanned surface (peak-valley roughness, R_a, R_q, etc.). The samples were imaged with the 50× objective with an additional 1.5× magnification for a total magnification of 65×. As form was not a concern in these polishing tests, a sphere was subtracted from the raw data to emphasize the short spatial frequency features. Additionally, there were no spikes removed on data sets used to calculate reported values.

3.2.5 Profilometer

The roughness of surfaces that are not specular cannot be measured on the white light interferometer, as the steep slopes of the topography do not reflect light back to the instrument. Thus, for lapped samples a Mitutoyo SJ-400 profilometer was used. This contact measurement moves a small stylus across the sample surface and measures several roughness parameters. Each trace with the SJ-400 consisted of five individual 0.8 mm segments, the averages of which were reported. Prior to use, the system was verified against a known roughness standard supplied by Mitutoyo.

3.2.6 Atomic Force Microscope

The AFM used in this research was a Dimension 3110 Atomic Force Microscope, from Digital Instruments, part of the Veeco Metrology Group (www.veeco.com). The AFM was controlled by a Nanoscope Dimension 3100 Controller and NanoScope IIIm Scanning Probe Microscope Controller. The system is housed in the Duke Centennial building in room 136, with the AFM seated on a vibration isolation table from Kinetic Systems. The tips used were Veeco model NCHV Antimony Doped Silicon with uncoated front and back sides, having an initial tip diameter of less than 12 nm.

Scan sizes were typically 40 µm × 40 µm to match the scan size from the confocal microscope. The scan area was also converted a resolution of 256 × 256 pixels, to match the confocal microscope images. The integral and proportional gains were set around 0.65 and 0.85 respectively with a deflection setpoint of 1.1 V. Some measurements deviated slightly from these settings in the interest of signal stability at

the time of measurement. The scan rates were at 0.1 Hz to prevent the tip from skipping across the surface.

3.2.7 Confocal Microscope

The confocal microscope used in these experiments is a custom piece of equipment designed by Dr. Patrick Moyer in the department of Physics and Optical Science and Dr. Stuart Smith in the Department of Mechanical Engineering and Engineering and Engineering Science at UNC Charlotte as well as several graduate students [95]. It consists of 3 main components, the excitation source, the photon detector and the sample stage which interact as shown in Figure 3-6 below.

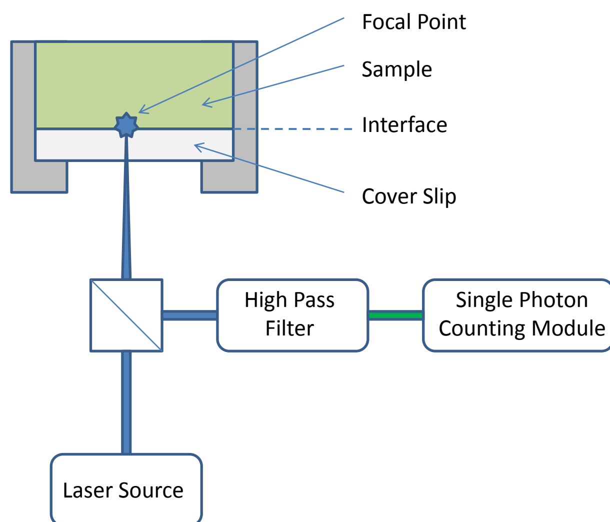

Figure 3-6: Schematic of the Confocal Laser Setup

Excitation is provided at 470 nm by a PicoQuant PDL 800 diode laser driver pulsed at 10 MHz. The light illuminates the sample causing fluorescent material that is present to fluoresce. The light from the fluorescence is reflected through a corner cube to a long pass filter. The 538 nm long-pass filter is used to reject any reflected light reflected from the laser. Finally, the small aperture of the EG&G SPCM single-photon avalanche diode acts as the pinhole in a traditional confocal microscope to reject fluorescence outside of the focal plane.

The sample stage was designed and built by Kevin Elliot to enable intracellular measurements which were not a capability in commercially available systems [96]. The stage is a flexure based design that keeps the optics stationary while moving sample in a raster pattern during the scan. The sample stage design accommodates samples which can fit on a 25 mm × 25 mm glass cover slip (used to prevent contaminating the optics with fluorescent material) and provides motion in x, y and z directions with ranges of 64.5 μm, 49.7 μm and 31.5 μm respectively [96]. Movement in each axis is achieved with a piezoelectric actuator, having a length of 20 mm and a range of travel of 17 μm over a drive voltage of 0-150 volts [96]. Position information is measured with capacitance gage sensor on each axis. Coarse sample alignment is achieved with micrometers.

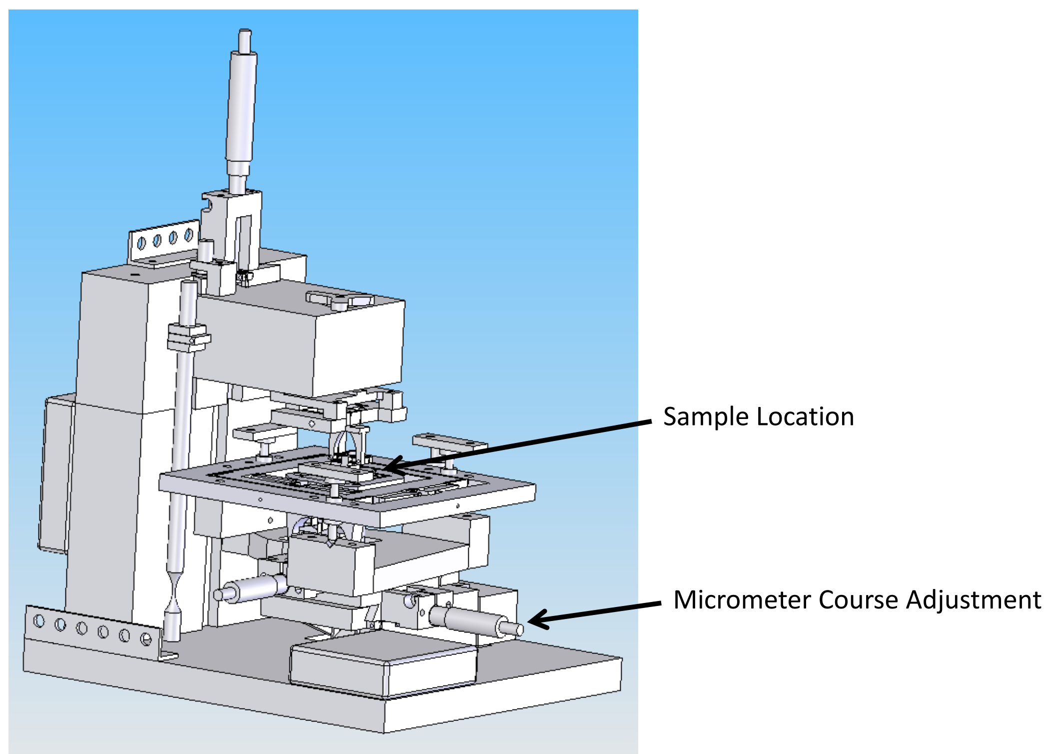

Figure 3-7. Illustration of the Confocal Microscope Sample Stage

Operation

Once a sample is mounted in the stage, the first task is to focus on the surface. At a start this is determined by visually observing the laser spot size on the sample and adjusting it minimize the diameter of the spot size. This process is complicated by two factors. The first is that the blue light of laser makes it difficult to sharply discern the edge of the focal spot. The second is the fact that the sample sits on a glass cover slip. The close proximity of the cover slip makes it possible to inadvertently focus on the surface of the cover slip instead of the surface of the sample. To alleviate this, the data trace from the Nanoscope is used as well to determine the focus on the surface. As the sample stage is moved in the z-axis with the micrometer control, it moves the samples with respect to the stationary focal plane. As the focal plane coincides with the coverslip there is an increase in the fluorescent signal as there is greater scatter and autofluorescence from the surface of the coverslip. This fluorescence however drops as the focal plane moves into the small gap that often exists between the sample and coverslip. The fluorescence increases once again however when the focal plane coincides with the surface of the sample, particularly when fluorescent material is present on the sample surface. This relationship is shown in Figure 3-8.

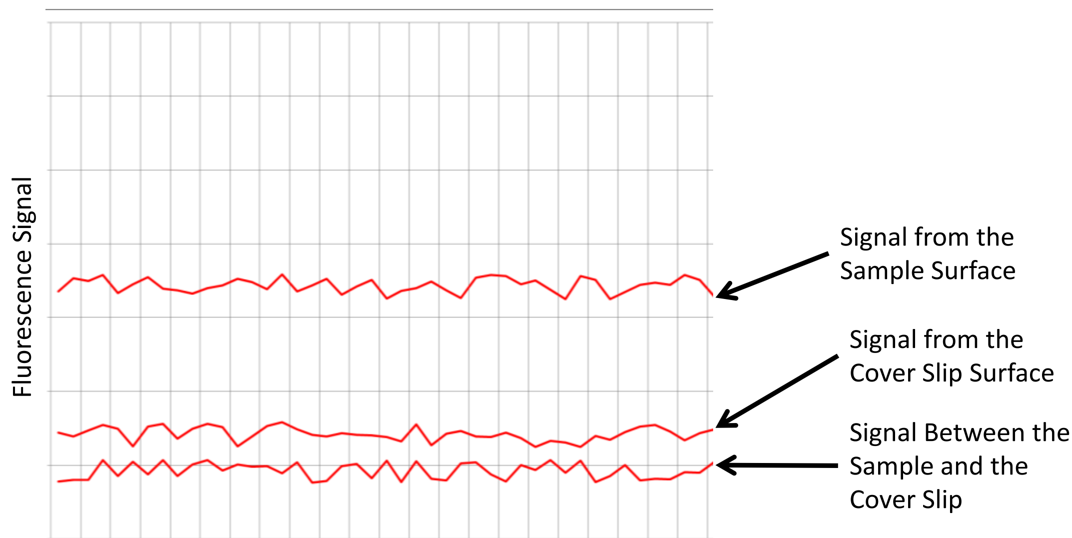

Figure 3-8. Determination focus on the surface based on fluorescent response.

Development of Confocal Fluorescence Measurement Analysis Techniques

Data acquistion and processing takes place in 3 phases for the confocal fluorescence microscopy images. First, the photon counts acquired by the Single Photon Counting Module (SPCM) are collected by the Nanoscope software. Second, the data in the Nanoscope files is exported as an ASCII file. Finally, the ASCII file is read into several MATLAB programs written specifically for this project that calculate several relevant values which are exported and outputs images of the fluorescence maps and a histogram showing the distribution of the data values for the scan (Appendices 2). These MATLAB programs were required as the work previously done in Dr. Moyer's research group with fluorescence resonance energy transfer (FRET), quantum dot blinking statistics and cellular imaging was satisfied with TIFF screenshots of the relative fluorescence maps which were then analyzed with image processing software (Adobe Photoshop or GIMP). Using the raw ASCII data file eliminates the limitation or influence

of the colormap chosen to represent the data values in the Nanoscope software. This has led researchers in Dr. Moyers group to started using the raw ASCII values for their analysis as well.

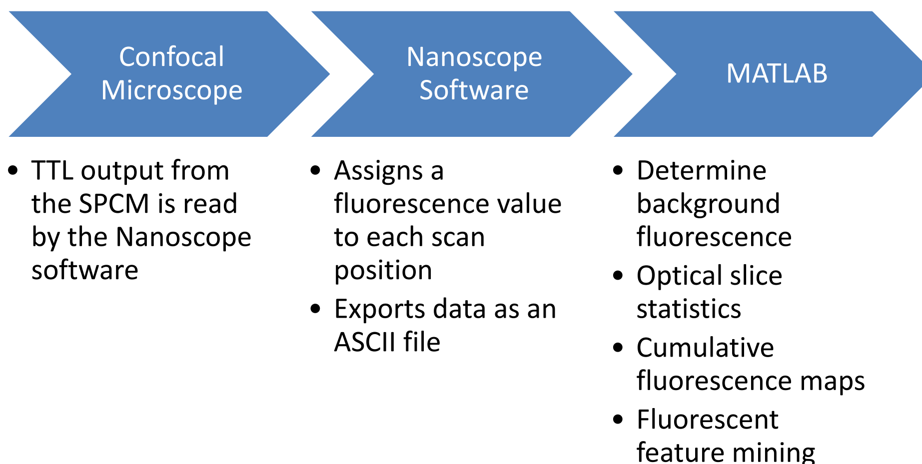

Figure 3-9. Overview of fluorescence data flow from the confocal microscope

The photon counts from the sample are detected by the SPCM which exports those counts to the Nanoscope software via TTL, which assigns the counts to the appropriate location based the scan parameters (scan rate, samples per line and scan size). The Nanoscope software is designed to be used with atomic force microscope (AFM) and as such has numerous options for dataprocessing and filtering such as plane fitting and low pass filtering. Though a topography of sorts is generated from the map of fluorescence, plane fitting was not performed as it was not seen as having a physical relevance to the measurement. The only occasion where plane fitting is done is when images are being viewed in the Nanoscope software, where the plane fitting process also sets the datascale appropriately to see the image.

The data from the Nanoscope is exported (without any planefitting or other manipulation) to an ASCII file. Headers must be included as the MATLAB code pulls key variables from this region. Naming convention has been 'MMDDYYNN.txt', where MM are two digits representing the month, DD is two digits representing the data, YY is two digits representing the year and NN is two digits representing the scan number. For example scan number 00 taken on the 7th of January 2009 should be saved as '01070900.txt'. This naming convention is important as the MATLAB code requires filenames in this format so that it can output the compiled data indexed by scan number.

To account for variations in the laser power, component alignment and background light sources, the confocal data files are compared to samples which have not been exposed to fluorescent material that are imaged with the same settings and conditions as the other scans taken that session. In this way, samples are always compared to the fluorescent response of an untreated sample. These control samples will exhibit some fluorescence due to the darkcount of the detector, variations of background fluorescence are due to differences from the following sources: imperfections in the filtering, laser scatter off the surface and stray sources of light. Imperfections in the filtering allow some light that is intended to be reject, to make it through to the detector. Laser scatter off the surface and autofluorescence tend to increase with the laser power.

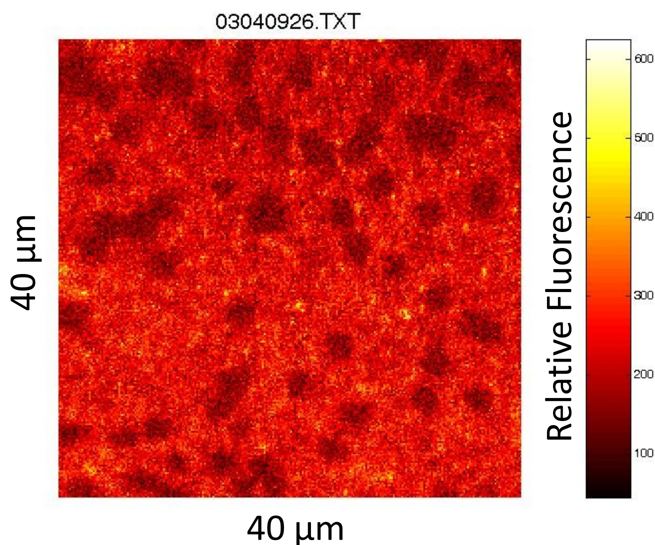

Figure 3-10. Confocal scan of a glass sample (which was not exposured to fluorescent material). The fluorescent response is due to laser scatter and autofluorescence at high laser power.

Finally, the SPCM is very sensitive to light sources, even the light from computer monitors and indicator LEDs in the laboratory. If these sources are not fully blocked during imaging, it can contribute to higher background fluorescence readings. With the contribution of all of these factors, the maximum fluorescence detected on a sample that has not been exposed to fluorescent material (in terms of the raw ASCII exported value) can vary from values as low as 40 in some setups to values as high 600 on other occasions and is recorded for an experimental setup as the background fluorescence threshold. This variation is what necessitates referencing the fluorescent values in particular scans back to control samples measured under equivalent circumstances.

With an understanding of the fluorescence readings for an untreated sample, the fluorescence maps from processed samples can be analyzed. Any variations or trends that occur at values below the fluorescence threshold are disregarded as they

cannot be attributed to fluorescence from the addition of quantum dots. This holds true in the three different ways in which the fluorescent data is analyzed in MATLAB. Optical slice statistics look solely at the aggregate data for a single focal plane at a location. Cumulative fluorescence maps combine the data from multiple planes from a location (X and Y coordinates) into a single image used to identify features and regions of interest. Finally, fluorescent feature mining looks at a small subset of region of the fluorescent scan and observes how the fluorescence in that subset changes through adjacent focal planes.

Optical Slice Statistics

Optical slice statistics are the first that are calculated from the ASCII datafiles that are exported from the NanoScope. The MATLAB program fiat.m (Fluorescence Image Analysis Tool) extracts the dataset (typically a 256 × 256 array) from the ASCII export as well as filename, scan rate, and datascale parameters. In addition, the program calculates two sets of statistics which are saved to a comma separated variable file. The first statistics are for the entire dataset and include the maximum, minimum, mean, and standard deviation. The second set excludes all datapoints which fall below the background fluorescence threshold when calculating the maximum, minimum, mean, and standard deviation. The percentage of datapoints above the threshold is also recorded.

In practice, the fiat.m code is run on background sample datafiles first to establish the background fluorescence threshold. The datafiles corresponding to the processed samples are then batch run utilizing the value for the background

fluorescence threshold to normalize the data, by dividing the raw values by the background fluorescence threshold. This means that only values greater than one should be considered as 'fluorescing sites' and the greater the value, the greater the confidence that such a signal is due to fluorescent material and not a function of the material or setup. In the event that raw ASCII values are desired, a threshold value of one can be chosen during the batch processing.

Additional outputs from the fiat.m code are a surface plot of the fluorescence values over the scan area (saved as a .jpeg file), a histogram showing the distribution of fluorescence values over the scan area (saved as a .jpeg file), and a MATLAB file containing just the dataset (in array format) for quick access in further computations.

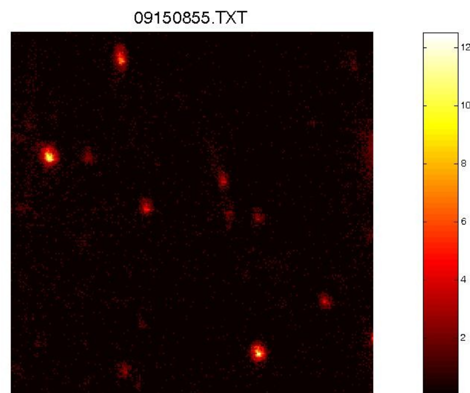

(a)

Figure 3-11. A surface plot of relative fluorescence from the fiat.m MATLAB code.

By themselves these statistics do not provide information about the trends in the fluorescence, but when the statistics are associated with the focal position at which they

were taken and assembled as a group it is possible to look at how the confocal scan statistics change with focal depth.

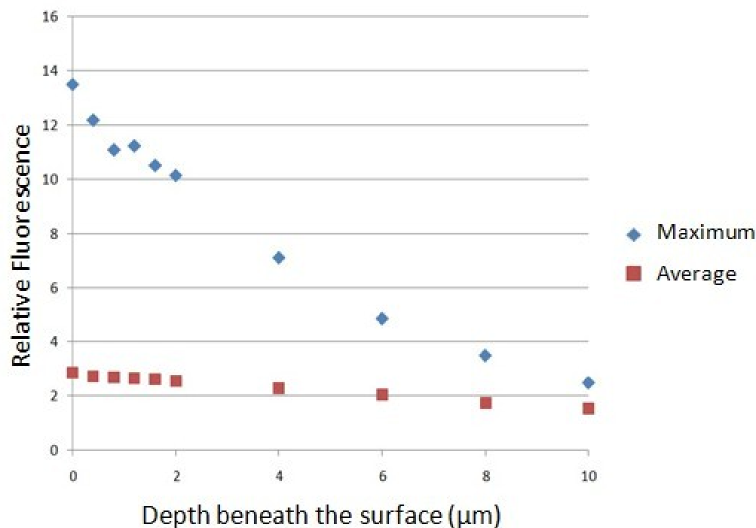

Figure 3-12. Changes in the maximum and average relative fluorescence above the background fluorescence threshold in a sample lapped and polished with quantum dot slurry then pitch polished for 5 minutes.

A limitation of these optical slice statistics is that they do not denote where the sites of high fluorescence intensity are distributed through each scan. In Figure 3-12 for example, the maximum value observed at a depth of 2 µm beneath the surface may be at the same coordinates as the maximum value 6 µm beneath the surface, but there is nothing in this presentation of the data to either support or disprove that hypothesis. Such questions are answered with the fluorescent feature mining technique noted below.

Cumulative Fluorescence Maps

While the optical slice statistics provide a great deal of information about the fluorescent response of the material at different focal planes, it can be difficult to keep

track of the characteristics at each focal plane and visualize the how the response changes from plane to plane. To address this and provide an intuitive map of regions of interest, cumulative fluorescence maps were built with the datasets by utilizing the data arrays that were previously saved by the fiat.m program. The arrays corresponding to the surface, 2 µm, 4 µm, 6 µm, 8 µm, and 10 µm beneath the surface were averaged and saved as a new array. High values in this array corresponded to X and Y coordinates that had high levels of fluorescence or fluorescence that was consistent through several focal planes. Conversely, low values in this array corresponded to coordinates that rarely if ever showed high fluorescence. Intermediate values could be a result of coordinates with a moderate level of fluorescence that persisted for several focal planes or coordinates with high fluorescence values that diminished rapidly in adjacent focal planes. These maps serve as a qualitative measure of the types of fluorescent features that are present in a scan, whether it be a multitude of low intensity sites that only span a couple of focal planes or features of high intensity that are present in all the focal planes observed.

Fluorescent Feature Mining

While cumulative fluorescence maps accumulate data from the entire scan range over several focal planes, fluorescent feature mining hones in on specific features to observe their specific response to changes in focal depth. With a focal plane data array loaded in MATLAB, the users runs the mine.m program, which allows the user to move a 7 × 7 pixel region through the dataset and extract the maximum, minimum, mean and standard deviation of the forty-nine pixel subset. Fluorescing material that is in focus

will appear as a distinct feature with crisp edges amid a darker background, while fluorescent material that is out of the focal plane will produce a broader, more diffuse fluorescence of lower intensity. This means that while the material moves out of focus, the average fluorescence over the 7 × 7 region may actually increase as out of focus fluorescence spills into adjacent points. This concept is illustrated in Figure 3-13, where a high intensity (bright) feature is evident in the topmost optical slice, but that feature spreads in the X and Y directions and drops in intensity at greater focal plane depths. This type of fluorescent response is consistent with material that is on a surface, but does not extend into or beneath a surface.

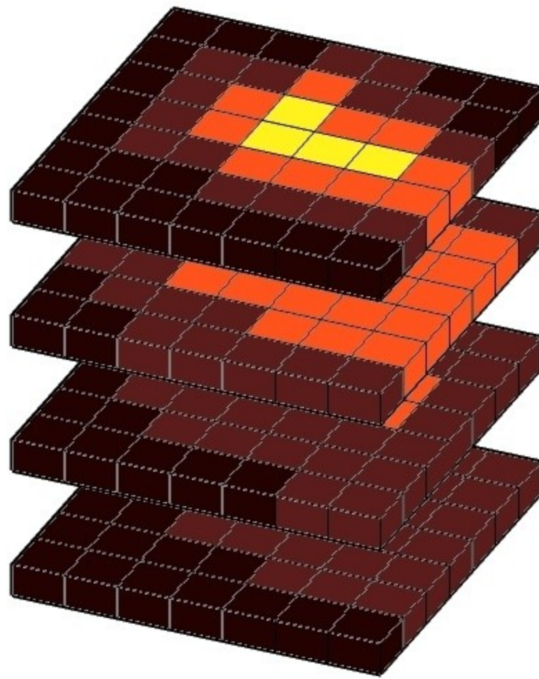

Figure 3-13. Conceptual drawing of the fluorescent response of a feature at four successive focal planes. Lighter blocks denote higher intensity pixels and dark blocks denote lower intensity pixels.

The cumulative fluorescence maps outlined previously are used to determine areas of interest on the fluorescent scans. These areas are then observed with the mine.m program and the statistics are manually recorded in a spreadsheet. In some cases, the center of the 7 × 7 region must be moved slightly from focal plane to focal plane to keep the feature in question centered. This is due to a slight tilt in the sample that causes the Z movement that changes the focal depth to also cause a relative X Y shift in the sample. This shift is typically small (1-2 pixels) and consistent with increasing focal depth. The data from the spreadsheets is then graphed to show how the fluorescence of individual features varies with focal depth (Figure 3-14).

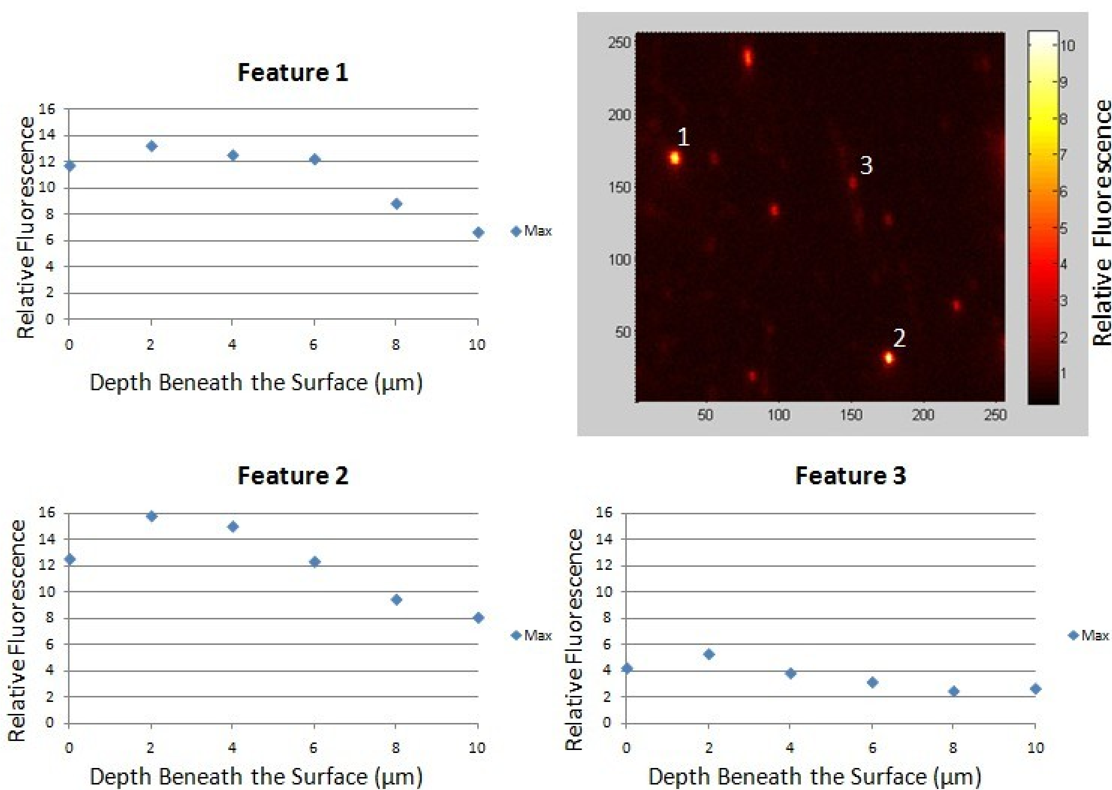

Figure 3-14. Relative fluorescent response of individual features in a confocal scan of a glass sample lapped and polished in the presence of quantum dots.

Curve Fitting the Fluorescent Feature Data

In order to determine the depth of fluorescent material (and by implication the defect housing the fluorescent material), Equation 2-9 for measured fluorescence intensity with respect to focal plane position was transformed into format where linear regression could be applied to it.

$$I = I_0 e^{\frac{-2}{w^2}\left(x^2+y^2+\frac{z^2}{K^2}\right)}$$

$$\ln\left(\frac{I}{I_0}\right) = \frac{-2}{w^2}\left(x^2 + y^2 + \frac{z^2}{K^2}\right)$$

Equation 3-1 and 3-2

The x and y terms were dropped as only the focal plane was changed.

$$\frac{-w^2}{2}\ln\left(\frac{I}{I_0}\right) = \frac{z^2}{K^2}$$

Equation 3-3

A variable transform of z^2 and K^2 to Z and C respectively resulted in an equation in form suitable for linear regression.

$$Z = z^2$$

$$C = \frac{1}{K^2}$$

$$\frac{-w^2}{2}\ln\left(\frac{I}{I_0}\right) = CZ$$

Equation 3-4, 3-5, and 3-6

Models for the fluorescent location in different treatments were generated from the data gathered in the fluorescent feature mining previously discussed. The I_0 value in these models was set equal to the maximum intensity observed for a feature in among the various slices, and w was taken to be 0.25 µm based on discussion with Dr. Moyer regarding the confocal volume of the system.

3.2.8 Confocal Fluorescence Control Samples

A variety of samples were used to calibrate the confocal microscope system and develop baseline measurements of fluorescence in a variety of glass samples. This was performed to isolate the impact of adding quantum dots to the abrasive slurries when looking at the fluorescent data.

Test Grid

The test grid is a key control sample that serves two purposes in calibrating the confocal microscope. It consists of a layer of quantum dots mixed in a polymer that has been cured on a glass slide over a gold grid pattern. First, it provides a reliable sample to ensure that the confocal microscope is capable of detecting fluorescence. Inability to detect fluorescence from the test grid leads to troubleshooting focused on determining what component in the assembly (mirrors, detectors, objectives, etc.) is out of alignment. The second use is that it gives a sense that the stage control parameters are set appropriately and the fluorescent image is not distorted (Figure 3-15). The distortions that appear are the result of the stage not moving as directed and imaging the same position for a longer period of time. That signal is attributed to the intended position instead of the actual position, leading to features being stretched. This is somewhat visible in Figure 3-15a, where the array of dots transitions from being sharp and distinct on the left to larger and more diffuse on the right. A more striking example is Figure 3-15b, where the stage is sticking and slipping as shown by the vertical bands at the bottom of the scan. These bands indicate that the stage has not moved

incrementally in the vertical direction and continues to scan the same line until it slips free and jumps to the next line.

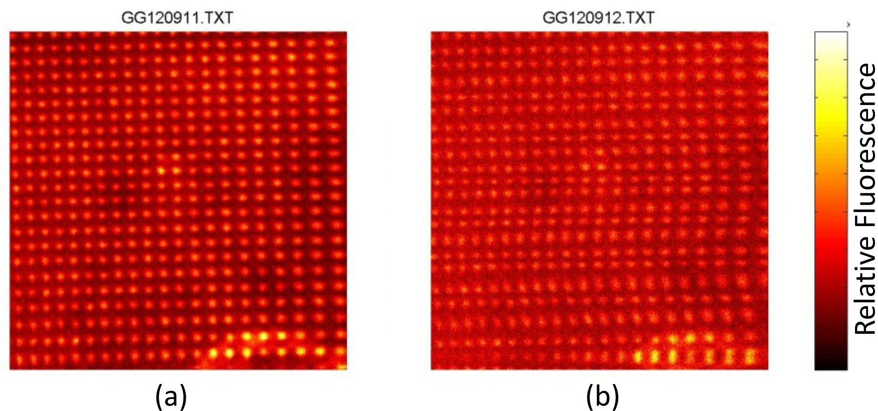

Figure 3-15. Confocal fluorescence images from the calibration grids showing (a) normal operation and (b) distortions due to scanning stage problems.

Surface Contaminated

In order to characterize the fluorescence of quantum dots on a surface, quantum dots solutions at both 0.4 nmol/mL and 60 nmol/mL were applied to glass samples and allowed to dry. As expected, high levels of fluorescence were detected at both concentrations, but with clearly different appearances based on the concentration. At low concentrations, discrete agglomerations of quantum dots could be seen on the confocal fluorescence images (Figure 3-16). The low concentration samples were examined over a 20 µm range to see how the falloff progressed at greater fluorescent depths. On samples treated with higher concentrations of quantum dots, there were no discernible features on the confocal fluorescence images (Figure 3-17).

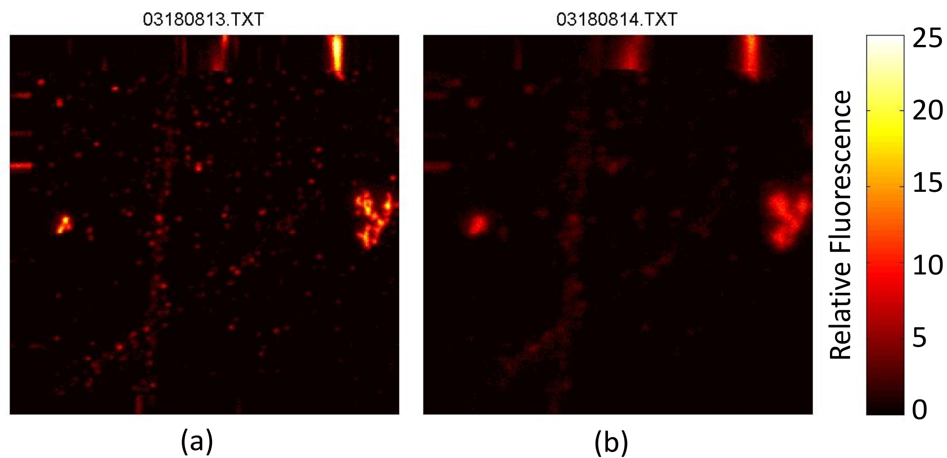

Figure 3-16. Confocal Fluorescence Image of a Glass Surface with Quantum Dots in Solution (0.4 nmol/mL) applied and allowed to dry, imaged at a) the surface and b) 10 µm beneath the surface. Note that the streaks at the top of the image are due to the sample stage not scanning correctly.

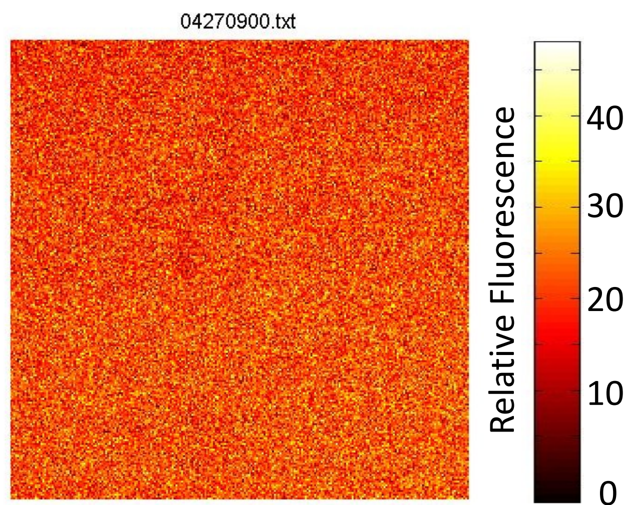

Figure 3-17. A Confocal Fluorescence Image of a Glass Surface with Quantum Dots in Solution (60 nmol/mL) applied and allowed to dry shows a uniform scan area with no discernible features.

Confocal Microscopy: Optical Slice Statistics

As expected, the optical slices statistics for the samples with quantum dots dried on the surface had a peak value near the surface that dropped off as the focal plane moved deeper into the sample (Figures 3-18 and 3-19).

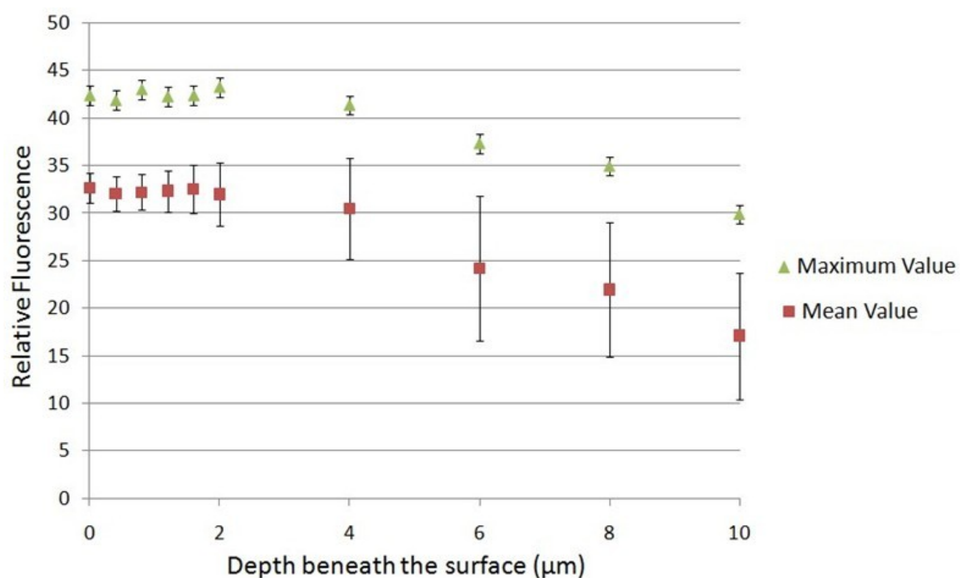

Figure 3-18. The maximum and mean relative fluorescence measured for glass samples exposed to a 60 nmol/mL solution of quantum dots that was allowed to dry on the surface.

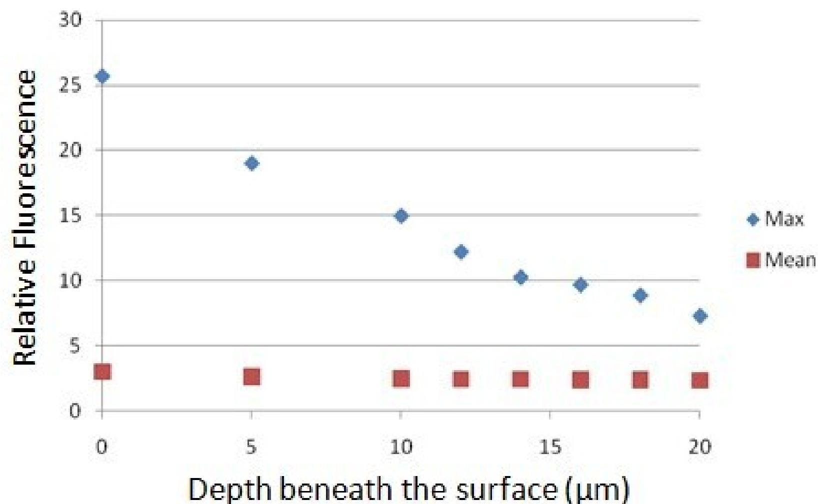

Figure 3-19. The maximum and mean relative fluorescence measured for glass samples exposed to a 0.4 nmol/mL solution of quantum dots that was allowed to dry on the surface.

The peak fluorescence values observed were higher for the 60 nmol/mL concentration of quantum dots than the 0.4 nmol/mL concentration. The mean values are much greater for the higher concentration of quantum dots, reflecting even distribution of high quantities of fluorescence across the sample.

Confocal Microscopy: Cumulative Fluorescence Maps

While the high concentration samples did not produce any identifiable features on the cumulative fluorescence maps, the 0.4 nmol/mL solution of quantum dots produced an abundance of features that were selected for further analysis with by mining the fluorescent profile of the features (Figure 3-20).

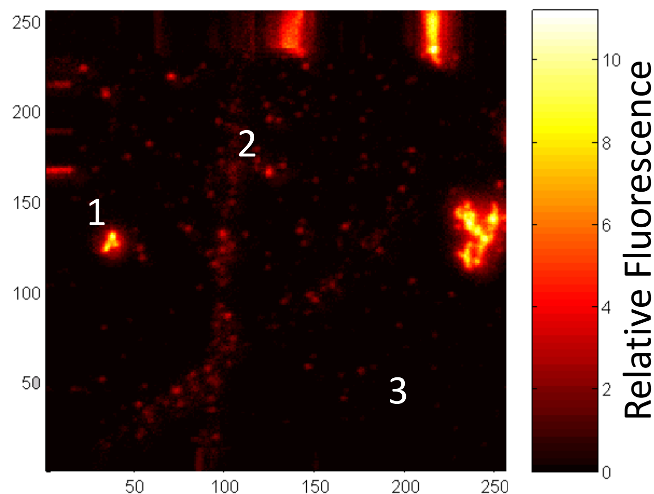

Figure 3-20. Cumulative Fluorescence Profile of a Glass Sample treated with 0.4 nmol/mL quantumd dot solution. Note again that the streaks at the top of the image are due to the sample stage sticking and not scanning correctly.

Confocal Microscopy: Fluorescent Feature Mining

While the sample exposed to a high concentration of quantum dots did not exhibit any discernible features to mine, the sample exposed to a low concentration did produce discrete features to probe at various depths. The behavior of these features matched that of the optical slices, with the peak fluorescence readily decaying as the focal plane moved from the surface. The mean values for the features are higher as would be expected for focusing in on the region around intense fluorescent features.

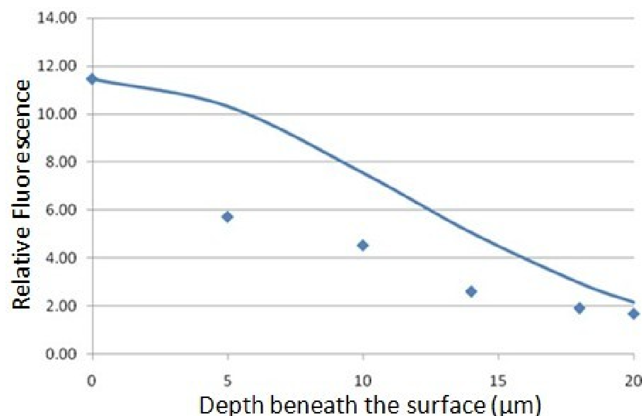

Figure 3-21. Maximum relative fluorescence feature profile data for a feature on a glass surface treated with 0.4 nmol/mL concentration of quantum dots, along with the model fit with K value determined as 87.7 and a R^2 value of 0.888.

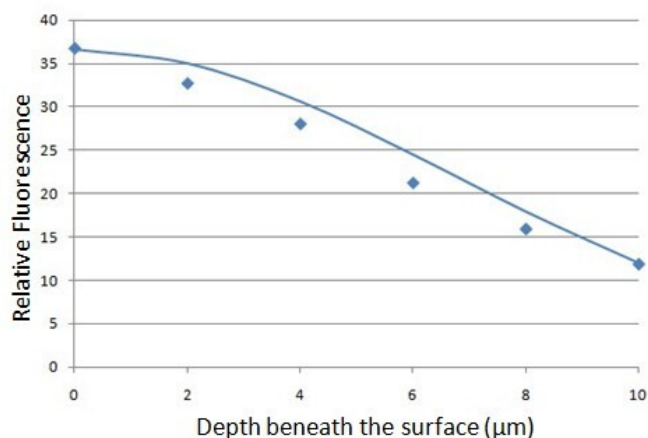

Figure 3-22. Maximum relative fluorescence feature profile data for a 60 nmol/mL concentration of quantum dots on the surface, along with the model fit with K value determined as 52 and a R^2 value of 0.9823.

3.2.9 A Note about the Sequence of Measurements

Samples which were exposed to quantum dots were not examined with optical microscopy or white light interferometry until the confocal fluorescence microscopy had been performed. Until it was established that photobleaching was not a critical concern, this was done to prevent possible degradation of the fluorescent signal of the

quantum dots (by the bright lights of both instruments) before they were even imaged. For a similar reason, atomic force microscopy was delayed until after the confocal microscopy so as not to dislodge any dots which were strongly adhered to the surface.

3.3 Etching

As noted in the literature review, etching has long been used as technique for detecting the presence of subsurface damage beneath a polished surface. Etching is used because it is a relatively straightforward procedure that does not require special equipment. While simple to perform, the technique does have limits in that it is destructive and it offers limited information about the depth of the fractures exposed.

In addition to removing material that may be covering the fractures, etching also enhances the visibility of the fractures by widening them. This is due to the acid equally attacking all available surfaces of the fracture which has the effect of reducing the aspect ratio of the feature (widening it) (Figure 3-23).

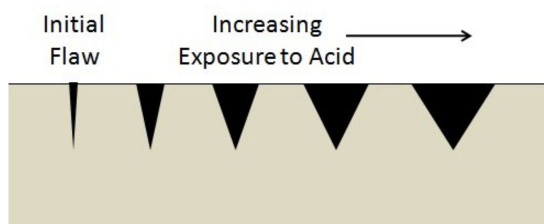

Figure 3-23. Increased etching of a fracture has the effect of widening it as seen in the progression of sketch fractures from left to right (in order of increasing exposure to the etchant).

The effect is more pronounced once limited ability of fresh acid to access the very tip of the crack is considered, leading to an increasingly cratered appearance to the defects. In their work at Lawrence Livermore, Miller et al found that the width of the

fractures exposed by etching MRF tapers was directly related to the time of exposure to the etchant [59]. For this reason, etching can best serve as a high end estimate of the depth of fractures by etching the sample until there is no visible evidence of the fractures (no distinction from the bulk material).

3.3.1 Etching Equipment

Safety Equipment

All etching was performed within the Polishing Lab fume hood. A lab coat, face shield, and appropriate gloves were employed when handling the etchants.

Etchants

Hydrofluoric acid was used to etch the glass samples in this research. The stock 49% hydrofluoric acid (by volume) was diluted with distilled water to a concentration of 2% by volume. This dilution was performed to slow the etch rate and enable greater control of the amount of material removed during the etching.

YAG samples were etched with ortho-phosphoric acid. The acid was shipped at a concentration of 85% (by volume) and was not diluted before use.

Glassware

A Teflon beaker was used with the hydrofluoric acid, as the acid readily attacks glass. A 400 mL glass beaker was used with the phosphoric acid. Assorted glassware was used for the distilled water used to rinse the samples.

Magnetic Stirrer

Agitation of the hydrofluoric acid was provided by a magnetic stirrer. Similar agitation of the phosphoric acid was deemed unnecessary due to the heating process inducing visible convective currents in the etchant.

Corning Hotplate

The phosphoric acid used to etch YAG was heated on a Corning hotplate. The hotplate provides digital readout of the temperature which can be set in 5°C increments up to 550°C.

3.3.2 Glass Etching

To confirm the existence of SSD, the glass samples were etched in a 2% solution of hydrofluoric acid for 30 seconds. The samples were held in the acid by a metal clip to ensure equal exposure to all faces and a magnetic stirrer was employed in the bottom of the beaker to ensure the etchant remained well mixed (to avoid regions of depleted etchant accumulating near the surfaces and diminishing the etch rate). Slight damage could be observed with the naked eye where the clip attached to the sample. In response, the samples were clipped near the edge, well away from where any subsequent observation or measurement would be made.

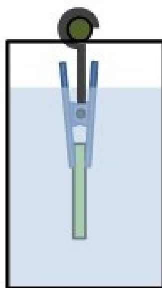

Figure 3-24. Glass sample suspended in dilute hydrofluoric acid to etch the surface.

3.3.3 YAG Etching

In theory the etching of the YAG laser crystals follows the same processes as etching of glass. Etching of YAG however is accomplished under more extreme conditions such as concentrated hydrochloric acid under high temperature and pressure, phosphoric acid at high temperature or a mixture of phosphoric and sulfuric acid at elevated temperature [97]. In an effort to avoid using high temperature acids in the polishing lab, the material removal rate of YAG when subject to room temperature phosphoric acid was investigated. Unfortunately, neither concentrated phosphoric acid or a mixture of concentrated phosphoric acid and concentrated sulfuric acid resulted in any measurable mass removal, even when subject to etch durations up to a week. Some in industrial settings control the temperature profile over many hours (up to 24) with microcontrollers, but this was not a viable option for the polishing lab at UNC Charlotte.

Instead, the general approach of Gerber [98]was followed, where the heating is applied quickly to get the YAG sample to a temperature where it will be etched by the phosphoric acid. The etching is complicated by the fact that before the phosphoric acid reaches a sufficient temperature to etch the YAG, the elevated temperature starts to decompose the primary form of phosphoric acid into secondary and tertiary forms, neither of which etch YAG [98]. This means that etching YAG with phosphoric acid is a balancing act, where elevated temperatures are required for etching to take place and higher temperature speed the etching process, but higher temperatures increase the rate at which the primary form phosphoric acid is degraded into secondary and tertiary

forms of no use in the etching process [98]. In the representative figure below, the blue profile is preferable to the red profile as it quickly achieves a temperature where it can etch the YAG, while the red temperature profile shows a process that spends a great deal of time in the shaded region where the acid is not hot enough to etch the YAG, but is decomposing into those secondary and tertiary forms which are of no value to the etching process.

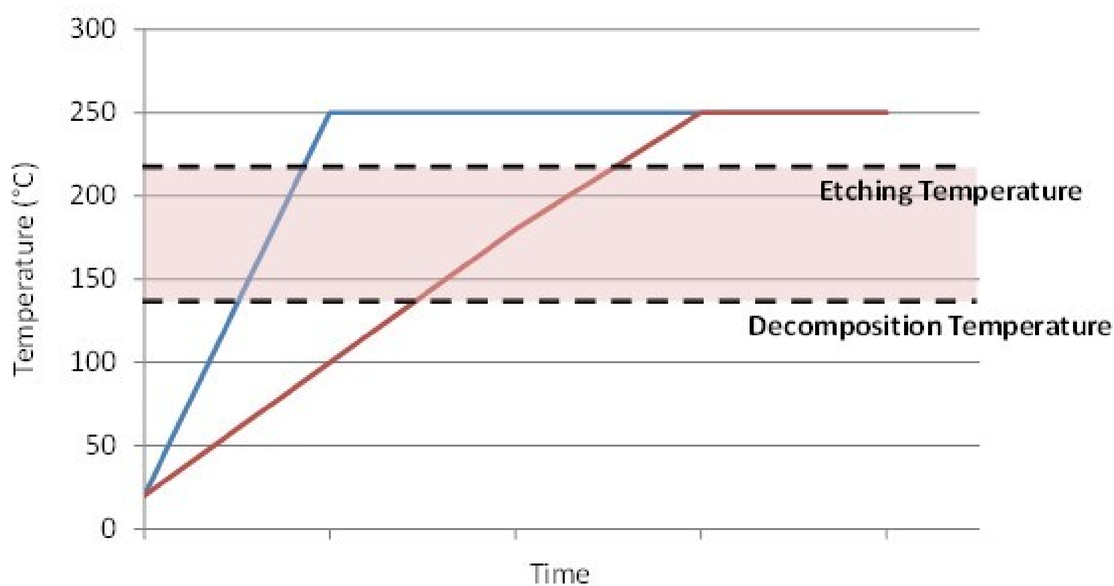

Figure 3-25. Differing temperature profiles and the effect on etching YAG with phosphoric acid.

To minimize the time that the phosphoric acid was in elevated temperature region that degraded the primary form into the secondary form and tertiary forms, without being at sufficient temperature to etch the YAG, the YAG samples were placed in a beaker with 80 mL of 85% phosphoric acid which was heated quickly on a hot plate. The samples were placed with the curved surface down and in contact with the wall of the beaker. This was done to expose both flat faces fully to the etchant and to minimize

the contact area between the beaker and the samples, Figure 3-26. This minimal contact was required to ensure that each face of the samples had ample exposure to the etchant. As an example, a cylinder positioned with one of its faces down might have diminished etching on that face because contact with the container limits access of fresh active etchant to the surface.

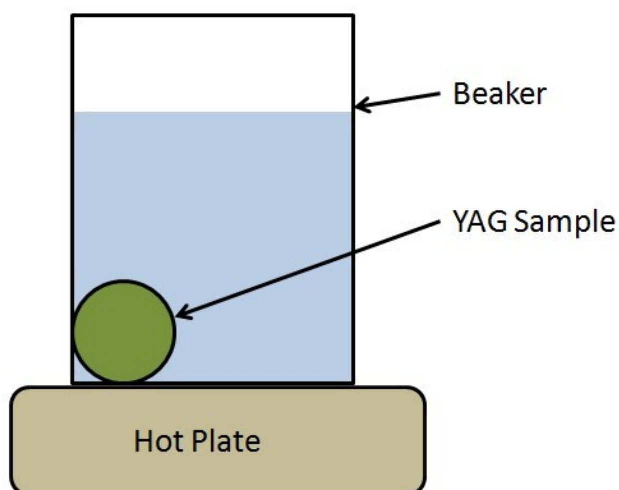

Figure 3-26. YAG sample orientation in the beaker for etching.

The beaker was covered with aluminum foil to prevent evaporation and hold in heat. The size of the beaker was found to be important, with a large diameter beaker being preferable as the larger contact area with the hot plate made for quicker heating of the acid. It is important to note that most glassware is not recommended for use with high temperature phosphoric acid. The risk of damaging the glassware is mitigated by a) keeping the temperature below 400°C b) only using small volumes of acid and c) inspecting the glassware for excessive damage prior to use. The hot plate was set to 350°C, but the actual temperature of the beaker was not measured. After 12 minutes, the hot plate was turned off. After allowing the beaker to cool for 25 minutes, the YAG

samples were carefully removed from the water (the hot plate still indicated a hot surface). The samples were then placed in a water bath prior to being weighted and examined under the optical microscope.

The depth of material etched away was calculated dividing the mass removed by the density of YAG to get the volumetric removal rate of the process. This volume was then divided by the calculated surface area of the sample to solve for the depth removed as shown in Equation 3-7.

$$\frac{\Delta m}{\rho_w(\frac{\pi D_S^2}{2}+\pi D_S h)} = \Delta d \qquad \text{Equation 3-7}$$

Where Δm is the changed in mass, ρ_w is the density of YAG, D_S is the diameter of the sample, h is the height of the sample and Δd is the depth removed. These calculations assume that a) a small amount of material is removed and b) material is removed equally from all sides. Given that the barrels of the YAG samples have a matte finish, they are expected to have greater actual surface area compared to the geometrically calculated surface area than the faces of the sample which have been polished to a specular finish. This greater effective surface area on the barrel would lead to a higher etch rate. This means that the actual depth of material removed from the polished end faces is less than what is calculated based on the change in mass.

3.4 Initial Loose Abrasive Processing Results

Examination of the loose abrasive processing samples provided the confirmation that the process would produce high quality surface beneath with a requisite layer of subsurface damage beneath. Such confirmation was a required before experiments detailed in Chapter 5 could begin.

3.4.1 Glass Process

The lapping process resulted in a matte surfaces with average R_a values of 0.37 µm (σ=0.03 µm) and removed a depth of approximately 17.5 µm (estimated based on mass loss). The polished surfaces had a roughness values of approximately 1 nm R_a as measured on the white light interferometer, while AFM measurements gave R_a values on the order of 1.5 nm. Pad polishing removed an average of 1.8 µm of material was removed from each of the samples (based on sample weight loss).

The etching procedure removed approximately 130 nm (based on mass loss). Optical images of the surface were acquired on a Mitutoyo Finescope microscope at magnifications ranging from 20× to 100×. The etched samples showed definite cracks and pitting that were not present in the pre-etch images (Figure 3-27).

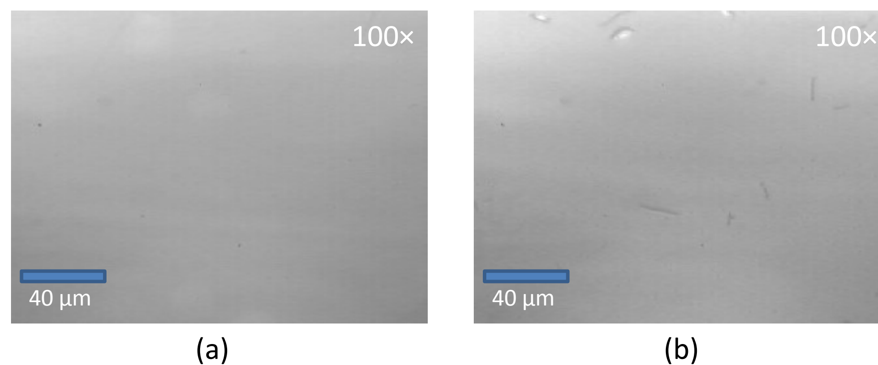

Figure 3-27. Microscope image of a lapped and polished glass surface (a) before it has been etched and (b) after it has been etched to remove ~ 250 nm of material (based on mass loss) to reveal subsurface damage.

Further confirmation that these defects were induced by the processes was provided by the fact that defects were not present on the back side of the samples that did not undergo the lapping and polishing processes, but were etched.

The finishing procedure described above has been shown to consistently produce a quality surface with surface roughness values on the order of 1 nm R_a as with the white light interferometer. Etching of these samples to remove a couple hundred nanometers of material revealed fractures and pits in the subsurface that can been observed with optical microscopy. Establishing a procedure for lapping and polishing glass that reliably results in a layer of subsurface damage is a requisite step for future studies where novel techniques for assessing subsurface damage.

3.4.2 YAG Process

The lapping was found to produce a uniform matte surface on the samples with average R_a values of 0.33 µm (σ= 0.06 µm) and removed 22.2 µm of material (estimated based on mass loss). It was important to remove this much material to ensure that any preexisting SSD was lapped through so as not to be confused with damage resulting from the processing in these experiments. The pad polishing removed 7.2 µm of material (estimated based on mass loss).

After five hours of polishing, pits were still readily visible with the Mitutoyo Finescope under 100× magnification (Figure 3-28). While these pits were not common, they were viewed as too significant in size and frequency for a quality surface. The average surface roughness measured as 0.7 nm R_a (σ= 0.1 nm) over three samples and three locations per sample (9 total locations) using the Zygo WLI. The defects that were visible in the optical microscopy images at this point (Figure 3-28) were not apparent in the 65× Zygo WLI scans.

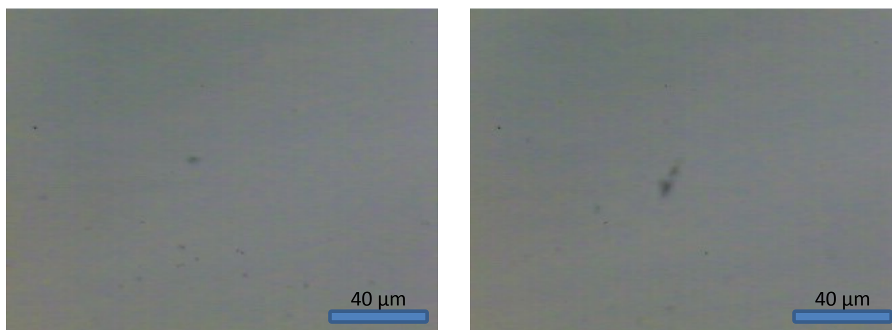

Figure 3-28. Microscope images from the Mitutoyo Finescope (100×) of YAG samples that have been pad polished for 5 hours.

After an additional hour of polishing (6 hours total) on the polyurethane pad, no evidence of pits or cracks were visible under 100× magnification (Figure 3-29) and the average surface roughness improved slightly to 0.6 nm R_a (σ= 0.1 nm) over three locations on three samples and three locations per sample.

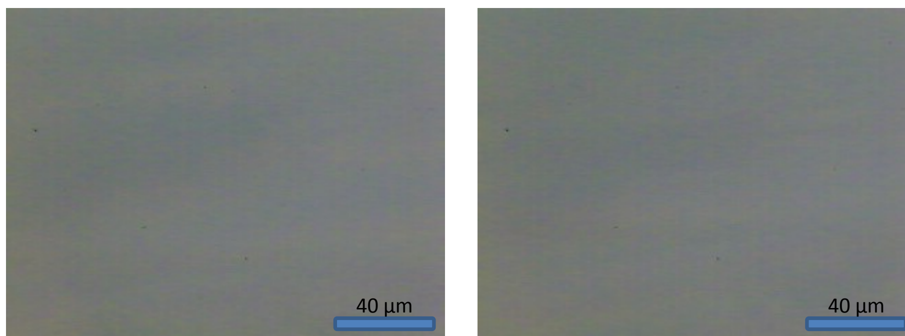

Figure 3-29 Microscope images from the Mitutoyo Finescope (100×) of YAG samples that have been pad polished for 6 hours

The etching procedure detailed above removed an average depth of 1.6 µm from each face of the YAG samples. Removing this layer of material revealed defects when examined with the optical microscope (Figure 3-30).

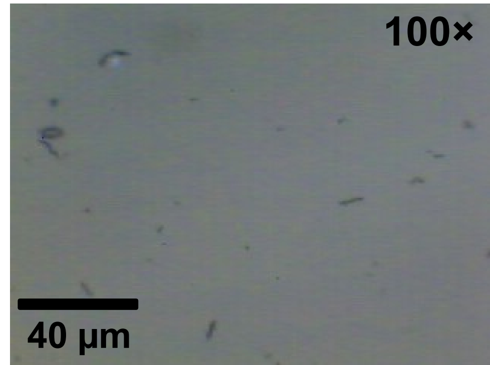

Figure 3-30. Image of a YAG sample lapped and polished, then etched in hot phosphoric acid removing 1.6 μm to reveal SSD.

As with the glass finishing process, the YAG finishing process has been shown to reliably produce a quality surface with average roughness values of less than 1 nm R_a on the white light interferometer and an underlying layer of subsurface damage.

CHAPTER 4. MODEL OF QUANTUM DOT AND SURFACE INTERACTIONS

This chapter presents a model of the quantum dot interaction with a glass surface as well as the effect of hydrodynamic forces during polishing. This modeled is followed by initial testing related to cleaning, diffusion, and the ability of the confocal microscope to image known surface defects containing fluorescence.

4.1 Model

The work presented here investigates if quantum dots (nano-meter scale semiconductor crystals that fluoresce at a given wavelength [13]) can provide a means to quickly detect SSD. By using a confocal fluorescence microscope, these fluorescent materials which are smaller than the diffraction limit of the optics can be detected (though they will appear as diffraction limited spots). In addition to SSD detection, the technique has the potential to provide new insights into how material is removed during lapping and polishing processes. This chapter starts with a theoretical model of the forces acting on quantum dots near a glass surface. Initial tests to assess the feasibility follow where imaging and cleaning procedures were developed. Finally the chapter includes details of experiments where quantum dots were added to the abrasive slurries used to lap and polish glass samples.

4.1.1 Hypothesized Interactions of Quantum Dots with the Lapped and Polished Surface

The method consists of tagging the abrasive slurries used at different stages of the finishing process with quantum dots. These dots will be present for all the dynamic events that may occur during polishing, i.e. cracks opening up to the surface etc. Their small size (diameters of 3.2-5.8 nm[99]) should enable them to travel into sample defects if they are open to the surface (Figure 4-1).

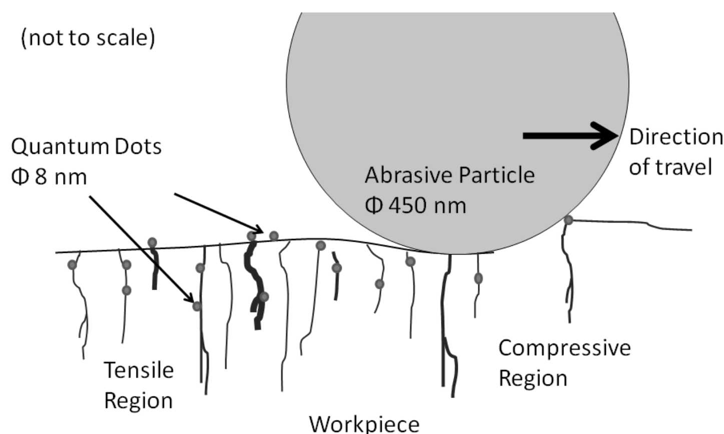

Figure 4-1. Hypothesized Interaction Between Quantum Dots and the Sample Surface During Lapping and Polishing.

After polishing the samples will be examined for fluorescence. A confocal microscope that scans areas on and beneath the surface will detect fluorescence from any remaining dots and provide information regarding their location.

4.1.2 Model for Quantum Dot Interaction with the Glass Surface

In addition to quantum dots being strongly adhered in defects two other possible interactions with the workpiece surface are evaluated; 1) attractive forces between the quantum dots and the workpiece are so high that they are effectively

adsorbed into the workpiece and they remain on the surface even after cleaning, 2) the hydrodynamic forces of the slurry flowing over the workpiece surface removes the quantum dots from the immediate surface. This would prevent the quantum dots from interacting with surface damage sites. To assess the possibility of these interactions the magnitude of the forces attracting and holding the quantum dots on the surface must be first estimated and then considered with respect to workpiece surface energies (absorption) and slurry hydrodynamic forces.

In the case of small particles (diameters <50µm) electrostatic or van der Waals forces are the primary acting forces [100]. Other electrostatic forces (camsir and electric double layers) are considered negligible as are gravitational, and inter-atomic forces [101]**.** The equation governing the van der Waal force between a particle and surface is given in Equation 4-1 below;

$$F_{VDW} = \frac{AD}{12r^2} \quad \text{(N)} \qquad \text{Equation 4-1}$$

where A is the Hamaker constant (Nm), D is the particle diameter(m), and r is the distance separating the particle and the surface (m). The Hamaker constant is a measure of the strength of the van der Waals forces in a system and depends on the geometry and composition of the interacting material pairs. Equation 1 does not take into account any deformation of the particle or the surface when the two bodies come in contact. As the deformation will increase the contact area, and thus the adhesive van der Waal forces, it should be factored into Equation 1. The Derjaguin–Mueller–Toporov (DMT) theory [102], which was developed to calculate the elastic deformation of small hard particles is used. Tabor based analysis [103, 104] of DMT and the Johnson–

Kendall–Roberts (JKR) theory [105], which focuses more on larger compliant diameter particles, confirms the suitability of DMT for this application. The contact diameter, a_0, of the particle on the surface under zero loading is given by Equation 4-2.

$$a_0 = \left(\frac{\pi \Delta \gamma D^2}{2K} \right)^{\frac{1}{3}} \quad \text{(m)} \qquad \text{Equation 4-2}$$

Where $\Delta\gamma$ (J/m^2) is the work of adhesion (a measure of the force required to separate two materials [106]), and K is the composite Young's Modulus (Pa). The composite modulus, E_K, incorporates the elastic modulus, E, and poisson's ratio, ν, values of both the particle, (E_1, ν_1), and the surface, (E_2, ν_2), see Equation 4-3.

$$E_K = \frac{4}{3}\left(\frac{1-\nu_1^2}{E_1} + \frac{1-\nu_2^2}{E_2} \right) \quad \text{(Pa)} \qquad \text{Equation 4-3}$$

As per Visser [107], Equation 4-1 is modified to include the additional contact area, Equation 4-4 [104]. The equilibrium spacing, ε, is the point of zero potential where the van der Waal forces shift from being attractive to repulsive due to the overlap of electron orbitals.

$$F_{VDW} = \frac{AD}{12r^2}\left(1 + \frac{2a_0^2}{\varepsilon D} \right) \quad \text{(N)} \qquad \text{Equation 4-4}$$

By taking parameter values from literature best suited to the materials used in the experimental work (see Table 3) the values of a_o and F_{VDW} are calculated to be in the order of 0.58 nm and 0.5 nN respectively.

According to work done by Zhang et al. [108] for small particles to be removed from a surface by the action of a fluid flowing over the surface, the moment applied by

the hydrodynamic force at 70% of the particle diameter must be greater than the moment created by the van der Waals force applied at a distance equal to the contact radius. The hydrodynamic force, F_D, can be described by Equation 5 [108].

$$F_D = C_D \rho \frac{v^2}{2} A_P \quad \text{(N)} \qquad \text{Equation 4-5}$$

Where C_D is the coefficient of drag, ρ is the density of the slurry, v is the velocity and A_P is the cross sectional area of the particle. For low Reynolds number flows (Equation 6), the coefficient of drag is given by Equation 7.

$$\mathrm{Re} = \frac{\rho v D}{\mu} \qquad \text{Equation 4-6}$$

$$C_D = \frac{24}{\mathrm{Re}} \qquad \text{Equation 4-7}$$

where μ (Pa.s) is the viscosity of the fluid, *v* (m/s) is the mean velocity of the fluid and *D* (m) is still the particle diameter. The same approach as taken by Visser [107] and Busnaina [109] to estimate the mean fluid velocity in chemical mechanical planarization (CMP) is taken here. The approach assumes that the peak fluid velocity occurs at a distance equal to the slurry abrasive particle diameter (not the quantum dot) from the workpiece surface. The velocity acting on the quantum dots will be a small fraction of the peak velocity as the ratio between the quantum dot and the abrasive is 1:56.25. As an extreme case, the velocity (v_{max}) was taken to be the rotational speed of the platen (ω) multiplied by the radius of the platen (*R*), Equation 8.

$$v_{\max} = \omega R \quad \text{(m/s)} \qquad \text{Equation 4-8}$$

The mean velocity acting on the quantum dots is then determined by Equation 9.

$$v = v_{\max} \frac{D}{D_{abrasive}} \qquad \text{(m/s)} \qquad \text{Equation 4-9}$$

A value of 0.31 m/s and 0.0055m/s were determined for v_{max} and v respectively. Substituting this value of v into Equation 5 gives a hydrodynamic force of 4.3×10^{-13} N. Table 3 details the values of the other parameters used in the calculations.

Table 3. Values of parameters used in Equations 2-9 and their sources.

Symbol	*Name*	*Value*	*Ref*
A	*Hamaker Constant*	1×10^{-20} J	[110]
D	*Diameter of the Quantum Dot*	*7.8 nm*	[111]
$D_{abrasive}$	*Diameter of the Abrasive*	*450 nm*	
$\Delta\gamma$	*Work of Adhesion*	$0.6\ J/m^2$	[112]
E_1= (Zinc-Sulfide)	*Modulus of Elasticity (ZnS)*	*74.5 GPa*	[113]
E_2= (Glass)	*Modulus of Elasticity (Glass)*	*75 GPa*	[114]
v_1	*Poison ratio (ZnS)*	*0.28*	[113]
v_2	*Poison ratio (Glass)*	*0.2*	[114]
ε	*Equilibrium Spacing*	*0.4 nm*	[104]
ρ	*Density of slurry*	*1.02 g /cc*	
ω	*Rotational speed of the platen*	*20 rpm*	
R	*Radius of the platen*	*300 mm*	

The moment induced by the hydrodynamic force at 70% of the quantum dot diameter, M_{hydro}, is 3.3×10^{-12} N nm. The moment applied by F_{vdW} at the contact radius, a_0, is 1.0×10^{-10} N nm. As $M_{vdW} > M_{hydro}$ it is not expected that the quantum dots will be 'flushed' off the surface by the polishing slurry. Therefore the quantum dots can remain in the vicinity to interact with the workpiece surface.

The other interaction to be considered is the absorption or diffusion of the quantum dots into the workpiece surface in the absence of any polishing action. When diffusion takes place, it is a result of diffusing atoms moving into the interstitial space between the existing atomic lattice [115] or the random movement of diffusing atoms jumping into voids in the existing lattice [115]. Both scenarios are aided by higher temperatures, where the lattice spacing is greater and there is more energy available to

facilitate movement. In the case of interstitial movement, the diffusing atom needs to be significantly smaller than atoms in the matrix to be able to 'squeeze in between' as is the case for carbon diffusing into iron. In the case of 'Hops Yellow' quantum dots the overall dot diameter is approximately 7.8 nm. This makes it impossible for the quantum dots to move through the interstitial spaces which are at least an order of magnitude smaller (angstroms instead of nanometers). By the same logic it would take much more than a single void in the crystal structure to accommodate a quantum dot. These considerations in addition to the interactions taking place at room temperature make it unlikely that there would be any significant diffusion of quantum dots into the glass sample.

4.1.3 Assumptions of the current presented model

Material of the Quantum Dots

The quantum dots are modeled as ZnS spheres, this neglects both the CdSe core as well as the ligand layer. The CdSe core is less of a concern as those molecules would be inside the ZnS shell and the ligand layer. The ligand layer however is more significant as it is in direct contact with the surface of the glass. In a review of literature, details about the ligand coatings were difficult to come by and the Hamaker constants required for attraction calculations even more difficult.

Material for the Glass

The material of the glass is modeled as silica due to the availability of Hamaker constants for ZnS acting on silica surfaces across a medium of water. The actual glass used in the experiments was a soda lime glass which includes several other constituents.

Slurry Composition

The calculations for van der Waals attraction were based on water as a medium. While the slurry is water based, the quantum dots are suspended in toluene which is then diluted with acetone making for a significantly more complex medium.

Surface Geometry

The glass surface is not a geometrically flat which is used to model it. Deviations from this model are likely to introduce additional points of contact [107] and generally work to make it more difficult to remove the adhering particle.

Other Quantum Dot Interactions

Given a lack of information about Hamaker constants, the van der Waals attraction between abrasive particles and the quantum dots has not been calculated. Geometrically, the small size of the quantum dots in relation to the abrasive particle makes it unlikely that the quantum dots adhered to the surface would be in close enough proximity to be dramatically influenced by a travelling abrasive. One area of potential interaction is attraction between the quantum dots and the abrasive particle while suspended in the slurry. Prior to contact with the sample surface, the attraction between the abrasive and quantum dot could dominate.

In a similar vein, attraction calculations between the tool and quantum dots are absent for the same lack of documented Hamaker constants for the pad and pitch tools used in polishing.

Limitations with respect to understanding of chemistry

This final category encompasses all of the relevant information that the author does not know he does not know. While not a chemist or expert on surface interactions, the author developed this model as a best estimate of the interactions between the quantum dot and the surface. Instead of working to refine the this model of particle interaction, time and resources were devoted to several experiments to provide empirical results as to whether quantum dots would introduced to an abrasive slurry would remain after cleaning.

Sensitivity of the model to these limitations

The uncertainties with regard to the composition of the quantum dots, the composition of the workpiece, and the general chemistry of the slurry can be wrapped up in the Hamaker constant. Given that the adhesion force varies linearly with the Hamaker constant as shown in Equation 4-1, it would take a shift of several orders of magnitude in the Hamaker constant for the hydrodynamic forces to overcome the adhesion. The Hamaker constant chosen could be larger or smaller than the actual value and thus increase or decrease the van der Waals force, but any deviation of the workpiece surface from a geometrically flat plane is going to provide additional contact area that adds to the adhesive force retaining the quantum dots. Thus losses in the adhesive force because of a lower than estimated Hamaker constant could be offset in part by the topography of the surface not being a perfect plane.

4.2 Cleaning Tests

With a model that showed that quantum dots would adhere to a glass surface it was import to be able to clean those adhered dots off the surface as well. This was to insure that fluorescence in subsequent tests was a result of quantum dots being embedded in the surface or trapped in the subsurface, it was crucial to develop an effective cleaning protocol to remove dots that were simply adhered to the surface. As a variety of surface measurements were to be taken, it was crucial that the method employed not add undue damage to the surface in the form of scratches and pits. There are numerous methods of cleaning optics [116], several of which were tested on glass samples which had quantum dot solutions deposited on the surface. As rinsing the surface and drying it with compressed air left unacceptable streaks and residue, a wipe based method was tested.

Quantum Dot Solution

A quantum dot solution of 60 nmol / mL of 'Hops Yellow' EviDots from Evident Technologies was used in these studies. These particles consist of a cadmium selenide core surrounded by a zinc-sulfide shell, resulting in an estimated crystal diameter of 3.8 nm. This shell in turn is surrounded by a 2 nm thick layer of ligands giving a final particle diameter of 7.8 nm. The ligands allow the dots to remain in colloidal suspension. The quantum dots have an emission peak at 553 nm ±10 nm and are excited by wavelengths shorter than 540 nm.

4.2.1 Cleaning Test Procedure (Wide Field Fluorescence)

Two drops of the quantum dot solution were allowed to dry on a glass sample, then half of the sample was wiped with a lint free tissue and held with locking forceps after soaking the tissue with several drops of isopropyl alcohol [116]. The forceps held the tissue near the folded edge, providing both strength and flexibility. The tissue was then dragged across the surface with contact, but minimal force between the tissue and surface. The tissue was wiped across the surface once, it was discarded and the process repeated with a second tissue.

4.2.2 Wide Field Test Results

The sample was examined with an Olympus Biosystem IX81 Wide Field Fluorescence Microscope. The boundary between the side which was wiped and the side left untouched is clearly seen in Figure 4-2 below.

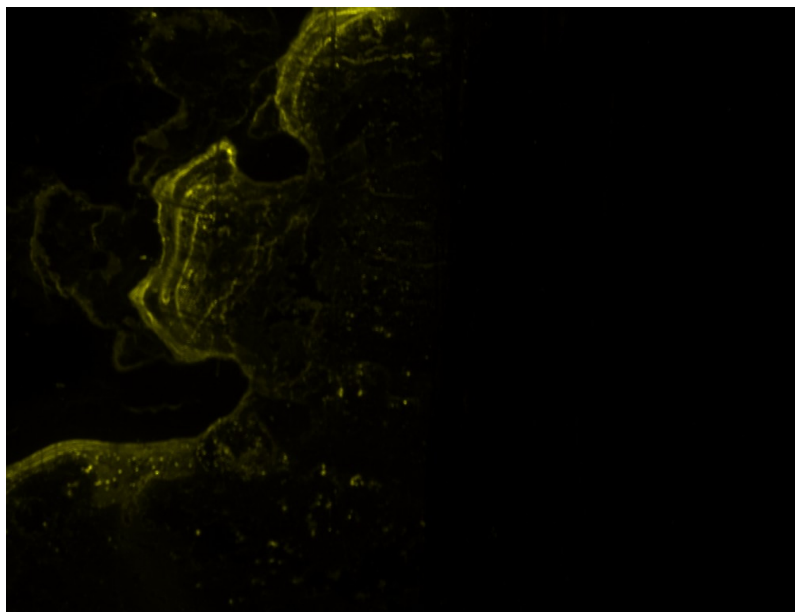

Figure 4-2. Wide field Fluorescence Image of Cleaning Validation Sample. Left Side: not cleaned. Right Side: wiped twice with IPA soaked tissues.

This data was further analyzed by examining the intensity of the signal at each pixel. The software maps the intensity value detected at each pixel to 8-bit value, with 0 denoting no fluorescence and 255 corresponding to the saturation of the detector. The maximum fluorescent signal on the wiped side was roughly 12% of the max on the region that was not cleaned.

4.2.3 Cleaning Test Procedure (Confocal Fluorescence)

While the results from the wide field fluorescence examination were promising, the confocal fluorescence microscope is much more sensitive and similar tests were performed to confirm effective cleaning of the quantum dots from the glass surface. Due to the sensitivity of the confocal microscope, the quantum dot solution was diluted in acetone to a concentration of 0.4 nmol/mL. Two drops of the solution were applied to each sample surface. The surfaces were cleaned with the IPA moistened tissues as described previously after 15 minutes, 75 minutes and 270 minutes respectively.

4.2.4 Cleaning Test Results (Confocal Fluorescence)

The results of the confocal fluorescence microscopy showed that the cleaning procedure could remove quantum dots from glass samples cleaned quickly after exposure to quantum dots [117].

Table 4. Quantum Dot Exposure and Cleaning Results

Sample Cleaned After	*Average Number of Fluorescing Pixels*	*Mean Relative Intensity of Fluorescing Points*
15 minutes	*6 to 7 pixels*	*1.2*
75 minutes	*20 pixels*	*1.4*
270 minutes	*589 pixels*	*2.4*
Not Cleaned	*3736 pixels*	*2.3*

4.3 Micro Indentation Tests

Prior to testing samples in search of subsurface damage, preliminary studies were carried out looking at known defects which were introduced onto the surface of the sample. These known defects provided features that could be easily imaged with other instruments such as the optical microscope to provide a comparison as the author became accustomed to using the confocal fluorescence microscope.

4.3.1 Equipment

The surface defects were created with a Knoop point on a Wilson Tukon Series 200 micro indenter. The micro indenter was chosen for the ability to create repeatable indents. The Knoop point was chosen for its distinctive shape with a clear long and short axis to the diamond.

4.3.2 Micro Indentation Process

Two drops of the 0.4 nmol solution of quantum dots previously mentioned were added to the surface of the glass slide. The slide was immediately placed on the micro indenter where an array of indents was produced on the sample. The array was used to aid in the detection of the defects in subsequent observations and increase the likelihood that an indent would be detected within the limited field of view of the confocal fluorescence microscope. During the final indent in the array, the sample stage was translated produce a scratch that served as a reference scribe mark during optical and fluorescence microscopy.

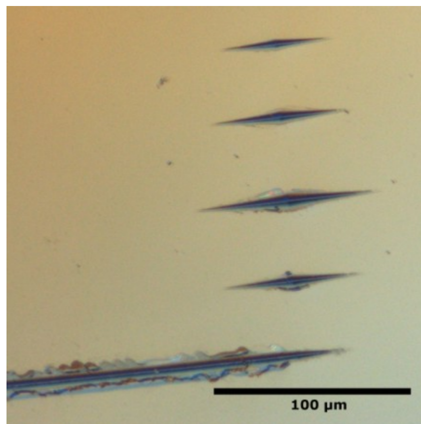

Figure 4-3. Image of an array of indents and scribe mark taken with the Mitutouo Finescope.

Following indentiation, the sample surface was immediately cleaned using the procedure from the previous chapter. The indenter tip was also cleaned thoroughly to prevent contamination. The indents were then measured with the atomic force microscope (AFM) as a comparison to the optical images (Figure 4-4).

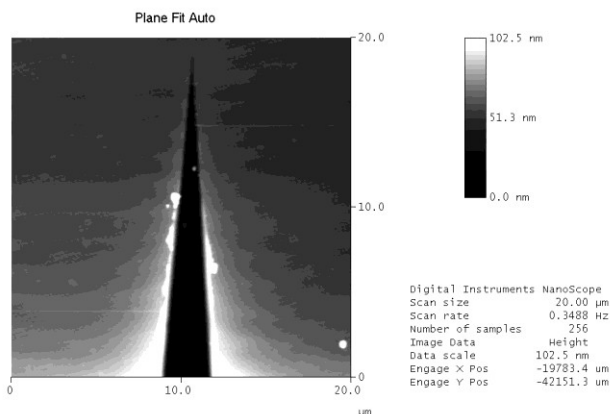

Figure 4-4. AFM scan of the tip of an indent in a glass sample.

4.3.3 Fluorescence Results

With clear optical images and AFM scans of the Knoop micro indents for comparison the samples were imaged with the wide field fluorescence microscope and confocal fluorescence microscope.

Widefield Fluorescence Microscopy

Examining the indent array with the widefield fluorescence microscope revealed fluorescent features that correlated strongly with the optical images of the indent array (Figure 4-5). The shape, orientation and relative size (due to varied loads) of the indents is captured in the fluorescent image. The fluorescence is concentrated at the periphery of the Knoop shape, outlining the diamond, but not filling it. Discrete pockets of fluorescence are noted in the scan outside the indented areas, showing that not all the fluorescent material had been removed from the surface. In some cases this fluorescence coincides with surface defects that are visible with the optical microscope. This suggests that unintended defects outside the indent array are also capable of retaining sufficient amounts of quantum dots to be detected after cleaning. Finally, the reference scratch clearly displays fluorescence both in the scratch and in the plastically deformed material pushed out of the scratch.

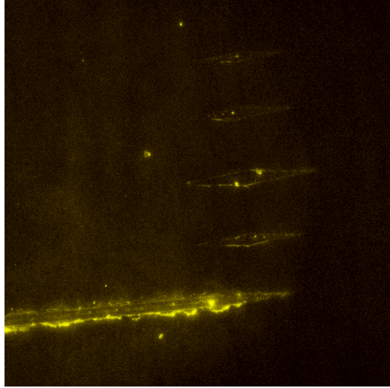

Figure 4-5. Widefield fluorescence image of an indent array produced in the presence of quantum dots (contrast enhanced).

Confocal Fluorescence Microscopy

The indented glass samples were then imaged on the custom inverted confocal fluorescence microscope (Chapter 3.2.7). The confocal images show the general shape expected of the Knoop indent (Figure 4-3), but the angle at the tip was measured as 14.5° instead of the 10° measured on the optical images. Differences can also be noted between (Figure 4-6 upper) a scan taken at the surface and (4-6 lower) a scan taken several microns deeper into the sample. The scan at the surface has a higher background signal as evidenced by the darker grey around the indent, while the scan at a lower focal plane is nearly white indicating low fluorescence. It is also worth noting that the clumps of fluorescence (dark regions in Figure 4-6) are more distinct in the lower Figure 4-6 with crisp edges that are consistent with a fluorescent material that is in the plane of focus. Like the widefield fluorescence, the confocal fluorescence also shows the outline of the indents as well as some features/structure within the indent.

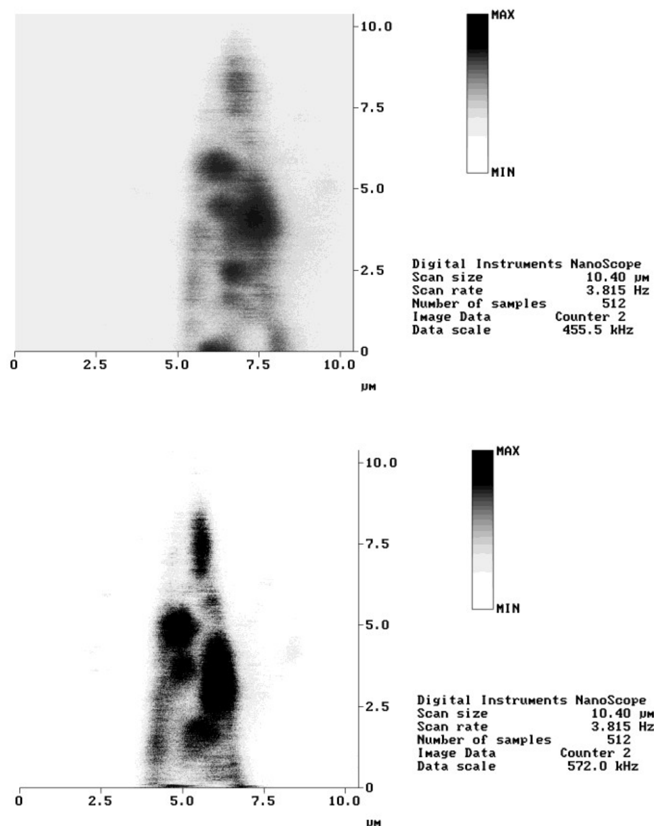

Figure 4-6. Confocal fluorescence images of the tip of an indent in a glass sample (top) near the surface and (bottom) several µm beneath the surface.

4.4 Discussion

The model that is presented in this chapter provides some confidence that quantum dots in abrasive slurries have a good chance of adhering to a glass surface and not simply be whisked away by the relative motion of the fluid moving across the workpiece. While there are uncertainties associated with the model, particularly in the area of the specific surface chemistry for the ligand coating on the quatum dot shell and composition of the glass, the calculated adhesion forces could be drastically reduced and still be sufficient to prevent quantum dots from being washed off the surface.

At the other extreme, the cleaning test shows that a surface exposed to quantum dots can be sufficiently cleaned with IPA soaked tissues, but as with the CMP cleaning literature particle removal becomes more difficult the longer the exposure. Finally the micro indentation tests show that quantum dots can be retained and successfully imaged in known surface defects like the Knoop indents. The widefield fluorescence microscope images showed additional defects such as surface pits as well as the plastically deformed material pushed out of the reference scratch had retained fluorescence as well. The fluorescent signature in these defects is particularly encouraging as it was unintended, but in the case of the surface pits worked to highlight features that were otherwise difficult to discern with conventional optical microscopy.

The fluorescence of the reference scratch is also a promising sign. Fluorescence in the material that had been pushed out of the reference scratch indicates that quantum dots may become embedded in the plastic flow of material, which is of interest given that plastic flow is proposed mechanism for material removal in polishing. An alternative mechanism would be that quantum dots were embedded in the surface during the initial indentation then dragged to other locations on the surface as the indenter was moved through the specimen.

CHAPTER 5. QUANTUM DOTS IN LOOSE ABRASIVE SLURRIES WITH GLASS

With the base procedures established in Chapter 3 showing the ability to produce specular surfaces with underlying subsurface damage, modifications were made to introduce quantum dots at various points in the process to assess if quantum dots could travel into defects as they were created (as described in Chapter 4).

5.1 Procedures

The following procedures use the glass samples, polishing equipment, and consumables detailed in Chapter 3. The solutions of quantum dots are identical to the 60 nmol/mL concentration described in Chapter 4. In addition to these processes several additional procedures were used for process analysis and are detailed in 5.2.2 and 5.2.4-7.

5.1.1 Lapped and Polished with no Quantum Dots

These glass samples were lapped and polished with the procedure established in the Chapter 3 to produce SSD beneath a high quality surface. These samples were imaged with the confocal fluorescence microscope to determine whether the presence of SSD in the sample without quantum dots would produce features in the fluorescence scans.

5.1.2 Immersion 110

To discern if the fluorescence was retained as a result of the dynamics of lapping and polishing or simply a result of exposed to the quantum dot solution, glass samples were immersed in the 60 nmol/mL quantum dots solution described in Chapter 3 for 110 minutes (the total process time that the LPQ samples were exposed to quantum dots during the lapping, immersion and polishing). While these samples were exposed to the same concentration of quantum dots for the same amount of time, it is actually a higher concentration as the exposure of the LPQ samples to quantum dots is diluted during the pad polishing step by the recirculation of slurry.

5.1.3 Lapped and Polished with Quantum Dots (LPQ)

These glass samples were finished with the procedure described in Chapter 3.1.3 with the following exceptions.

- A solution of quantum dots in acetone was added to the lapping slurry to achieve a concentration of 60 nmol of quantum dots / mL of slurry.
- Following lapping, the samples were immersed in a 60 nmol/mL quantum dot solution for sixty minutes.
- During the pad polishing operation, 10 mL of the 60 nmol/mL quantum dot solution were applied directly to the polishing pad at the start of the pad polishing as well as 5, 10, 15, 20, and 25 minutes into the pad polishing process.

5.1.4 Lapped and Polished with Quantum Dots then Etched (LPQ-E)

Examination of LPQ samples with the atomic force microscope detected features that appeared to be agglomerations of quantum dots on the surface (see Chapter 5.2.3).

In order to determine if the fluorescence that was detected on the LPQ samples was a result of quantum dots adhered on the surface or in the subsurface of the sample, a LPQ sample with recorded fluorescence and AFM scans showing the apparent agglomerations on the surface was subject to the quick etch described in Chapter 3.1.4. The purpose of this etch was to remove a small portion of the topmost layer of the sample, dislodging any quantum dots that were adhered to the surface so that any fluorescence that remained could be decisively attributed to quantum dots in the subsurface.

5.1.5 Lapped and Polished with Quantum Dots the Pitch Polished (LPQ-P)

As a result of incompatibilities between the hydrofluoric acid etchant used in the previous process and the quantum dots (see Chapter 5.2.4), LPQ samples were pitch polished as per Chapter 3.1.4 to remove any dots adhered to the surface. Two LPQ samples were processed in this manner. The first was pitch polished for five additional minutes and the second for ninety additional minutes.

5.1.6 Pad Polished with Quantum Dots PQ30

After confocal fluorescence results showed that LPQ and LPQP samples retained a significant number of quantum dots, a test was devised determine whether the pad polishing portion of the process was adding quantum dots to the sample. This glass sample was finished according to the procedure described in Chapter 3.1.3 with the following exceptions.

- The glass samples were not lapped

- During the pad polishing operation, 10 mL of the 60 nmol/mL quantum dot solution were applied directly to the polishing pad at the start of the pad polishing as well as 5, 10, 15, 20, and 25 minutes into the pad polishing process.

5.1.7 Lapped, Immersed in Quantum Dots, Pad Polished without Quantum Dots (LIQP)

After results for the LPQ and LPQP samples showed that lapped samples were retaining quantum dots (Chapter 5.2), the question became whether that was due to the dynamics of lapping embedding the quantum dots in the glass sample or if the lapped surface was simply providing suitable topography to allow the quantum dots to adhere. To test this, a glass sample was finished according to the procedure described in Chapter 3.1.3 with the following exceptions.

- Following the normal lapping process (without quantum dots), the sample was immersed in a 60 nmol/mL solution of quantum dots for sixty minutes.
- After sixty minutes, the sample was removed from the solution and cleaned with IPA soaked tissues
- The sample was observed with the wide field fluorescence microscope
- The sample was then pad polished as per Chapter 3.1.3

5.1.8 A note about sample storage

The various samples noted above were stored in plastic containers and general care was taken to keep them from being exposed to light prior to fluorescence imaging. There was no evidence that the brief exposure to light while extracting other samples

caused any degradation through photobleaching. Testing of samples over twelve months after their initial processing still revealed fluorescence, which is a testament to the robustness of the quantum dots as a fluorescent tag.

5.2 Results

In assessing the fluorescent response of the glass samples, only those samples which were lapped and polished in the presence of dots showed significant fluorescence. Those samples which showed significant fluorescence were probed further to determine prevalence of the fluorescence and an estimate of the depth at which the fluorescence occurred in the sample and to investigate the material removal mechanism.

5.2.1 Lapped and Polished (without Quantum Dots) LP

As expected, the samples lapped and polished without quantum dots did not display any significant fluorescence above the background threshold. In twenty-five scans over 3 locations, only four pixels registered fluorescence above the background threshold. The peak fluorescence from these 4 pixels was only 13% above the background.

5.2.2 Immersion 110

The maximum relative fluorescence observed in these samples was 75% above the background threshold, but relatively few pixels fluoresced above the background threshold. On average only 7 pixels (.01% of the total) registered values above the threshold within a dataset and 42 pixels (.06% of the total) above the threshold was the

maximum number of observed on any scan. This agrees with our cleaning tests that showed the ability to clean quantum dots of the glass surface.

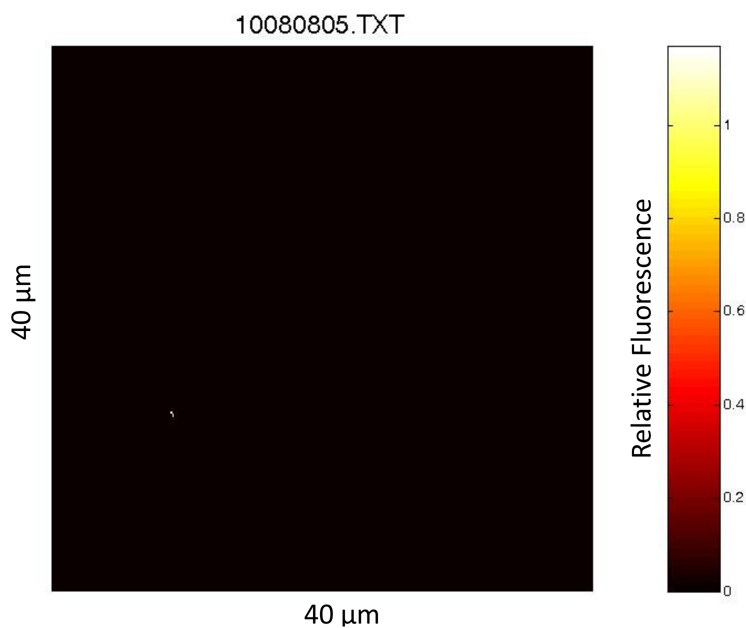

Figure 5-1. Confocal Fluorescence Image of a Glass Sample Immersed in Quantum Dots for 110 minutes then wiped clean.

While fluorescence was detected in the sample, the maximum intensities of the signal were observed at the surface or 2 µm beneath the surface. After this, the intensity quickly dropped to the background threshold (relative fluorescence = 1), with no pixels at focal planes 8 µm or 10 µm deep registering fluorescence above the background threshold.

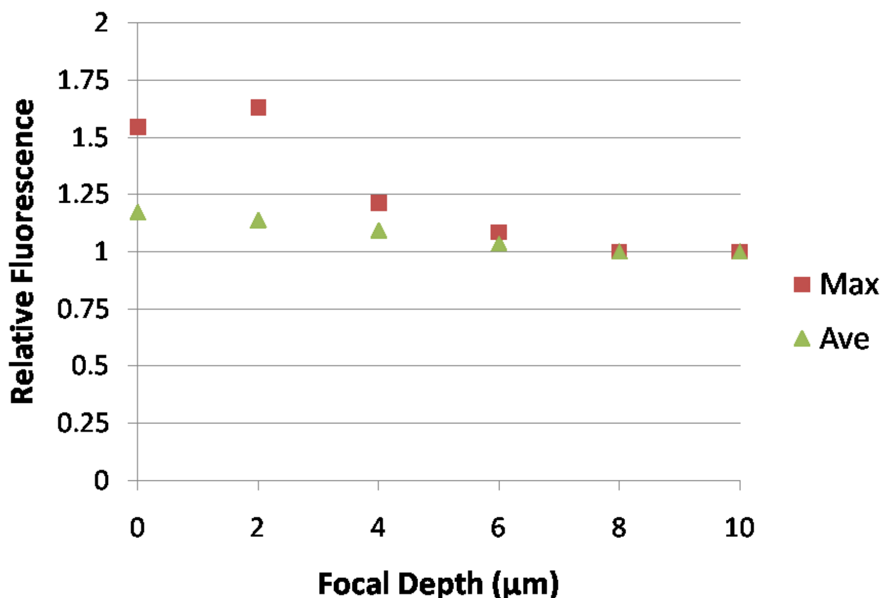

Figure 5-2. Optical slice statistics for a glass slide immersed in quantum dot solution for 110 minutes then cleaned.

5.2.3 Lapped and Polished with Quantum Dots (LPQ)

Optical Images revealed the sample surfaces were largely clear of visible defects. The average surface roughness was approximately 1 nm R_a as measured with the Zygo WLI. AFM scans of the LPQ samples revealed features and structure that were unseen with both optical microscopy and white light interferometry. Scratches can clearly be seen crossing the scan area as well as small features protruding above the nominal surface that are broadly distributed across the scan. These small spots on the AFM scans are consistent with the height of agglomerations of quantum dots from previous tests. It is important to note here that the dots do not occur preferentially in the scratches that on the AFM scan, instead appearing randomly about the surface. The surface roughness in these scans was on the order of 1.5 nm R_a as measured by the AFM.

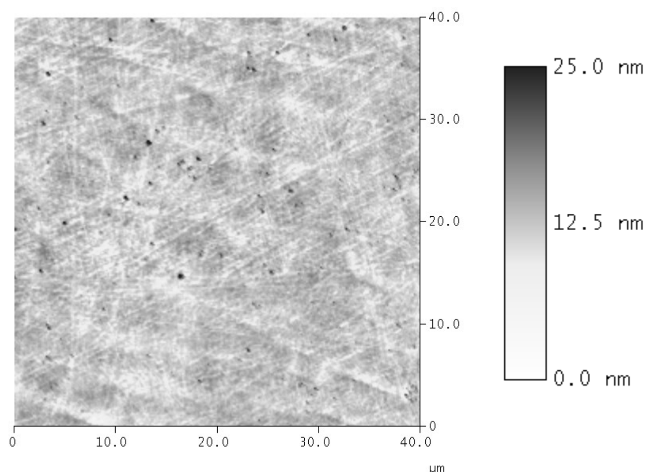

Figure 5-3. An Atomic Force Microscopy (AFM) scan over a 40 µm × 40 µm area of a glass sample lapped and polished in the presence of quantum dots.

Confocal fluorescence microscopy of these samples showed an abundance of fluorescent features that were distributed across both the scan areas and the locations imaged (Figure 5-4). The fluorescent features were also of significant intensity to be easily distinguished from the background signal (frequently an order of magnitude higher than the background signal). These features as well as other lower intensity (but still significantly above the background) features provided an abundance of datasets for analysis in MATLAB. The fluorescence in these samples was only present in discrete locations, with an average of 1% of the pixels registering fluorescence above the background threshold. Interestingly, the sites of fluorescence occurred with similar frequency to the spots on the AFM scan fostering the belief that quantum dots were strongly adhered or embedded in the surface.

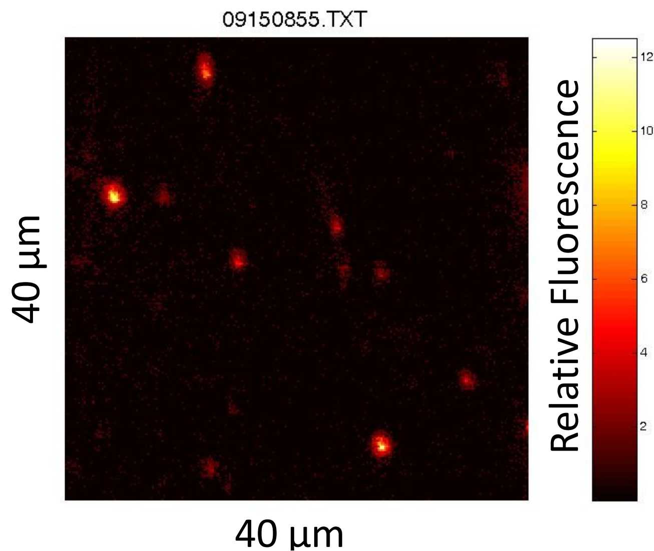

Figure 5-4. A confocal fluorescence image of a LPQ glass sample taken at the surface shows an abundance of fluorescent sites.

The cumulative fluorescence maps for the LPQ samples showed a multitude of fluorescent spots. In Figure 5-5 below for example, two different locations are shown. Both locations have several sites of high cumulative fluorescence as well as numerous sites with lower intensity cumulative fluorescence. On both locations, the coordinates with high intensity fluorescence are averaging fluorescent readings more than ten times the background fluorescence threshold.

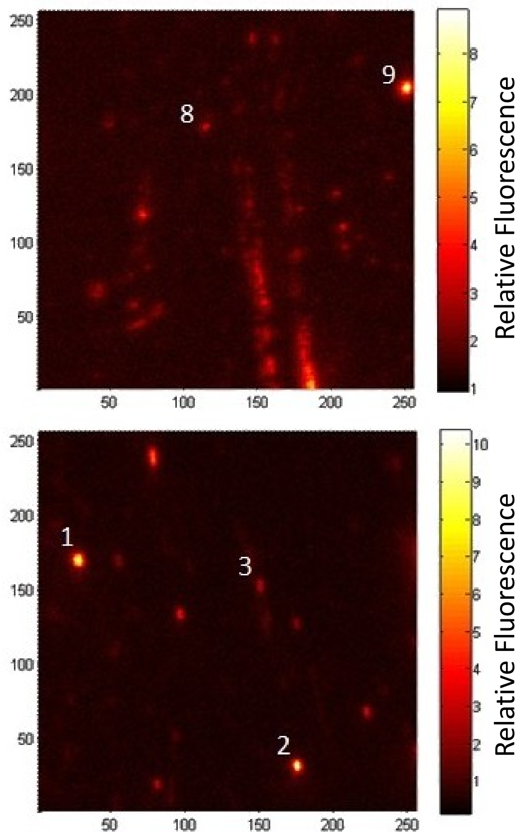

Figure 5-5. Cumulative fluorescence maps of a glass sample lapped and polished in the presence of quantum dots. Each image is an average of 40 µm × 40 µm scans at the surface, 2 µm, 4 µm, 6 µm, 8 µm, and 10 µm beneath the surface.

The cumulative fluorescence maps shown in Figure 5-5 highlighted numerous features of interest which were mined for the fluorescent response of the features at increasing depth of the focal plane. Features 1, 2, and 9 represent the high intensity coordinates within the scans while features 3 and 8 represent lower intensity coordinates of interest.

Features 1 and 2 have a peak fluorescence that occurs at a depth of 2 µm beneath the sample surface (Fig 5-5). The peak fluorescence drops off by roughly 50% once the focal plane is 10 µm beneath the surface. Trends in the minimum and mean

feature fluorescence are less distinct, but show a general degradation as the focal depth increases in the case of mean signal and either a slow degradation of constant value for the minimum feature fluorescence. For the purpose of the models, the peak in these two datasets is assumed to at 2 µm and the line is fit accordingly (Figures 5-6 and 5-7).

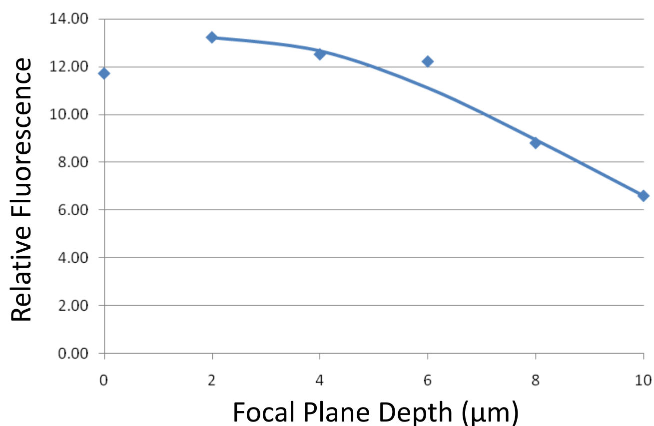

Figure 5-6. Maximum relative fluorescence feature profile data for feature 1 on a LPQ glass sample, along with the model fit with K value determined as 53.4 and a R^2 value of 0.9767.

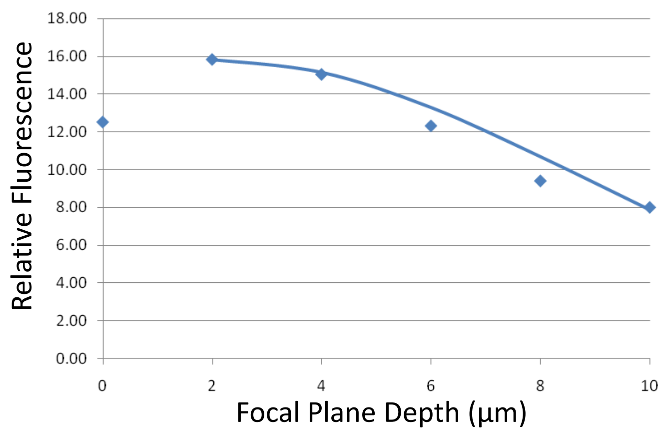

Figure 5-7. Maximum relative fluorescence feature profile data for feature 2 on a LPQ glass sample, along with the model fit with K value determined as 54.2 and a R^2 value of 0.9574.

The model for both equations achieves a good fit of the data with R^2 values greater than 0.95, bolstering the assumption that the fluorescent material is located close to 2 µm beneath the surface. The K values are also comparable to others calculated for the microscope (within 10%).

Feature 8 and 9 show a peak fluorescence occurring at focal depths of 6 to 8 µm beneath the surface. At these depths, the fluorescence is twice that of the fluorescence at the surface, which is the location with the lowest maximum fluorescence for both features 8 and 9. The peak fluorescence was assumed to be 8 µm beneath the surface in for both datasets and the fit calculated accordingly (Figures 5-8 and 5-9).

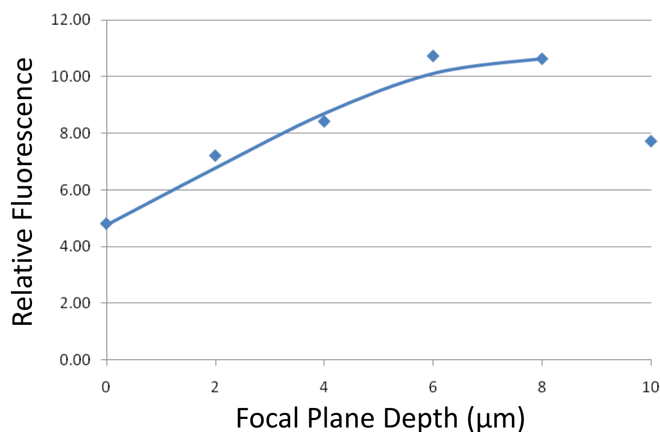

Figure 5-8. Maximum relative fluorescence feature profile data for feature 8 on a LPQ glass sample, along with the model fit with K value determined as 50.6 and a R^2 value of 0.9845.

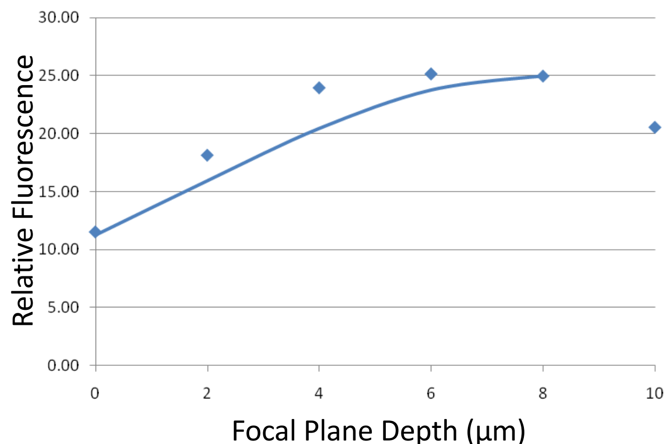

Figure 5-9. Maximum relative fluorescence feature profile data for feature 9 on a LPQ glass sample, along with the model fit with K value determined as 53.4 and a R^2 value of 0.9591.

Once again, the lines are a good fit to the data, with R^2 values greater than 0.95 and the K values are comparable to other results for the system. These models reinforce the assertion that the fluorescence detected in features 8 and 9 is roughly 8 µm beneath the surface. It would be reasonable to approach these findings with suspicion and wonder if it was simply a case of inappropriately determining the location of the surface. That possibility however has been discounted as background values (resulting from laser scatter off the surface at locations away from fluorescent material) peak at the focal plane associated with Z=0 µm, which indicates that the surface was correctly identified.

While this step had been performed on samples which had gone through an identical process except for the presence of quantum dots, this step was performed on a LPQ sample which had been imaged with the confocal fluorescence microscope and found to have fluorescent features. As definitively damaged layer existed beneath the

polished surface and was clearly visible after 1 µm had been removed from the surface (Figure 5-10).

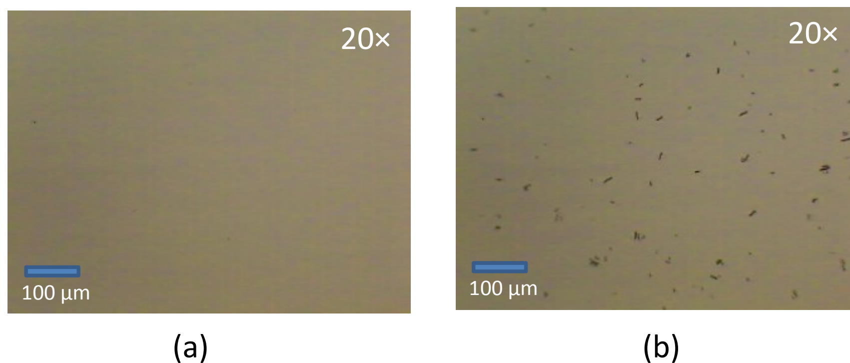

Figure 5-10. The surface of a glass sample lapped and polished in the presence of quantum dots a) before being etched and b) after 1 µm has been etched away with dilute HF acid.

The thin, sharp fracture appearance of the defects transitioned into more oblong and rounded shapes as the depth of material removed by the etching increased (Figure 5-11).

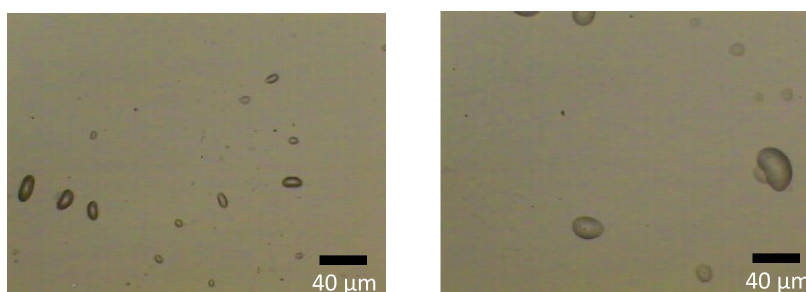

Figure 5-11. The surface of a glass LPQ sample lapped after (left) 7.2 µm and (right) 25.5 µm has been etched away with dilute HF acid.

Continued etching showed the trend to continue up to a depth of 86.4 µm (well below any estimates for the depth of damage on these samples), where the surface was covered with etched out craters of roughly circular shape (Figure 5-12). These shapes

were consistent with etch craters that occurred in unprocessed glass samples at similar depths.

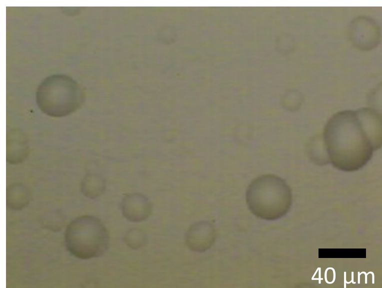

Figure 5-12. The surface of a glass LPQ sample lapped after 86.4 µm has been etched away with dilute HF acid.

Since a damage free region was not found during the etching process, it is difficult to produce even a high side estimate of the damage depth. The images down to a depth of 9.1 µm showed a strong resemblance to the fractures initially uncovered by etching, while images at depths of 11.1 µm or greater showed only the oblong shape characteristic of etch induced craters. A reasonable estimate for the depth of damage would be 10 µm, with the understanding that the estimate is subjective based on the observer's perception of the defect shape.

5.2.4 Lapped and Polished with Quantum Dots then Etched (LPQ-E)

The glass sample exposed to a brief hydrofluoric acid (2%) etch to dislodge any quantum dots lodged in the surface did not show any appreciable fluorescence beyond the background threshold. Similar to the samples which were lapped and polished without quantum dots, no more than a 5 or 10 pixels registered above the background threshold and even then less than 12% above the threshold. Based on conversations with Evident Technologies it is suspected that the etchant damaged the surface

properties of the quantum dots, leaving them unable to fluoresce [118]. A simple study confirmed this when a sample contaminated with quantum dots was briefly exposed to a dilute solution of hydrofluoric acid, it visibly reduced the fluorescence in the area of etchant contact, leaving the adjacent fluorescence unchanged. Examination of the sample with the AFM confirmed that quantum dots were still present on the surface, even though they were not fluorescing.

5.2.5 Lapped and Polished with Quantum Dots the Pitch Polished (LPQ-P)

Based on the appearance of spots indicative of quantum dots on the surface in the AFM, LPQ samples were pitch polished in an attempt to dislodge and remove any quantum dots that were adhered or embedded in the surface. These lapped and polished glass samples which received additional pitch polishing appeared defect free under optical microscopy.

Five Minute Pitch Polish

The five minute pitch polishing improved the surface roughness slightly as the average R_a dropped to 0.8 nm as measured with the Zygo WLI while removing 250 nm of material. The five minute pitch polishing sample showed a noted reduction in the number of spots appearing in the AFM scan (Figure 5-13). The average surface roughness measured in these AFM scans was 1.7 nm R_a which is comparable to the LPQ samples prior to the pitch polishing.

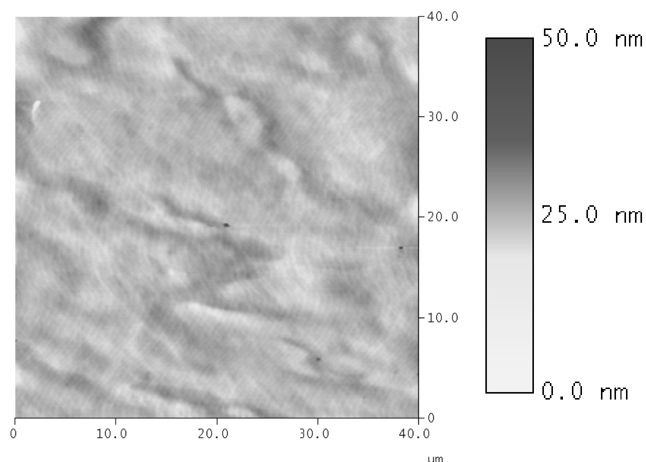

Figure 5-13. The AFM scan of a glass sample lapped and polished in the presence of quantum dots then given an additional 5 minutes of pitch polishing in the absence of quantum dots shows a reduction in the number of spots compared to the LPQ sample (40 µm × 40 µm area).

In addition to the reduction in the number of suspected quantum dots in the AFM scan, the morphology apparent in the AFM scan is quite different from the LPQ images. The obvious scratches are gone and the surface has taken on a wavy, melted appearance.

The LPQ glass sample which was pitch polished for only 5 minutes did have sites of significant fluorescence. The peak fluorescence values on this pitch polished sample were much lower (relative values of roughly 15 compared to peak relative values in the 30s and even 60s for samples prior to pitch polishing). Another key difference is the total absence of the low intensity sites of fluorescence which were scattered about on the confocal scans of the LPQ samples. The five minute pitch polishing has completely eliminated them.

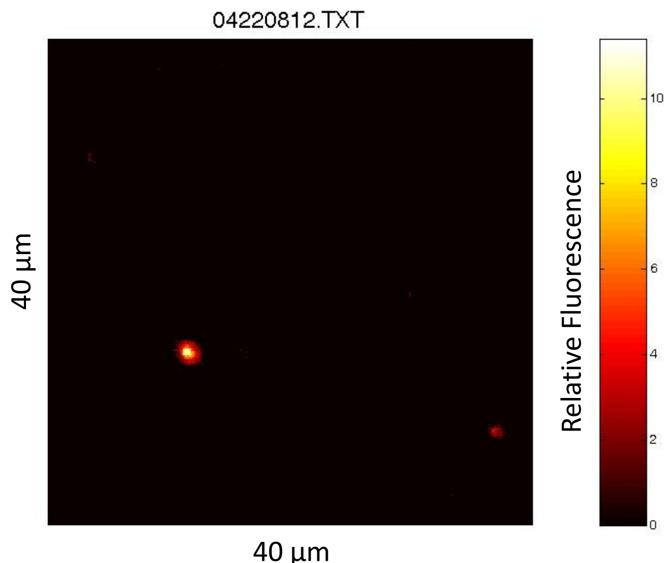

Figure 5-14. Confocal fluorescence image of a LPQP glass sample taken at the surface.

The cumulative fluorescence maps for the glass samples subject to an additional five minute pitch polishing step showed a drastic reduction in the number of low intensity fluorescing sites. The fluorescing sites that remained were highly consolidated as shown in Figure 5-15.

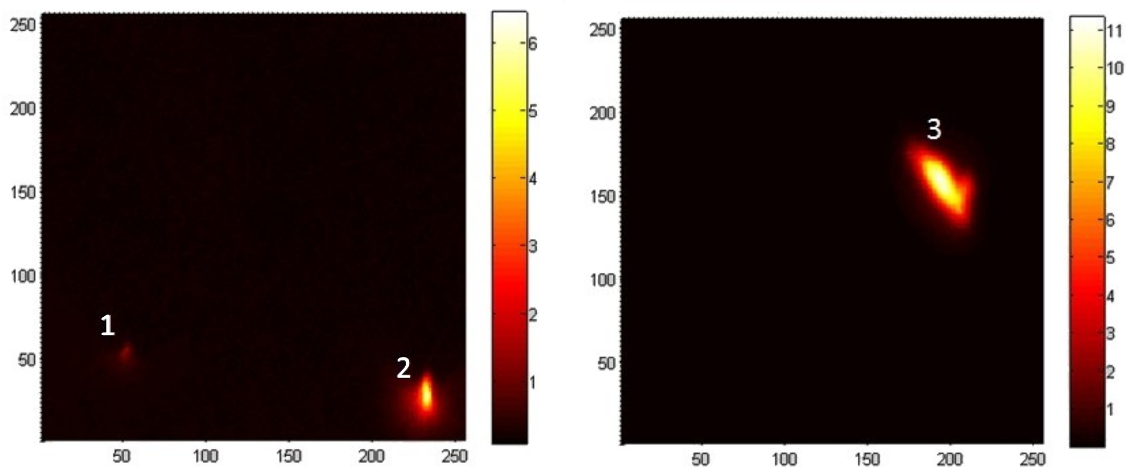

Figure 5-15. Cumulative fluorescence maps of a glass sample lapped and polished in the presence of quantum dots, then pitch polished without quantum dots for five minutes. Each image is an average of 40 µm × 40 µm scans at the surface, 2 µm, 4 µm, 6 µm, 8 µm, and 10 µm beneath the surface.

Pitch features 1 and 2 registered peak fluorescence at the surface and the fluorescence dropped off quickly with increasing depth (75% and 85% reduction in fluorescence at 10 μm depth for feature 1 and 2 respectively) (Figures 5-16 and 5-17). As with the glass samples that were lapped and polished in the presence of quantum dots (no final pitch polishing), the average shows a similar trend while the minimum feature fluorescence varies little with increasing focal depth.

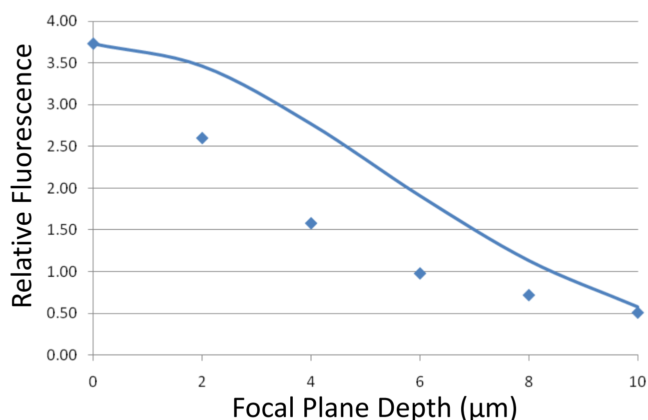

Figure 5-16. The maximum fluorescence values in pitch feature 1 with respect to focal depth beneath the surface, along with the model fit with K value determined as 41.5 and a R^2 value of 0.8871.

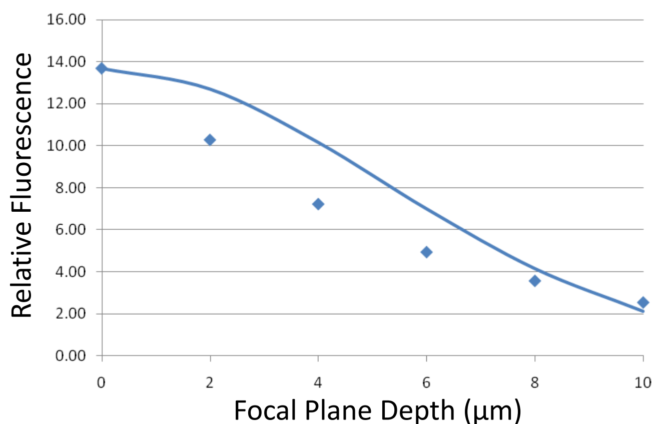

Figure 5-17. The maximum fluorescence values in pitch feature 2 with respect to focal depth beneath the surface, along with the model fit with K value determined as 41.5 and a R^2 value of 0.9278.

Pitch feature 3 exhibits a very different profile as the maximum and mean fluorescence for the feature remain nearly constant through focal planes from the surface to 10 µm beneath the surface (Figure 5-18). It is worth noting at this point that the location that includes feature 3 was imaged immediately after the location which included features 1 and 2, without a break in between. This close proximity in time makes it very unlikely that the different fluorescent profile which is observed for feature 3 is a result of a change in the experimental setup or a difference in the ambient conditions for the test. The exclusion of these influences gives confidence that difference observed is actually a function of the feature and not the measurement setup/environment.

As would be expected, attempting to fit the previous model to this data resulted in an extremely poor fit, with the K value and R^2 being calculated as 316 and 0.202 respectively. The R^2 value alone shows that this model is insufficient to describe the data, but to require the constant K to be 316 is conclusive evidence of a problem with this model for this feature. The reader will note that the calculated constant K has changed slightly between experimental sets, but never has the change been so dramatic in the middle of an experimental set.

The flaw in modeling feature 3 as the previous features, is the assumption of a single point source of fluorescence. This assumption has been adequate thus far as the features on the Q, LPQ and Pitch features 1 and 2 all exhibited a single clear peak. In order to make this model work for pitch feature 3, the model must be expanded to included fluorescent material at multiple focal planes. Unfortunately, multiple particles,

each with differing focal planes and relative concentrations makes it impossible to solve for all the unknowns given the datasets. Simulations however were performed that considered the predicted response of fluorescent particles at different focal planes, assuming the K value (41.5) that was calculated from pitch feature 1 and 2. While these simulations cannot decisively ascribe a particular distribution of quantum dots at certain focal planes, they can provide scenarios that would produce such a fluorescent response. The first scenario tested has equal quantities of fluorescent material at z=0, 2 µm, 4 µm, 6 µm, 8 µm, and 10 µm. The fluorescence in this model however has an obvious bow, with a peak at 5 µm, which is not reflected in the data for pitch feature 3 (Figure 5-18).

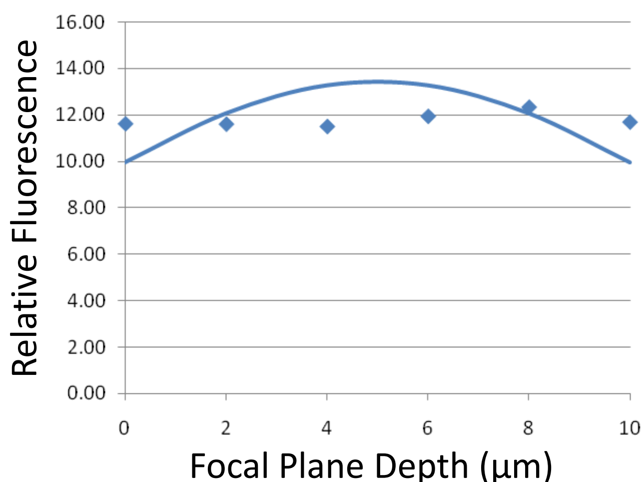

Figure 5-18. Maximum fluorescence data from pitch feature 3 alongside a fluorescence model considering equal point sources of fluorescence located at Z=0 µm, 2 µm, 4 µm, 6 µm, 8 µm, and 10 µm, with the w and K values of 0.25 µm and 41.5 respectively.

This shape was characteristic of all the models which had fluorescence evenly distributed at focal planes from the surface to 10 µm beneath the surface, regardless of the spacing. Any even distribution has this peak because at the extremes, of z=0 and

z=10 µm, out of focus fluorescence is only being gathered from one direction (as there is no fluorescence indicated at Z<0 µm or at Z>10 µm. The second scenario has fluorescent material concentrated at two locations, Z=0 µm (the surface) and Z=10 µm beneath the surface and looks to maintain the fluorescence value between these points with the contribution of out of focus fluorescence. While there is still a slight upward bow in the predicted fluorescence for this model it does a much better job of matching the observed values for pitch feature 3 (Figure 5-19).

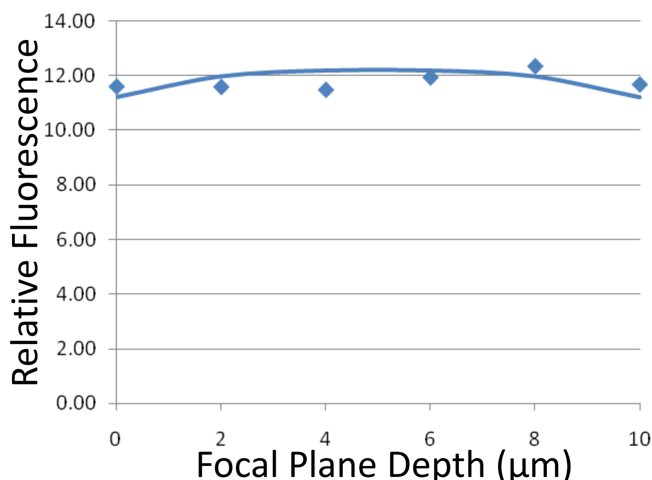

Figure 5-19. Maximum fluorescence data from pitch feature 3 alongside a fluorescence model considering two equal point sources of fluorescence located at Z=0 µm and Z=10 µm, with the w and K values of 0.25 µm and 41.5 respectively.

As this model seemed close, it was modified to shift the second concentration of fluorescent material from z=10 µm to z=11 µm. This further flattened the curve and made for a model that could be used to describe the data from pitch feature 3 with some confidence (Figure 5-20).

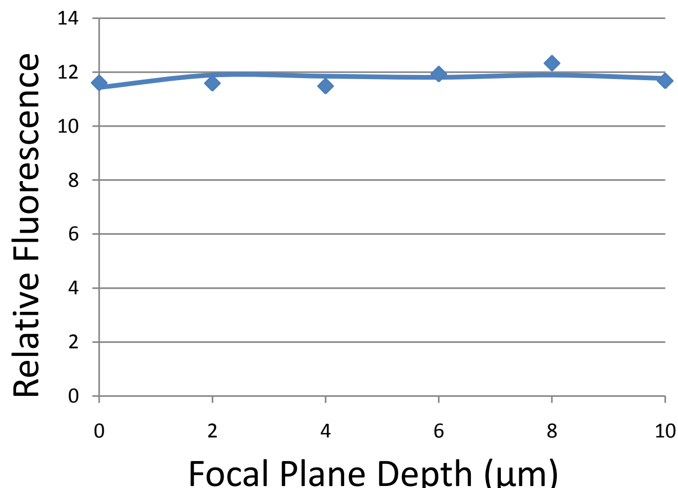

Figure 5-20. Maximum fluorescence data from pitch feature 3 (diamonds) alongside a fluorescence model considering two equal point sources of fluorescence located at Z=0 µm and Z=11 µm, with the w and K values of 0.25 µm and 41.5 respectively.

The glass LPQ sample which was given only five minutes of additional pitch polishing showed clear indications of subsurface damage after only 300 nm of material (based on mass loss) was etched away (Figure 5-21).

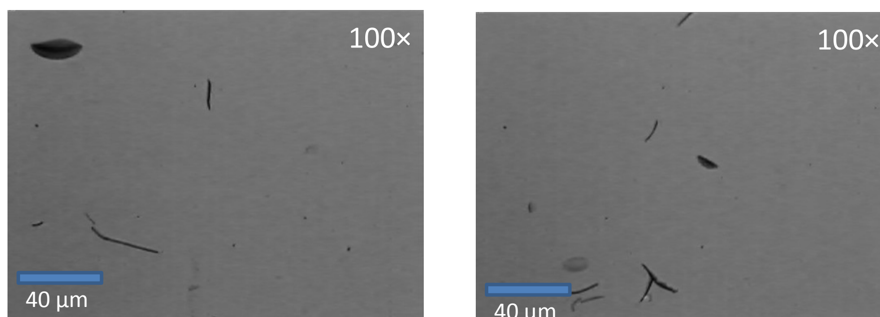

Figure 5-21. Subsurface damage revealed by etching to remove ~ 300 nm of material from the surface of glass samples lapped and polished in the presence of quantum dots then pitch polished for 5 minutes.

Further etching the sample continued to show signs of SSD, but the nature of the defects changed from the sharp features seen in the previous figures to more oblong and rounded shapes (Figure 5-22), as was seen with the LPQ samples.

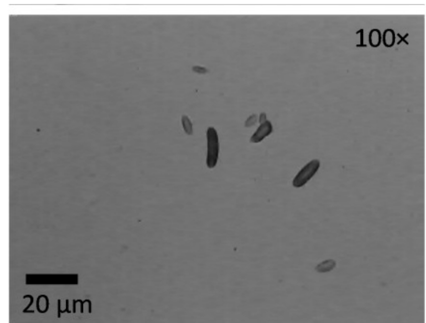

Figure 5-22. Subsurface damage revealed by etching ~3 µm of material from the surface of a glass sample lapped and polished in the presence of quantum dots then pitch polished for 5 minutes.

The dimensions of these etched out craters continued to increase as the depth of material etched away increased (Figure 5-23).

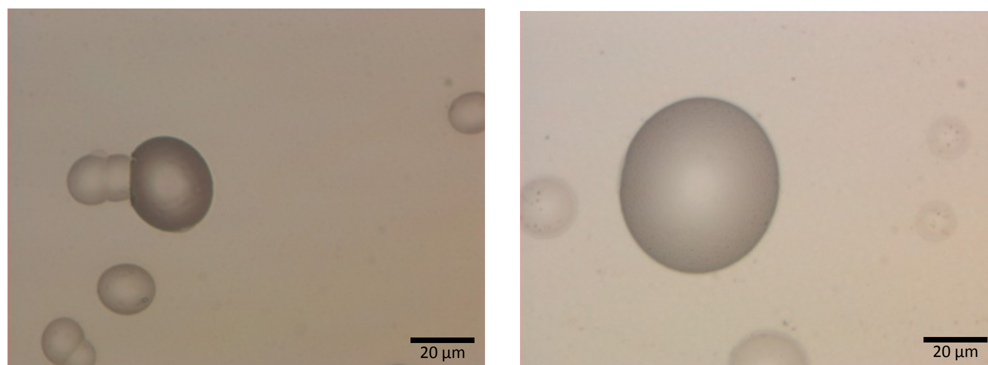

Figure 5-23. Images of LPQ-P samples etched to remove (left) 32 µm and (right) 78 µm of material show an increase in the size of the etched out craters.

As with the LPQ samples, this trend continued up to a depth of 260 µm beneath the surface, which is an order of magnitude beyond the highest estimates for the depth of subsurface damage in the sample (Figure 5-24) without reaching a damage free layer.

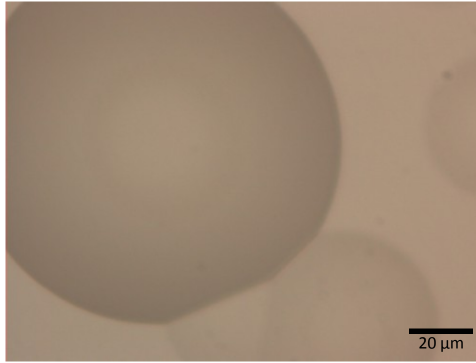

Figure 5-24. Image of the LPQ-P sample, etched to remove 260 µm of material from the surface shows

As was the case for the LPQ samples, interpreting the end of the subsurface damage layer is difficult from the etch images. The last depth where the defects have a structure reminiscent of the initially revealed fractures is at 6.8 µm beneath the surface while at 9 µm beneath the surface the defects are entirely the oblong etched out craters. Thus 9 µm serves as a reasonable estimate for the depth of damage.

Ninety Minute Pitch Polish

Atomic force microscopy of the glass sample subject to an additional 90 minutes of pitch polishing (after the lapping and polishing) showed a notable change from the AFM scans on the samples just lapped and polished with quantum dots. While a few scratches are still apparent in these scans, the small dot features rising above the nominal surface have been eliminated as seen in Figure 5-25.

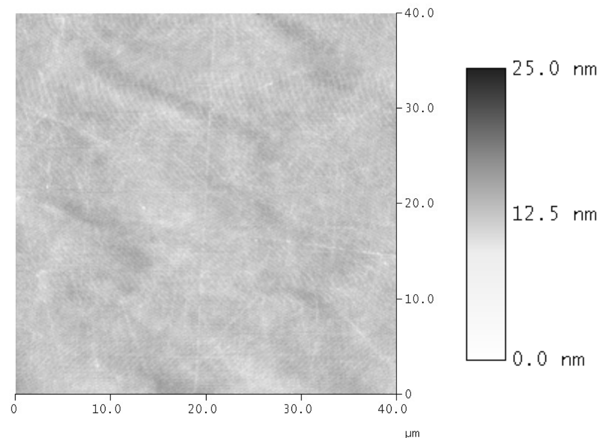

Figure 5-25. AFM scan of a 40 µm × 40 µm area of glass sample lapped and polished in the presence of quantum dots then pitch polished for 90 minutes without quantum dots.

The glass sample which was lapped and polished with quantum dots, then pitch polished for 90 minutes did not show any fluorescence beyond the background threshold.

The glass LPQ sample which underwent ninety minutes of additional pitch polishing was etched in dilute HF acid, but no evidence of subsurface damage was observed with the optical microscope (the lapped and polished side appeared equivalent to the unprocessed side with rare occurrence of pits).

5.2.6 Pad Polished with Quantum Dots PQ30

The glass samples which were only pad polished for thirty minutes (no lapping) displayed a high quality surface under optical microscopy (Figure 5-26). The average surface roughness was 1.16 nm R_a (σ=0.03 nm) as measured on the Zygo WLI.

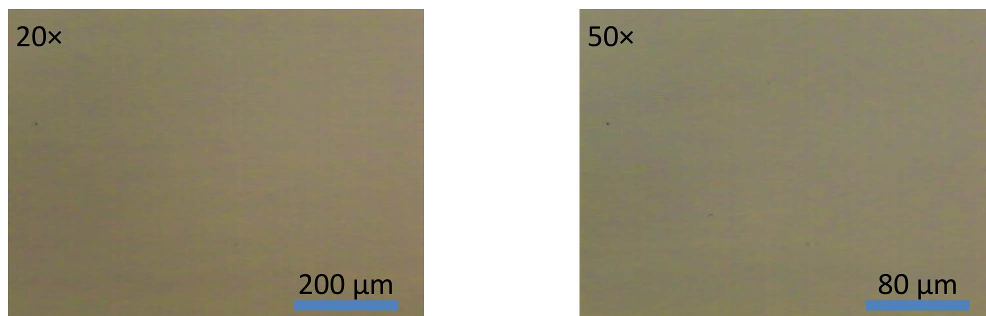

Figure 5-26. Optical Images taken on the Mitutoyo Finescope, showing a surface free of visible defects following 30 minutes of pad polishing with quantum dots.

Confocal microscopy of the glass samples which were simply pad polished in the presence of quantum dots did not show any significant fluorescence above the background. The peak fluorescence was never more than 14% above the background and only occurred in 1-4 pixels per scan area registered values above the background.

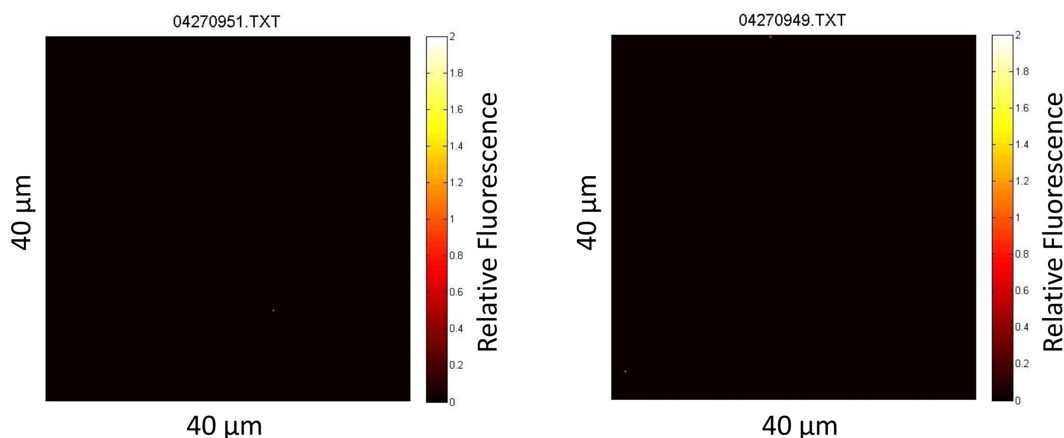

Figure 5-27. Confocal Images of samples pad polished with quantum dots. No significant fluorescence above the background is detected.

Examination of etched glass samples which were only pad polished in the presence of quantum dots (no lapping of the glass samples) revealed defect structures that were quite different from the samples which had been lapped and polished. Cracks

or fissures like those seen in Figure 5-21 were not observed on these samples. There were however approximately ten to twelve scratches that went across the surface (Figure 5-28).

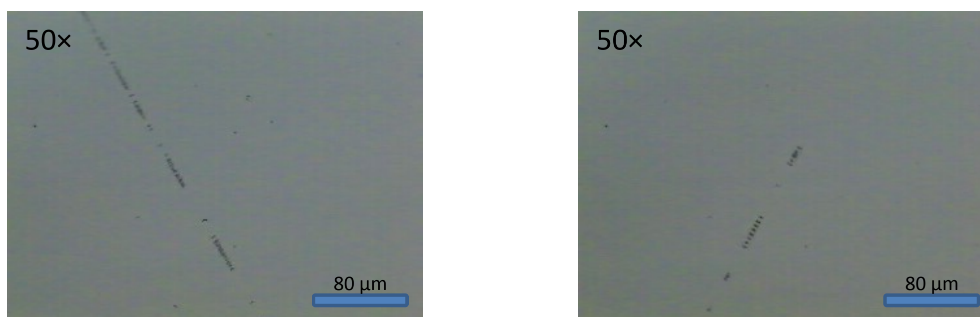

Figure 5-28. Glass Samples Pad Polished in the presence of Quantum Dots for 30 minutes, then etched to reveal SSD.

These scratches, upon closer examination and higher magnification, displayed the characteristic look of 'chatter marks' that are observed with an abrasive travelling across a workpiece.

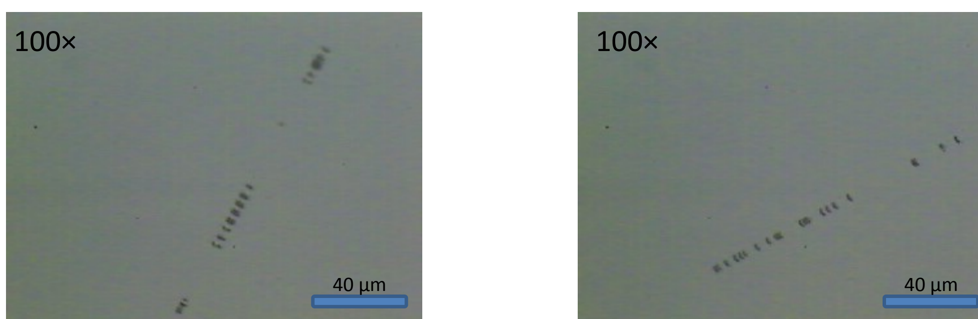

Figure 5-29. Glass Samples Pad Polished in the presence of Quantum Dots for 30 minutes then etched to expose SSD.

5.2.7 Lapped, Immersed in Quantum Dots, Pad Polished without Quantum Dots (LIQP)

To determine if quantum dots were being retained as a result of exposure to a lapped surface or a result of the lapping dynamics, a glass sample was lapped without quantum dots then immersed in quantum dots before being polished without quantum dots. The sample showed a defect free surface under optical microscopy with an average Ra value of 1.31 nm Ra (σ=0.18 nm) as measured on the Zygo WLI.

Prior to polishing the sample was observed on the widefield fluorescence microscope (using the previously noted settings). At the lapped stage it is clear that fluorescent material is retained in the topography, despite the fact that the surface had gone through the cleaning procedure (Figure 5-30).

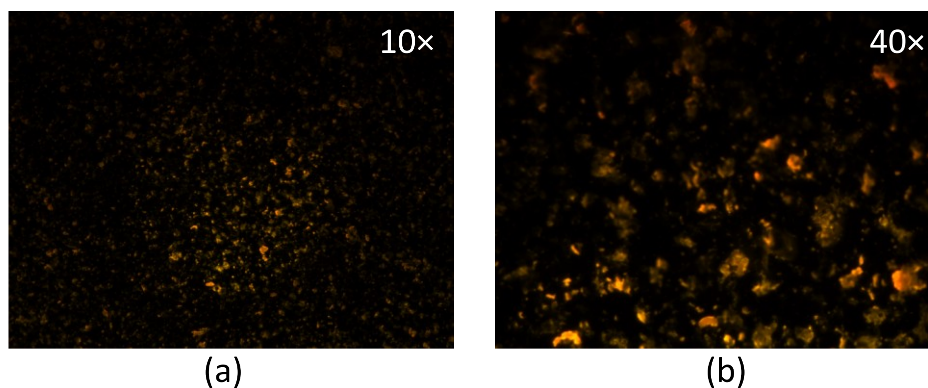

Figure 5-30. Wide field fluorescence image of a lapped glass surface immersed in quantum dots for thirty minutes, then cleaned. Images were taken at a) 10× and b) 40× magnifications.

Following polishing, the sample was imaged on the confocal fluorescence microscope and the fluorescence values were found to be much lower than either the LPQ or LPQ-P samples. Of four locations sampled, only two had significant fluorescence

above the background. The first location had only a single fluorescent feature, and that peaked at 33% above the background threshold (Figure 5-31). The second location had several points above the threshold, but none greater than 20% above the background. These values are comparable to values obtained for the glass immersion samples and do not reflect any increase retention of quantum dots. This suggests that it takes more than the lapped topography for quantum dots to remain adhered to the sample surface, that lappig dynamics are required for quantum dots to be retained.

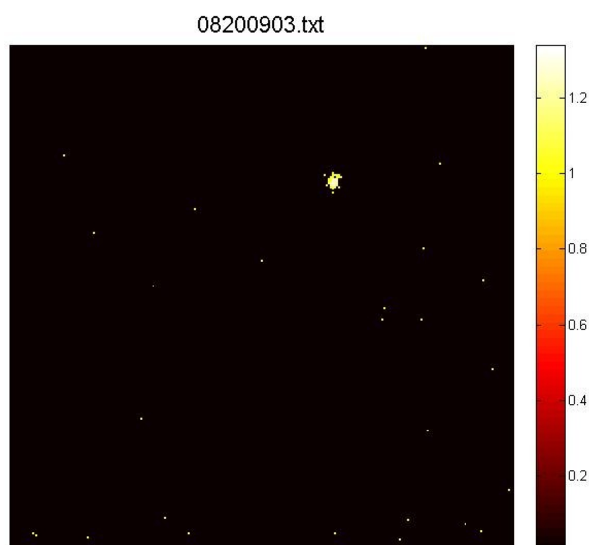

Figure 5-31. Confocal Image of a glass sample lapped, then immersed in a quantum dot solution before being polished shows a single low intensity fluorescent feature.

Piezo control of the focal plane was not available, so sectioning was not possible. Even slight adjustments of the focal plane by hand by the micrometer (estimated at 5 µm) resulted in the features losing all distinction and becoming part of the background.

5.3 Discussion

The results of these experiments show a clear differences in the degree of fluorescence which is retained by samples based on their processing. The differences

are summarized in the following subsection and the implications of those differences are discussed. The depth values calculated in fluorescent feature curve fitting are then compared to values from the estimates based in the literature and additional testing.

5.3.1 Retention of Quantum Dots based on Sample Processing

Quantum dots were only retained on glass surface is the presence of significant defects. This was first shown in the indent tests were quantum dots persisted in Knoop indents and scribe marks, while quantum dots on the surface were largely removed by the cleaning process.

Samples which were lapped and polished with quantum dots had two orders of magnitude more pixels fluorescing above the background than samples which were simply exposed to quantum dots and cleaned (Table 5).

Table 5. Normalized fluorescent response of glass samples exposed to quantum dots under varied conditions.

Test Details	*Maximum*	*Mean*	*# Pixels Fluorescing*
Baseline Testing			
Short exposure and cleaned	*1.59 (σ=0.19)*	*1.22 (σ=0.06)*	*0-1 pixels*
110 min exposure and cleaned	*1.75 (σ=0.32)*	*1.05 (σ=0.22)*	*9 pixels (σ=14 pixels)*
Exposed and not cleaned	*43.2 (σ=4.1)*	*28.9 (σ=5.1)*	*65536 pixels (σ=0%)*
Lapping & Polishing Tests			
Lapped & pad polished with quantum dots	*64.8 (σ=11.2)*	*2.04 (σ=1.05)*	*852 pixels (σ=1400 pixels)*
Lapped & pad polished with quantum dots, then etched	*1.09 (σ=0.03)*	*1.03 (σ=0.03)*	*4 pixels (σ=2 pixels)*
Lapped & pad polished with quantum dots + 5 minute pitch polish	*13.49 (σ=4.2)*	*2.86 (σ=1.14)*	*852 pixels (σ=583 pixels)*
Lapped & pad polished with quantum dots + 90 minute pitch polish	*1.21 (σ=0.09)*	*1.03 (σ=0.02)*	*74 pixels (σ=98 pixels)*
Pad polished with quantum dots	*1.13 (σ=0.04)*	*1.05 (σ=0.03)*	*0-1 pixels*
Lapped surface treated with quantum dots, cleaned and pad polished	*1.39 (σ=0.09)*	*1.02 (σ=0.01)*	*2746 pixels (σ=2346 pixels)*

The sample which was not lapped, but only pad polished in the presence of quantum dots had a very low fluorescent response comparable to the samples which were simply exposed and then cleaned, which shows that the quantum dots must be present on the lapped surface to be retained. While it would seem reasonable to attribute the retention of quantum dots to the relatively extreme topography of the lapped surface providing defects which would increase the adhesion between the quantum dot and surface, the lapped surface which was treated with quantum dots and then polished did not show any sites of fluorescence comparable to those seen on the

LPQ and LPQP slides. This implies that the material removal mechanisms at the lapping stage are critical to quantum dots being retained in the glass sample, with the assumption that the brittle fractures that remove material during lapping are responsible for trapping some of the quantum dots which are present in the slurry.

Review of the AFM scans for the LPQ samples shows an abundance of spots on the surface with dimensions that are consistent with earlier AFM images of quantum dots allowed to dry on a surface. Given that it has been shown that the cleaning method utilized is effective at removing quantum dots allowed to dry on a glass surface, these dots must be more strongly adhered to the surface, and likely embedded in the surface. AFM scans of samples which had been pitch polished for ninety minutes revealed an absence of spots and the corresponding confocal fluorescence images showed lack of fluorescent sites, suggesting a relationship between the two.

As quantum dots were not retained in the samples which were solely pad polished in the presence of quantum dots, this embedding must occur during the lapping stage. Subsequent etching of these samples however revealed some subsurface defects. These defects however were in the form of sleeks or scratches instead of the clear brittle fractures observed on the LPQ and LPQP samples. Based on this, it appears that the plastic deformation that creates these types of defects is insufficient to embed the quantum dots in the surface or does not provide significant enough defects to cause the quantum dots to adhere to the surface.

The quantum dots that were embedded in the lapped glass surface would be transported as the topmost layer was smeared and plastically deformed during the

polishing process. That transport could remove quantum dots from the system along with the material that is being removed (based on mass loss) or it could carry the quantum dots on the surface as material flows into surface cracks, filling them in. Such quantum dots would be trapped at limited depths, in the smooth topmost layer that extends perhaps 100 nm beneath the surface. This region is known to trap contaminants from the grinding and polishing process, with polishing and grind compounds being found in concentration of 10-1000 ppm at depths up to 100 nm [119]. These sites of quantum dot contamination in the smooth plastically deformed material are reflected in the abundance of small, low intensity sites that appear on the optical slices coincident with or adjacent to the surface on the confocal scans of the LPQ samples.

The five minute pitch polishing step removed all of these small sites of fluorescence, leaving behind only consolidated locations of high fluorescence (albeit at lower peaks than the LPQ samples). As this step removed an estimated 250 nm of material (based on weight loss), this 100 nm region typically associated with contamination should have been removed twice over. This suggests that the material removal mechanisms during the pitch polishing step are more effective at removing this topmost layer of material, even though the same type of ceria slurry was used (without quantum dots added). Instead of plastic deformation, the pitch tool may favor smearing where the large contact area with the workpiece drags off material that is chemically predisposed to removal. Chemical tooth might also be dominant during pitch polishing, where individual surface molecules of the workpiece are plucked away, leaving the

quantum dots exposed to be removed by the dynamics of the polishing process or subsequent cleaning of the sample.

Despite the removal of the topmost region which is both chemically altered and subject to contamination by slurry components, fluorescent sites were still present on the confocal fluorescence scans. This suggest that while there are an abundance of quantum dots which get embedded in the topmost layer and then are removed by pitch polishing, there are more egregious defects which retain quantum dots deeper than that topmost surface. These defects however could be missed without careful sampling of the surface due to the small field of view of the confocal microscope (Figure 5-32).

Figure 5-32. An overlay of the confocal fluorescence microscopes field of view (40 µm × 40 µm) on an image of an etched sample that reveals subsurface defects illustrates the possibility of missing defects without thorough sampling.

5.3.2 Comparison of Defect Depths

Estimates of the depth of subsurface damage from the surface roughness at the lapped stage vary from 12.6 µm based on the work of Edward and Hed [120], 8 µm based on the work of Aleinikov [57] and less than roughly 4 µm based on Lambropoulos's findings [48]. Given that my measures of the peak to valley roughness

at the lapped stage were measured with a profilometer, the estimates of Edward, Hed, and Aleinikov are more appropriate. Lambropoulous also estimates the depth of subsurface damage based on the abrasive particle diameter [60], which gives a rage from 2.3 μm to 24 μm, but that range should be considered high as it based on the more aggressive fixed abrasive grinding rather than the loose abrasive lapping that was performed on these samples.

Miller and colleagues at Lawrence Livermore looked at the distribution of SSD in fused silica samples subject to a number of fixed and loose abrasive processes [59]. In samples which were finished with a slurry of loose 15 μm abrasive particles, the SSD extended to ~12 μm before the obscuration (ratio of the area of the fractures to that of the total scan) fell below .02%. With slightly larger 20 μm loose abrasive used in the lapping stage in these experiments, we would expect greater obscuration (prevalence of damage) with depth. A conservative estimate based on Millers work would have readily visible damage (obscuration of roughly 1%) extending 10 μm beneath the surface.

The etching procedure utilized was very effective at identifying subsurface damage in the samples, but was ill suited for determining how deep that damage extended into the sample. The work by Miller et al [59] at LLNL indicated that the dimensions of the visible fractures on etched samples were strongly influenced by the duration of exposure to the etchant. Work by Yoshiyama et al [121] found that etching away the 300 nm of fused silica improved the laser induced damage threshold while Kamimura et al [122] found the etching of fused silica samples (~300 μm) degraded the surface such that they were unsuitable for laser optics without additional processing

(additional polishing and ion beam etching of the surface). The etching in this work is consistent with Kamimura's findings in that increased etching resulted in waviness of surface and a bubbly appearance. Part of this behavior could be attributed to the glass samples only being 1 mm thick. With such a thin sample, the internal structure of the glass may not have sufficient room to transition back to bulk/undisturbed properties before encounter the influence of the workpiece holder on the back side of the sample. Another explanation would be that the samples already have some level of defects (impurities or dislocations) internally that are exacerbated by the etching procedure. While this was not observed in unprocessed samples with small depths of material etched away, it was observed in samples that had not been lapped and polished after greater depths had been etched away (Figure 5-33).

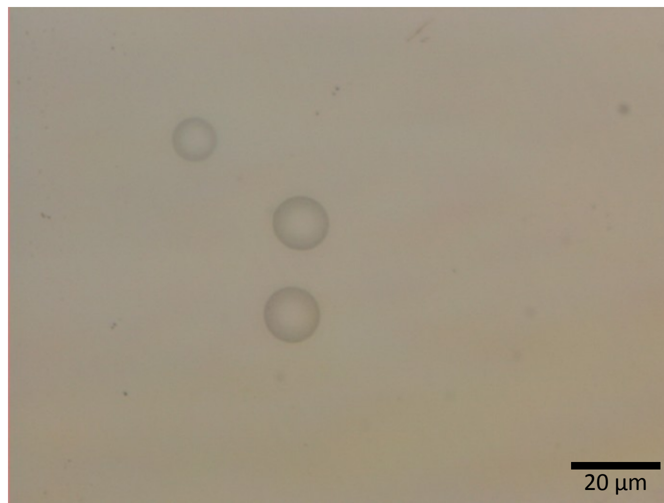

Figure 5-33. Image of a virgin glass slide (no lapping or polished performed) etched to remove 42 µm, revealing the emergence of etch craters.

Unfortunately, this transition from the obvious defects in the near surface to the bubbly etched surface well below the defect layer does not provide any objectively clear

line to serve as high end estimate of where the damage ends. For this reason, glass samples lapped under comparable conditions were fractured and examined to estimate the depth of the subsurface damage (Chapter 7.2).

The preponderance of the fluorescent features (84%) which were assessed in these studies had exhibited fluorescent peaks which were at the surface or 2 μm beneath the surface. As noted previously this region overlaps with the layer of chemically altered, plastically deformed smooth material which is subject to contamination from the slurry (0-100 nm). It comes as no surprise then that quantum dots would be located in this region. The work by Miller et al, [59] shows a precipitous drop the occurrence of fractures as depth beneath the surface increases. When finishing fused silica with 15 μm loose abrasive particles, fractures accounted for nearly 20% of the scan area at a depth of 5 μm [59]. That percentage dropped to less than 1% when the depth increased to 7 μm [59]. This suggests that truly deep subsurface fractures are rare, and that their limited appearance in the confocal fluorescence scans may not indicate that inability of quantum dots to travel into those deep fractures, but rather a limited number of available deep fractures. Beyond a certain depth from the surface, energy considerations would encourage deposition and adhesion to the sides fracture surface as the quantum dot would be removed from any significant motive force to drive it deeper into the fracture. A mechanism to overcome these energy considerations would be the tensile field acting on these fractures in the wake of a travelling abrasive. The tensile fields would tend to open the crack, reducing its aspect

ratio, reducing the likelihood of adhesion to the fracture wall and increasing the exposure of the quantum dot to motive forces from outside the fracture.

Despite the rarity of suitably deep fractures, and energy considerations that make deeper travel less likely, several fluorescent sites have been imaged in this research that indicate the presence of quantum dots far beneath the surface. These only occurred on samples which were lapped in the presence of quantum dots. Two of these features which were observed on the LPQ samples, display a fluorescence falloff graph with the characteristic shape we have come to expect with the confocal fluorescence microscope, with the exception that the peaks are offset occurring at roughly 8 µm beneath the surface. A third feature, from a LPQ sample subject to an additional 5 minute pitch polish, had a near constant fluorescence profile with increasing depth (up to 10 µm beneath the surface), which is inconsistent with a single source of fluorescence. While it is impossible in this case to conclusively determine the exact distribution of quantum dots with respect to depth beneath the surface, simple models of predicted fluorescence for quantum dots located at the surface and 10 µm beneath the surface fit the data well, and some distribution of quantum dots at varied focal planes is required to match the data.

5.3.3 Summary of Findings

Quantum dots in loose abrasive slurries can be used to highlight the presence of defects on the surface or in the subsurface region of a glass sample. The quantum dots must be present in the lapping slurry and experience the dynamics of lapping to become embedded in the sample or travel deep into any defects. Pad polishing does not cause

quantum dots to adhere to or embed in the surface. Pad polishing however can produce subsurface defects in the form of scratches that are not highlighted by quantum dots, so the absence of fluorescing quantum dots in a sample cannot be construed as the total absence of subsurface damage. The absence of fluorescing quantum dots does indicate the absence of subsurface damage in the form of brittle fractures associated with lapping.

Confocal fluorescence microscopy can not only detect the presence of quantum dots and the associated defects that house them, but also provide insights into depth at which the fluorescing dot (and housing defect) occur in the material. Confocal fluorescence microscopy has been shown to detect three different types of fluorescent feature in these experiments. The first, and most frequently observed features, are quantum dots which are embedded on the surface or trapped in the near surface, a smooth region of glass that has been chemically altered and plastically deformed. The second are quantum dots which have traveled deeper in surface, but concentrated a single focal plane. The third type of feature display a fluorescence which extends deeper into the sample and must be described by a distribution of quantum dots at multiple focal planes as fluorescence models based on a single source do not describe the measured data.

CHAPTER 6. QUANTUM DOTS IN LOOSE ABRASIVE SLURRIES WITH YAG

The work presented here expands on the YAG finishing procedure detailed in Chapter 3, by adding quantum dots in solution during the finishing process. YAG offers distinctly different material properties from the glass samples with a cubic structure, much higher elastic modulus, and much higher hardness. Testing YAG samples will show whether these varied parameters will make quantum dot retention as proposed in Chapter 4 more or less likely than in the glass.

6.1 Procedures

The following procedures utilize the polishing equipment, YAG samples, and consumables detailed in Chapter 3. The quantum dot solution is the 60 nmol/mL concentration detailed in Chapter 4.

6.1.1 YAG Control

YAG samples that went through the procedure noted in Chapter 3 were used as control samples for fluorescent analysis. While not exposed to quantum dots, these samples were not perfect samples in that they had been through the lapping and polishing process.

6.1.2 YAG Immersion 450

This YAG sample was immersed in the quantum dot solution for 450 minutes (equivalent to the processing time of the YLPG samples). The sample was then cleaned with IPA soaked tissues as noted in Chapter 3.

6.1.3 YAG Lapped and Polished in the presence of Quantum Dots (YLPQ)

These YAG samples were processed according to the procedure outlined in Chapter 3 with the following exceptions.

- A solution of quantum dots in acetone was added to the lapping slurry to achieve a concentration of 60 nmol of quantum dots / mL of slurry.
- Following lapping, the samples were immersed in a 60 nmol/mL quantum dot solution for sixty minutes.
- During the pad polishing operation, 2.5 mL of the 60 nmol/mL quantum dot solution were applied directly to the polishing pad at the start of the pad polishing as well as every ten minutes thereafter until the last application at 350 minutes (ten minutes before the finish of the pad polishing).

6.2 Results

The surface measurements of the YAG samples yielded similar results between the three processes. The confocal fluorescence measurements yielded some low intensity fluorescent sites on the immersions samples and the lapped and polished samples. There was no discernible difference between the immersion samples and the lapped and polished samples in terms of the frequency or intensity of fluorescence.

6.2.1 YAG Control

These YAG samples were used to establish the background fluorescence threshold. The samples were placed on a glass cover slip and imaged at same laser intensity.

6.2.2 YAG Immersion 450

Confocal fluorescence microscopy of the immersed YAG samples detected some sites of fluorescence (Figure 6-1). The peak values observed had a relative value of 2.3 times the background threshold.

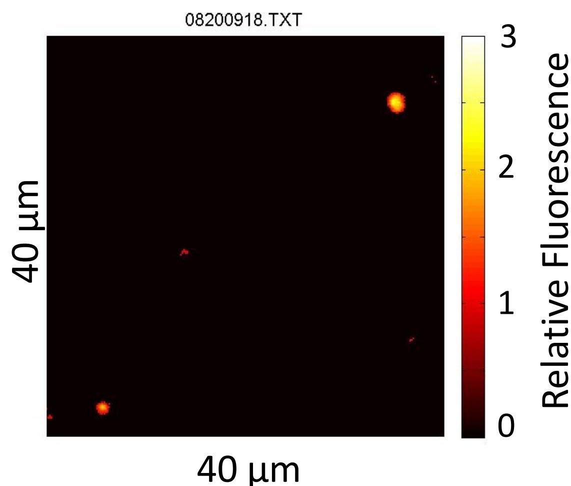

Figure 6-1. Confocal fluorescence image of a YAG sample immersed in a 60 nmol/mL quantum dot solution before being cleaned.

Due to problems with the piezo control of the Z-axis on the sample stage, optical slice data and fluorescent feature mining were not available for the immersion samples. Manual adjustment of the sample stage via 80 tpi screw estimated at a 5 µm change in the focal plane resulted in the fluorescent features at the surface becoming completely indistinguishable from the background.

The AFM images of the immersed YAG samples showed features extending above the surface with a similar occurrence to the fluorescent sites present on the confocal fluorescence scans. This means that quantum dots are being retained in certain locations on the YAG surface, despite the cleaning procedure. This suggests localize defects on the surface are providing suitable sites for the quantum dots to strongly adhere.

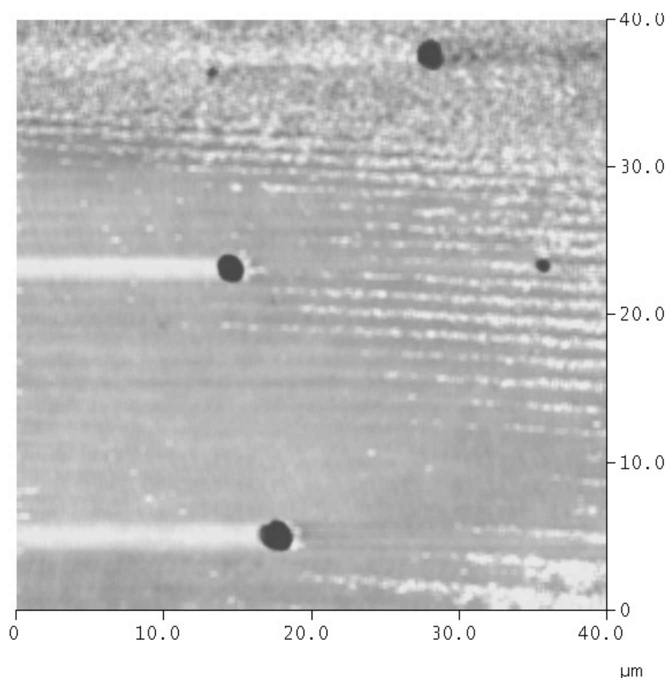

Figure 6-2. AFM scan of a YAG sample immersed in a quantum dot solution before being cleaned, showing numerous features adhered to the surface.

6.2.3 YLPQ

At the conclusion of the pad polishing operation, the polyurethane pad was heavily stained from the addition of quantum dots solution (Figure 6-3).

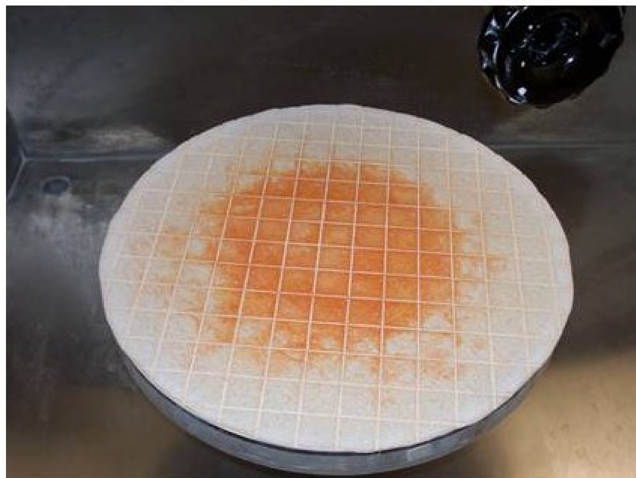

Figure 6-3. The polyurethane pad showed significant staining after polishing YAG samples with quantum dot solution added every ten minutes.

This shows that the YAG surfaces were in close proximity to quantum dots for the duration of the pad polishing process and dots were not simply flushed off the pad by slurry flow. Optical microscopy of the lapped and polished YAG showed sample surfaces that were free of defects with an average surface roughness value of 0.6 nm R_a (σ=0.1 nm) on the Zygo WLI.

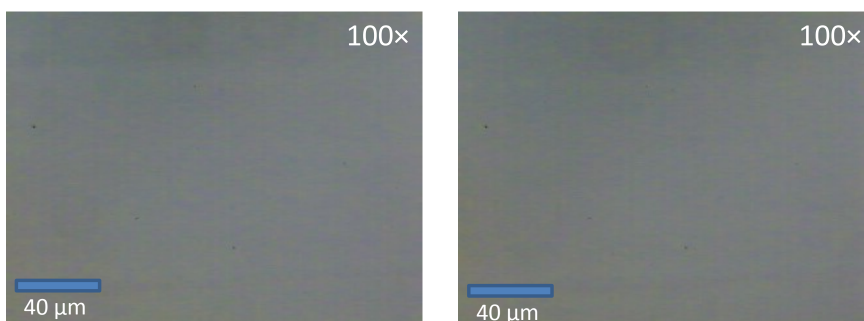

Figure 6-4. Optical images taken with the Mitutoyo Finescope (100×) of YAG sample 'D' taken after lapping and polishing in the presence of quantum dots show a high quality surface free of defect sites.

The fluorescent data from the YAG samples was analyzed in the same manner as the glass samples detailed in Chapter 5. Of three YAG samples (D, E, and F) which were lapped and polished in the presence of quantum dots, only sample D showed significant fluorescence roughly twice the background threshold (Figure 6-5). This level of fluorescence is comparable to the YAG immersion sample

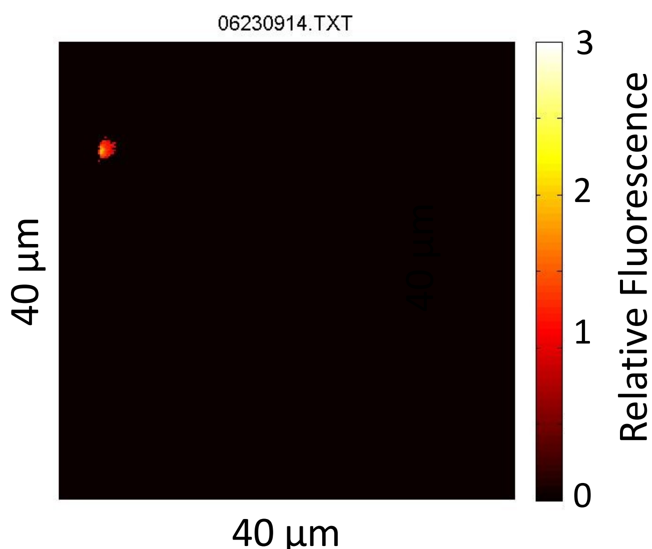

Figure 6-5. Confocal fluorescence image of YAG sample D which was lapped and polished in the presence of quantum dots (following a secondary cleaning).

A review of the optical slice statistics associated with this location on YAG sample D shows peak fluorescence occurring near the surface, with a drop off to background level fluorescence at a depth of 10 µm beneath the surface (Figure 6-6).

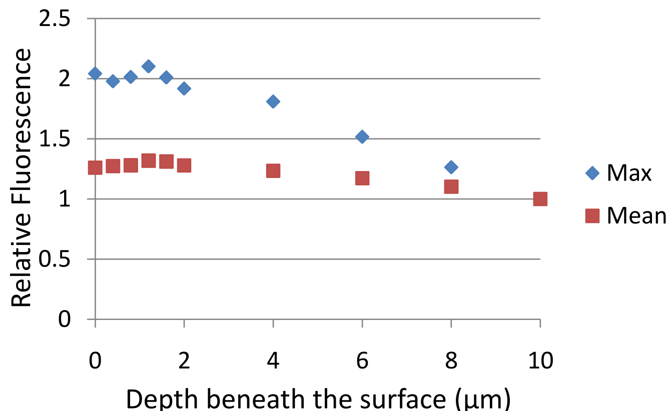

Figure 6-6. Optical slice statistics for YLPQ sample D.

Given the localized nature of the fluorescent feature shown in Figure 6-5, the fluorescent feature profile closely matches the maximum values seen in the optical slice statistics. The data was modeled as a point source of fluorescence located at the surface and a K value of 67.4 was calculated which produced a R^2 value of 0.997 for the model (Figure 6-7).

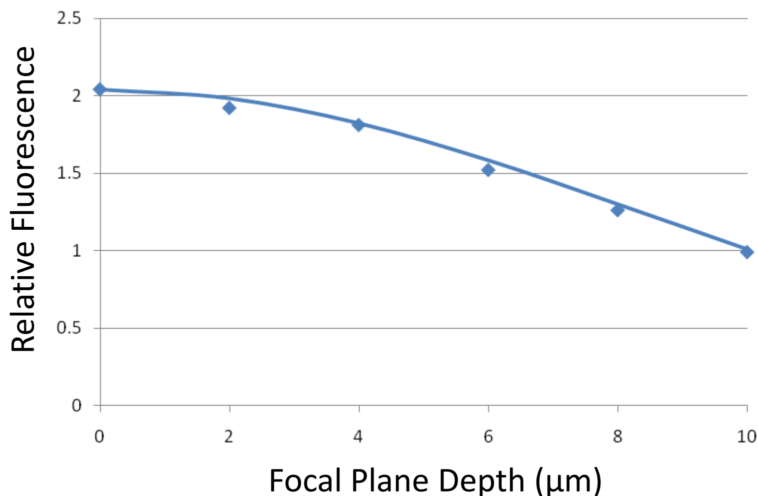

Figure 6-7. The fluorescent feature profile and calculated curve with K=67.4 and R^2=0.997.

When sample D was subsequently imaged with the atomic force microscope, several small features were discovered that are consistent with agglomerations of quantum dots adhered to the surface (Figure 6-8).

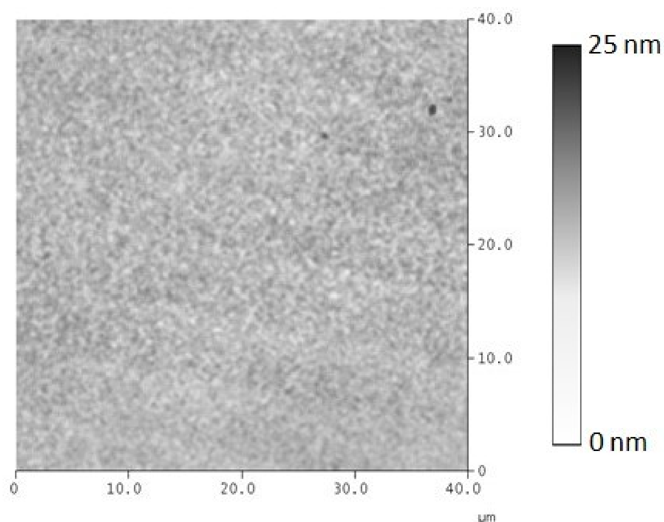

Figure 6-8. AFM scan of YAG sample D which was lapped and polished in the presence of quantum dots.

Sample E was etched according to the procedure in Chapter 3 to reveal a layer of defects beneath the polished surface (Figure 6-9). The microscope images revealed a mix of pits, fractures and scratches in the subsurface.

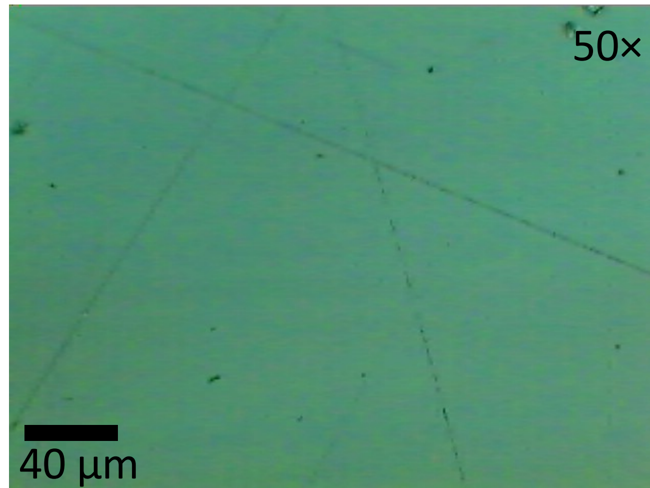

Figure 6-9. YAG Sample E, lapped and polished in the presence of quantum dots with 1 µm etched away to reveal a layer of subsurface damage.

Fractures are much less prevalent in the etched images of the YAG compared to the glass and the YAG fractures are smaller as well.

6.3 Discussion

The level of quantum dots retained on the YAG samples which were lapped and polished were comparable to samples which were simply immersed in a quantum dot solution for an equivalent amount of time. The fluorescence that remained on the immersion samples and the YLPQ samples may be highlighting surface defects that are hard to see with the other instruments as was seen with the microindentation testing in Chapter 4.

In light of the glass experiments of the previous chapter where there was a definitive increase in the fluorescence response for samples lapped and polished in the presence of quantum dots, there are several explanations for why the YAG samples behaved in a different fashion such as material properties or processing differences.

When considering YAG and the Corning 0215 glass, there are some stark contrasts in the materials. While YAG has a cubic structure, the glass is amorphous. The glass samples have a hardness of 6 to 7 on the Mohs scale, while YAG has a hardness of 8 to 8.5 on the Mohs scale. Similarly, the Young's modulus of glass and YAg are estimated at 70 and 280 GPa respectively. These material properties work in concert to make it less likely that quantum dots could become embedded in the surface of the YAG when compared to glass. This difference would account for the absence of widely distributed sites of low intensity fluorescence like those found on the glass LPQ samples.

Beyond the possibility of quantum dots embedded in the surface, the etched images show the presence of numerous defects, some of which could have housed defects. The scratches on the surface are unlikely candidates for retaining quantum dots given that the pad polished PQ30 glass samples did not show any retention of quantum dots and there were evident scratches in the etched images for those samples as well. The etch pits, which appear as discolored regions of roughly circular shape, are typically associated with dislocations in the crystal lattice of the YAG and may not have been open to the surface and accessible to the quantum dots. This leaves the sharply defined cracks and pits as the only viable sites where quantum dots might be deposited and retained. These sites represent a fraction of the damage area visible on the etched images, meaning viable sites are few and far between. The sites might also be less susceptible to the stress fields that accompany the traveling abrasives, making it less likely that the defects would be aggravated or made accessible to quantum dot intrusion.

The duration of the polishing process also contributes to a decreased likelihood of quantum dot retention. YAG polishes much slower than the glass, with the YAG samples requiring six hours of pad polishing while the glass samples required only half an hour. That means that any quantum dots on the surfaces were exposed to hydrodynamic forces for 12 times as long, increasing the opportunities for sufficient forces to arise and overcome the adhesion to the surface.

CHAPTER 7. DESIGN AND APPLICATION OF A LOOSE ABRASIVE PROCESS (LAP) MEASUREMENT HEAD AND PRELIMINARY RESULTS

While various setups have been used to measure the forces involved polishing, most have been restricted to full aperture polishing. To enable these types of measurements in sub-aperture polishing operations, a design task was undertaken to design a loose abrasive process measurement head for use in the polishing lab at UNC Charlotte. The polishing head was then used to measure variations in the axial loading during the lapping of glass. These samples were then examined to determine the influence of these changes on the material removal rate of the process, the surface roughness of the lapped glass, and the depth of cracks extending beneath the surface.

7.1 Design of the Loose Abrasive Process Measurement Head

The design of the Loose Abrasive Process measurement head went through a structured design process, with careful attention paid to identifying the design requirements. Once those requirements were identified, the design progressed from concepts to embodiment in the areas of mechanical design, electrical design and software design.

7.1.1 Design Requirements and Proposed Solution

The design needed to meet all the criteria found in Table 6 to be successful.

Table 6. Design Requirements for the LAP Measurement Head

Loose Abrasive Process Measurement Head Key Criteria
The device must easily couple to the IRB 140 robotic arm
The mass of the measurement head must not exceed 5 kg
It must measure the torque required to turn the workpiece or tool
It must measure the axial force keeping the tool and workpiece in contact
Torque and axial load values must update at 1 Hz or quicker
All measured values must be stored on a PC and readily retrieved

In addition to those criteria, there were several other metrics that if met would increase the capabilities and versatility of the device (Table 7).

Table 7. Additional Design Considerations

Additional Design Goals
The design should allow for coupling with other polishing setups (beyond the IRB 140)
Minimize the measurement head mass to maximize the working volume of the robot arm
Minimize axial loads carried by the motor shaft to prevent damage
Minimize parasitic torque reactions that could obscure subtle changes in the torque
Measure angular position, velocity and acceleration of the workpiece/tool
Measure axial vibration between the tool and workpiece

The first criterion of the design was that it interface with the IRB 140 industrial robot, a 6 axis robot manufactured by ABB Robotics (Figure 7-1). It is capable of coordinated movements of the axes with a reach of 810 mm [123]. The accurate working volume varies with load, with the highest load being 6.5 kg [123]. Within this envelope, the robot is capable of velocities up to 2.5 m/s, accelerations of 20 m/s^2 and position repeatability of 30 µm [123].

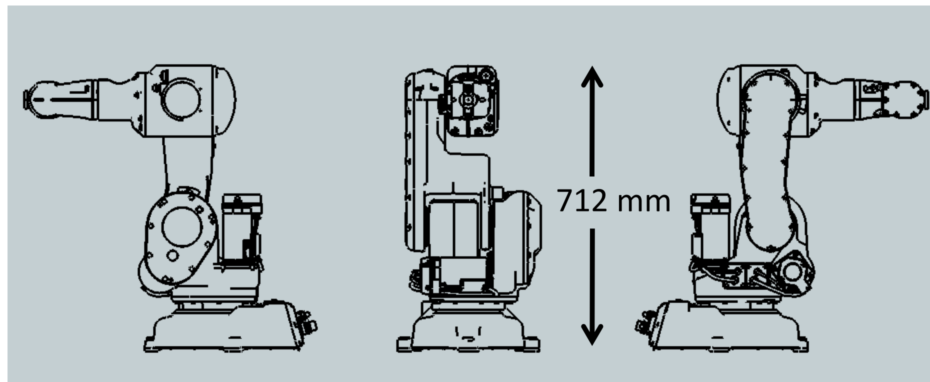

Figure 7-1. The IRB140 6-axis robot. Left, front and right views.

The concept for meeting these requirements is a motor which is free to translate and rotate within housing. Load cells will be used to oppose these motions and as a result provide a measure of the axial force and reaction torque that the motor is experiencing during the polishing process. Data from these load cells will be read into a PC via a data acquisition (DAQ) card. The motor selected will also employ speed control to maintain the set speed, independent of any variations in the torque. The key components of data acquisition and speed control are shown in Figure 7-2.

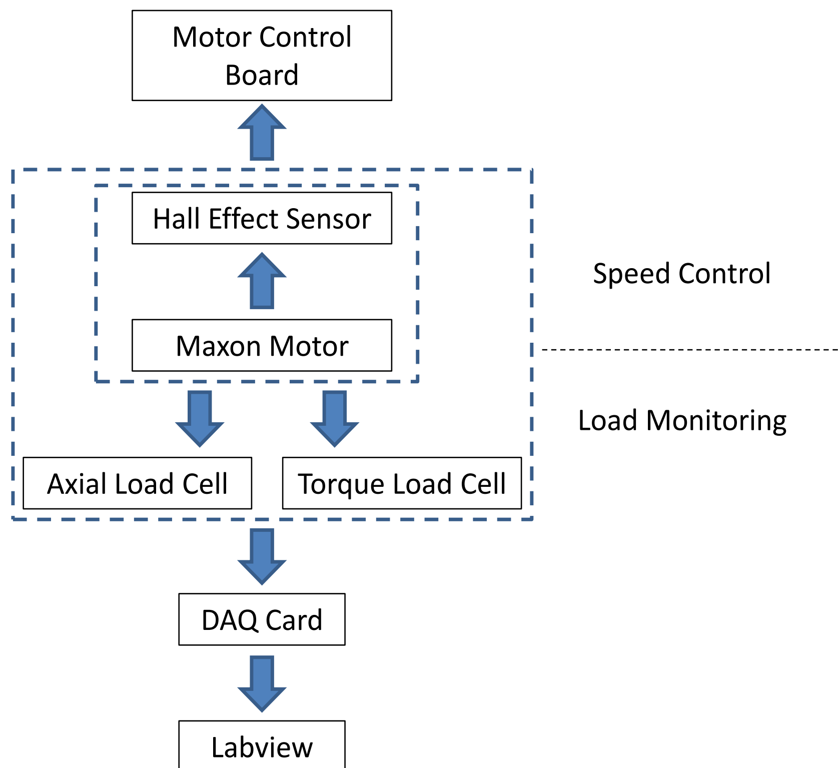

Figure 7-2. Block diagram of the key components for data acquisiton and speed control in the LAP measurement head. Items inside the small box are internal to the Maxon motor assembly, while items in the larger box are housed within the LAP measurement head.

7.1.2 Mechanical Design of the LAP Measurement Head

The housing for the LAP measurement head is comprised of hexagonal aluminum stock which has been bored out to an inner diameter greater than 32mm. This large bore does not extend all the way through the housing, instead a smaller aperture is used at the bottom of the housing and a small lip is preserved to retain the motor components in the housing (Figure 7-3). A plastic bushing is pressed onto the gearbox to provide a close running fit with the inner bore. This fit should allow for smooth translation and rotation of the motor components without perceptible angular play.

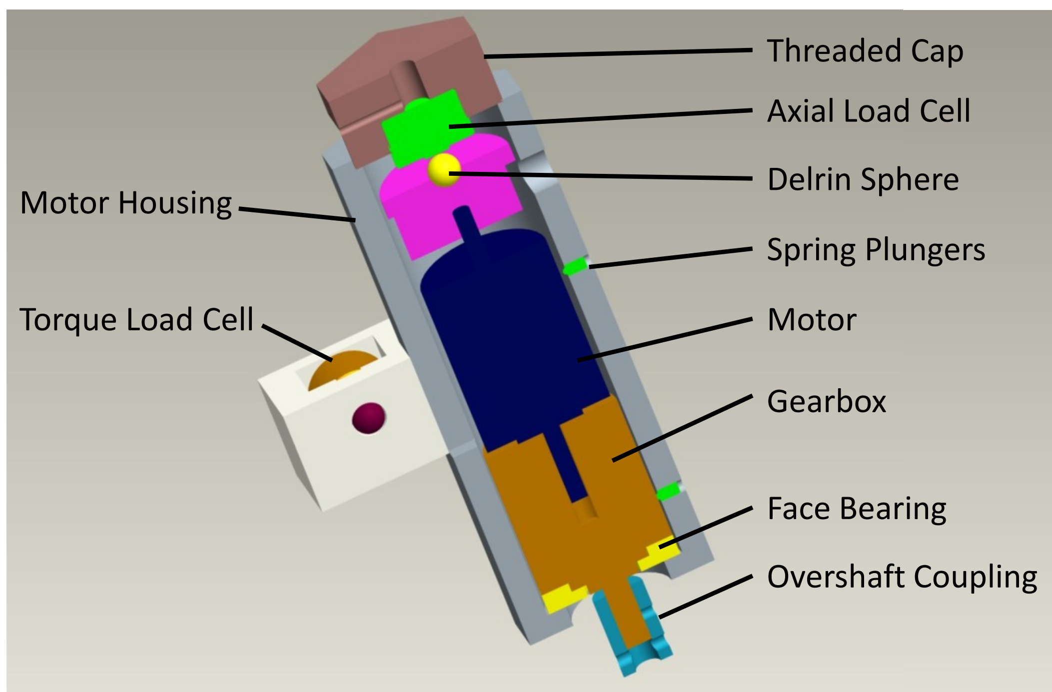

Figure 7-3. Section view of the Loose Abrasive Process Measurement Head (with the torque bar removed for clarity). The length of the motor housing is 125 mm for scale.

The motor housing itself has a feature called a torque bar pressed over its diameter. This torque bar consists of a thin walled cylindrical feature which has been slit for motor wiring access. Extending from this cylindrical feature is a rectangular cross section extended in the radial direction (Figure 7-4). This feature is used to transmit the reaction torque to a load cell mounted perpendicular to the axis of the motor. The torque bar was manufactured as a monolithic part by electro discharge machining it from a steel blank.

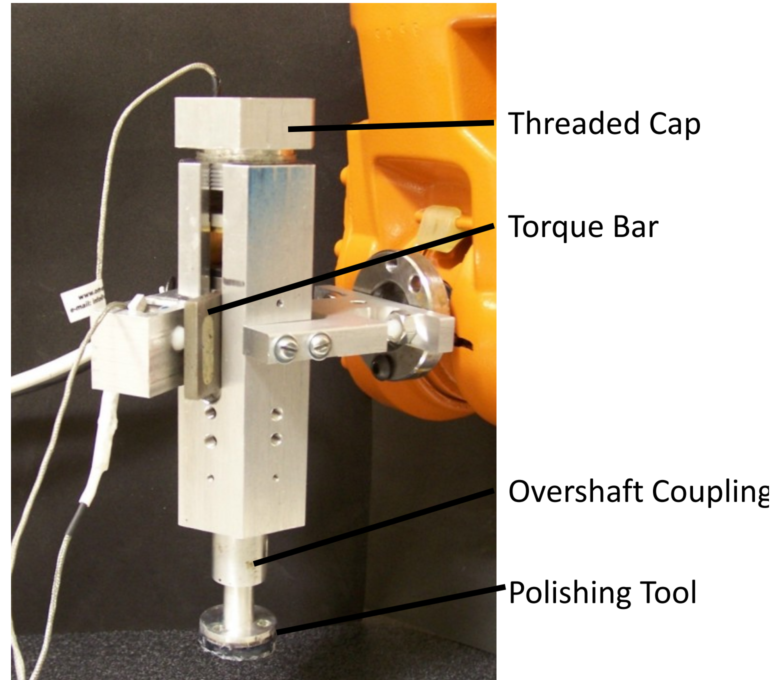

Figure 7-4. Photograph of the Loose Abrasive Process measurement head fitted to the IRB140 6-axis robot, showing the torque bar extending through a slot in the hexagonal aluminum housing.

Three spring plungers (120° apart) lightly contact the cylindrical surface of the torque bar to provide resistance to angular play. To accommodate the translation of the torque bar, a slot is milled into one of the faces of the hex stock.

Once these motor components are in place in the housing bore, a stack of wave springs capped with a disc are placed on top of the motor housing. The disc features a hole through the center which serves as a seat for a sphere. This sphere is the point contact by which the axial load is transmitted to the axial load cell.

The axial load cell is brought into contact with the Delrin (acetal copolymer) sphere as the cap in which it is embedded is threaded into the housing bore. This deflects the springs giving a finer resolution for controlling force than pressing directly

upon the housing. By only making contact with a sphere, the design minimizes the frictional torque from this contact, especially when the low coefficient of dynamic friction (0.2) of Delrin is considered [124].

At the bottom end of the housing the output shaft of the motor emerges. This shaft is coupled with an overshaft adapter which connects it to the tool. This overshaft adapted allows the tool to translate along the axis of the output, while restricting it to rotate with the output shaft. In operation, the housing is brought close to the workpiece such that the tool slides up the output shaft until it comes to rest on a pair of ring thrust bearings as shown in Figure 7-3. These bearings transmit the axial thrust forces through the motor housing and not the motor shaft while allowing the tool to rotate with respect to the housing without damaging the face of the motor.

Key Component Specifications

The motor selected was a brushless EC-max 30 (40W) from Maxon Motor. The brushless design was selected to minimize the electrical noise from the motor. This motor was paired with a planetary gearhead to reduce the speed down to the required range and increase the available torque. Additionally, the motor includes Hall effect sensors for speed control. This allows the controller to adjust the current to the motor windings to maintain the set speed with varying loads. To take advantage of these features a compatible motor controller was purchased from Maxon Motor, which allows for speed control via a potentiometer, Figure 7-5.

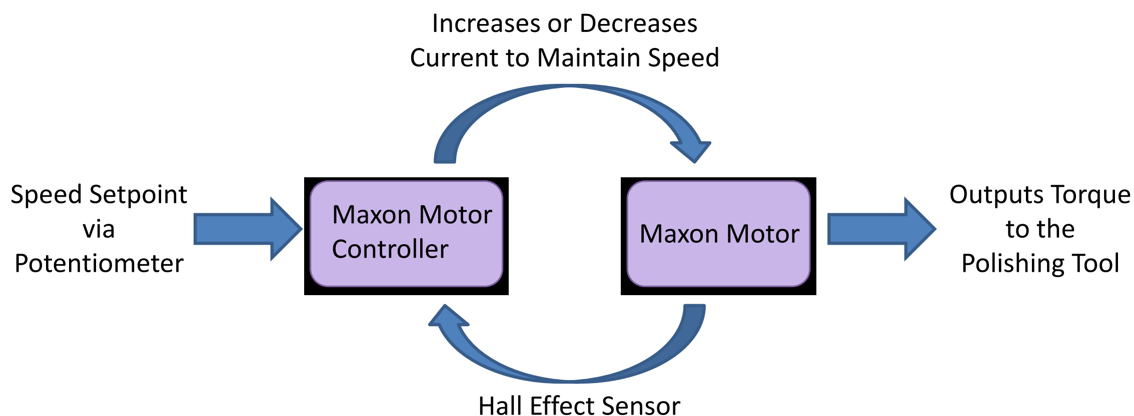

Figure 7-5. Speed Control Schematic for the Maxon Motor

Small button load cells from Omega were selected for the measurement head due to their small size (19mm diameter by 13mm height) and robust stainless steel construction. The force measurements are based on a strain gage which offers high accuracy and long term reliability. These load cells are used in both the axial force and the torque measurements. Several force ranges are available within the same load cell size, which allows them to be swapped out as required by the application.

Typically a 0-50 pound load cell was used for the axial measurements. This load cell is pressed into a bushing (to protect the load cell from damage and insulate it electrically) which is pressed into the threaded aluminum cap. The torque load cell is mounted in a fixture on the side of the housing which is separated from the housing by a thin insulating layer.

7.1.3 Electrical Design of the LAP Measurement Head

Simple, robust electronics were the goal in the measurement head electrical design. Care was taken to minimize disruptions to the acquired signals in order to

minimize filtering of the data with software. The axial and torque load cells are powered by a single 10V power supply and their outputs are fed into a Nation Instruments SCB-68 connector block which is cabled to the National Instruments Data Acquisition card.

The motor control is handled in a separate box. The motor controller board, power supply and wiring are housed in an enclosure. Knockouts provide access for a power cord going into the enclosure as well as two cords going to the motor. Two controls are provided on the motor, the first is an on/off switch for the motor. The second is a speed control knob which is connected to a potentiometer that is wired into the motor controller board to adjust speed.

In designing the electrical portion of this system, effort was made to minimize the electrical noise in the signals that are read into the data acquisition connector block. Towards that end, a brushless motor was selected and shielded wire was used to make the connections to the connection block. The load cells were also electrically isolated from the housing by using a Delrin bushing for the axial sensor and putting an insulating layer between the housing and the bracket holding the torque load cell. Through testing it became clear that the housing itself needed to be insulated from the robot, otherwise engaging the motors added significant noise to the signals from the load cells.

7.1.4 Labview Interface for the LAP Measurement Head

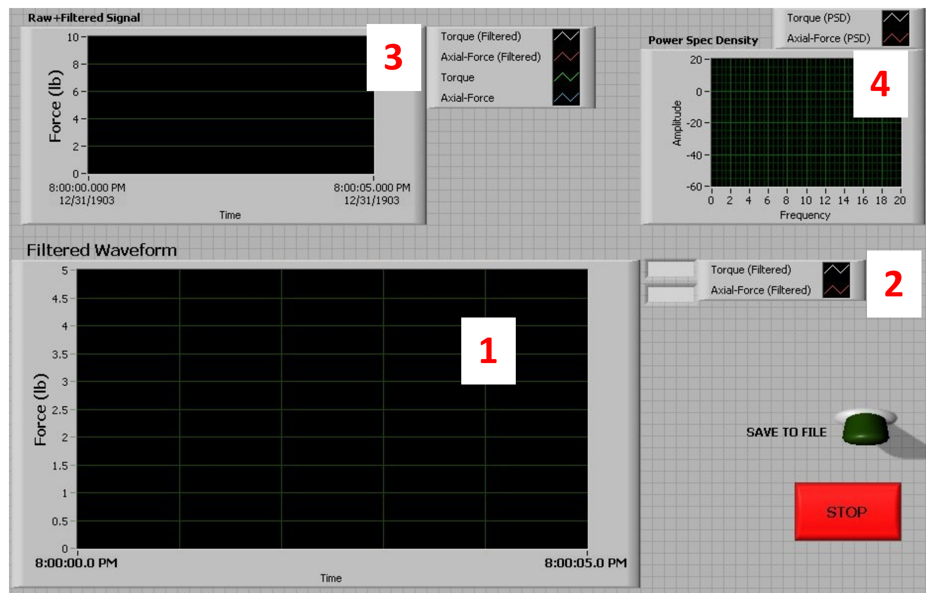

Figure 7-6. Labview Interfaces for Measuring Loose Abrasive Process Forces.

The Labview interface includes graphical displays of the axial load and torque load, readouts of both loads, a switch to start saving data, and a button to end monitoring. The main graphical display (Item 1) shows the filtered axial and torque load cell signals. The display shows the previous five seconds of data and is typically used as a process monitor during an experiment. To the top right of this graph (Item 2) there is a numerical display of the torque and axial loads. This is most useful when setting a load at a specific value for an experiment.

Item 3 above the main display reproduces the filtered axial and torque load cell signals, but it superimposes the raw unfiltered signal as well. Having both the raw and filtered data allows the user to see if the filtered data is representative of the raw data and can be useful in troubleshooting sources of noise. The final display (Item 4), shows

the power spectral density of the two raw signals. This power spectral density separates out the frequency components of the signal for troubleshooting or identifying contributions to the signal.

The large red stop button ceases the collection of data. Starting data collection is accomplished by clicking the run command on the Labview menu bar. The green toggle switch is used to save the collected data to a file. When the switch is toggled up, it is saving the data to a file and will be a lighter green. This feature is allows the experimenter to continue collecting data within one file, but stop saving data to that file during changes to setup. These breaks in data are clearly seen in the discontinuities in the time stamp associated with the load cell measurements.

7.2 Variable Load Lapping with the LAP Measurement Head

The construction of the LAP Measurement enabled a number of experiments investigating material removal mechanisms and subsurface damage in the lapping of glass. These basic tests investigated the influence of axial load on the material removal rate during lapping, the roughness of the resulting surface, and the depth of cracks extending beneath the surface. Crack depth was of particular interest given the difficulties in Chapter 5 with conclusively estimating the crack depth from etched images.

7.2.1 Equipment

The loose abrasive measurement head described in this chapter was attached to the IRB 140 6-axis robot for these polishing runs. Lapping was performed on a stationary iron platen the lapping slurry described in Chapter 3.

7.2.2 Procedures

Glass samples as described in Chapter 3 were affixed with foam backed tape to the polishing tool that mated with the overshaft coupler. The measurement head was moved into position by manual control of the IRB 140 until it was clear that the motor assembly was not resting on the internal housing lip. The axial load was adjusted to a value of 11.1, 22.2 or 45.5 N by advancing the threaded cap. The measurement head motor rotated the glass workpiece at 20 RPM while the IRB 140 provided a 10 mm/second translation as specified by a simple RAPID code program (consisting of MoveL commands that maintain the measurement head orientation while translating from point to point). Samples were lapped for twenty minutes before they were removed and cleaned.

A second round of samples were lapped in the same fashion described above, except that the threaded cap was advanced as necessary during the polishing run to maintain the load at the initial set values of X, Y and Z N. The samples were then fractured and the freshly cleaved surface was examined under the optical microscope for signs of the depth of fractures extended beneath the surface. To produce clean fractures, the sample face opposite the lapped face was scored with a carbide tipped scribe (Figure 7-7a). A small fulcrum was place under the sample (typically a drill rod less than 1mm in diameter) and even pressure is place on the sample until it fractures (Figure 7-7b). A nice clean fracture provides a window into the bulk of the sample that allows for viewing the sample in a section view from which the depth of surface fractures and subsurface fractures can be assessed (Figure 7-7d). As with dimpling, the

sample can be etched lightly to emphasize the defects that are present, making them easier to observe with optical microscopy.

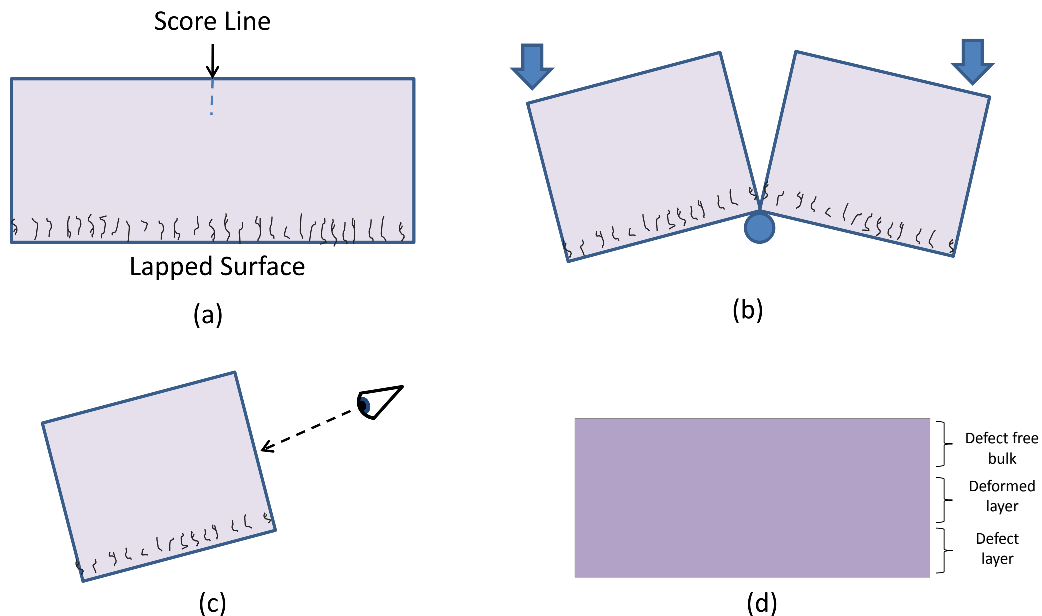

Figure 7-7. Side view of the sample fracturing process.

7.2.3 Material Removal Rate Results

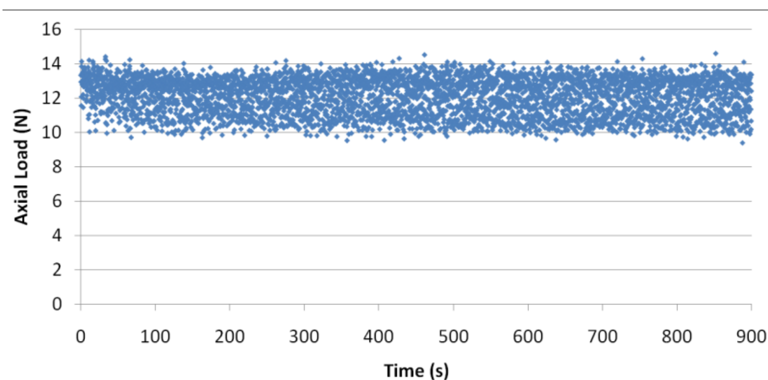

Figure 7-8. Measurement Head Load Readings from Low Load Lapping Operation.

The low load test was set for a nominal load of 11.1 N. The average load over the 15 minute lapping process was 12 N with a standard deviation of 1 N. The maximum load measured during the test was 14.6 N and the minimum load measured was 9.4 N.

Variations in the measurement are attributed to periodic shifts in load due to misalignments and electrical noise in the system. The measurement trend over the period observed showed a signal that is repeatable and at steady state.

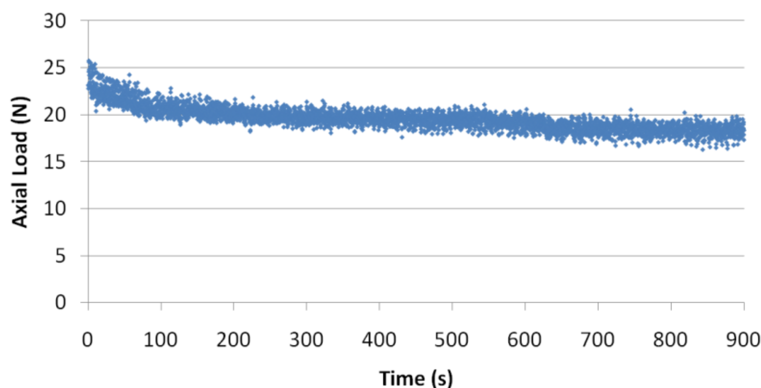

Figure 7-9. Measurement Head Load Readings from Medium Load Lapping Operation.

The medium load test was set for a nominal load of 22.3 N. The average load over the 15 minute lapping process was 19.6 N with a standard deviation of 1.2 N. The maximum load measured during the test was 25.7 N and the minimum load measured was 16.2 N. As before, the high frequency variations in the measurement are attributed to periodic shifts in load due to misalignments and electrical noise in the system. The long term trend of the load signal however shows an evident decay from the initial load of roughly 22.3 N to the final load of rough 17.8 N. This decay in the load could come from one or more of several sources as the load is transmitted from the robot, through the measurement head to the workpiece which are discussed in Chapter 7.2.5.

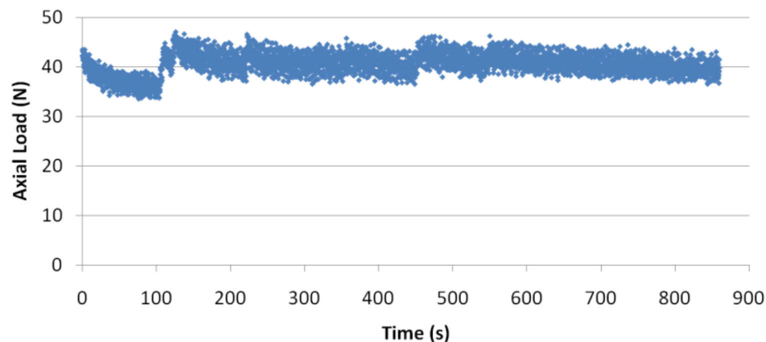

Figure 7-10. Measurement Head Load Readings from High Load Lapping Operation.

After observing the relaxation of the axial load during the medium load lapping process, user intervention was introduced during the high load lapping process to keep the actual load closer to the set load. This was done by watching the Labview readout during the lapping process and advancing the threaded cap when the load began to decay towards a value of 35.6 N (80% of the set value). Examples of this appear in the graph as a load signal that is decaying then abruptly increases (as seen near the 120 second mark in Figure 7-10 above. This resulted in an average load of 40.5 N with a standard deviation of 2.2 N. The maximum loads observed were 47 N and 33.5 N respectively.

7.2.4 Fractured Sample Results

The glass samples were fractured and the exposed surfaces examined with the Mitutoyo Finescope optical microscope as described in Chapter 3.2.2. The samples were held fractured edge up with clips to insure the samples were observed in the correct orientation. While the samples were held fractured edge up and nominally perpendicular to the sample stage, the actual exposed surface from the fracture varied due to the unpredictable way that the glass broke. This does not appear to have been a

significant factor in the images collected as a sample so skew to the observation plane would not keep features in focus across the entire field of view. For this reason, the observed fractures lengths are estimated to be within 15% of the actual value. Fractures extending from the lapped surface became apparent at magnifications of 50×, with clear images being taken at 100× (Figures 7-11 to 7-14).

Low Load

The exposed face of the sample lapped at 11.1 N had an average surface roughness of 0.39 µm R_a (σ=0.01 µm) and fractures which were obvious at higher magnifications, but they were not uniformly distributed across the edge. The fractures appeared in small clusters, typically in close proximity to pits or other defects on the surface (Figure 7-11). Based on the images, the fractures appear to extend 7 µm to 12 µm beneath the nominal surface.

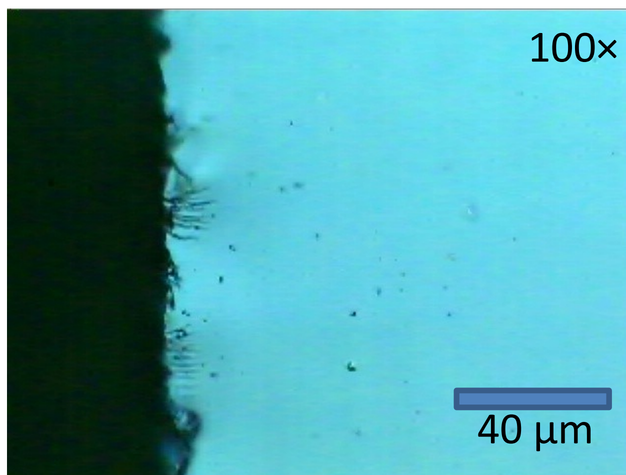

Figure 7-11. A view of the surface exposed by fracturing a glass sample that was lapped at and axial load of 11.1 N for 20 minutes with the LAP measurement head. Fractures can be seen extending from the lapped surface (left) into the bulk of the material.

Medium Load

At the medium load of 22.3 N, the average surface roughness increased to 0.49 µm R_a (σ=0.01 µm) and fractures become increasingly regular, defining a region that extends roughly 20 µm beneath the lapped surface.

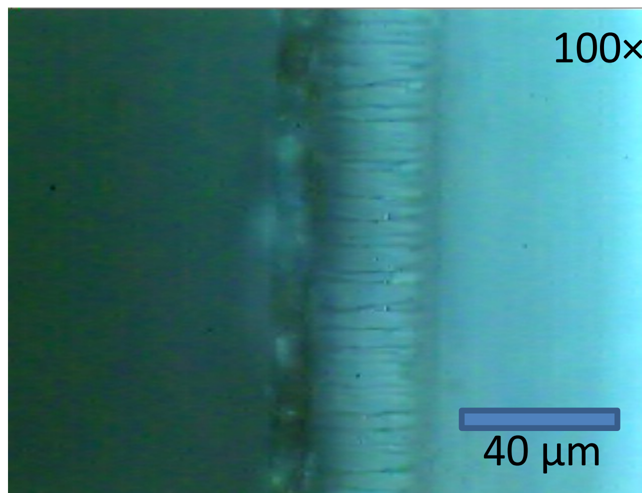

Figure 7-12. A view of the surface exposed by fracturing a glass sample that was lapped at an axial load of 22.3 N for 20 minutes with the LAP measurement head. Fractures can be seen extending from the lapped surface (left) into the bulk of the material.

High Load

The sample lapped at a load of 44.5 N had an average surface roughness of 0.63 µm R_a (σ=0.04 µm) and well defined fractures that extend over 20 µm from the surface into the bulk of material (Figure 7-13). While these fractures are distinct, other locations were observed on this sample where the fractures were much shorted and more sparsely distributed along the edge (Figure 7-14).

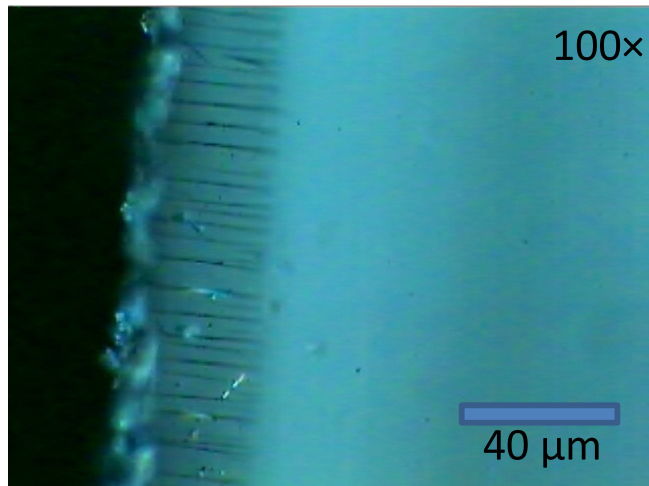

Figure 7-13. A view of the surface exposed by fracturing a glass sample that was lapped at an axial load of 44.5 N for 20 minutes with the LAP measurement head. Fractures can be seen extending from the lapped surface (left) into the bulk of the material.

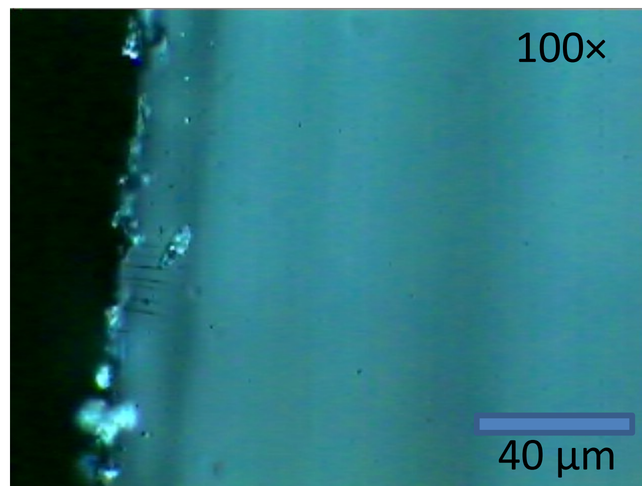

Figure 7-14. A separate location on the sample imaged in Figure 7-13, showing less distinct fractures that are more sparsely distributed.

7.2.5 Discussion

These brief experiments demonstrate the capability of the Loose Abrasive Process measurement head to record changes in the physical polishing parameters that

influence the material removal rate, lapped surface finish, and the depth of visible fractures beneath the surface.

Discussion of the Decay in the Axial Load

As was noted in Chapter 7.2.3 the axial load as measured by the load cell decayed from the initial set value as the lapping process progressed. The reason for the decay could be at one or more locations in the force loop connecting the robot to the workpiece (Figure 7-15). The axial force is transmitted from the 6-axis robot, through the threaded cap with embedded load cell to the Delrin sphere. The Delrin sphere transmits the load to the wave springs which carry the load to the motor housing. The motor housing transmits the axial load to the shaft coupling and finally through the foam backing to the workpiece.

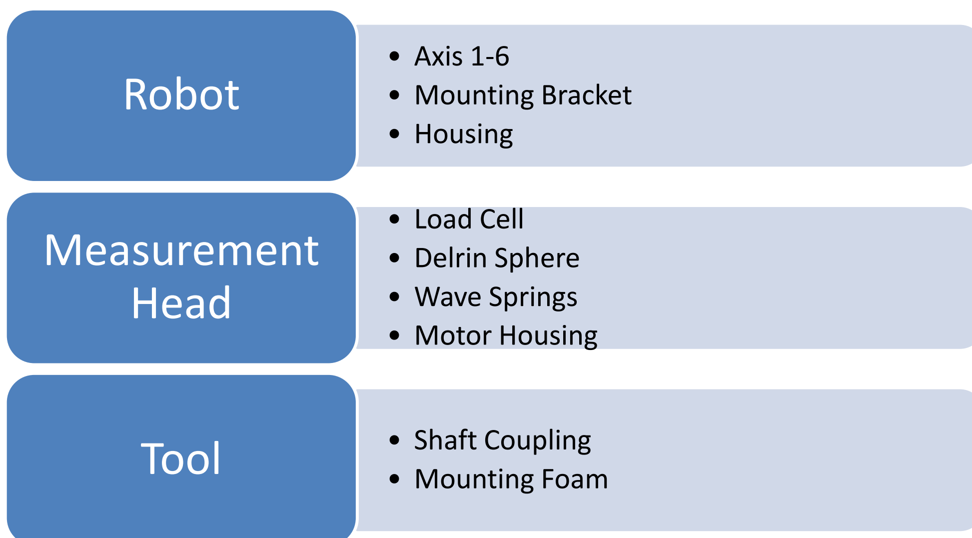

Figure 7-15. Simplified force path of the axial force from the robot to the workpiece and platen.

The first possible source is a relaxation or a shift in the position held by the robot. Such a movement could result in less compression of the wave springs that transmit force from the robot housing. Another possibility is a weakening of the wave springs that transmit the load from the load cell to the motor housing. Such a weakening would mean that the deflection which established the initial load would provide a lower load given a lower spring constant. Deterioration of the elastic properties of the foam between the sample and the shaft adapter would have a similar effect. A final consideration is the effect of the material removal rate on the load measurement. The low and medium load lapping processes removed 25 μm and 29 μm respectively. During operation, the button load cell experiences deflections ranging from 30 μm to 80 μm. As such the material removed is of the same order as the deflections of the load cell measuring the force. This means that as material is removed, there is more distance between the nominal surface and the load cell, resulting in less compression of the various components shown in figure 7-15. With lower compression, the elastic elements transmit less force to the workpiece.

Influence of the Lapping Load on the Material Removal Rate

As would be expected from the Preston equation, increases in the applied load increase the amount of material removed by the lapping process (Figure 7-16).

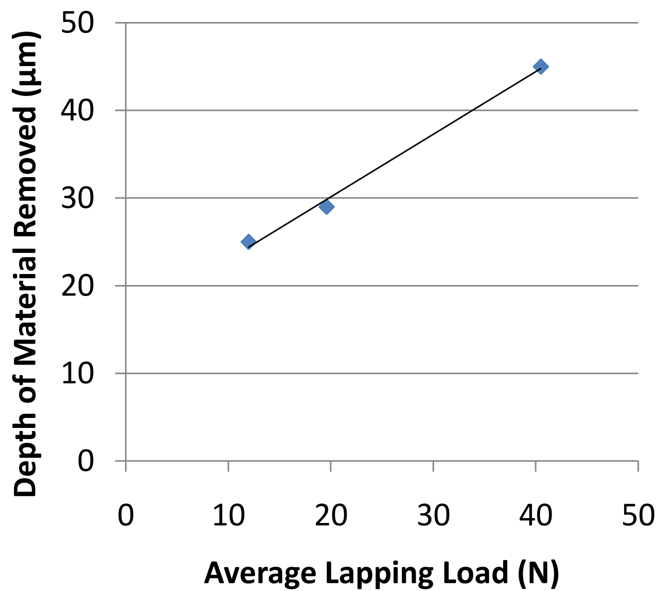

Figure 7-16. Depth of material removed as a function of average lapping load for samples lapped with the LAP measurement head.

While the linear fit to the data (y=0.72x+15.8) has an R^2 value of 0.995, the intercept is problematic as it suggests that at a load of 0 N, there will still be 15.8 µm of material removed.

The Labview interface has been programmed with an offset to account for the mass of the gearbox and motor assembly when calculating the applied axial load, as this internal assembly must be lifted off the inner ledge before the threaded cap is advanced to adjust the axial load. The 11.1 N load is primarily the weight of these internal components with only a minimal load contribution from deflection of the wave springs inside the housing. Since the 11.1N represents the low extreme the loads that can be applied, it may be worth revisiting those offsets to make sure that the measurements accurately reflect the 'dead weight' that is applied before the threaded cap is engaged.

Influence of the Lapping Load on Surface Roughness and Fracture Depth

The surface roughness was seen to increase with lapping load as well (Figure 7-17). The higher lapping loads lead to deeper fractures which generate a more extreme topography. This is also born out in the fractured sample images where the depth of the visible fractures increases notably from the samples lapped at 11.1 N to the samples lapped at 22.3 N and 44.5 N. It is also worth noting that the R_a values for the low load are comparable to those measured for the glass samples lapped (by hand with a comparable load) in Chapter 3 and 5.

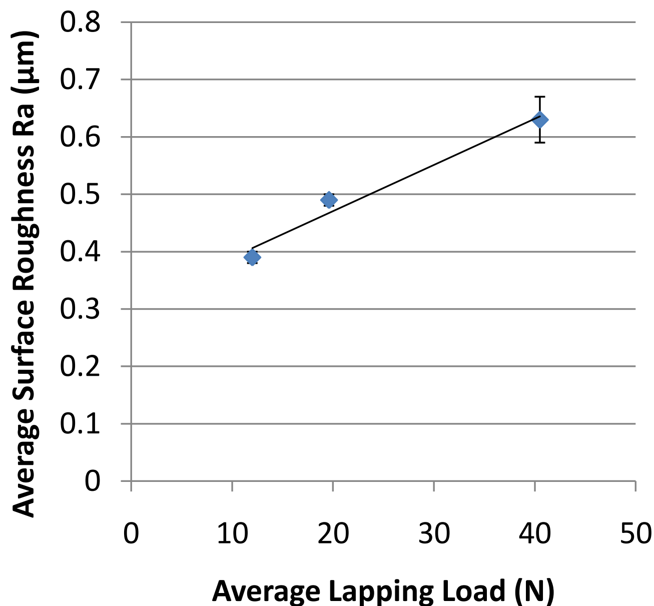

Figure 7-17. Average surface roughness (R_a) as a function of average lapping load for glass samples lapped with the LAP measurement head.

A key observation from the 22.3 and 44.5 N samples is the difference in the prevalence of fractures. While both of these samples had fractures that extended much further beneath the surface than those lapped 11.1 N, the samples lapped at 22.3 N had a much more uniform distribution of fractures. The fractures at 44.5 N had a more

sharp distinctive appearance in places, but other location along the fracture edge had only a small cluster of fractures within the field of view. A possible explanation for this is that the greater loading of the lapping abrasives leads to an accumulation of stress in the material around a travelling abrasive until it is released in the creation of a significant fracture or other defect.

As these fractures represent line cuts through the sample, it reinforces how subsurface damage is not a homogeneous process distributed equally about a sample surface. These images in conjunction with the multitude of etched surface images show that subsurface damage can occur at discrete locations scattered about a sample surface. For this reason, fields of view and sampling density have to be considered when making general statements about the level of subsurface damage in a specimen.

The fracture images at the 11.1 N axial load are particularly relevant as they match the lapping loads for the glass samples in Chapter 3 and 5. The prevalence of cracks visible in these fractured samples agrees with the etched images of lapped and polished glass, where defects were obvious, but not uniformly distributed across the surface. The depth of the fractures is also consistent with the depths of peak fluorescence calculated from feature mining data for LPQ and LPQP samples detailed in Chapter 5, where models suggested the presence of quantum dots at depths of 8 µm and 11 µm beneath the surface.

Images from the optical microscope provide very useful information about fracture depth, but they are limited by the diffraction limit of the optics as well as the resolution that was captured. By assuming a wavelength of 550 nm (middle of the

visible spectrum) and a numerical aperture of 1, the diffraction limit on resolution would be 275 nm. With images taken at a resolution of 640 × 480 pixels over a scan area roughly 170 µm × 128 µm, each pixel represents 265 nm. As these two resolutions are comparable, data is not being lost in the transition to a digital image, but data is not being saved at a resolution that greatly exceeds the ability of the microscope optics to resolve. Given both resolutions, it is clear that the system would be unable to resolve features smaller than 250 nm as that is below the diffraction limit and smaller than the size of a single pixel.

Fractures or defects that are smaller than this threshold could still be problematic in high energy applications. Fractures or voids alone can provide sites for absorption [125] or they can house absorbing inclusions of material whose heating and resulting thermal gradients can cause catastrophic failure. For this reason, while the fracture of lapped samples to observe the depth cracks extend beneath the surface is a useful exercise, the removal of that depth of material may be insufficient in high energy applications.

CHAPTER 8. CONCLUSIONS AND FUTURE WORK

Like most research, these experiments have produced results that answered some questions, left some unanswered and identified questions to be pursued in the future. This chapter first details conclusions from this work. That is followed by a selection of experiments that naturally follow from this work presented and finishes with broader goals and experiments that would require resources from beyond the polishing research group at UNC Charlotte.

8.1 Conclusions

This chapter is organized as a series of questions with the associated discussions and conclusions.

Can Quantum Dots Added to Loose Abrasive Slurries Detect Subsurface Damage in Glass?

Yes. Quantum dots added to loose abrasive slurries were detected in glass samples that showed no indication of damage from optical microscopy, white light interferometry, or atomic force microscopy. The presence of this damage was confirmed with both sample etching and sample fracturing. The LPQ and LPQP samples both displayed peak fluorescence well above the background and well above that of samples simply exposed to quantum dots in solution.

Can Quantum Dots Added to Loose Abrasive Slurries Detect Subsurface Damage in YAG?

It is inconclusive. The YAG samples finished in this research did not display any significant retention of fluorescence beyond that of a sample immersed in a quantum dot solution. That finding however is tempered by a) the limited amount of lapping damage in the YAG samples and b) the surface condition of the YAG immersion samples. Etching of the lapped and polished YAG samples showed some brittle fractures, but they were sparsely distributed. This is due to the superior hardness and strength of YAG when compared to the glass specimens making fracture difficult. Fewer lapping defects means there are fewer sites on the surface to accommodate quantum dots. This would lead to a lower fluorescent response than the glass, which is what was observed.

The history of the YAG immersion samples also warrants review to put the retention of quantum dots on those samples in perspective. While no processing was done on these samples at UNC Charlotte, they are by no means pristine, untouched material. As is the case with all YAG sample used in this work, they were grown as a boule of material at Northrop Grumman Synoptics. Cylinders of YAG were then core drilled from the boule, sawed to the rough length, subjected to fixed abrasive grinding to normalize the height, and then lapped and polished. The polishing step was solely to achieve an ‘inspection polish’ which is sufficiently specular for the samples to be examined with interferometers when assessing the flatness and perpendicularity of the faces. Given that these surfaces are not polished to a final finish and definitely not polished to remove subsurface damage, it is probable that there are small defects on

the surface. As will be addressed in the question below, the defects could house quantum dots, leading to a higher fluorescent response than a truly pristine YAG surface immersed in quantum dots.

So with the immersed then cleaned YAG sample having a greater likelihood of retaining quantum dots and the processed YAG sample not having an abundance of brittle fracture defects to house quantum dots, the similarities between their fluorescent response is not enough to rule out the possibility that quantum dots in loose abrasive slurries could detect subsurface damage if the processing was more aggressive in inflicting brittle fractures upon the material.

Can Quantum Dots Highlight Surface Defects in Glass and YAG?

Yes. Indentation testing with glass showed not only that quantum dots were retained in the Knoop indents, but quantum dots detected with wide field fluorescence microscopy highlighted incidental damage sites outside the indents as well (Figure 4-5).

Are there defects that Quantum Dots Do Not Detect?

Yes. Quantum dots have not been found in subsurface scratches on either glass or YAG specimens. These scratches are a result of plastic deformation and unlike the higher load brittle fractures of lapping do not appear to be created by a sufficiently energetic process to adhere or embed quantum dots into the surface. The etched results from the pad polished PQ30 samples provide a clear image of subsurface scratches that were not detected with quantum dots (Figure 5-28). Similarly, the etched results for the YAG YLPQ reveal subsurface scratches that were not detected by quantum dots. YAG dislocation faults are another defect that cannot be detected with

quantum dots. They appear as pits during etching, but if they were not open to the surface, there is not a mechanism for quantum dots to travel into them.

Can Confocal Fluorescence Microscopy Provide Depth Information about Defects in Glass?

Yes. The LPQ and LPQP samples provided numerous fluorescent features where depth information could be discerned. Most fluorescent features (84% of the ones sampled) had fluorescence that peaked between the surface and 2 µm beneath the surface. This first 100 nm of this region corresponds to a hydrated and plastically deformed layer that has been shown to contain impurities from the polishing process. As such, it is not surprising that quantum dots were found in this region of the sample. A small number (12%) of the fluorescent features had peak fluorescence 6 µm to 8 µm beneath the surface. These features displayed the same characteristic shapes as the other features, with the exception of the peak occurring well below the surface. A single feature stood out from the other twenty four in that the fluorescent response did not drop or rise with changes in the focal plane. The single source model of fluorescence response used for the previous features was insufficient for this data. Though numerous solutions are a possibility, a model of fluorescence located at both the surface and 11 µm beneath the surface provided a good fit to the data. The depth values calculated from the confocal fluorescence data were comparable to the cracks depths observed on lapped samples that were fractured and examined under the microscope.

Can Quantum Dots be Used as a Non-Destructive Assessment of Subsurface Damage?

Yes, in the case of glass. Quantum dots detected with a confocal fluorescence microscope indicate the presence of damage sites on or beneath the surface. Surface defects such as pits can be detected as well as brittle fractures in the subsurface. The absence of fluorescing quantum dots does not insure the absence of subsurface damage, as plastic deformations such as scratches are not highlighted by the quantum dots.

Can the LAP Measurement Head Measure Axial Load Variations that Influence Material Removal Rate, Surface Roughness and Subsurface Damage Depth?

Yes. The LAP measurement head was capable of measuring differences in the axial load that corresponded to changes in the material removal rate, surface roughness, and subsurface damage depth. As expected, the material removal rate and surface roughness increased with increasing axial load. The depth and prevalence of subsurface damage was seen to increase from the low (11.1 N) to medium (22.3 N) axial load. At high loads, the depth increased marginally, but the prevalence of the defects decreased.

What can be learned from the Experiments about the Material Removal Mechanisms of Lapping?

Brittle fracture is the primary material removal mechanism for lapping and only samples that had been lapped showed signs of fracture defects in the subsurface damage. The rate of material removal, the roughness of the resulting surface, and the

depth of fractures extending beneath the surface were seen to increase with axial load. The increased strength and hardness of the YAG samples compared to glass, reduced the prevalence of brittle fractures compared to the glass samples. These findings match expectations, as higher axial loads lead to more egregious fractures that result in aggressive material removal that leaves greater damage on the surface and in the subsurface.

What can be Learned from the Experiments about the Material Removal Mechanisms of Pad Polishing?

Unlike lapping, pad polishing glass did not create brittle fractures in the subsurface. Instead of fractures, scratches were the defects that were revealed when the pad polished glass was etched. These scratches indicate that plastic deformation is taking place during the pad polishing of glass. The YAG samples responded similarly to the pad polishing, as YLPG samples that were etched showed scratches in the subsurface as well as a small number of etch pits and fractures. While the YAG samples showed a much greater resistance to the brittle fracture of lapping, plastic deformation appears prevalent in the pad polishing of both glass and YAG.

What can be Learned from the Experiments about the Material Removal Mechanisms of Pitch Polishing?

The glass LPQ samples which were pitch polished (becoming LPQP samples) showed a markedly different morphology than the baseline LPQ samples. The texture and scratches which were apparent in the AFM scans of the LPQ samples were eliminated by the pitch polishing process. Even the short, five minute, pitch polishing

process resulted in a dramatic change of surface structure with a smooth, but wavy and melted appearance. This suggestions that material is being smeared about instead of removed via brittle fracture (lapping) or scratching/plowing (pad polishing). This difference is likely due to greater contact between the pitch tool and the workpiece. While asperities on the polishing pads may drag abrasives through the workpiece surface with locally high loads, the compliance of the pitch tool allows for highly loaded abrasive particles to embed further into the tool, reducing their protrusion above the nominal plane. This regulation of high abrasives would result in a more even load distribution that could drop the load per particle below the threshold for effective plastic deformation. In the absence of plastic deformation, material removal could take place though purely chemical means or more likely through a chemo-mechanical process by which the pitch tool smears and removes the topmost layer of workpiece material that has been weakened by chemical reactions with the slurry.

8.2 Future Work

The future work is divided up into two categories; recommended experiments that can immediately be implemented and projects that will require resources outside the polishing research group.

8.2.1 Recommended Experiments

These recommended experiments require only resources and equipment that are currently available in the polishing lab, in the mechanical engineering department, or with existing collaborators outside the department.

Higher Load Lapping of YAG Samples

As was discussed earlier in this chapter, while there was not a significant difference in the fluorescence retained by a YAG sample that was lapped and polished in the presence of quantum dots, the processes did not provide many brittle fractures to house quantum dots either. Modifying the process for YAG used in Chapter 5 to include higher lapping loads would induce more fractures to house quantum dots and answer the question of whether a more significantly damaged subsurface layer in YAG could be detected.

Microindentation of YAG Samples

From Chapter 6, it is clear that quantum dots are not being embedded in the YAG samples during the lapping and polishing presence. It would be a worthwhile experiment to step back and look at inducing known surface defects into the YAG samples in the presence of quantum dots in a direct analogy to what was done with the glass samples in Chapter 4.3. In addition to the answering obvious question of whether quantum dots would be retained in these defects, the size and shape of the indents themselves would provide a valuable comparison between the structure and behavior of the YAG and glass surfaces.

Nanoindentation

The microindentation procedure outlined in Chapter 4 was successful in producing Knoop indents as surface defects that retained quantum dots after the sample surface was cleaned. These microindents however had dimensions on the order of 100 µm for the long axis and 10 µm for the short axis. In comparison,

nanoindentation can produce indents with micrometer or submicrometer scale dimensions. For that reason it is worth replicating the work that was done with the microindenter and quantum dots with the nanoindenter.

In addition to the simple question of retention, experiments with nanoindentation could also provide insights into the interactions of specific material removal mechanisms and the quantum dots. Knoop and Vickers indents for example can exhibit tip fractures at higher loads as well as regions of material that are plastically deformed and pushed out of the indent. In addition to static loads, using the nanoindenter to produce scratches on the material would be analogous to the mechanisms that produce the subsurface scratches on the YAG and glass samples. It would be interesting to see if and where exactly quantum dots were retained in these intentionally induced surface defects. If dots were not retained in these scratches, it would conclusively show that the mechanisms of plastic deformation do not sufficiently disrupt the surface to allow dots to become embedded.

Fracturing Lapped and Pad Polished Glass Samples

This duplicates the procedure described in Chapter 7 for fracturing glass samples and examining the depth of cracks that are visible along the fracture surface, but adds in a pad polishing step prior to the sample fracture. This polishing step would smooth the surface of the specimen compared to the rough topography of the lapped samples which would aid in determining the depth of fractures by providing a clear starting point. More importantly it would provide insight into whether the technique is capable of capture the presence of cracks beneath a surface that is polished smooth. Pad

polishing as described in Chapter 3 would be sufficient as it produced quality surfaces while only removing 1.8 µm of material on average, thus it would not polish through the depth of damage seen in Chapter 7.

Fluorescent Observation of Lapped and Fractured Glass Samples

The lapped and fractured samples described in Chapter 7.2.4 provided very clear images of fractures extending from a lapped glass surface into the bulk of the material. As noted in Chapter 7.2.4 though there is a limit to size of defects that can be resolved. Repeating the lapping procedure with the addition of quantum dots to the slurry would be easily accomplished or samples could be conventionally lapped as per the lapping portion of the procedure described in Chapter 5.1.3. Either process would produce widefield or confocal fluorescence images that clearly show the depth at which dots occur in the sample, with the possibility of the fluorescence highlighting features that would otherwise be below the limit of optical resolution. These measurements would serve as further comparison to the depth information calculated from the fluorescent feature profiles.

Use the Confocal Microscope to Investigate Defect Scatter without Fluorescent Material

This experiment would be a replication of the work by Fine et al [61] in detecting the scatter from subsurface defects with a confocal microscope. In these experiments, no fluorescent tag is used. Instead, the photodetector measures the scatter from subsurface defects. While the concept is well described, there are few details about the either the processing of the measured samples or the characteristics of the defects

(beyond the crack depth). As such, there is room for a more investigation treatment of the technique to evaluate its suitability for detecting subsurface damage under conditions of interest to both technicians and researchers.

Further Integration of the LAP Measurement Head

While the LAP measurement head has been shown to meet the initial goals of measuring axial loads as well as torque loads during loose abrasive finishing, there are numerous avenues for improvement with the device. Several of the desired (but not required) criteria for the measurement head have not yet been met. In particular, monitoring and recording the rotational speed in realtime. Currently, the speed is set via a potentiometer on the motor control board, but all the speed regulation is handled internally, without any data about the position, speed or acceleration of the shaft being output. That position, speed and acceleration data would be useful in determining the types of interactions that occur between the workpiece and platen (smooth hydrodynamic flow, stick-slip, etc.).

There was also a desire to measure axial vibrations on the tool during loose abrasive finishing. Such vibrations might influence the surface roughness and/or the depth of subsurface damage that is induced. Placing an accelerometer on the tool/workpiece holder provides some additional challenges, requiring either a slip ring to connect power and signal to the accelerometer (which is rotating) or a wireless accelerometer. At the time of the design, either of these components would have increased the mass of the LAP measurement head, reducing the overall working volume.

Whatever outputs are available from the measurement head, another key avenue for advancement is integrating those outputs with control of the IRB-140 6-axis robot. The robot provides a flexible mechanical platform and software platform for future use and is capable of receiving signal inputs from external devices to affect changes in its behavior via programs. Work done by Rahul Vajarapanu in the UNC Charlotte Polishing Lab, established how these inputs could be used to control the robot and assessed the accuracy of those controls. While intermediate steps would be required, having the robot read the axial load and keep it within a specified range would be a reasonable goal to continue pushing the capabilities of the robot.

8.2.2 Recommended Larger Projects

The following projects are important to further investigation into material removal mechanisms during loose abrasive polishing in general and subsurface damage in particular. They do require an investment of time and expertise from resources outside the polishing group at UNC Charlotte.

Upgrades to Confocal Fluorescence Microscope for Assessing SSD

The confocal microscope has been a critical tool in this research for investigating the suitability of using quantum dots as a fluorescent tags for assessing subsurface damage in glass and YAG samples which have been lapped and polished. If further research into subsurface damage is to be done with the microscope, it could benefit from augmentations in both the sample stage and the optics.

Unfortunately at the time of writing (late Summer 2009), the sample stage has suffered a malfunction which does not permit the fine piezo control of the focal plane

position. This leaves focal plane adjustments to be handled with an 80 threads per inch screw, which comes out to roughly 318 μm per rotation. Assuming that an operator could reliably produce 5° turns of the screw, there would be 4.5 μm between the optical slices. Consistency would be a major concern, particularly given that such manual adjustments would take place in the dark during imaging, with no visual references available. For this reason, further investigations with the confocal microscope would necessitate repairs to the existing sample stage to recover the previous performance for sectioning images or a new sample stage with similar performance. If a new stage were built it should a) be able to consistently adjust the focal plane with 0.25 μm increments, b) have a linear range of motion of 50 μm, and c) readily adjusted through a voltage control or ideally a software interface.

The excitation side of the optics setup is more than sufficient in its current configuration for continued work investigating polishing mechanisms with quantum dots. A couple of small augmentations on the detection side however could greatly increase the capability of the system in assessing the presence and depth of subsurface damage. The first such augmentation is a variable aperture pinhole for the detector. The pinhole plays a crucial role in determining the sensitivity of the microscope to out of plane fluorescence. A variable aperture pinhole would allow for a large aperture when initially establishing focus, which lets more light to the detector when trying to assess whether fluorescence is present. Once fluorescence was detected, a reducing the aperture would increase the sharpness of the image due to the increased rejection of out of focus fluorescence. Such a device provides improvements in throughput

compared to a fixed small aperture pinhole, where determining the surface is difficult and fluorescent sites can be missed all together if the focus is not perfect. It also provides improvements compared to a fixed large aperture, where the limited rejection of out of plane fluorescence makes determination of the peak fluorescence and thus the location of fluorescence difficult.

The detector filtering on the detector should also be shifted from a long pass filter to a bandpass filter. The longpass filter was used in these experiments because of a proven track record with this confocal microscope with the other experiments involving quantum dots. The longpass filter however allows light scatter from the laser at wavelengths above the cutoff to make it back to the detector. This scatter contributes to higher background readings that obscure the fluorescent signal of the quantum dots. A bandpass filter in contrast would attenuate any scatter at wavelengths above and below the cutoffs for the filter, allowing only the wavelengths corresponding to the quantum dot through. Such a filter is required to take full advantage of the tuneability and narrow emission spectra of the quantum dots.

One place where laser scatter is useful however is in determining the location of the surface. As the laser beam focuses on the surface, there is a rise in the fluorescence which is detected due to the scatter off the surface. At this stage, it would be useful to block the contribution of any fluorescing material which complicates determination of this rise. Thus a bandstop tuned to the emission spectra of the quantum dots would be helpful at this stage to quickly and clearly determine the samples surface. Thus an arrangement of where a bandpass and bandstop filter (both tuned to the emission

spectra of the quantum dots being used) could be readily interchanged would be ideal for future studies.

Cross Departmental Collaborations for Investigating Material Removal Mechanisms

As discussed in the literature review, the material removal mechanisms hypothesized for loose abrasive finishing spans several disciplines. Understanding all of these mechanisms requires competence in the areas of chemistry, colloidal science, surface interaction, material science, fracture and indentation. If there is significant research in material removal mechanisms going forward, it would be wise to assemble a multidisciplinary group to serve as a sounding board for ideas and experiments. While any researcher would still need to develop proficiency in these disciplines on their own, such a group could serve as advisors to determine the relative importance of any one proposed mechanism for a system. Most importantly, this group could help to educate one another on critical details that they unaware that they do not know. Such an education could save countless hours in the lab and in analysis. UNC Charlotte is well positioned to create such an interdisciplinary group by drawing on resources within the faculty within the departments of mechanical engineering, optical science, and nanoscale science.

REFERENCES

1. Machinery's Handbook, 20 ed. (Industrial Press, Inc., New York, NY, 1978).

2. Tool Engineers Handbook (McGraw-Hill, New York, 1959).

3. Mark's Standard Handbook for Mechanical Engineers, 9 ed. (McGraw-Hill, Inc., New York, 1987).

4. P. J. Lu, "Scratching the Surface of Polishing Physics," Junior Paper (Princeton University, 1999).

5. P. J. Lu, N. Yao, J. F. So, G. E. Harlow, J. F. Lu, G. F. Wang, and P. M. Chaikin, "The Earliest Use of Corundrum and Diamond in Prehistoric China," Achaeometry **47**, 1-12 (2005).

6. R. O. Woods, "Clear as Glass," Mechanical Engineering, 2006, pp. 38-41.

7. I. Newton, Opticks: Treatise of the Reflections, Refractions, Inflections and Colours of Light, 4th edition ed. (1730).

8. Rayleigh, "Polish," Proceedings of the Royal Institute of Great Britain (1901).

9. Rayleigh, "The Surface Layer of Polished Silica and Glass with Further Studies on Optical Contact," Proceedings of the Royal Society of London. Series A, Mathematical and Physical Sciences **160**, 507-526 (1937).

10. W. H. Peake and T. L. Oliver, " The Response of Terrestrial Surfaces at Microwave Frequencies," (Ohio State University, Electroscience Laboratory, Columbus, Ohio, 1971).

11. S. Kalpakjian and S. R. Schmid, Manufacturing Processe for Engineering Materials, 4 ed. (Prentice Hall, 2003).

12. "PERFORMANCE SPECIFICATION: OPTICAL COMPONENTS FOR FIRE CONTROL INSTRUMENTS; GENERAL SPECIFICATION GOVERNING THE MANUFACTURE, ASSEMBLY, AND INSPECTION OF," in MIL-PRF-13830B, D. o. Defense, ed. (1997).

13. A. Lindquist, S. D. Jacobs, and A. Feltz, "Surface Preparations for Rapid Measurement of Sub-surface Damage Depth," in Science of Optical Finishing Topical Meeting, 1990),

14. F. Y. Genin, A. Salleo, T. V. Pistor, and L. L. Chase, "Role of light intensitification by cracks in optical breakdown on surfaces," J. Opt. Soc. Am. A **18**, 2607-2616 (2001).

15. G. T. Beilby, Aggregation and Flow of Solids (Macmillan and Company Limited, London, 1921).

16. C. J. Evans, E. Paul, D. A. Dornfeld, D. A. Lucca, G. Bryne, M. Tricard, F. Klocke, O. Dambon, and B. A. Mullany, "Material Removal Mechanisms in Lapping and Polishing," CIRP Annals **52**(2003).

17. G. T. Beilby, Transactions of the Optical Society **9**(1907).

18. J. W. French, "More Notes on Glass Grinding and Polishing," Transactions of the Optical Society.

19. J. W. French, "The Polishing of Surfaces," Nature **119**, 527 (1927).

20. J. M. Macaulay, "The Polishing of Surfaces," Nature **118**, 339 (1926).

21. F. P. Bowden and T. P. Hugher, "Physical Properties of Surfaces IV-Polishing, Surface Flow and the Formation of the Beilby Layer," Proceedings of the Royal Society of London. Series A, Mathematical and Physical Sciences **160**, 575-587 (1937).

22. G. O. Rawstron, "The nature of polished glass surfaces," Journal of the Society of Glass Technology, 253-260 (1958).

23. W. C. Levengood and W. E. Fowler, "Morphology of Fractures in Polished Glass Surfaces," Journal of the American Ceramic Society **40**, 31-34 (1957).

24. N. K. Adam, "The Polishing of Surfaces," Nature **119**, 162-163 (1927).

25. F. W. Preston, "The theory and design of plate glass polishing machines," J. Soc. Glass Technol **11**, 214-256 (1927).

26. L. M. Cook, "Chemical Processes in Glass Polishing," Journal of Non-Crystalline Solids **120**, 152-171 (1990).

27. N. J. Brown, "Some Speculations on the Mechanisms of Abrasive Grinding and Polishing (pre-print)," in Fourth International Precision Engineering Seminar, (Lawrence Livermore National Laboratory, 1987),

28. "Slurry Particle Size Evolution During the Polishing of Optical Glass," LLE Review **61**, 25-39.

29. A. A. Tesar, B. A. Fuchs, and P. P. Hed, "Examination of the polished character of fused silica," Applied Optics **31**, 7164-7172 (1992).

30. A. A. Tesar, B. A. Fuchs, and P. P. Hed, "Improvements in the polishing of fused silica," Applied Optics **30**, 4459 (1991).

31. E. Paul, "need to double check this reference...conflicting page numbers," Journal of the Electrochemical Society **148**(2001).

32. E. Paul, "A Model of Chemical Mechanical Polishing II. Polishing Pressure and Speed," Journal of the Electrochemical Society **149**, G305-G308 (2002).

33. E. Paul, "A Model of Copper CMP," Journal of the Electrochemical Society **152**, G322-G328 (2005).

34. E. Paul and R. Vacassy, "A Model of CMP III. Inhibitors," Journal of the Electrochemical Society **150**, G739-G743 (2003).

35. J. Luo and D. A. Dornfeld, "Material Removal Mechanism in Chemical Mechanical Polishing: Theory and Modeling," IEEE Transactions on Semiconductor Manufacture **14**, 22 (2001).

36. J. Luo and D. A. Dornfeld, "Effects of Abrasive Size Distribution in Chemical Mechanical Planarization: Modeling an Verification," IEEE Transactions on Semiconductor Manufacture **16**, 469-476 (2003).

37. J. Luo, D. A. Dornfeld, Z. Mao, and E. Hwang, "Integrated Model for Chemical-Mechanical Polishing Based on A Comprehensive Material Removal Model," in Sixth International Conference on Chemical-Mechanical Polish (CMP) Planarization for ULSI Multilevel Interconnection (CMP-MIC), (Santa Clara, CA, 2001).

38. A. Landis, "FACTORS INFLUENCING MATERIAL REMOVAL AND SURFACE FINISH OF THE POLISHING OF SILICA GLASSES," (UNC Charlotte, Charlotte, NC, 2006).

39. T. Suratwala, R. Steele, M. D. Feit, L. Wong, P. Miller, J. Menapace, and P. Davis, "Effect of rogue particles in the subsurface damaged of fused silica during grinding/polishing," Journal of Non-Crystalline Solids **354**, 2023-2037 (2008).

40. H. J. Kim, H. Y. Kim, H. D. Jeong, E. S. Lee, and Y. J. Shin, "Friction and thermal phenomena in chemical mechanical polishing," Journal of Materials Processing Technology **130-131**, 334-338 (2002).

41. B. A. Mullany, "Chemical Mechanical Polishing of Oxide Coated Silicon Wafers," (University College Dublin, Dublin, Ireland, 2002).

42. D. J. Stein and D. L. Hetherington, "Prediction of Tungsten CMP Pad Life Using Blanket Removal Rate Data and Endpoint Data Obtained from Process

Temperature and Carrier Motor Current Measurements," Proceedings of SPIE **3742**, 112-119 (1999).

43. S. E. Grillo, J. E. Field, and F. M. van Bouwelen, "Diamond polishing: the dependency of friction and wear on crystal orientation," J. Phys. D: Appl. Phys. **33**, 985-990 (2000).

44. X. Nie, W. W. Chen, A. A. Wereszczak, and D. W. Templeton, "Effect of Loading Rate and Surface Conditions on the Flexural Strength of Borosilicate Glass," J. Am. Ceram. Soc. **92**, 1287-1295 (2009).

45. P. P. Hed, D. F. Edwards, and J. B. Davis, "Subsurface Damage in Optical Materials: Origin, Measurement and Removal," Applied Optics (1989).

46. D. W. Camp, M. R. Kozlowski, L. M. Sheehan, M. A. Nichols, M. Dovik, R. Raether, and I. Thomas, "Subsurface damage and polish compound affects the 355-nm laser damage threshold of fused silica surfaces," Proceedings of SPIE **3244**, 356-364 (1998).

47. B. R. Lawn and T. R. Wilshaw, "Review Indentation Fracture: principles and applications," Journal of Material Science **10**, 1049-1081 (1975).

48. J. C. Lambropoulos, Y. Li, P. Fukenbusch, and J. Ruckman, "Non-contact estimate of grinding-induced subsurface damage," Proceedings of SPIE **3782**, 41-50 (1999).

49. G. M. Hamilton and L. E. Goodman, "The stress field created by circular sliding contact," Journal of Applied Mechanics **33**, 371 (1966).

50. J. C. Lambropoulos, S. Xu, and T. Fang, "Loose abrasive lapping hardness of optical glass and it's interpretation," Applied Optics **36**, 1501-1516 (1997).

51. "Subsurface Damage in Microgrinding Glasses," LLE Review **73**(1997).

52. B. R. Lawn, Fracture of Brittle Solids, 2nd ed., Cambridge Solid State Science Series (1993).

53. E. Brinksmeier, "State of the art of non-destructive measurement of sub-surface material properties and damages," Precision Engineering **11**, 211-224 (1989).

54. D. A. Lucca, E. Brinksmeier, and G. Goch, "Progress in Assessing Surface and Subsurface Integrity," Annals of the CIRP **47**, 669-693 (1998).

55. J. Shen, S. Liu, K. YI, H. He, J. Shao, and Z. Fan, "Subsurface damage in optical substrates," Optik **116**, 288-294 (2005).

56. F. W. Preston, "The Structure of Abraded Glass Surfaces," Transactions of the Optical Society **23**, 142-164 (1922).

57. F. K. Aleinikov, "The Effect of Certain Physical and Mechanical Properties on the Grinding of Brittle Materials," Sov. Phys. Tech. Phys. **27**, 2529-2538 (1957).

58. D. F. Edwards and P. P. Hed, "Optical glass fabrication technology. 1: Fine grinding mechanism using bound diamond abrasives," Applied Optics **26**, 4670-4676 (1987).

59. P. E. Miller, T. I. Suratwala, L. L. Wong, M. D. Feit, J. A. Menapace, P. J. Davis, and R. A. Steele, "The Distribution of Subsurface Damage in Fused Silica," Proceedings of SPIE **5991**(2005).

60. J. C. Lambropoulos, "From Abrasive Size to Subsurface Damage in Grinding," (Optical Society of America, Washington D.C.,, 2000).

61. K. R. Fine, R. Garbe, T. Gip, and Q. Nguyen, "Non-destructive, real time direct measurement of subsurface damage," Proceedings of SPIE **5799**, 105-110 (2005).

62. J. Neauport, P. Cormont, P. Legros, C. Ambard, and J. Destribats, "Imaging subsurface damage of grinded fused silica optics by confocal fluorescence microscopy," Optics Express **17**, 3543-3554 (2009).

63. P. A. Temple, "Total internal reflection microscopy: a surface inspection technique," Applied Optics **20**, 2656-2664 (1981).

64. S. N. Jabr, "Total internal reflection microscopy: inspection of surfaces of high bulk scatter materials," Applied Optics **24**, 1689-1692 (1985).

65. L. M. Sheehan, M. R. Kozlowski, and D. W. Camp, "Application of Total Internal Reflection Microscopy for Laser Damage Studies on Fused Silica," in XXIX Annual Symposium on Optical Materials for High Power Lasers, (Boulder, CO, 1997).

66. C. F. Kranenberg and K. C. Jungling, "Subsurface damage identification in optically transparent materials using a nondestructive method," Applied Optics **33**, 4248-4253 (1994).

67. R.-J. M. v. d. Bijl, O. W. Fahnle, H. v. Brug, and J. J. M. Braat, "In-process monitoring of grinding and polishing of optical surfaces," Applied Optics **39**, 3300-3303 (2000).

68. A. During, M. Commandré, C. Fossati, B. Bertussi, J.-Y. Natoli, J.-L. Rullier, H. e. Bercegol, and P. Bouchut, "Integrated photothermal microscope and laser damage test facility for in-situ investigation of nanodefect induced damage," Optics Express **11**, 2497-2501 (2003).

69. B. Bertussi, J.-Y. Natoli, and M. Commandré, "High-resolution photothermal microscope: a sensitive tool for the detection of isolated absorbing defects in optical coatings," Applied Optics **45**, 1410-1415 (2006).

70. Z. L. Wu, L. Sheehan, and M. R. Kozlowski, "Laser modulated scattering as a nondestructive evaluation tool for defect inspection in optical materials for high power laser applications," Optics Express **3**, 376-383 (1998).

71. D. A. Lucca, R. L. Rhorer, C. J. Maggiore, and Y. W. Seo, "Assessment of Subsurface Damage in Ultraprecision-Machined CdS by Ion Channeling," Annals of the CIRP **44**, 513-516 (1995).

72. D. A. Lucca, C. J. Wetteland, A. Misra, M. J. Klopfstein, M. Nastasi, C. J. Maggiore, and J. R. Tesmer, "Assessment of subsurface damage in polished II–VI semiconductors by ion channeling," Nuclear Instruments and Methods in Physics Research B **219-220**, 611-617 (2004).

73. G. S. Lodha, K. Yamashita, H. Kunieda, Y. Tawara, J. Yu, Y. Namba, and J. M. Bennett, "Effect of surface roughness and subsurface damage on grazing-incidence x-ray scattering and specular reflectance," Applied Optics **37**, 5239-5252 (1998).

74. "Magnetorheological Finishing-A Deterministic Process for Optics Manufacturing," LLE Review **63**, 135-144.

75. J. A. Randi, J. C. Lambropoulos, and S. D. Jacobs, "Subsurface damage in some single crystalline optical materials," Applied Optics **44**, 2241-2249 (2005).

76. "Subsurface Damage and Microstructure Development in Precision Microground Hard Ceramics Using MRF Spots," LLE Review **110**, 98-114.

77. M. Abramowitz, Microscopes: Basics and Beyond (Olympus America Inc., Melville, NY, 2003), Vol. 1.

78. R. Hocken, N. Chakraborty, and C. Brown, "Optical Metrology of Surfaces," CIRP annals **54**, 705-719 (2005).

79. Interferogram Interpretation and Evaluation Handbook, 4th ed. (Zygo Corporation, Middlefield, CT, 1993).

80. "A Practical Guide to SPM: Scanning Probe Microscopy," (Veeco, 2005).

81. B. Herman, V. E. C. Frolich, J. R. Lakowicz, D. B. Murphy, K. R. Spring, and M. W. Davidson, "Basic Concepts in Fluorescence" (2003), retrieved 1 January 2009, 2009,

http://micro.magnet.fsu.edu/primer/techniques/fluorescence/fluorescenceintro.html.

82. M. Minsky, "Microscopy Apparatus," 3013467 (1961).

83. D. E. Wolf, "What is the Confocal Volume?", retrieved October 1, 2008, 2008, www.fcsxpert.com.

84. S. Rüttinger, V. Buschmann, B. Krämer, R. Erdmann, R. Macdonald, and F. Koberling, "Determination of the Confocal Volume for Quantitative Fluorescence Correlation Spectroscopy," Proceedings of SPIE **6630**(2007).

85. D. Semwogerere and E. R. Weeks, "Confocal Microscopy," in Encyclopedia of Biomaterials and Biomedical Engineering (Taylor & Francis, 2005).

86. A. J. Winn, A. R. Boccaccini, N. Imam, and P. A. Trusty, "Examination of microhardness indentation-induced subsurface damage in alumina platelet reinforced borosilicate glass using confocal scanning laser microscopy," Journal of Microscopy **186**, 35-40 (1997).

87. "Fluorescence SpectraViewer" (Invitrogen Corporation), retrieved 22-Aug-2009, 2009, http://www.invitrogen.com/site/us/en/home/support/Research-Tools/Fluorescence-SpectraViewer.html.

88. "Biography of Louis E. Brus," Proceedings of the National Academy of Sciences **102**, 1277-1279 (2005).

89. T. Jamieson, R. Bakhshi, D. Petrova, R. Pocock, M. Imani, and A. M. Seifaliana, "Biological applications of quantum dots," Biomaterials **28**, 4717-4732 (2007).

90. A. M. Iga, J. H. P. Robertson, M. C.Winslet, and A. M. Seifalian, "Clinical Potential of Quantum Dots," Journal of Biomedicine and Biotechnology **2007**(2007).

91. "The future of fluorescence: Qdot nanocrystal technology" (Invitrogen), retrieved 1-January-2009, 2009.

92. "Soda Lime Glass 0215 Corning Glass Slides" (Ted Pella Inc.), retrieved www.tedpella.com/technote_html/0215%corning%20glass.pdf.

93. "Neodymium: Yttrium Aluminum Garnet," (Northtrop Grumman Synoptics, 2003).

94. "Polishing Pad Selection Guide," (Pace Technologies).

95. F. Lin, K. E. Elliott, W. Parker, N. Chakraborty, C. S. Teo, S. T. Smith, G. D. Elliott, and P. J. Moyer, "Confocal and force probe imaging system for simultaneous

three-dimensional optical and mechanical spectroscopic evaluation of biological samples," Review of Scientific Instruments **80**, 055110-055111-055110-055117 (2009).

96. K. Elliott, "Development of a Versatile Scanning System for Multi-Probe Biomedical Measurements," (University of North Carolina at Charlotte, Charlotte, NC, 2008).

97. R. Feldman, Y. Shimony, E. Lebiusha, and Y. Golan, "Effect of hot acid etching on the mechanical strength of ground YAG laser elements," Journal of Physics and Chemistry of Solids **69**, 839-846 (2007).

98. M. Gerber and T. Graf, "Optimum parameters to etch Nd:YAG crystals with orthophosphoric acid H3PO4," Optics & Laser Technology **33**, 449-453 (2001).

99. "Quantum Dots Features" (Evident Technologies, 2008), retrieved April 14, 2008, http://www.evidenttech.com/quantum-dots-explained/quantum-dot-features.html.

100. R. A. Bowling, in Particle on Surface I, K. L. Mittal, ed. (New York, 1988).

101. M. Wautelet, "Scaling laws in the macro-, micro- and nanoworlds," European Journal of Physics **22**, 601-611 (2001).

102. B. V. Derjaguin, V. M. Muller, and Y. P. Toporov, "Effect of contact deformations on the adhesion of particles," Journal of Colloid Interface Science **53**, 314 (1975).

103. D. Tabor, "Surface forces and surface interactions," J. Colloidal Interface Sci. **58**(1977).

104. G. M. Burdick, N. S. Berman, and S. P. Beaudoin, "Describing hydrodynamic particle removal from surfaces using the particle Reynolds number," Journal of Nanoparticle Research **3**, 455-467 (2001).

105. K. L. Johnson, K. Kendall, and A. D. Roberts, "Surface energy and the contact of elastic solids," Proc. R. Soc. London A **324**, 301-311 (1971).

106. Y.-P. Zhao, X. Shi, and W. J. Li, "Effect of Work of Adhesion on Nanoindentation," Rev. Adv. Mater. Sci. **5**, 348-353 (2003).

107. J. Visser, "Particle Adhesion and Removal: A Review," Particulate science and technology **13**, 169-196 (1995).

108. F. Zhang and A. A. Busnaina, "Submicron particle removal in post-oxide chemical–mechanical planarization (CMP) cleaning," Applied Physics A. Material Science and Processing **69**, 437-440 (1999).

109. A. A. Busnaina, H. Lin, N. Moumen, J.-w. Feng, and J. Taylor, "Particle Adhesion and Removal Mechanisms in Post-CMP Cleaning Processes," IEEE Transactions on Semiconductor Manufacture **15**, 374-382 (2002).

110. L. Bergstrom, "Hamaker constants of inorganic materials," Advances in Colloid and Interface Science **70**, 125-169 (1997).

111. "Nanomaterials catalog Vol 7," (Evident Technologies, 2005).

112. Z. Wang, L. L. Daemen, Y. Zhao, C. S. Zha, R. T. Down, X. Wang, Z. L. Wang, and R. J. Hemley, "Morphology-tuned wurtzite-type ZnS nanobelts," Nature Materials **4**, 922-927 (2005).

113. "Zinc Sulfide Specifications" (ISP OPTICS), retrieved www.ispoptics.com.

114. "Soda Lime Glass 0215 Corning Glass Slides," in Technical Notes, (Ted Pella Inc.).

115. E. L. Cusser, Diffusion: Mass transfer in fluid systems (Cambridge University Press, New York, NY, 1984).

116. E. Kubaki, "The Dirt on Cleaning Optics," Photonics Spectra, March, 2006.

117. W. B. Williams, B. A. Mullany, M. H. Randles, P. Moyer, and W. C. Parker, "Characterizing Quantum Dots for use in Detecting Subsurface Damage," in Proceedings of of the 23rd Annual Meeting of the American Society for Precision Engineering, (American Society for Precision Engineering, 2008), 440-443.

118. M. Hines, Evident Technologies, Troy, NY (personal communication, 2008).

119. M. R. Kozlowski, I. Hutcheon, J. Carr, L. Sheehan, D. Camp, and M. Yan, "Depth profiling of polishing-induced contamination on fused silica surfaces," Proceedings of SPIE **3244**(1997).

120. P. P. Hed and D. F. Edwards, "Relationship between subsurface damage depth and surface roughness during grinding glass with diamond tools," Applied Optics **26**, 2491 (1987).

121. J. Yoshiyama, F. Y. Genin, A. Salleo, I. Thomas, M. R. Kozlowski, L. M. Sheehan, I. D. Hutcheon, and D. W. Camp, "A Study of the Effects of Polishing, Etching, Cleaving and Water Leaching on the UV Laser Damage of Fused Silica," Proceedings of SPIE (1997).

122. T. KAMIMURA, S. AKAMATSU, H. HORIBE, H. SHIBA, S. MOTOKOSHI, T. SAKAMOTO, T. JITSUNO, T. OKAMATO, and K. YOSHIDA, "Enhancement of Surface-Damage Resistance by Removing Subsurface Damage in Fused Silica and

Its Dependence on Wavelength," Japanese Journal of Applied Physics **43**, L1229-1231 (2004).

123. "IRB 140 Industrial Robot" (ABB Robotics, 2009), retrieved www.abb.com/robotics.

124. Ensinger-Hyde, "Delrin" (2007), retrieved 2009, http://eiecomprod.shopforplastics.com/Ensinger/pdfs/delrin.pdf.

125. M. D. Feit and A. M. Rubenchik, "Influence of Subsurface cracks on Laser Induced Surface Damage," Proceedings of SPIE - The International Society for Optical Engineering **5273**, 264-272 (2003).

APPENDIX A: MATLAB CODE FIAT.M

```
% fiat
% Fluorescent Image Analysis Tool Sep 2008
% based on the threshb, confocalb and confocals programs
% batch file processing of confocal images
% divides by threshold value in the control sample to normalize the data
% based on the TiffAverage Program
% used to read in ASCII File Data
% Wesley B. Williams
% updated 12-Jan-09

%% Notes
% make sure program is in the same directory as the file
% projected outputs -mean value and standard deviation
% updated 20-March-2008 to improve speed of operation
% vectorizing some of the operations to reduce the use of for loops
% currently intended for ASCII files with headers
% mostly tested with ASCII files with headers
% updated 2-Apr-2008 following testing to solve problem w/ exporting
% surface plots to JPEG format
%
% updated to use same structure as batch processing in June-2008
% updated in June 2008 to include threshold value for normalization,
% use 1 for no threshold value
% updated July-2008 to include filename, scan rate and datascale collection
% updated Sep-2008 to make log plots on the histograms and add granularity
% to the histograms
% update late Sep-2008 to use constant scalebar for graphs

clear;
home;
%% Start the file gathering code here
disp('Confocal Image Analysis---W. Williams updated March-08')
disp('use Ctrl-C to break out if program locks')
disp(' ')
disp('The following files will be processed in this job.')
disp('They should be ASCII files w/ headers still attached.')
disp('The filename should be MMDDYY##')
files=dir('*.txt');
dir('*.txt');
%% Allows for a single file to be selected instead of all that are in the
%% directory
singlef=input('analyze only a single file (y/n) ?','s');
if singlef=='y'
   files=[];
   singlefname=input('input single filename ', 's');
   files.name=singlefname;
end
%% allows for common scaling of the output images
tmaxyn=input('do you want to set the colorbar maximum for the fluorescence maps? (y/n) ','s');
if tmaxyn=='y'
```

```
   tmax=input('enter a max value for the colorbar ');
end
%
datafile=input('filename to save numerical results?  ','s');
threshold=input('input threshold value?  ');
for bloop=1:numel(files)
   n=files(bloop).name;  %sets the filename for the routine

%
%% start routine code below here
disp(' ');
disp('Confocal Image Analysis---W. Williams updated March-08')
disp('use Ctrl-C to break out if program locks')

tic

disp('processing file');
disp(n);disp(' ');
%% collect the filename number as a variable
fnum=n;
for i=1:4;fnum(:,9)=[];end;
cc=1:6;fnum(:,cc)=[];
fnum=str2num(fnum);
%%
o=2;
if o==1
   % removed from batch processing
elseif o==2
   % nhead=357;  %number of header lines to skip
   ncols=256;  %default number of columns in the data set
   fin = fopen(n,'r');
   % for i=1:nhead,  buffer = fgetl(fin);  end
     for bump=1:500
      buffer=fgets(fin);
      % bump  % used to test the loop
      space=double(buffer);
      % need to check for scan rate
      if space (1,2)==83  % looks for a 'S' in the 2nd character
         if space(1,7)==114 % looks for a 'r' in the 7th character
            if space(1,8)==97 % looks for an 'a' in the 8th character
               scanrate=space;
               for count=1:12
                  scanrate(:,1)=[]; %removes the first 12 characters
               end
               sr=char(scanrate);sr2=str2num(sr);
            end
         end
      end
      if space(1,3)==90  %looks for a "Z" in the 3rd character
         if space(1,5)==109  %looks for a "m" in the 5th character
            dscale=space;
            count=1:26;dscale(:,count)=[];
            dscale=char(dscale);dscale=str2num(dscale);
```

```
        end
      end

      % check for the blank line after the header
      if space(1,1)==32
        break
      end
    end

    %  Read in the x-y data.  Use the vectorized fscanf function to load all
    %  numerical values into one vector.  Then reshape this vector into a
    %  matrix before copying it into the x and y matrices for return.
    Z = fscanf(fin,'%f');  %  Load the numerical values into one long vector
    fclose('all');
    nd = length(Z);       %  total number of data points
    if nd==262144   %resets the number of columns if the data is 512x512
      ncols=512
    else if nd==16384
        ncols=128
    end
    nr = nd/ncols;           %  number of rows; check (next statement) to make sure
    Z = reshape(Z,ncols,nr)';   %  notice the transpose operator

end

%adjust the offset by adding 32767 to the values
a=size(Z);b=a(1,1);c=a(1,2);
Z=Z+32767*ones(b,c);
   %Z=Z*(3.17/10.71); %corrects for scan rate difference on 10-Dec-07

%% divide by the threshold
Z=Z/threshold;
b=find(Z<=1);
Z(b)=[0];

%% calculate average
pts=a(1,1)*a(1,2);
total=sum(sum(Z)');
average=total/pts;

%% calculate std deviation
Y=reshape(Z,1,[]);a=size(Y);
sd=std(Y);
%% calculate the maximum and minimum
%Y=reshape(Z,1,[]);a=size(Y);
MaxVal=max(Y);
MinVal=min(Y);
%% calculate the # of non-zero values
disp('Warning...with 512x512 data sets, the current step can take 10+ minutes')

NZdata=Y;
% using the find function instead of the previous loop and boolean test to
% remove the zero values from the NZ data.  Seems to provided a notable
```

```
% increase in the speed June-11-08
b=find(NZdata==0);
NZdata(:,b)=[];

nztot=size(NZdata);NonZero=100*nztot(1,2)/pts;

%% calculate stats on the NZdata
NZmean=mean(NZdata);if NonZero==0;NZmean=0;end
NZmed=median(NZdata);if NonZero==0;NZmed=0;end
%NZmode=mode(NZdata);
NZmode=2;
b=size(NZdata);
%NZ2=ones(1,b(1,2));
%for k=1:b(1,2)
%    NZ2(k)=(NZdata(k)-NZmean)^2;
%end
%NZsd=(sum(NZ2)/b(1,2))^.5;
NZsd=std(NZdata);

disp(' ')
ValueS=[fnum average sd MaxVal MinVal NonZero NZmean NZmed NZsd sr2 dscale];
disp(ValueS);
disp('  file# | Average | Std Dev |  Max | Min | Non Zero% | NZ mean | NZ med | NZ sd | scanrate |
Dscale')
% matrix to send to the text file for analysis

%% plot routine for image and histogram
%g=input('Plot the file? (y/n)','s');
g='y';
if max(Y)==0
   g='n';
   fn=double(n); %convert the filename to a double
   for ct=1:8;trial(1,ct)=fn(1,ct);end  %takes the first 8 characters
   jfile=char(trial);
end
if g=='y'
   figure(1)  %resets the graphical output to Figure 1
   Z=reshape(Z,ncols,[]);
   mesh(Z);view(0,90);
   %title(n,'Fontsize',16);axis equal;axis off;colorbar;
   %xlabel('50 microns');ylabel('50 microns');
   binvec=MinVal:1:MaxVal;
   %add the following code to provide greater granularity on the threshold
   %plots
   if threshold>1
      binvec=MinVal:(MaxVal-MinVal)/100:MaxVal;
   end
   %end added code
   q=a(1,2);  %the number of points in the data set
   [nval,xout]=hist(Y,binvec);  %creates the freq data for the histogram
   %nval=nval/q;  %normalizes the freq based on the number of data points
   %add the following code to provide greater granularity on the threshold
   nval=log10(nval);
```

```
    %end added code
    figure;  %creates a new figure to display the normalized histogram
    bar(xout,nval);title(n,'Fontsize',16);
    xlabel('Fluorescence Value', 'Fontsize',12);
    ylabel('log10 of # of Occurrence', 'Fontsize',12);
    if tmaxyn=='y'
       axis([-1 tmax 0 5])
    end


    % now to save the histogram to a file
    fn=double(n); %convert the filename to a double
    for ct=1:8;trial(1,ct)=fn(1,ct);end  %takes the first 8 characters
    jfile=char(trial);

    % sh=input('Save the histogram to current file? (y/n)','s');
    sh='y';
    if sh=='y'
       print('-djpeg',jfile);
    end
end

%% data saving routines
%h=input('Save data to current file? (y/n)','s');
h='y'; %hardcoding the value for massive data runs

%% save Z matrix for later use 12-Jun-09
save(jfile,'Z');
if h=='y'
    % dlmwrite(datafile, ValueS, 'Delimiter',' ','-append')
    datamat(bloop,:)=ValueS;
end
toc

% commands to generate a surface plot w/o grid lines
% commented out 2-Apr-08 to attempt to rectify printing issues
if NonZero>0 %only plot the files with values above the threshold
    figure(1)
    h=surf(Z);axis equal;axis off;
    title(n,'Fontsize',16);axis equal;axis off;colorbar;
    if tmaxyn=='y'
          caxis([0 tmax]);
    end
    colorbar;view(0,90);shading flat;colormap(hot);
    xlabel('50 microns');ylabel('50 microns');
    set(h,'LineStyle','none')
    fn=double(n); %convert the filename to a double
    for ct=1:8;trial(1,ct)=fn(1,ct);end
    trial(:,5)=[];trial(1,5)=45;j2file=char(trial);
    print ('-djpeg','-zbuffer','-r100',j2file)
end

%% Additional Code that may be of use
```

```
%the following line allows for a jpeg export that doesn't include hordes of
%missing data [2-Apr-2008]
%print -djpeg -zbuffer -r100 'filename'

%imwrite(Z,colormap(hot),'testtif','tif')
%creates a TIF of array Z using the hot colormap
%does not include scalebars or colorbar

% array for scan rate starts as
% 92 83 99 97 110 32 114 97 116 101 58 32   ---the text and spaces for
% "\Scan rate: "
%% Clearing out Variables
if singlef~='y'
   clear MaxVal MinVal NZdata NZmean NZmed NZmode NZsd NonZero ValueS Y
   clear Z a ans average b binvec buffer bump c count ct fin fn g h i jfile
   clear n ncols nd nr nval o pts q scanrate sd sh space sr total trial xout
   clear nztot
   close all %closes the figure windows
end
%%
end
end
dlmwrite(datafile, datamat);
disp(' ');disp('Batch Finished');
```

APPENDIX B: MATLAB CODE HOTSPOT.M

```
%hotspot
%to pull out the hot spot data from confocal data files
%created 9-Jun-2009
%Wesley Williams
hotthresh=input('Threshold Value');
[r,c]=find(Z>hotthresh);
[a,b]=size(r);
spotdat=[r,c];
for count=1:a
   spotdat(count,3)=Z(spotdat(count,1),spotdat(count,2));
end
spotdat
spotfile=input('filename to save numerical results?  ','s');
dlmwrite(spotfile, spotdat);
```

APPENDIX C: MATLAB CODE FIAT.M

```
%% mining program
% created by Wesley Williams
% modified on 8-Jul-2009
% to zoom in on fluorescent features in the data set
% this file must be run after fiat.m while the Z matrix of data values is
% still in memory or after the Z matrix has been loaded into memory
zrow=input('row? ');  %the location of the data feature
zcol=input('column? ');
spread=3; %the number of pixels in each direction that are pulled for the stats
Zin=Z((zrow-spread):(zrow+spread),(zcol-spread):(zcol+spread));
Zin=reshape(Zin,1,[]);
fmax=max(Zin);  %calculate the max, min, mean, and std deviation
fmin=min(Zin);
fave=mean(Zin);
fstd=std(Zin);

[fmax;fmin;fave;fstd]
% provides 2 graphs, one zoomed in around the feature and one one of the total scan area
Zin=Z((zrow-spread-10):(zrow+spread+10),(zcol-spread-10):(zcol+spread+10));
subplot(1,2,2);surf(Z);view(0,90);shading flat; axis square; axis tight; colorbar
subplot(1,2,1);surf(Zin);view(0,90);colormap(hot); shading flat; axis square; axis tight;
```

APPENDIX D: ADDITIONAL CONFOCLAL FLUORESCENCE IMAGES AND FEATURE PROFILES

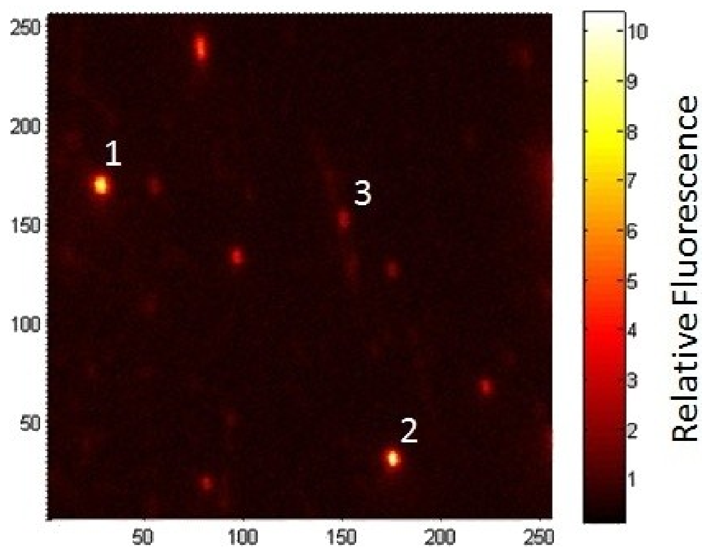

D-1. Cumulative Fluorescence Profile of a Glass LPQ sample showing several fluorescence sites.

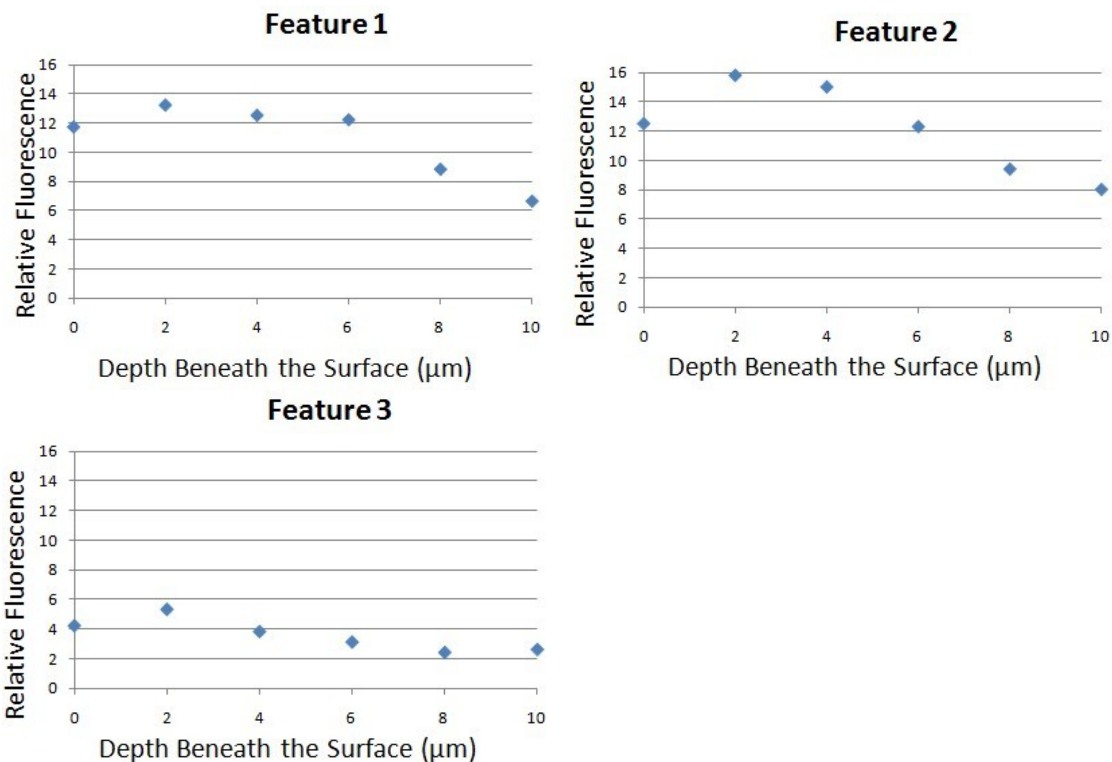

D-2. Maximum fluorescence at varied focal depths beneath the surface for features highlighted in Figure D-1.

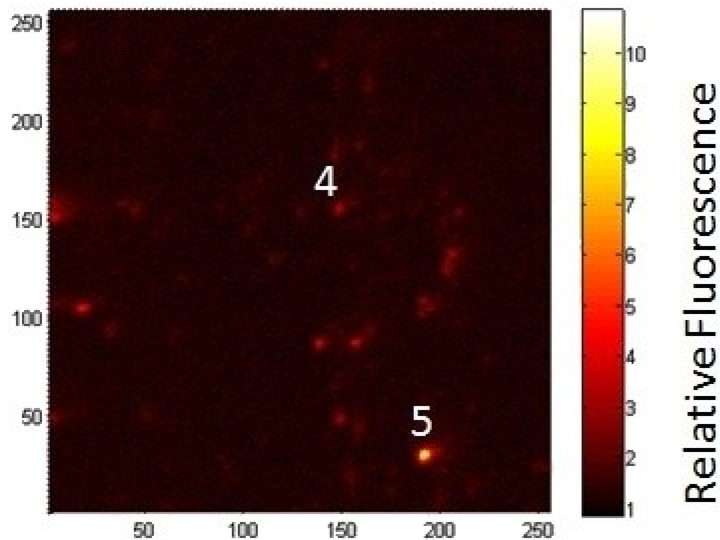

D-3. Cumulative Fluorescence Profile of a Glass LPQ sample showing several fluorescence sites.

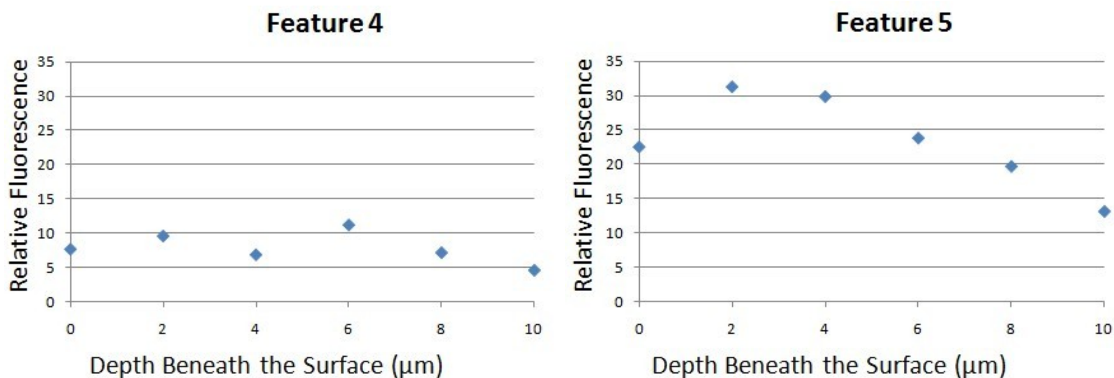

D-4. Maximum fluorescence at varied focal depths beneath the surface for features highlighted in Figure D-3.

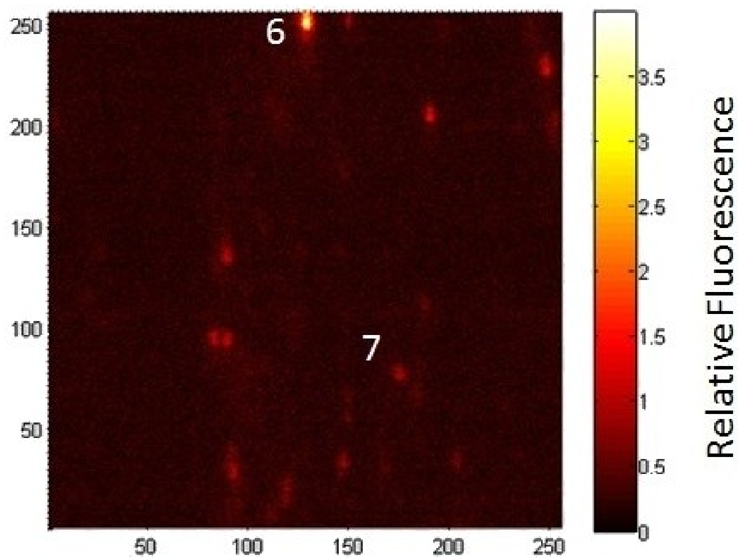

D-5. Cumulative Fluorescence Profile of a Glass LPQ sample showing several fluorescence sites.

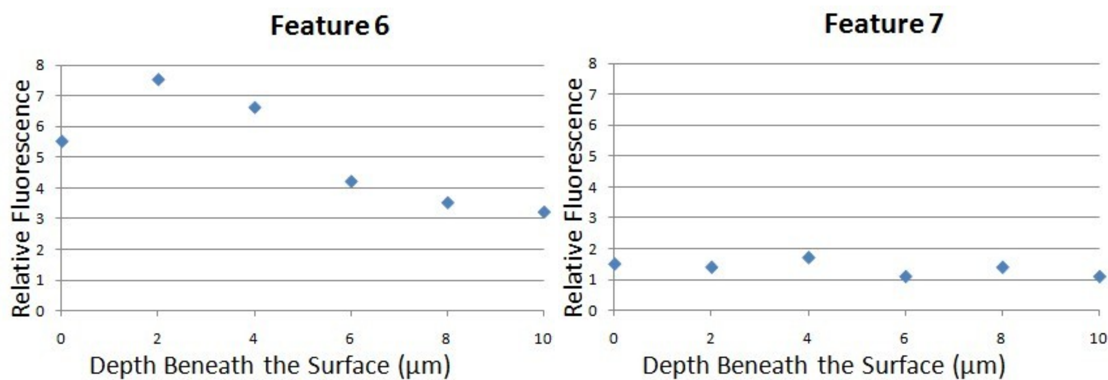

D-6. Maximum fluorescence at varied focal depths beneath the surface for features highlighted in Figure D-5.

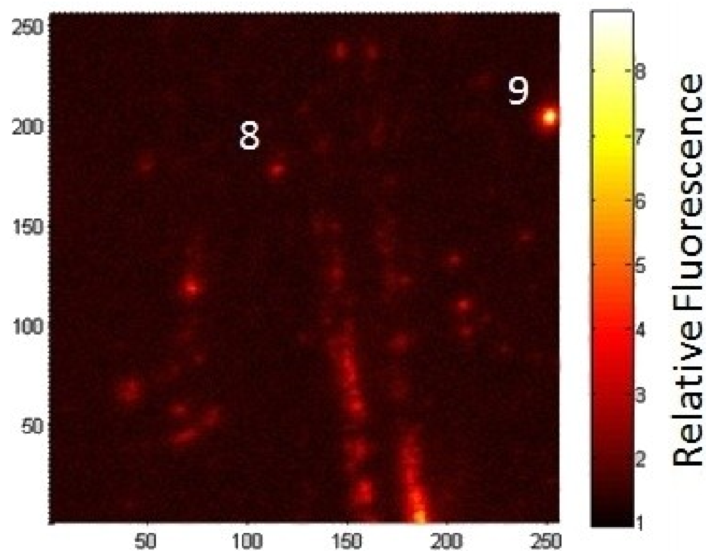

D-7. Cumulative fluorescence profile of a glass LPQ sample showing several fluorescence sites.

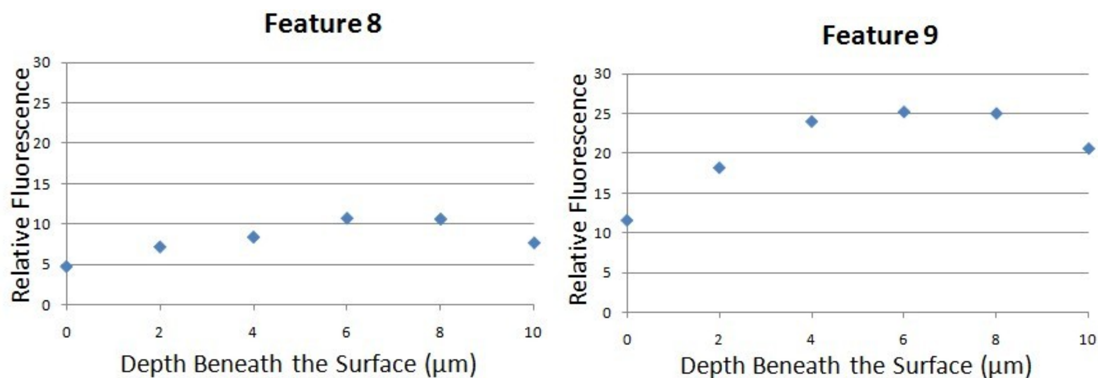

D-8. Maximum fluorescence at varied focal depths beneath the surface for features highlighted in Figure D-7.

APPENDIX E: PUBLICATIONS AND PRESENTATIONS OF THIS RESEARCH

Journal Publications

W. Williams, B. Mullany, P. Moyer, W. Parker, M. Randles, “Using Quantum dots to Tag Subsurface Damage in Lapped and Polished Glass Samples”, Applied Optics, Vol. 48, No. 28, October 2009.

Conference Proceedings

“Testing Quantum Dots as a Means of Assessing Subsurface Damage in Polished Glass”, American Society for Precision Engineering Conference, October 2009

W. Williams, B. Mullany, P.Moyer, W. Parker, "Adding quantum dots to abrasive slurries to detect subsurface damage in polished glass", Technical Digest, Optifab 2009, Rochester, TD06-34, May 2009

W. Williams, B. Mullany, M. Randles, P. Moyer, W. Parker, "Evaluating Quantum Dots as a Means to Detect Subsurface Damage in Polished Glass", Global COE First International Symposium on Atomically Controlled Fabrication, Feb 2009

B. Mullany, A. Landis, W. Williams, P. Murray, I. Roberts, “Pitch polishing of silica - Correlation between material removal rates and obtainable surface finishes”, Optifab 2007, CD 260, TD04-53, May 2007.

W. Williams, B. Mullany, “Real time Measurement of Friction and Vibration during Polishing”, American Society for Precision Engineering Conference, October 2006.

Invited Talks

"Evaluating Quantum Dots as a Means to Detect Subsurface Damage in Polished Glass" presented at the Young Researchers Workshop on Ultraprecision Machining, Osaka University, Feb 2009